The University Of Sheffield.

The interplay between cell shape and planar polarity

By:

Su Ee Tan

A thesis submitted in partial fulfilment of the requirements for the degree of Doctor of Philosophy

The University of Sheffield
Faculty of Sciences
Department of Biomedical Science

May 2019

ABSTRACT

Within the plane of epithelial sheets, there are two striking levels of organisation. One is the orderliness of cell packing, with a regular hexagonal array of cells being an example of a well-ordered state. The other is planar polarisation, which controls the coordinated orientation of cells in the plane of the epithelium, often generating highly aligned structures such hairs or trichomes.

Previous work has established that during *Drosophila* wing development, the orderliness of both planar cell packing and planar polarisation increase in concert. However, how hexagonal cell packing relates to polarisation and activity of the planar polarity proteins remain unclear. Here, I investigate the interplay between cell packing and planar polarisation in the *Drosophila* pupal wing using loss-of-function genetics, laser ablation assays, temporal control of gene expression and quantitative image analysis.

Focusing on the key “core” protein Frizzled, my findings highlight that different methods of acutely and non-acutely disrupting epithelial organisation can affect the ability of pre-existing core planar polarity protein complexes to redistribute, but do not affect the efficiency of *de novo* core protein planar polarisation. I hypothesise that this reflects a difference in the ability of cells to redistribute “stable” pre-existing complexes, as opposed to depositing them in a planar polarised pattern *de novo*. Moreover, my work establishes that global proximodistal-oriented polarity alignment correlates with directional cell junctional rearrangement and is independent of tissue organisation and cell shape.

My work also uncovers that regulation of cell shape, tissue organisation and cell junctional rearrangement are independent of the Frizzled activity during *Drosophila* pupal wing morphogenesis.

DECLARATION OF AUTHORSHIP

I, Su Ee Tan, certify that the work presented here is,

"The interplay between cell shape and planar polarity''

to the best of my knowledge and belief, original and the results of my own investigations, except as acknowledged and has not been submitted, either in part or whole, for a degree, diploma or other qualification at this or any other university or other institute of higher learning.

May 2019

CONTENTS

FIGURE INDEX

ACKNOWLEDGEMENT

First and foremost, I would like to express my deepest gratitude to my supervisor, David Strutt for giving me the opportunity to work in this interdisciplinary project and his continuous support and encouragement throughout my project, in particular with frequent discussions and helpful suggestions. I would like to thank him for giving me the opportunity to continue deepen the work and for raising my interest into developmental cell biology field. Without his guidance, technical support, moral encouragement and persistent help, this dissertation would not have been possible.

I am deeply grateful to David Strutt, Helen Strutt, Samantha Warrington, Katherine Fischer and Tan Weijie for critical reading and correcting on the revisions of this manuscript. Many thanks go to Helen Strutt, Natalia Bulgakova, Simon Fellgett, Katherine Fisher, Samantha Warrington, Elizabeth Manning and Josh Greig for their continuous help, guidance and support throughout these years.

Millions of thanks go to Suzanne Eaton for her generosity in hosting me and providing me with all the necessary resources in her laboratory to make my experiment possible. I am deeply grateful to Stephan Grill for providing me the access and technical support to the laser ablation microscope in his laboratory. I owed a huge debt of gratitude to Franz Gruber, Lokesh Pimpale, Venkatesan Iyer and Romina Piscitello-Gómez from Max Planck Institute for providing me with technical guidance in *Drosophila* pupal dissection, mounting and laser ablation.

My special thanks go to Tan Weijie for his great patience and assistance in helping me out with all those questions concerning mathematics in general. Last but not least, I would like to express my gratitude to my beloved family and friends for their continuous moral support throughout my studies and, of course, for the inspiration to do so!

This project has received funding from the European Union's Horizon 2020 research and innovation programme under the Marie Sklodowska-Curie grant agreement No *641639.*

CHAPTER 1

General Introduction

1.1 Symmetry breaking

"Monarch butterfly" by Harrelson K.D/ CC BY 2.0

Symmetry in nature such as a butterfly with its elegant wings depicts a well-balanced system, therefore it is often beautiful and astonishing. Mathematically, symmetry of a system means invariance to transformation, such as reflection, rotation, and translation, where the system appears the same from multiple viewpoints.

However, in biology, symmetry breaking along a well-defined axis is an essential mechanism to accommodate increasing complexity and functional specialization. For instance, to transform a spherical oocyte into a functional organism requires a breaking of symmetry in order to specify where is the head, the tail, the limbs, and so on. In fact, asymmetries can be observed in multiple scales ranging from molecular assemblies, to subcellular structures, to specific cell types, to tissue architecture, and embryonic body axes.

Understanding symmetry breaking in developmental biology is evidently crucial because polarised architecture is fundamental to every physiological process and required for patterning of the anterior-posterior body axis, cell fate determination due to asymmetric cell division and generation of polarised tissues [Horvitz et al., 1992; Etemad-Moghadam et al., 1995; Izumi et al., 1998; Hirokawa et al., 2009; Vladar et al., 2009; Goodrich and Strutt, 2011; Kang et al., 2015; Hale et al., 2015] and many more. One interesting example: symmetry breaking on the mammalian left-right body axis is initiated by the asymmetries in the molecular composition and orientation of cilia in the node, which then generate leftward unidirectional beating to guide flow of the extracellular fluid across a tissue that ultimately results in left-right asymmetry gene expressions [Hirokawa et al., 2009]. This unidirectional planar beating of nodal cilia is governed by the orientation of central pair microtubules within the cilia [Hirokawa et al., 2009].

Over several decades, the use of animal models such as yeast, *Caenorhabditis elegans* and *Drosophila melanogaster* have helped to shed some lights in understanding the molecular components that govern symmetry breaking processes. Combining conventional genetics, biochemistry with mathematics and physics has contributed to major breakthroughs in understanding of symmetry breaking processes. This has led to discovery of key molecular players underlying symmetry breaking in numerous animal models.

1.2 Biology of epithelial tissues

Organised establishment of asymmetries within cells, also known as cell polarisation, is essential for numerous cellular functions, such as proliferation, differentiation, migration and growth [Drubin and Nelson, 1996]. Cell polarisation generally requires spatially asymmetric localisation of molecular components to specific cellular domains. The ability to polarise is a fundamental property of many cell types, from multicellular to unicellular organisms such as yeast and protozoa. For instance, the budding yeast *Saccharomyces cerevisiae* is highly polarised and divided asymmetrically to distinguish mother cell from its daughter; migrating cells are polarised in the direction of movement, creating distinct leading and trailing structures; eggs and embryos exhibit polarised localisation of RNAs and proteins to establish anterior-posterior and dorsal-ventral axes early during development [Amberg, 1998; Akhshi et al., 2014; Campanale et al., 2017].

Multicellular tissues such as epithelial tissues exhibit two main forms of polarity: apical-basal polarity and planar polarity. The former gives rise to apical and basolateral membrane domains with different compositions and functions to establish barrier function. The latter instructs the epithelial cells to orient and align within the epithelial sheets [Goodrich and Strutt, 2011; Wallingford, 2012]. Evolutionarily, epithelia are the first tissue to emerge during ontogenesis and the most archetypal polarised tissue in metazoan organisms [Bryant and Mostov, 2008]. In mammalian system, there are over 150 epithelial and epithelial-derived-cell types that dictate key roles in proper functions of digestive, respiratory, reproductive,

neural sensory, vascular and hormonal systems [Albert, 2010]. Therefore, epithelial cells play a crucial role in developmental processes.

In the next section, I will introduce the general concept of planar polarity in epithelial cells.

1.3 Planar polarity

Planar polarity, the focus of this thesis, refers to the breaking of cellular symmetry within the plane of the epithelial sheet. The establishment of planar polarity is a common mechanism, observed across diverse species. It plays a crucial role in coordinating the polarity of a group of cells to generate highly organised or polarised structures at the level of tissues and organs, that are essential for their specialised functions. A planar polarised tissue is characterised by its highly aligned orientation of external structures, such as *Drosophila* wing hairs on the wing surface, mammalian hairs covering the body surface, bristles covering the insect epidermis or reptilian scales covering the body surface, and stereocilia bundles in the organ of Corti (Figure 1.1A, 1.1C and 1.1E) [Zallen, 2007; Goodrich and Strutt, 2011]. Planar polarity pathway has also been suggested to play a role in coordinating the behaviour of a group of cells such as oriented cell divisions [Gong et al., 2004; Ségalen et al., 2010; Mao et al., 2011], unidirectional planar beating of cilia in the trachea and brain ventricles [Tissir et al., 2010; Vladar et al., 2012] and lung branching [Yates et al., 2010].

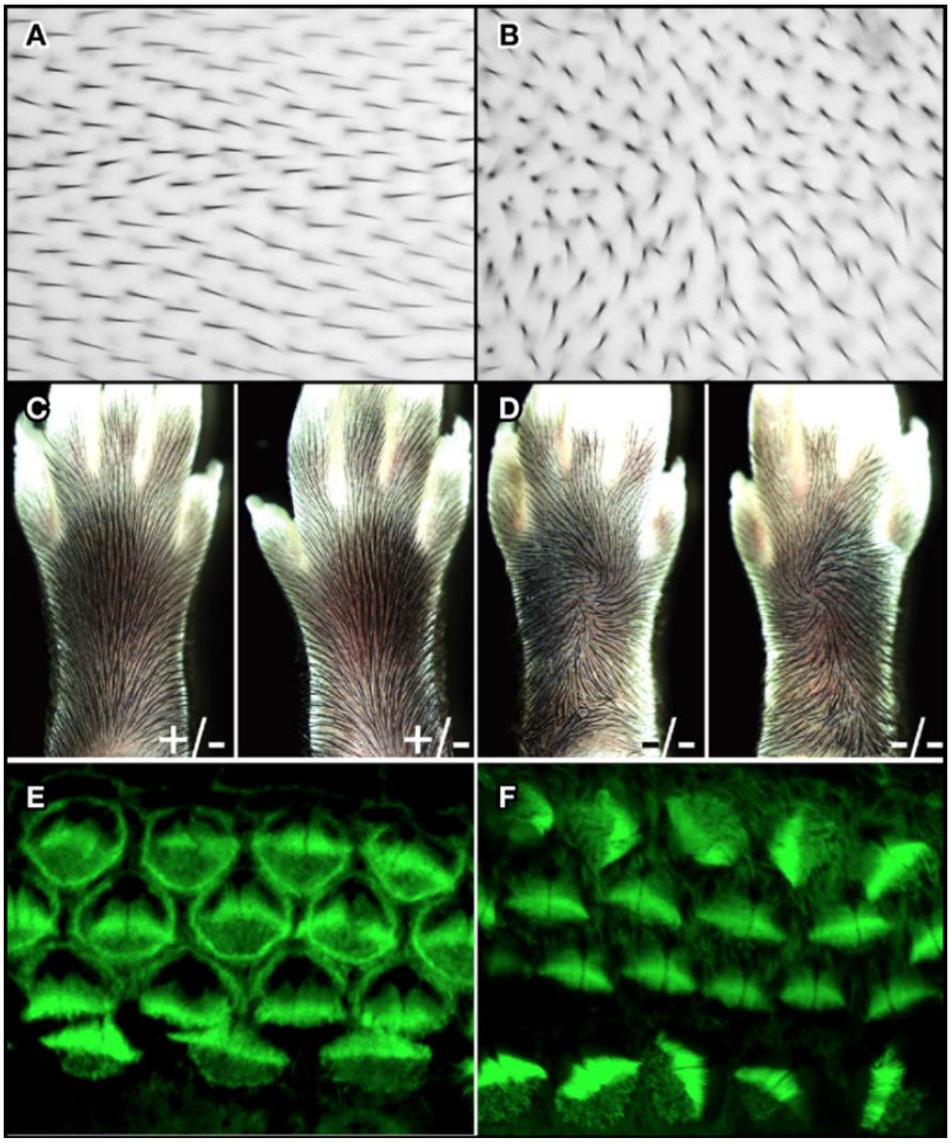

Figure 1.1: Examples of typical planar polarity features in epithelia

(A) *Drosophila* wing hairs are coherently pointed towards the distal direction of the tissue.

(B) Mutation of planar polarity components lead to disoriented wing hair placement.

(C) Proximal-distal orientations of hairs on mice paw skin in planar polarity heterozygote mutant mice.

(D) Hair swirl phenotype in planar polarity homozygote mutant mice.

(E) Alignment of actin-rich stereocilia bundles in the organ of Corti.

(F) Loss of alignment in planar polarity mutant.

Images in (A), (B), (E) and (F) reproduced with permission from [Zallen et al., 2007].

Images in (C) and (D) reused with permission from [Guo et al., 2004] Proc. Natl. Acad. Sci. USA 101, 9277– 9281. Copyright 2004, National Academy of Sciences, USA.

Discoveries over the last few decades show that the function of evolutionarily conserved planar polarity genes is also required in various processes such as convergence and extension during vertebrate gastrulation, axon guidance in the nervous system and cochlear development [Tissir and Goffinet, 2013; Sienknecht, 2015; Williams and Solnica-Krezel, 2017; Nikolopoulou et al., 2017]. Planar polarity disruption in animal models leads to incomplete closure of neural tube during embryonic development, commonly known as neural tube defects (NTDs) or *"spina bifida"* [Kibar et al., 2001; Merte et al. 2010]. Evidently, human genetic screening results revealed that mutation in these evolutionarily conserved planar polarity genes are associated with human developmental anomalies and pathologies such as congenital heart defects and neural tube defects [De Marco et al., 2014; Qiao et al., 2016; Wang et al., 2018]. Therefore, understanding the mechanisms of planar polarity signalling pathways provides opportunities in novel therapeutic development.

The fruit fly, *Drosophila melanogaster* is an ideal model organism for studying planar polarity because the insect wings are composed of a simple bilayer epithelium that forms polarised external structures known as actin-rich hairs or trichomes governed by planar polarity pathways. For my thesis, I use the well-studied pupal wing as a model system to study the role of planar polarity during wing morphogenesis. Two major pathways that govern planar polarisation behaviour in *Drosophila* wing are the "core" planar polarity and the Fat-Dachsous-Four-Jointed (Ft-Ds-Fj) system [Goodrich and Strutt, 2011; Adler, 2012; Peng et al., 2012]. Here, and henceforth, I focus predominantly on core planar polarity system as the role of Ft-Ds-Fj pathway in pupal wing morphogenesis has effects on both planar polarity and tissue growth, making it difficult to disentangle the cause-and-effect relationship between cell shape and planar polarity [Cho and Irvine, 2004; Cho et al., 2006; Mao et al., 2006; Merkel et al., 2014].

Core planar polarity genes were originally discovered in the eye and cuticle of an insect [Lawrence and Shelton, 1975; Gubb and García-Bellido, 1982]. Prior to becoming polarised in the plane of the epithelium, these core planar polarity proteins are asymmetrically distributed to opposite cell junctions. In *Drosophila* wing, this asymmetric enrichment of proteins in distinct cellular compartments within each

epithelial cell then controls the morphological asymmetry of the actin-rich trichomes. In vertebrates, these molecular asymmetries are also observed in mammalian epidermis [Devenport and Fuchs, 2008] and the stereocilia bundles in the organ of Corti [Montcouquiol et al., 2006; Deans et al., 2007; Song et al., 2010]. Mutation in core planar polarity genes causes misorientation of these cellular structures (Figure 1.1B, 1,1D and 1.1F), suggesting the importance role of core planar polarity pathway in patterning and morphogenesis during development.

Although this phenomenon is widely regarded as planar cell polarity (PCP), which refers to polarisation of single cell structures, such as fly wing hairs, in the plane of an epithelium. However, it is important to note that multicellular structures such as mammalian hair follicles, feathers and ommatidia in the fly eye also exhibit planar polarisation. Hence, I followed the general termed “planar polarity” which might be more appropriate to cover all of these.

In the following section, I will briefly introduce wing development during pupal stages. Then, I will provide an overview of the role of core planar polarity pathway during pupal wing morphogenesis.

1.4 Development of the *Drosophila* pupal wing

The *Drosophila* life cycle takes about 10 days (at 25°C) from egg to adult, although the rate of development is temperature-dependent, being more rapid at higher temperatures. The life cycle consists of four distinct stages: embryogenesis, larval stages, pupation and adulthood (Figure 1.2) [Weigmann et al., 2003]. The embryo body plan is established during embryogenesis. Once hatched, the resulting white, segmented worm (larvae) grow for approximately four days (at 25°C) while molting twice at second and third instar larval stages. The larvae then undergo puparium formation follow by metamorphosis for about 4 days (at 25°C) before eclose (emerge) to form adult flies. Female flies become sexually mature 8 to 10 hours after eclosion and ready to reproduce.

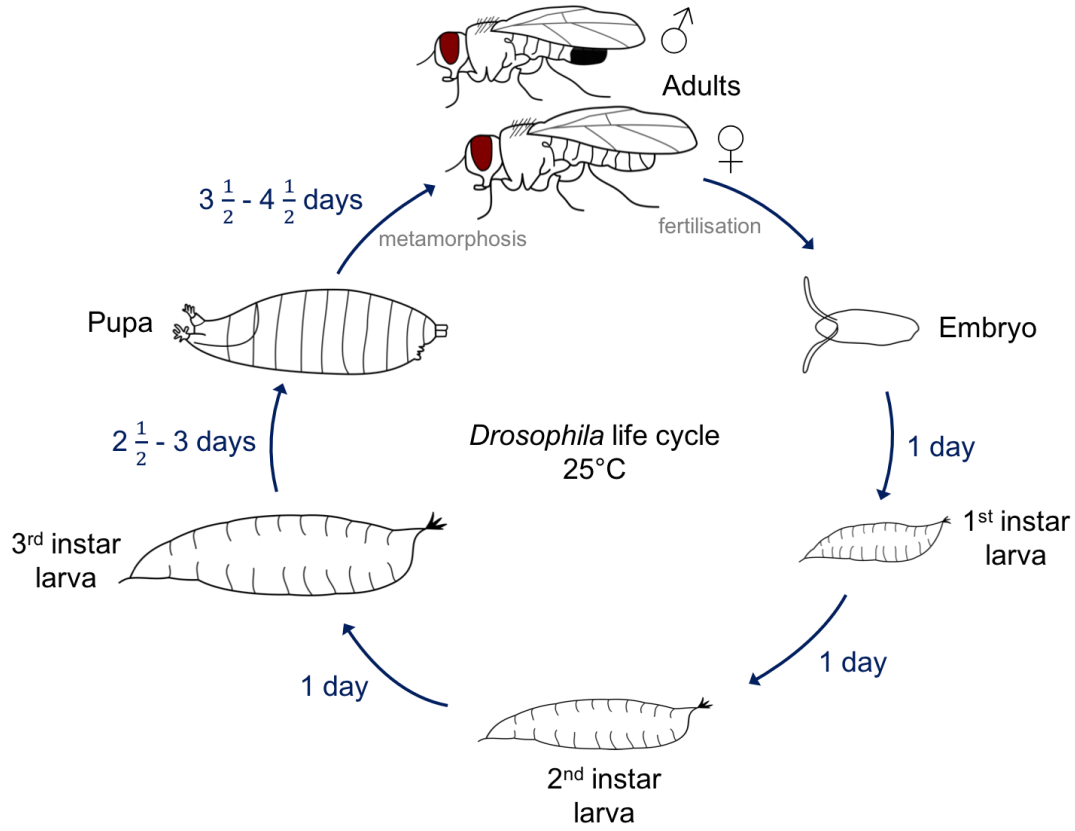

Figure 1.2: The *Drosophila melanogaster* life cycle

Schematic diagram showing the entire *Drosophila* life cycle from egg to adult. The above cycle is for temperature of about 25°C. Anterior is to the left for each stage of development.

The wing is derived from a single layered epithelium known as the wing imaginal disc in the larval stage [Fristrom and Fristrom, 1993]. At this stage, the wing disc undergoes dramatic shape changes whereby it elongates into the wing blade via an eversion process. This process produces a body wall proximally, wing hinge centrally and wing blade distally as illustrated in Figure 1.3. Cell divisions and cell rearrangements occur in parallel with the eversion process as the wing expands and changes their shape [Taylor and Adler, 2008; Kanca et al., 2014]. Shortly before puparium formation, the larva stops feeding on the food and transforms into a white prepupa when it finally comes to rest. However, this transition stage lasts only for minutes to an hour before hardening and darkening of the cuticle take place. Therefore, it can be used as an accurate developmental time to mark the beginning of puparium stage. This stage will be referred to as 0 hour after puparium formation (hAPF).

The most prominent changes in this transformation process occur in the pupal stages. During pupal stages, the initially monolayered wing disc folds along the dorsal-ventral boundary forming a double-layered epithelium [Fristrom and Fristrom, 1993]. At approximately 6 hAPF, the epithelial cells begin to secrete chitinous sheath between the bases of epithelial bilayer holding them together while the wing expands and swells [Waddington, 1939; Waddington, 1940]. The wing is made up of the hinge region and the blade region. At about 16 hAPF, as the wing hinge begins to contract, thereby reducing its apical area by half. This generates a force pulling on the wing blade resulting in a convergent-extension like elongation of the wing blade along the PD axis and shrinking along the AP axis, maintaining a constant area of the wing blade [Aigouy et al., 2010]. The fact that the wing blade does not retract upon hinge contraction led to speculation that a counterforce may be involved in this process. Indeed, it was demonstrated that there are connections between wing margin and the pupal cuticle, which act to counteract forces from hinge contraction [Etournay et al., 2015; Ray et al., 2015]. Dumpy (Dpy), which is a gigantic extracellular matrix protein, forms a fibrous meshwork that connects the wing to its overlying cuticle at various regions [Etournay et al., 2015; Ray et al., 2015]. Removal of these connections between wing blade margin and the cuticle via perturbation with UV laser ablation or by mutating Dumpy gene, both result in a significantly shorter wing

blade phenotype [Etournay et al., 2015; Ray et al., 2015].

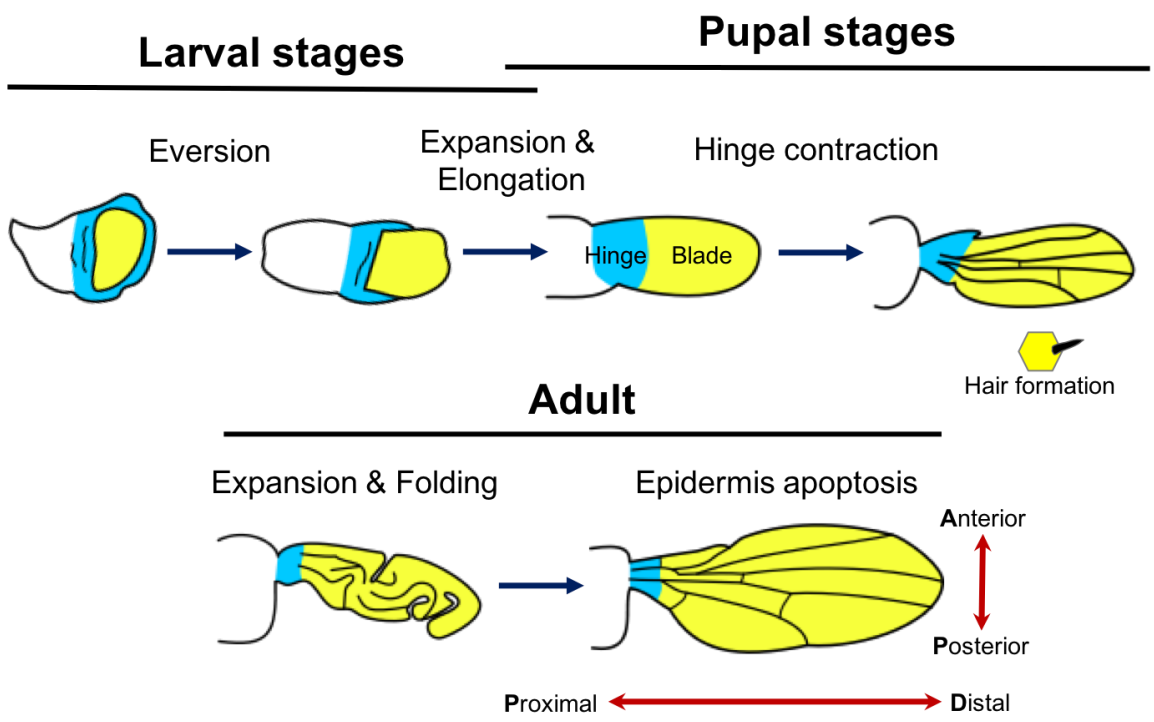

Figure 1.3: Macroscopic changes throughout *Drosophila* wing development
Illustration of wing development from wing disc to the adult wing. The adult wing is made up of two regions: wing hinge (blue) and wing blade (yellow). The anterior-posterior (AP) axis runs perpendicularly across the anterior and posterior compartments. The proximal-distal (PD) axis runs radially from the wing hinge to the tip of wing blade.
Images redrawn from [De La Loza and Thompson, 2017].

Between 18 hAPF to 30 hAPF, as the wing differentiates, vein and intervein cells become morphologically distinct and form the pattern of adult wing veins [Waddington, 1939; Waddington, 1940; Blair, 2007]. Veins are hollow tubes, filled with hemolymph and may contain tracheal tubing as well as nerves. They act as stabilising mechanical structures for flight [Wootton, 1992]. There are two distinguishable groups of veins: the longitudinal veins which originate from the hinge and bifurcate towards the wing margin and the cross veins which intersect the longitudinal veins (Figure 1.4A). During late pupal stages, there are approximately 10^4 cells on a single epithelial layer in the blade region [Blair et al., 2007]. There are three primary body axes in the wing. First, the anterior-posterior axis runs perpendicularly across the anterior and posterior compartments (Figure 1.3). Cells in each compartment share a common ancestry. Therefore, the compartmental identity

of a cell is inherited by their daughter cells. Second, the proximal-distal axis runs radially from the hinge to the tip of the wing blade (Figure 1.3). Third, the dorsoventral (DV) axis runs from the top to the bottom of the wing [Dahmann et al., 2011]. For this thesis, I standardise the wing images such that the distal of the wing is to the right and anterior is up, if not otherwise stated.

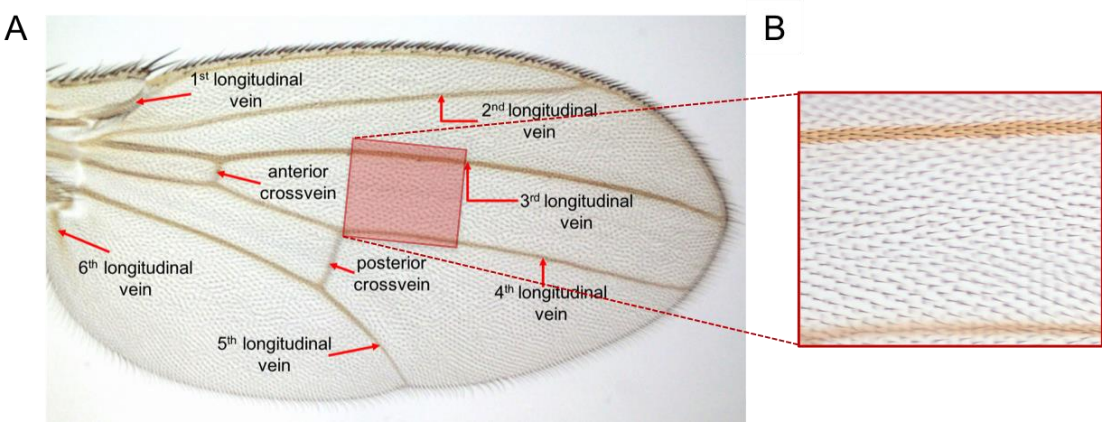

Figure 1.4: *Drosophila melanogaster* adult wing structure with labelled veins

(A) The adult fruit fly wing has a distinctive characteristic of wing veins, namely the longitudinal veins and the cross veins. There are a total of six longitudinal veins and two cross veins, which are the anterior cross vein and posterior cross vein.

(B) Wing hairs are coherently oriented towards the distal direction of the tissue.

Wing images courtesy of Helen Strutt.

The global coordinated orientation of adult wing hairs across the surface of the wing develops under the control of the planar polarity signalling pathways by instructing the position of hair initiation (Figure 1.4B). Disruption of the planar polarity signalling pathway results in misoriented wings hair [Gubb and García-Bellido, 1982]. The presence of polarised wing hairs orientation has been implicated to direct airflow smoothly past the wing during flights [Wootton, 1992].

1.5 Architecture of the core planar polarity pathway

The process of asymmetrically distributing planar polarity complexes to opposite sides of the adherens junctions, generating a coherent pattern across the tissue requires an energy investment to overcome entropy. In this section, I will discuss the active mechanisms through which such asymmetry is achieved and maintained.

1.5.1 The core planar polarity system

Drosophila wing hair polarity is governed by the core planar polarity pathway (Figure 1.5A-1.5B). Core pathway activity generates asymmetric protein distributions which provide the tissue with spatial information that aligns the cells locally. The core machinery is composed of six “core” polarity proteins including the seven-pass transmembrane proteins Frizzled (Fz; FZD in vertebrates) and Flamingo (Fmi; also known as Starry Night (Stan) or CELSR in vertebrates), the four-pass transmembrane protein Strabismus (Stbm; also known as Van Gogh (Vang) or VANGL in vertebrates) and the cytoplasmic proteins Dishevelled (Dsh; DVL in vertebrates), Prickle (Pk) and Diego (Dgo; ANKRD6 in vertebrates) (Figure 1.5C). These components are involved in amplifying asymmetries and coordinating polarisation between neighbouring cells, to produced locally aligned polarity.

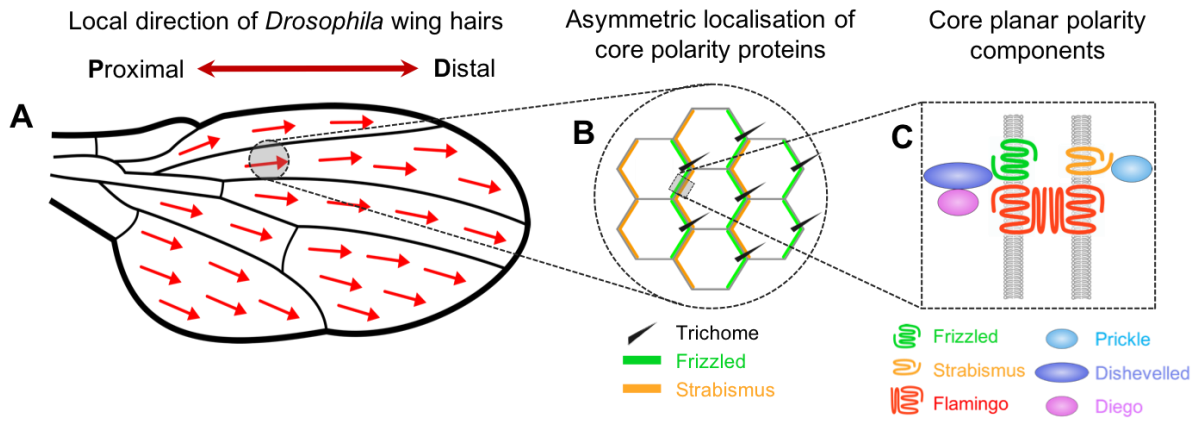

Figure 1.5: Asymmetric localisation of core planar polarity components

(A) Wing blade of the *Drosophila melanogaster*. The red arrows indicate the local wing hair orientation.

(B) Core planar polarity proteins asymmetrically localise on the opposite sides of the cell, where the placement of the trichome on the distal side of each cell is strongly colocalised with Frizzled (green). For simplicity, only the localisation of Frizzled and Strabismus (orange) on the cell junctions are shown.
(C) Asymmetric distribution of core planar polarity components along the apical cell boundaries.
Images redrawn from [Goodrich and Strutt, 2011].

The atypical cadherin Fmi was the first planar polarity protein discovered that exhibits asymmetric distribution, enriched to both proximal and distal apical cell junctions [Usui et al., 1999; Shimada et al., 2001] and formed Fmi:Fmi homodimers across junctions between cells (where ":" represents proteins binding intercellularly) [Chae et al., 1999; Usui et al., 1999]. Unipolar asymmetry was first identified as Fz [Strutt, 2001] and the cytosolic protein Dsh [Axelrod, 2001] localised on the distal cortex of each wing epithelial cell. It was later discovered that another cytosolic protein Dgo was also distally localised on the cell cortex [Das et al., 2004]. On the other hand, both Stbm and Pk are both highly enriched on the proximal end of the cell junctions [Tree et al., 2002; Bastock et al., 2003]. Importantly, cellular asymmetry localisation of all these apical core planar polarity complexes to the PD junctions is proposed to be mediated by the positive inter- and intracellular feedback loops [Usui et al.,1999; Axelrod, 2001; Strutt, 2001; Strutt et al., 2011].

The most solid proof for intercellular signalling feedback comes from the studies that clones mutant for the core proteins *fz* or *stbm* can reorganise the polarity of neighbouring non-mutant tissue, also known as domineering non-autonomy effects [Vinson and Adler, 1987; Taylor et al., 1998; Adler et al., 2000a]. Non-autonomous effects on trichome polarity in *stbm* clones causes proximal neighbouring cells to orient their hairs away the clone, whereas *fz* clones causes distal neighbouring cells to orient their hairs towards the clone [Vinson and Adler, 1987; Taylor et al., 1998; Adler et al., 1997; Adler et al., 2000a]. These observations also suggest that that cell polarity is intrinsically linked between adjacent cells, which enable local coordination of polarity independent of tissue-level cues. As elucidated by several theoretical models that polarity disruption at a clone boundary can propagate between cells [Amonlirdviman et al., 2005; Le Garrec et al., 2006].

Unlike *fz* and *stbm* mutant clones, [Chae et al., 1999; Usui et al., 1999] reported that *fmi* mutant clones do not exhibit non-autonomy effect on surrounding wild-type cells. Despite of that, Fmi has been demonstrated to involve in intercellular signalling in *Drosophila* (e.g., abdomen and wing [Lawrence et al., 2004; Strutt and Strutt, 2007]). In Fmi overexpressed clones of cells, Fz is recruited to the clone boundaries, suggesting that Fmi mediates asymmetric interaction between Fz and Stbm [Chen et al., 2008; Strutt and Strutt, 2008]. Fmi without its intracellular C-terminus results in increasing distal localisation, suggesting that the Fmi C-terminus interacts with Stbm to localise on the proximal cell junctions [Strutt and Strutt, 2008]. Additionally, Fmi co-localises with Fz on the distal junctions, suggesting that Fz interacts with Fmi:Fmi homodimers at the junctions to form Fz-Fmi:Fmi complexes (where "-" denotes proteins binding in the same cell (intracellularly), while ":" represents proteins binding intercellularly) [Strutt, 2001; Chen et al., 2008]. Fz and Stbm across cell junctions may interact intercellularly, as shown using *in vitro* assays [Wu and Mlodzik, 2008], or through Fmi [Chen et al., 2008; Lawrence et al., 2004; Strutt and Strutt, 2008]. Further evidence to support the latter is that Fz-Fmi:Fmi can form asymmetric heterodimers in the absence of Stbm. This implies that Fz and Stbm may not need to form direct intercellular interaction [Strutt & Strutt, 2008].

On the other hand, mutant clones lacking core cytoplasmic components, such as Dsh, Dgo and Pk, do not exhibit non-autonomous cell effect on surrounding wild-type cells [Lawrence et al., 2004; Strutt and Strutt, 2007]. It is likely that core cytoplasmic components play a role in autonomous cell signalling [Amonlirdviman et al., 2005; Chen et al., 2008; Strutt and Strutt, 2007]. Additionally, the function of core cytoplasmic proteins seems to be required for planar polarity later in pupal wing development, prior to wing hairs formation, whereas the function of core transmembrane proteins, such as Fmi, Fz and Stbm, are required earlier in development [Strutt and Strutt, 2002; Strutt and Strutt, 2007; Wu and Mlodzik, 2008]. This indicates the potential role of core cytoplasmic proteins in amplifying intracellular asymmetry of the transmembrane core proteins. In support of this, recent work from our lab further demonstrated that Pk acts via Stbm to stabilise Fz in neighbouring cell and via Dsh to destabilise Fz in the same cell [Warrington et al.,

2017]. It has been proposed that positive feedback interactions occur between core planar polarity complexes such that complexes with common orientation are clustered and stabilised, meanwhile, negative feedback interactions occur between core planar polarity complexes such that opposite oriented complexes are excluded and destabilised [Strutt et al., 2011; Warrington et al., 2017]. These processes are indispensable for polarised subcellular localisation of core planar polarity complexes.

Thus, taken together these results indicate that there is a correlative interdependence among core planar polarity components for feedback interactions to establish stable sorted membrane complexes [Strutt et al., 2011]. Importantly, all the core planar polarity components are indispensable for polarity amplification to take place. Disruption to any single core planar polarity protein will severely affect the asymmetric patterning, resulting in wing hairs that no longer point distally [Gubb and Garcia-Bellido, 1982; Adler et al., 1990; Adler, 1992; Wong and Adler, 1993; Usui et al., 1999; Strutt, 2001; Axelrod, 2001; Shimada et al., 2001; Feiguin et al., 2001; Adler, 2002; Tree et al., 2002; Bastock et al., 2003; Rawls and Wolff, 2003; Das et al., 2004; Strutt and Strutt, 2008].

The main morphogenetic outcome of molecular asymmetry of the core polarity protein complexes is the localisation of wing actin-rich hair (trichome) at the distal cell edge. There are a group of specific planar polarity downstream effectors that govern the distal positioning and number of wing hairs: Fuzzy (Fy), Inturned (In) and Fritz (Frtz) [Gubb and Garcia-Bellido, 1982; Wong and Adler, 1993; Park et al., 1996; Collier and Gubb, 1997; Collier et al., 2005]. These downstream effectors require the activity of core polarity proteins to be localised proximally in the cells and act to stabilise Multiple Wing Hairs (Mwh) to locally restrict actin polymerisation and bundling activities to the distal apical surface of the wing cells. [Adler et al., 2004; Strutt and Warrington, 2008; Yan et al., 2008]. In addition to downstream effectors, other proteins such as small GTPases RhoA and its effector kinase Drok, are involved in the regulation of actin dynamics to ensure distal wing hair localisation [Strutt et al., 1997; Adler et al., 2000b; Winter et al., 2001]. The polymerisation of actin and microtubules within dense “pimples” produces “a single prehair”, which emerges from the distal vertex of each epithelial cell and points parallel to the

longitudinal wing veins. Mutation of *fy*, *in* and *frtz* results in multiple wing hair outgrowth with swirling patterns [Gubb and Garcia-Bellido, 1982; Wong and Adler, 1993; Park et al., 1996; Collier and Gubb, 1997; Lee and Adler, 2002; Collier et al., 2005]. On the other hand, mutation of *mwh* results in the production of multiple wing hairs [Gubb and Garcia-Bellido, 1982].

Apart from that, it has been reported that core polarity pathway is required to regulate hexagonal cell packing during pupal wing morphogenesis [Classen et al., 2005]. During pupal wing morphogenesis, wing epithelial cells undergo junctional rearrangement that relaxes irregular packed cells into a regular hexagonal packing prior to wing hair outgrowth (see Section 1.6). These hexagonally packed array of cells then give rise to hexagonally packed hairs that are regulated by the planar polarity pathways [Classen et al., 2005]. Our lab further showed that the core polarity system plays a role in regulating E-Cadherin endocytosis, which might mediate junctional rearrangement during pupal wing morphogenesis [Warrington et al., 2013].

1.5.2 The establishment of coordinated polarity

It is generally believed that the overall coordination of planar polarisation across the tissue is determined by tissue-level global directional cues. These cues are thought to establish polarity orientation in relative to the tissue axes by biasing core protein activity across cell axes. The asymmetric distribution of core polarity components is then amplified by feedback mechanisms to reinforce the asymmetry. While the core planar polarity pathway functions to locally polarise the cells, how core planar polarity components interpret global directional cues to align cell polarity over large distance remain a subject of active investigation. Ten of millions of birds migrate across the northern hemisphere to warmer places during winter season. These birds acquire directionality information using celestial cues from the sun, the stars and by sensing the earth's magnetic field. Similarly, core planar polarity components interpret long-range or "global" cues to align cell polarity over large distance. This is further supported by theoretical modelling, which indicate that a global directional cue is needed to form long-range polarity from an initially disordered patch of cells. This has then led to model where a global tissue cue could align cells along the

tissue axes [Amonlirdviman et al., 2005; Le Garrec et al., 2006; Burak and Shraiman, 2009]. Recent works have revealed several potential global polarity cues, such as expression gradients of the Ft–Ds–Fj pathway, Wnt signalling gradients and morphogenetic forces.

The Ft-Ds-Fj pathway consists of two atypical cadherins: Fat (Ft) [Mahoney et al., 1991] and Dachsous (Ds) [Clark et al., 1995] that form heterophilic interactions with their long extracellular domains across cellular junctions (Figure 1.6A). This pathway also consists of a transmembrane kinase Four-jointed (Fj) [Villano and Katz, 1995; Brodsky and Steller, 1996] that modulates Ft and Ds binding affinity [Brittle et al., 2010; Simon et al., 2010; Hale et al., 2015] and an effector of this pathway which is an atypical myosin called Dachs [Mao et al., 2006] (Figure 1.6). Tissue-wide opposing gradients of Fj and Ds were discovered along the axis of planar polarity in the eye and wing *Drosophila*. In the fly wing specifically, these opposing gradients result in intracellular asymmetric localisation with Ds distally and Ft proximally in the cell, similar to core planar polarity asymmetry, thus making these gradients an attractive cue to establish long-range global polarity alignment across the tissue. It was speculated that Ft-Ds pathways could act as an upstream cue of the core proteins because in the absence of *ft* or *ds*, the core protein alignment was mis-orientated [Strutt and Strutt, 2002; Ma et al., 2003]. In support of this, Ft-Ds regulates the alignment of apical microtubules in wing cells [Shimada et al., 2006; Harumoto et al., 2010], which is reported to be required for directional trafficking of core polarity proteins to the PD cell junctions [Shimada et al., 2006]. Moreover, it was further demonstrated that Pk acts to uncouple core polarity and Ft-Ds-Fj pathway during tissue flow to ensure proper orientation of wing hair distally [Merkel et al., 2014].

However, there are several findings that challenged this notion. First, the orientation of core planar polarity patterns with respect to the Fj-Ds gradient varies in different tissues. In the *Drosophila* eye and anterior compartment of the abdomen, the core planar polarity system points towards high Ds expressions [Casal et al., 2002; Yang et al., 2002], meanwhile, in the *Drosophila* wing and posterior compartment of the abdomen, the core system points away from high Ds expressions [Strutt and Strutt, 2002; Ma et al., 2003; Matakatsu and Blair, 2004; Casal et al., 2006]. Second, it was

thought that Ft and Ds were important for establishing global polarity coordination because knockout of *ft* or *ds* activity results in severe wing hair swirling phenotype [Yang et al., 2002; Strutt and Strutt, 2002; Ma et al., 2003]. However, uniform expression of the gradients throughout the wing rescues the swirling wing hair phenotype except in the proximal regions and cross-veins of *Drosophila* adult wing [Simon, 2004; Matakatsu and Blair, 2004; Brittle et al., 2012; Sagner et al., 2012], suggesting that the swirling phenotype is caused by other factors such as wing overgrowth. Evidently, by suppressing overgrowth via manipulation of Wts-Hpo pathway activity, polarity defect is significantly reduced [Mao et al., 2006; Matakatsu and Blair, 2006; Feng and Irvine, 2007; Brittle et al., 2012]. Therefore, how the Ft-Ds-Fj system could be an upstream global cue for the core planar polarity system to generate long-range polarity during pupal wing morphogenesis still needs to be deciphered.

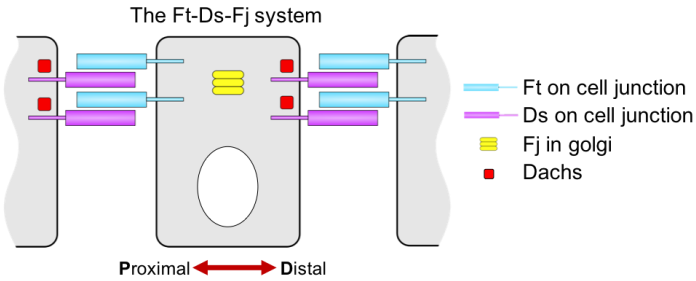

Figure 1.6: Architecture of Ft-Ds-Fj polarity system

Localisation of Ds and Ft on the distal and proximal side of the cell respectively. Dachs, a downstream effector of the Ft–Ds pathway, is asymmetrical distributed to the distal side of each cell.

Aside from the Ft-Ds-Fj system, the involvement of Wnt gradients as tissue-level global polarity cues has been very attractive since Wnt family ligands can bind to Fz family receptors [Logan and Nusse, 2004]. However, the role of Wnts in directing core planar polarity system remains controversial in *Drosophila*. Earlier studies suggest that there is evidence against the role of Wnts as polarising factors for core planar polarity system in *Drosophila* [Lawrence et al., 2002; Chen et al., 2008]. Nevertheless, there are some recent studies in vertebrates demonstrated an instructive role of Wnts acting as orientating cue for planar polarity [Chu and Sokol, 2016; Gao et al., 2018].

As tissues undergo dynamic changes in shape during growth and morphogenesis, anisotropic tensions that are generated can instruct the orientation of planar polarity patterns. Anisotropic mechanical stress has been proposed to guide the global reorientation of core planar polarity proteins along the PD axis of the wing tissue [Aigouy et al., 2010]. Polarised tissue orientation can be remodelled in response to anisotropic tension. For instance, during early *Drosophila* pupal wing morphogenesis, core proteins localise to the anterior-posterior junctions, parallel to the wing margin. However, upon proximal wing-hinge contraction, epithelial cells respond to these stresses by undergoing dramatic morphogenetic changes including cell elongation, oriented cell divisions and cell rearrangement that ultimately result in reorientation of core proteins along PD axis of the wing (Figure 1.7). These stresses can then be propagated from one epithelial cell to another throughout the entire tissue since epithelial cells are glued together with adhesive molecules. It has been demonstrated that by withdrawing the anisotropic mechanical stress from the system, for example by severing the hinge of the wing, cell flow patterns and global polarity reorientation are perturbed [Etournay et al., 2015]. This strongly suggests that anisotropic mechanical stress is required to drive tissue flows that will ultimately remodel global polarity orientation in the wing. The roles of Ft-Ds-Fj and Wnts pathways acting as global cues in *Drosophila* pupal wing have been controversial and difficult to prove, however it seems clear that the establishment of coordinated polarity pattern during late pupal wing development is due to mechanical forces.

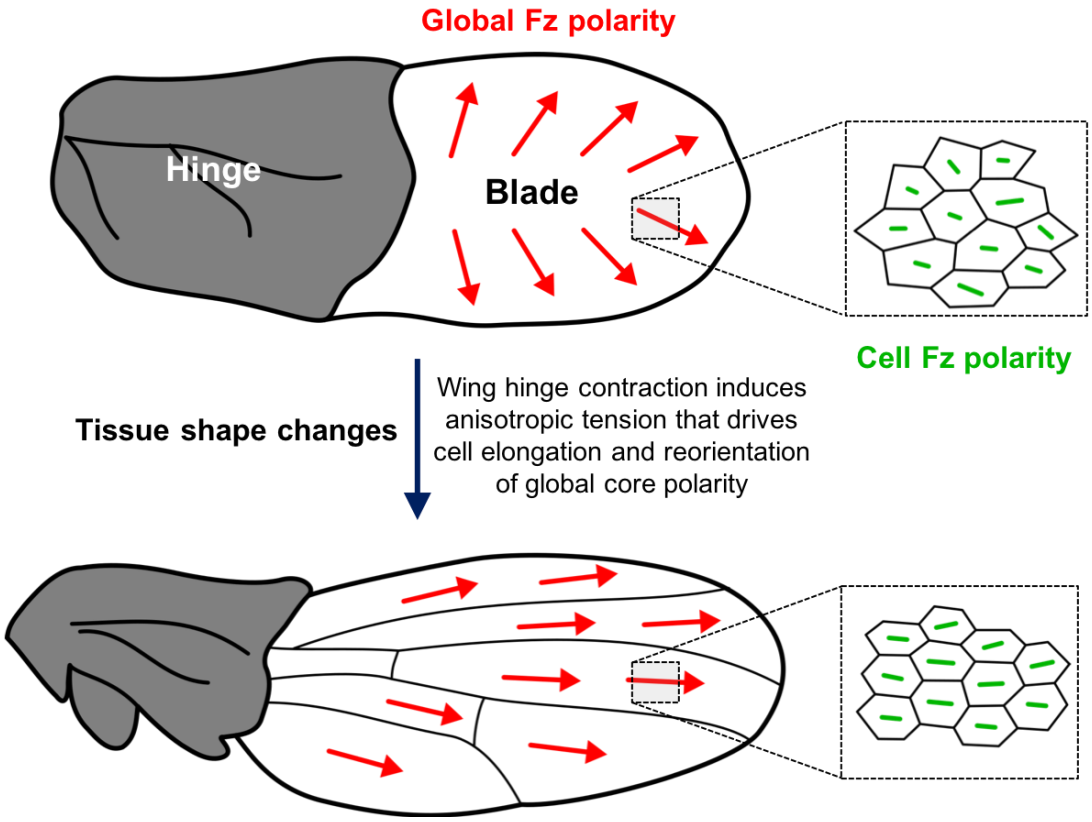

Figure 1.7: **Wing-hinge contraction induces tissue remodelling and core polarity reorientation in response to anisotropic tension**

Proximal wing-hinge contraction results in anisotropic mechanical tension that drives simultaneous active tissue remodelling such as oriented cell divisions, cell elongation and directional cell rearrangements. The changes in dramatic morphogenetic events drive the reorientation the core planar polarity from pointing towards the wing margin to pointing along the PD axis.

Images modified from [Aw et al., 2017].

1.6 Linking wing epithelial cell shape, packing and planar polarisation

To shed some light on the cues that orient core polarity proteins, the understanding of temporal dynamics of core protein polarisation in the wing is essential. Several studies have proven that core polarity proteins establish their polarity as early as the late third instar and early prepupal stages [Classen et al., 2005; Aigouy et al., 2010]. At 16 hAPF, local cell polarity along the PD axis of the wing diminishes and from 18 hAPF onwards, core polarity proteins become increasingly polarised until shortly before wing hair formation at 32 hAPF. This coincides with the beginning of dramatic morphogenetic reorganisation of the wing epithelium. Wing cells undergo oriented cell division, cell elongation and oriented cell junctional rearrangement extensively. Local cell shape changes occur in two distinct phases. During phase I (from 15 hAPF to 24 hAPF), changes in tissue shape are governed by oriented cell division and cell elongation along PD axis due to hinge-contraction [Classen et al., 2005; Aigouy et al., 2010; Etournay et al., 2015]. Cell junctional rearrangement occurs through the extension and contraction of cell-cell junctions in the apical plane, resulting in junctional exchange between neighbouring cells, which is known as T1 transition (Figure 1.8A). Due to wing margin constraints, cells mainly elongate in the anterior-posterior axis under active AP-oriented T1 transition. This is similar to convergent-extension process, in which a tissue elongates in PD direction, while shrinks in the AP axis. Cell elongation reaches its peak at around 22.5 hAPF while cell division gradually diminishes by 24 hAPF. Meanwhile, in phase II (from 24 to 32 hAPF), changes in tissue shape are governed by only PD-oriented T1 transition as elongated cells relax (Figure 1.8B). The intriguing switch of directional bias of T1 transition along PD axis results in formation of new cell junction parallel to the PD axis, thus increasing the amount of hexagonally packed cell [Aigouy et al., 2010; Etournay et al., 2015].

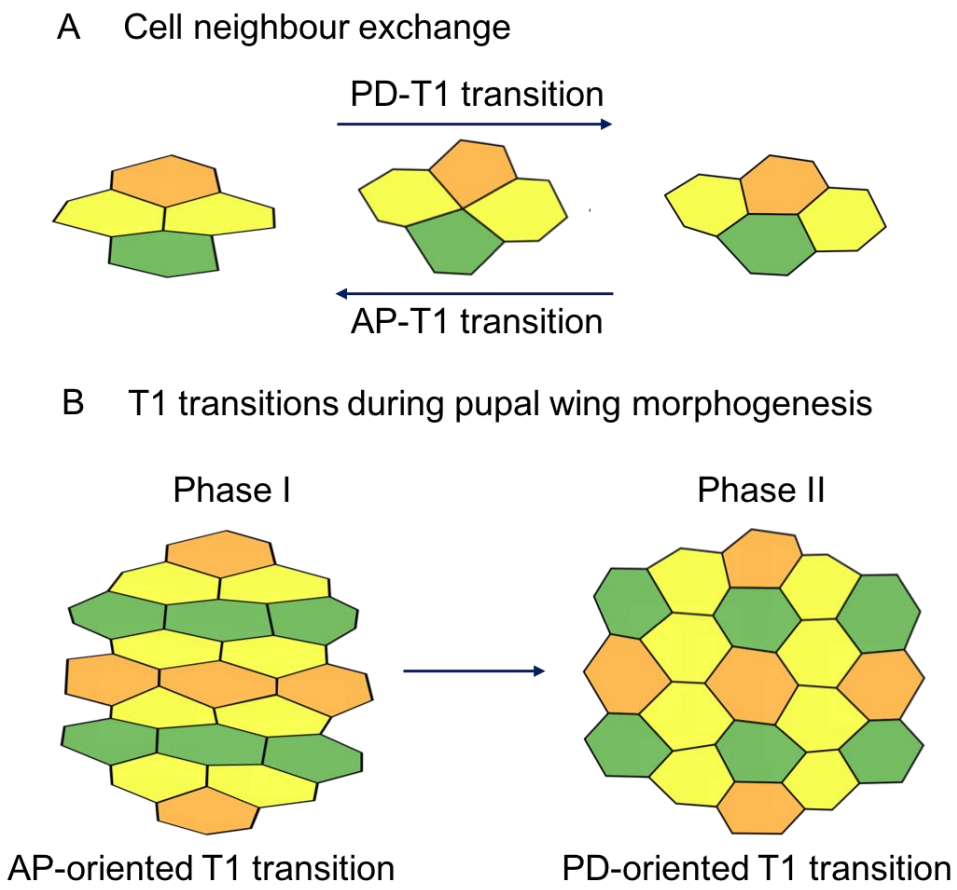

Figure 1.8: **Influence of cell junctional rearrangement (T1 transitions) on epithelial tissue shape deformation**

(A) Process of junctional remodelling or T1 transition.

(B) In phase I, hinge contraction elongates cells under AP-oriented T1 transition. As anisotropic tension gradually diminishes in phase II, PD-oriented T1 transition relaxes elongated cells.

The *Drosophila* wing epithelium consists of highly irregular cell shape and is poorly packed throughout both larval and prepupal development, whereby majority of the cells are non-hexagonal cells [Classen et al., 2005]. During pupal wing development, the wing cells become more regularly packed with a prominent increase in the fraction of hexagonal cells. By the time the wing hair emerges at approximately 32 hAPF, the wing epithelium has been repacked into an array of regular cells resembling honeycomb geometry, with approximately 80% hexagonal cells [Classen et al., 2005; Aigouy et al., 2010]. A little explanation on hexagonal packing geometry: Balance of cell pressure and cell junctional tension produces reproducible polygonal geometry (for example, the eventual fraction of hexagonal cells) in the epithelium

[Lecuit and Lenne, 2007]. For instance, a single isolated cell exhibits a spherical shape in the absence of internal or external forces. However, when cells come into contact, their cell shapes change to a non-spherical shape, to minimise contact between the cells and to reduce surface tension. This phenomenon is also observed in the two-dimensional geometry of soap bubbles, in which bubble edges form three-way vertices at 120° angles, which corresponds to a hexagonal network. Therefore, hexagonal packing geometry is favoured to achieve optimum packing with minimal surface energy [Lecuit and Lenne, 2007].

In phase I, it was demonstrated that the reorientation of core polarity is correlated with cell elongation along PD axis [Aigouy et al., 2010]. Interestingly, microtubules are aligned in parallel to the axis of cell elongation and are essential for trafficking of Fz distally in the cell, hence contributing to Fz asymmetry within a cell in phase I [Shimada et al., 2006]. Therefore, it is possible that cell shape may contribute to the asymmetric localisation of core polarity proteins within the cell. In phase II, it was speculated that PD-oriented T1 transition reorients the global core planar polarity pattern along the PD axis of the wing, as hexagonal cell packing is completed, and it remains unchanged until the prehair emerges [Aigouy et al., 2010].

1.7 Aims

The *Drosophila* pupal wing is an excellent model system to study planar polarity and tissue morphogenesis. This work will investigate the interplay between core planar polarisation and epithelial cell packing geometry in the wing epithelium. Previous work showed a temporal correlation between hexagonal cell packing and core planar polarisation during pupal wing morphogenesis [Classen et al., 2005]. Prior to wing hair formation, the magnitude of core planar protein polarisation intensifies drastically when cells achieve a regular hexagonally packed geometry (Figure 1.9). The precise temporal correlation of these events indicates the possibility of cross regulation.

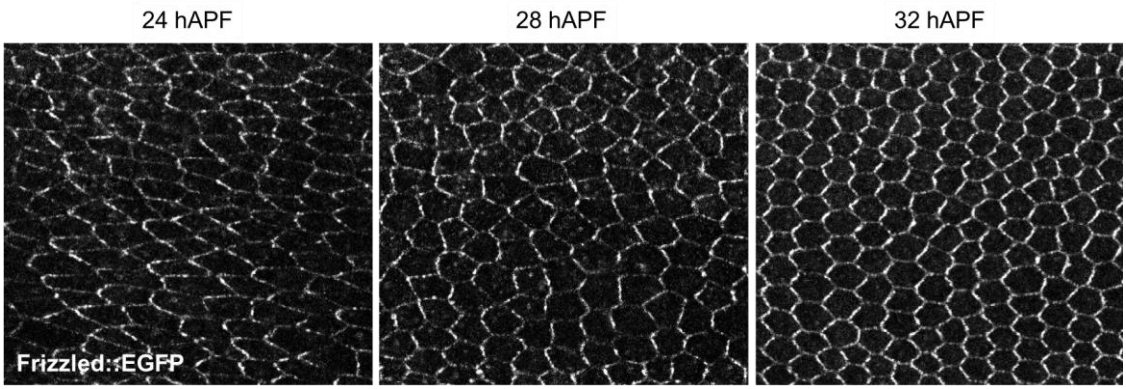

Figure 1.9: Temporal correlation between core planar polarisation and cell packing geometry at different developmental time points
Confocal images of Fz::EGFP expressing wings at 24, 28 and 32 hAPF (hour After Puparium Formation) respectively. Prior to the emergence of polarised wing hairs, Fz becomes increasingly polarised along the wing PD axis, while cells become more regular in shape and hexagonally packed.

As mentioned previously, disruption of molecular pathways that control planar polarisation can also result in reduction of hexagonal cells [Classen et al., 2005]. Conversely, it is less clear whether disruption of cell packing can reduce the ability of the tissue to planar polarise. Therefore, the question of how epithelial cell packing correlates with planar polarisation of pupal wing development and vice versa still requires further investigation. I wish to know how the planar polarisation machinery is

affected by different cell shapes, sizes and packing geometries, as a route to understanding molecular mechanisms of tissue planar polarisation.

For simplicity, I break the problem down into two inter-related questions:

I. Effects of epithelial cell packing on core planar polarisation
II. Effects of core planar polarity pathway on epithelial cell packing

As a prerequisite for this, I have developed analysis tools required for quantifying planar cell polarity, cell morphological parameters, and epithelial tissue organisation. Using these quantification tools, I first characterised the temporal correlation between core planar polarity and cell packing in different regions of wild-type pupal wings. To investigate the effects of epithelial cell packing on planar polarisation during pupal wing morphogenesis, I altered epithelial cell packing in the *Drosophila* pupal wing *in vivo* using different genetic manipulations and laser ablation assays. This allowed me to determine the causation of cell packing on core planar polarisation. Apart from that, to understand how different cell packing may affects polarity *de novo*, I used a genetic approach to temporally induce core protein expression in mutant background and allowed polarisation to establish in wings with different cell packing. With this, I hope to gain insight into how establishment of polarity *de novo* is affected by different cell packing.

To address the previously described role of core planar polarity pathway on hexagonal packing [Classen et al., 2005], I aim to quantify cell packing and tissue organisation in wild-type and core planar polarity mutant wings using time-lapse imaging and quantitative image analysis. This should provide insights into the extent of core planar polarity system involvement during pupal wing morphogenesis.

CHAPTER 2

Quantitative image analysis and computational tools

2.1 Introduction

During *Drosophila* pupal wing morphogenesis, core planar proteins become increasingly polarised from initially random distributions, as epithelial cells relax into a more regular shape and hexagonally packed prior to emergence of polarised wing hairs [Classen et al., 2005; Aigouy et al., 2010]. However, due to the lack of quantitative tools, the dynamical processes by which planar polarity is established and maintained, as cells change shape and rearrange within the plane of a tissue, has not been studied in detail. Therefore, there is an acute need for a comprehensive quantitative analysis of epithelial morphogenesis in order to address these questions.

. During development, dramatic morphogenetic events such as cell migration, proliferation, convergent extension of epithelial cells lead to striking changes in the organisation of cells [Bertet et al., 2004; Blankenship et al., 2006; Escudero et al., 2007; Farhadifar et al., 2007; Lecuit and Lenne, 2007; Pilot and Lecuit, 2005; Girdler and Roper, 2014]. It has been suggested that epithelial tissues display a degree of orderliness [Lewis, 1928]. For example, the *Drosophila* retinal epithelium is made up of highly organised and regular hexagonal cells. Similarly, the initially disorganised tissue of developing *Drosophila* pupal wing becomes highly organised with up to 80% of hexagonal cells prior to wing hair formation [Classen et al., 2005]. However, how tissues regulate their organisation during development remains unclear. This could be largely due to the lack of methodology to analyse and quantify the arrangement or organisation of a group of cells.

.

. Epithelial tissue organisation arises from local changes in cell shapes and behaviours. Majority of published quantification studies on epithelial organisation have been based predominantly on the basic geometric characteristics of individual cells such as cell area, cell eccentricity and the number of cell sides, as presented in Section 2.4.1 [Zallen and Zallen, 2004; Classen et al., 2005; Blankenship et al., 2006; Farhadifar et al., 2007; Nagpal et al., 2008; Patel et al., 2009; Kram et al., 2010; Mao et al., 2011; Escudero et al., 2011; Gibson et al., 2011; Heller et al., 2016; Sanchez-Gutierrez et al., 2016]. In spite of that, cell area, eccentricity or number of

sides per se are insufficient to clearly distinguish between organised and disorganised tissue. Recent work compares the organisation of different naturally packed tissues to mathematical tessellations generated using Centroidal Voronoi tessellations (CVT) based on their polygon distributions [Sanchez-Gutierrez et al., 2016]. However, polygon distribution alone is inadequate to characterise the degree of tissue organisation. Tissue consisting of cells with varying geometry or packing can exhibit identical polygonal distribution [Sanchez-Gutierrez et al., 2016]. Thus, there is an acute need for an objective quantification method for classifying the level of epithelial tissue organisation.

Realistically, cells are not always a perfect hexagon. During early pupal wing morphogenesis, cell shape becomes more elongated and irregular in response to anisotropic tension generated by wing-hinge contraction [Etournay et al., 2015]. Eventually, wing cells relax into a more regular geometry as tension diminishes later in development. Due to variations in cell geometry during development, it is, therefore, crucial to have an algorithm that quantifies planar cell polarity independently of cell geometry. In the sense that larger cells should not be identified as more polarised as compared to smaller cells. Similarly, more elongated cells should not be less polarised as compared to less elongated cells. There are two widely known published methods for quantifying planar polarity, namely the Fourier Series and the Ratio method [Aigouy et al., 2010; Strutt et al., 2016]. However, owing to lack of validation on these methods, it is not known whether these methods are sensitive to variations of wing epithelial cell geometry. This makes it difficult to detach the effects of cell geometry from that of an asymmetrical protein distribution. Therefore, I set out to develop a new method for quantifying planar cell polarity, independently of cell geometry.

2.2 Aims

In this chapter, I focus my attention on developing quantification methods and tools for measuring cell packing geometry and planar polarisation. In Section 2.3, I perform several key image post-processing steps on microscopy images such as cell segmentation, labelling and vertices identification. Next, I present in Section 2.4 methods for quantifying cellular level morphological parameters. Additionally, in Section 2.5, I develop a new method for quantifying the level of epithelial tissue organisation, which combines packing density and deviation of apical cell area within groups of cells to capture the degree of orderliness of any packed tissue. I validate this method on both simulated Centroidal Voronoi tessellation data and experimental data.

In Section 2.6, I develop a new method to quantify core protein localisation on cell junctions based on Principal Component Analysis (PCA). I provide comparison between different methods of quantifying planar polarity at both cellular and tissue-level scales. Additionally, I validate these polarity methods against simulated models as well as experimental data in order to evaluate the performance and accuracy of the new PCA method versus two published methods (Fourier Series and Ratio method). The quantification methods presented here based on the definition of planar polarity are essential for analysis of experimental data in the following chapters, unifying the theme of this thesis. Finally, I develop QuantifyPolarity, a user-friendly graphical user interface, for performing quantitative analysis of planar polarity.

2.3 Image post-processing

During phase II (from 24 to 32 hAPF) of pupal wing morphogenesis, cells undergo dynamic shape relaxation and junctional rearrangement into a more regular hexagonal packing. In order to study the interplay between conserved mechanisms that regulate planar polarisation and cell packing geometry, it is relevant to study the morphogenesis of pupal wing in phase II, when cell shape changes mainly occur through junctional rearrangement with negligible contributions from oriented cell divisions, cell apoptosis, cell flow, and cell elongation [Aigouy et al., 2010]. Using time-lapse imaging of cell behaviours *in vivo*, mechanisms of epithelial morphogenesis at single-cell resolution can be elucidated. Therefore, I performed *in vivo* live imaging of pupal wings for approximately 6 to 8 hours from 24 hAPF onwards. For a detailed protocol on live imaging of pupal wings, please refer to the Section 7.3 in Chapter 7. Generally, microscopy images are pixelated images containing merely intensity information. Pre-processing step are performed on these raw images, as described in Section 7.4 in Chapter 7. Next, the following post-processing steps are employed to extract useful information out of the pre-processed images (Figure 2.1A).

(i) Cell segmentation

In an image, each cell is represented by a set of pixel coordinates (x_i, y_i), where *i* refers to the pixel number, together with their corresponding pixel intensity, I_i. Cell segmentation software such as Packing Analyzer is utilised to identify cell boundaries using watershed algorithm [Aigouy et al., 2010]. This procedure semi-automatically identifies and produces a binary skeletonised representation of the cell boundaries for further image analysis (Figure 2.1B). Additional manual correction is often required to obtain precise segmentation of cell boundaries. Thus, all images are checked and corrected manually for segmentation errors such as under-segmentation and over-segmentation. Boundary cells and small cells are automatically removed based on the thresholds set by users, which vary according to the image size and specifications. This is because boundary cells do not contain all the edges, therefore, it is not possible to quantify the area or eccentricity of boundary cells.

(ii) Cell labelling and cell vertices identification

Each cell is labelled with a unique identification number (Figure 2.1C). A vertex can be determined by calculating the vertex degree, which gives information on the number of edges attached to one vertex (Figure 2.1D). The process of vertex-degree calculation is fairly simple. Firstly, the number of vertices present in each cell is detected using pattern recognition algorithm. By going through the 4-connectivity binarized image, the sum of pixels within the 3x3 neighbourhood of each foreground pixels (for a binary image, 1 is the foreground pixel and 0 is the background pixel) are determined. Therefore, the vertex degree, *k*, may be written as

$$k = n_{3\times3} - 1, \tag{1}$$

where n_{3x3} is the number of foreground pixels in the 3x3 neighbourhood.

From a biological point of view, a vertex is where multiple (i.e. three or more) edges meet. Therefore, k has to be bigger or equal to 3 in order to be considered as a vertex point. This results in a polygonal lattice of cells, in which each of the polygons consists of a unique set of vertices and edges that are crucial for further cell shape and topology analysis as well as polarity quantification in the following sections.

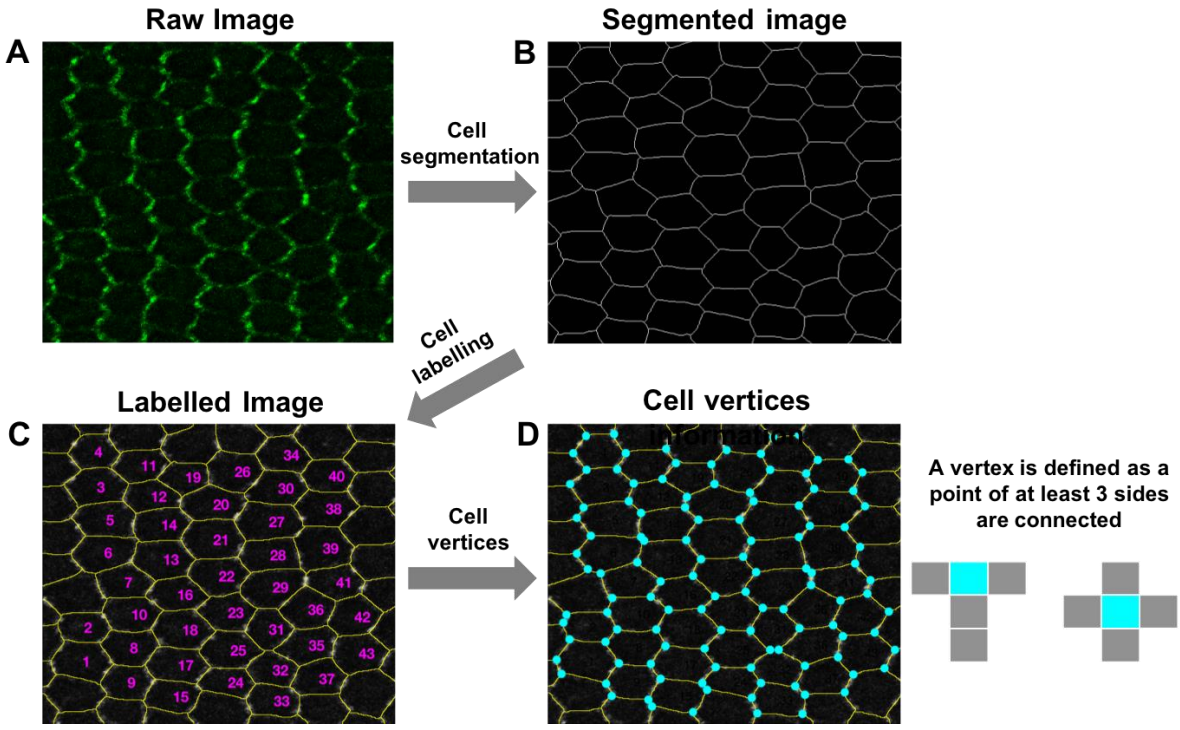

Figure 2.1: Cell segmentation, cell labelling and cell vertices identification

(A) Confocal microscopy image of pupal wing with cell apical junctions expressing the core protein, Frizzled tagged with a EGFP (Fz::EGFP) at 28 hour after prepupa formation (hAPF). This stage shows planar polarised localisation such that proximal/distal cell edges show increased intensity as compared to anterior/posterior edges. All confocal images presented in this thesis are oriented with proximal to the left and anterior at the top.

(B) A binary skeletonized mask containing cells boundaries is obtained from Packing Analyzer, a cell-segmentation software. Further descriptions of this software can be found in [Aigouy et al., 2010].

(C) Result obtained from individual cell labelling. As depicted, the yellow contour is the segmented cell boundaries overlaid onto the original image. Each cell is represented as a single object with a unique identification number (in magenta).

(D) Each vertex (in cyan) is defined as a point where at least three edges or sides are connected.

2.4 Cellular level morphological analysis

Automated image analysis tools are essential to rigorously analyse the temporal dynamics of cell shape changes over time in order to determine how changes in these properties affect planar polarisation and vice versa. The two-dimensional analysis of the apical surface of epithelial cells is sufficient to capture many predominant characteristics of cell shapes, topology (relationship with neighbours) and junctional dynamics. In this section, I will provide an in-depth description of all the cell morphological features as illustrated in Figure 2.2.

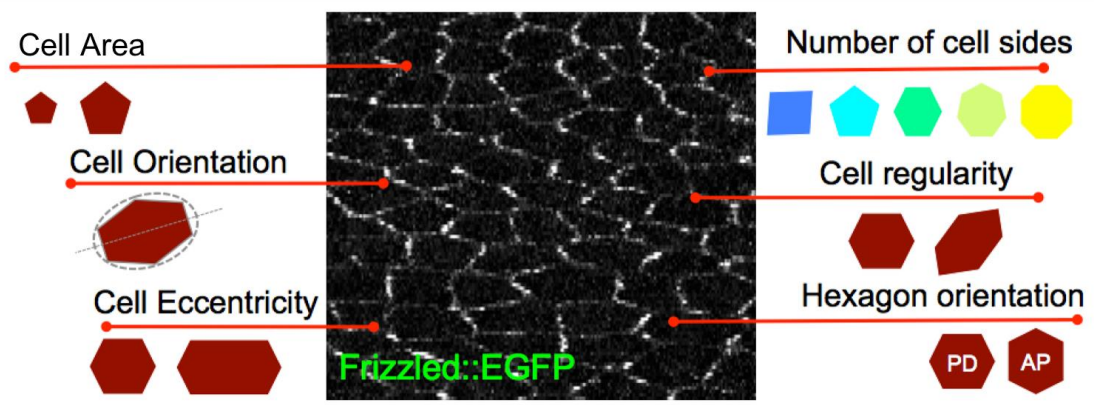

Figure 2.2: Overview of cell morphological features

List of cell morphological features that are extracted from pupal wing image for in-depth quantitative analysis of cell geometry.

2.4.1 Image analysis: Cell morphological parameters measurements

Apical cell area. This measures the apical surface of each cell, henceforth referred to as “Apical cell area”. The apical cell area (pixel^2) for each cell can be determined from the labelled images using MATLAB built-in function (“*regionprops*”).

Cell eccentricity/elongation and cell orientation. Wing epithelial cells may be more structurally elongated or eccentric at different developmental times. Hence, it is crucial to extract cell shape information, such as cell eccentricity and orientation

as illustrated in Figure 2.3A. A robust ellipse fitting approach is utilised to extract these parameters. It is a shape-based method where the cell boundaries are used as a reference landmark for ellipse fitting [Young, 2010]. Any ellipse can be described by the following (general) equation:

$$u_1x^2 + u_2y^2 + u_3xy + u_4x + u_5y + u_6 = 0, \tag{2}$$

where u_i is the unique coefficients of each distinct ellipse and (x, y) are the coordinates of the cell boundaries. The least squares method is used to determine the most optimal set of coefficients u_i for every single cell. Then, the parameters of an ellipse can be determined using the following equations:

$$a = \frac{1}{2}(u_1 + u_2) + \frac{1}{2}\sqrt{(u_1 - u_2)^2 + u_3^2}, \tag{3}$$

$$b = \frac{1}{2}(u_1 + u_2) - \frac{1}{2}\sqrt{(u_1 - u_2)^2 + u_3^2}, \tag{4}$$

$$\theta = \frac{1}{2}\tan^{-1}\left(\frac{u_3}{u_1 - u_2}\right), \tag{5}$$

where a, b are the semi-major and semi-minor axes respectively with $a \geq b$, and θ represents the ellipse or cell orientation (Figure 2.3A).

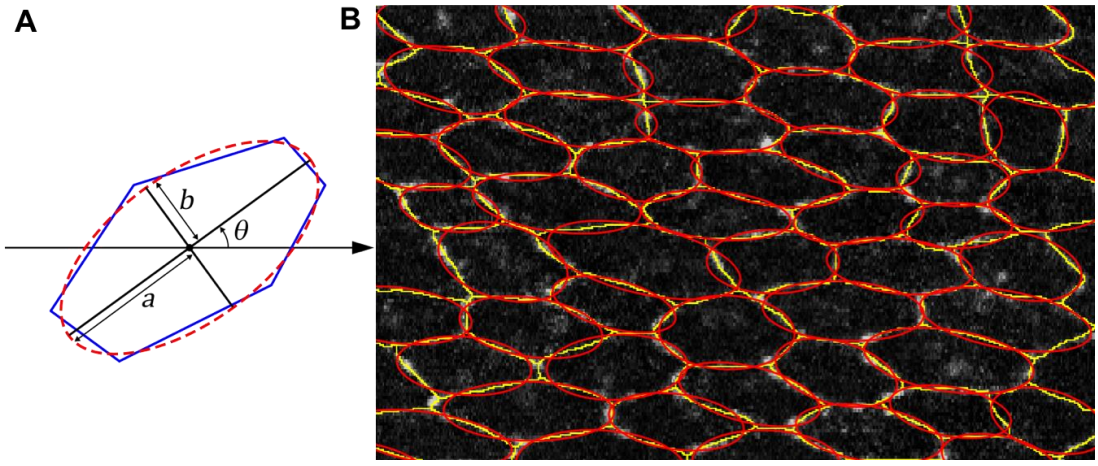

Figure 2.3: Ellipse fitting method to compute cell eccentricity and orientation

(A) A schematic representation of an ellipse (red dotted line) fitted onto a cell (blue boundary) to determine parameters such as semi-major axis a, semi-minor axis b and ellipse orientation θ.

(B) Example of an ellipse fitted onto each epithelial cell (represented by red dotted line) of wild-type wing at 24 hAPF, where cells are more eccentric as compared to later developmental time points. Cell boundaries are depicted by yellow lines.

Hence, by fitting an ellipse onto the geometry of a cell, morphological parameters including eccentricity and orientation can then be extracted. The eccentricity can be calculated using the following formula:

$$\varepsilon = 1 - \frac{b}{a}. \tag{6}$$

The value for cell eccentricity ε ranges from 0 to 1 in arbitrary units, with 0 represent no elongation (or circular) and 1 being highly eccentric. On the other hand, cell orientation, which is the ellipse orientation, has value ranges from $-90°$ to $+90°$, with $0°$ oriented along the proximal-distal (PD) axis and $\pm 90°$ oriented along anterior-posterior (AP) axis.

Number of cell sides and junctional length. A cell edge is the common boundary between two cells. Since I have already defined the location of cell vertices, cell edge length can be determined by summing up cell junction pixels between two vertices (Figure 2.4A). However, a cell side or edge that is below 10% of average cell side length will not be considered as a side of a cell. Once cell sides are defined, the number of sides which is equivalent to number of neighbouring cells can be determined (Figure 2.4B). In pupal wing, the number of sides present in each cell varies from four up to eight [Classen et al., 2005]

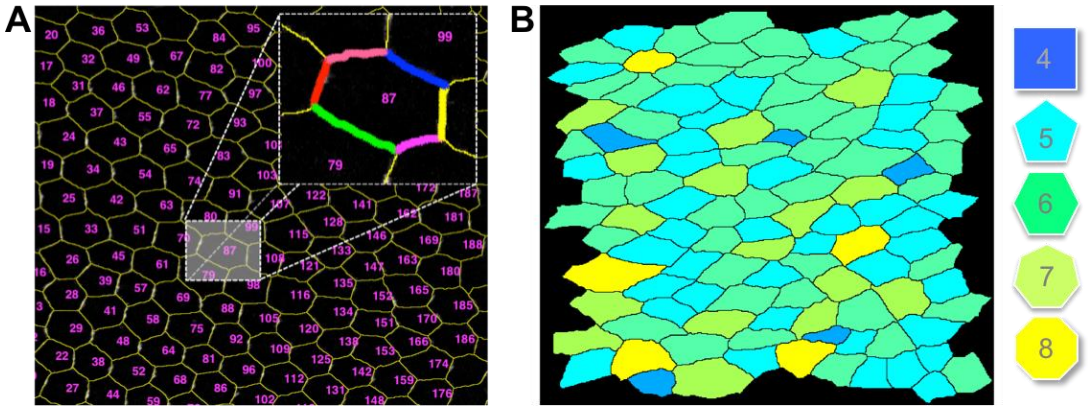

Figure 2.4: Quantification of junctional length and number of sides

(A) The individual edge or junction length between two vertices of a labelled cell is quantified and colour-coded as shown in the inset image.

(B) Quantification of number of cell sides. Each cell is classified into quadrilateral, pentagon, hexagon, heptagon and octagon classes and colour-coded as indicated.

Cell shape regularity. To quantify the shape regularity of a cell based on how "far" it is from a regular polygon, I implemented a measure focusing on the equilateral and equiangular properties of a polygon [Chalmeta et al., 2013]. From the lengths of the edges (l_i), I first determine the median length of edge (l_{median}) and the sum of all edge length (l_Σ). Then, an intermediate term D can be calculated as follows:

$$D = \sum_{i=1}^{n} \left| \frac{l_i - l_{\text{median}}}{l_\Sigma} \right| + \sum_{i=1}^{n} \left| \varphi_i - \left(\pi - \frac{2\pi}{n} \right) \right|, \tag{7}$$

where n is the number of sides, and φ_i are the interior angles of a cell. Finally, cell shape regularity measure μ can be obtained as follow:

$$\mu = \begin{cases} 1 - \frac{D}{\frac{1}{2} + \frac{4\pi}{3}}, & \text{if } n = 3; \\ 1 - \frac{D}{1 + \left(4 - \frac{8}{n}\right)\pi}, & \text{if } n \geq 4. \end{cases} \tag{8}$$

The value of cell regularity (arbitrary units) ranges from 0 to 1, with 0 represent highly irregular and 1 being perfectly regular with equal length of cell edges and interior angles.

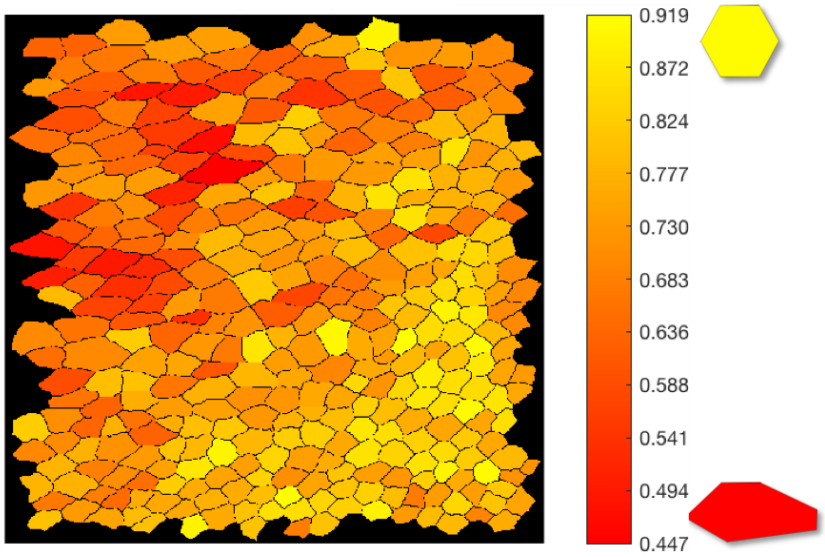

Figure 2.5: Quantification of cell shape regularity

Each cell is colour-coded according to its cell shape regularity value. The value of cell regularity (in arbitrary units) ranges from 0 to 1, with 0 represent highly irregular (in red colour) and 1 being perfectly regular (in yellow colour).

Hexagonal cell orientation. During phase II of *Drosophila* pupal wing morphogenesis, the relaxation process towards hexagonal packing is achieved mostly via directional cell junctional rearrangement (also known as PD-oriented T1 transition) [Aigouy et al., 2010]. The orientation of cell junctional rearrangement is biased along the wing PD axis in response to tension due to wing-hinge contraction; resulting in the shrinkage of AP-junctions and expansion of new cell junctions parallel to the PD axis (PD-junctions) [Aigouy et al., 2010; Etournay et al., 2015]. Consequently, PD-oriented cell junctional rearrangement increases the fraction of PD-oriented hexagonal cells in wild-type tissue [Sugimura and Ishihara, 2013]. Hence, the orientation of hexagonal cell is a useful readout of efficient PD-oriented cell junctional rearrangement. The orientation of a hexagonal cell can be computed using the following formula adapted from [Sugimura and Ishihara, 2013]:

$$\text{Hexagon orientation} = \frac{1}{6}\sum_{i=1}^{n}\cos\left(6\theta_i\right), \tag{9}$$

where θ_i is the angle enclosed between the x-axis and the line which passes through the cell centroid and the i-th vertex (Figure 2.6A). The value of hexagon orientation ranges between -1 and 1, with 1 being PD-oriented hexagonal cell and -1 being AP-oriented hexagonal cell. This method is useful to quantify average hexagonal cell orientation later in development when wing cells exhibit higher fraction of hexagonal cells.

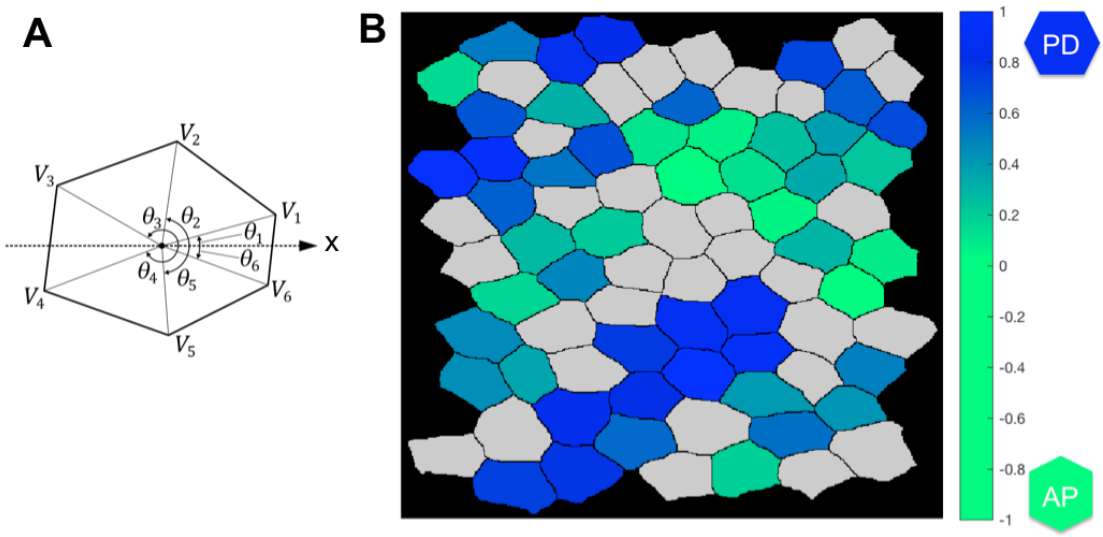

Figure 2.6: Quantification of hexagon orientation as a readout of directional cell junctional rearrangement

(A) Schematic representation of a hexagon with 6 vertices $V_1, V_2, V_3, \ldots, V_6$ and its corresponding angle $\theta_1, \theta_2, \theta_3, \ldots, \theta_6$.

(B) Hexagonal cells are colour-coded according to their orientation. The value will be closer to 1 as hexagonal cell gradually orient along the PD axis (blue) and approaching -1 when hexagonal cells orient along the AP axis (green). Grey cells represent non-hexagonal cells.

Hence, most of the cellular level analysis presented here will be utilised to quantify cell morphological parameters in *Drosophila* pupal wings of different genotypes or conditions in the subsequent chapters.

2.5 Tissue level morphological analysis

2.5.1 A new measurement tool to quantify organisation of packed tissues

Here, I present a new quantification measure, known as “Level of tissue disorganisation”, which combines packing density and deviation of apical cell area of a group of cells to capture the degree of tissue disorganisation. Void packing density captures the area that is not covered by the inscribed circle of the given cell. The inscribed circle is the largest circle contained in the cell, with at least three tangents to the cell’s sides. This measure is calculated based on one minus the ratio of the sum of apical area of inscribed circle $\tilde{A}_i$ to the sum of apical area A_i of individual cell. Therefore, for an irregular cell, one can imagine there will higher uncovered area by the inscribed circle as opposed to a regular cell. Besides that, average absolute deviation of cell area, is incorporated into the measurement, as packing density by itself is insufficient for capturing organisation in tissue level. This is because tissue can be densely packed even with high inhomogeneity in cell area. The deviation of cell area is normalised using its average area $\tilde{A}_{\text{average}}$. Hence, the level of epithelial tissue disorganisation S can be calculated as follows:

$$S = 100 \cdot \underbrace{\left(1 - \frac{\sum_{i=1}^{n} \tilde{A}_i}{\sum_{i=1}^{n} A_i}\right)}_{\text{Void density}} \cdot \underbrace{\frac{1}{n} \frac{\sum_{i=1}^{n} \left|\tilde{A}_i - \tilde{A}_{\text{average}}\right|}{\tilde{A}_{\text{average}}}}_{\text{Deviation of cell area}}. \quad (10)$$

The value of S (in arbitrary units) ranges from 0 to ∞, with 0 represents perfect organisation where all the cells are homogenous in terms of shapes and sizes and vice versa.

2.5.2 Quantification of epithelial organisation in simulation

To validate the robustness of this measurement in capturing and quantifying the changes in tissue organisation, I first used Voronoi relaxation, also known as Lloyd’s algorithm, to generate Centroidal Voronoi Tessellation (CVT) diagrams with distinct level of organisation. Given a randomly generated Voronoi diagram (a tessellation in

which each polygon represents the set of points nearest to the centroid), Lloyd's algorithm iteratively moves the current centroid to the new centroid of each cell until it reaches a steady state. At each iteration, Lloyd's algorithm relaxes irregular configuration into regular one with higher proportion of hexagons, which corresponds to a stable configuration (Figure 2.7A). I then computed the level of tissue disorganisation, as described in Section 2.5.1, on all the Voronoi diagrams (Figure 2.7B-D). In the 1st iteration, the diagram consists of highly irregular and inhomogeneous cells in terms of shapes and sizes. Therefore, it has significantly higher level of tissue disorganisation due to high void density and deviation in cell area as compared to subsequent iterations (Figure 2.7B-D). Subsequently, the diagram gradually relaxes towards better tissue organisation, with decreasing void density and deviation of cell area up to the 10th iteration (Figure 2.7B-D). As the diagram reaches "steady" state by the 10th iteration, there are no significant changes in the level of tissue disorganisation up to the 50th iteration.

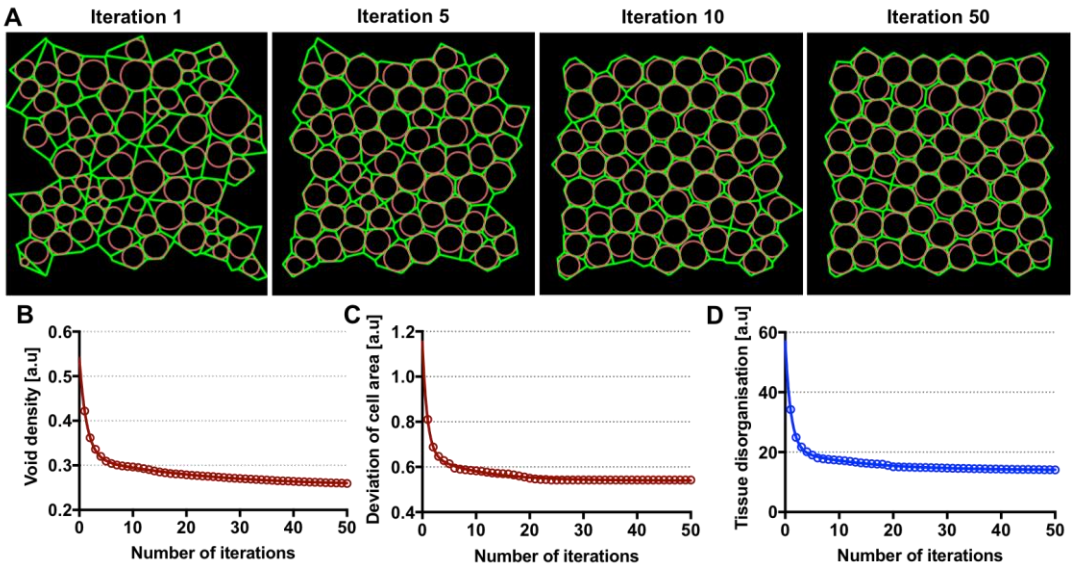

Figure 2.7: Quantifying the changes in tissue organisation as Voronoi diagram relaxes

(A) Lloyd's algorithm is used to generate Voronoi diagrams, from iteration 1 to iteration 50. For each iteration, a circle is inscribed into each cell (cell boundaries are labelled in green and inscribed circles are labelled in red).

(B) As Voronoi diagram relaxes, the void packing density decreases as cells become more regular and homogenous in shape.

(C) Similarly, the deviation in apical cell area decreases as cells become more homogenous in terms of sizes.

(D) The level of tissue disorganisation decreases over time indicating that there is an

increased homogeneity in shapes and sizes of the cells.

2.5.3 Quantification of epithelial organisation on pupal wings at different developmental time points

As a proof of principle of the capabilities of this method, I quantified the relaxation of epithelial tissue towards regular hexagonal packing during *Drosophila* pupal wing morphogenesis since it is a well-known event with highly dynamic rearrangement of cells. I first performed *in vivo* time-lapse imaging of a wild-type pupal wing expressing Fz::EGFP from 26 hAPF to 31 hAPF (Figure 2.8A). With these time-lapse images, I then quantified the level of tissue disorganisation at every 15-minute interval from 26 to 31 hAPF (Figure 2.8B). At 26 hAPF, epithelial tissue is highly disorganised because the cells are more inhomogeneous in terms of shapes and sizes. Similar to Lloyd's relaxation, as the tissue gradually relaxes towards a more regular packing by 31 hAPF, the level of tissue disorganisation decreases with increasing homogeneity in shapes and sizes of the cells.

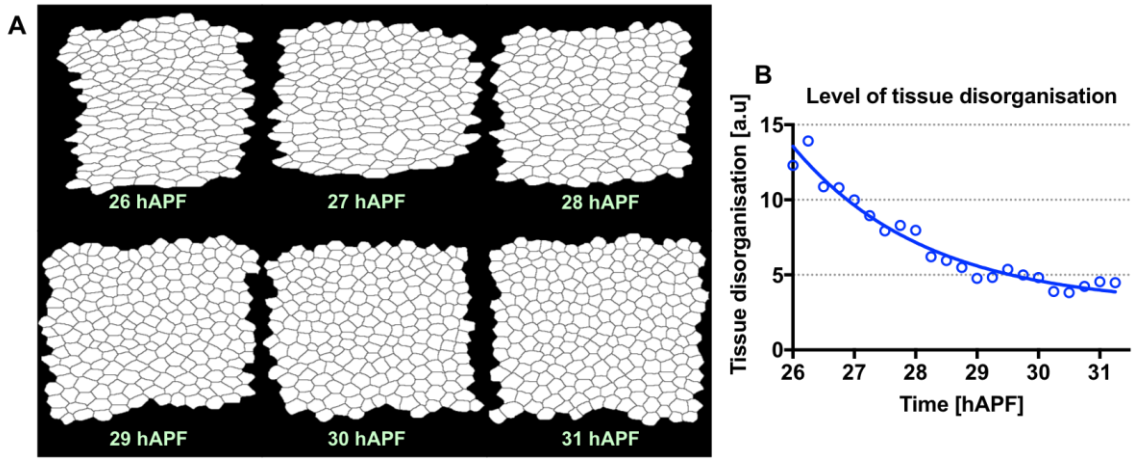

Figure 2.8: Quantifying the changes in epithelial tissue organisation in wild-type pupal wing at different developmental time points

(A) Segmented cell boundaries of pupal wing images expressing Fz::EGFP from 26 to 31 hAPF.

(B) The level of tissue disorganisation gradually decreases as tissue relaxes towards more regular packing by 31 hAPF.

2.6 Quantification of planar polarity

2.6.1 Quantitative definition of planar polarised protein distributions

As mentioned previously, the aim of this project is to investigate the effects of cell packing geometry on the asymmetry distribution of core polarity proteins and vice versa. Therefore, it is necessary to have a robust and systematic method to quantify planar polarity independently of cell geometry. First, it is necessary to list out several quantifiable polarity phenotypes before developing a method for quantifying planar polarity. Essentially, there are three primary characteristics of planar polarity in the *Drosophila* pupal wing [Hazelwood and Hancock, 2013]:

a) Asymmetric distribution of core planar polarity proteins on the cell junctions. For instance, Fz is asymmetrically localised on the distal boundaries of cells prior to trichome initiation. However, due to the limited resolution of confocal microscopy, protein localisation on proximal or distal cell boundaries cannot be distinguished. Therefore, in a cell, there will be peak cell perimeter intensity, $I(\theta)$ at angle θ and also $\theta + \pi$ contributed by distal localisation of Fz within the proximally neighbouring cell (Figure 2.9).

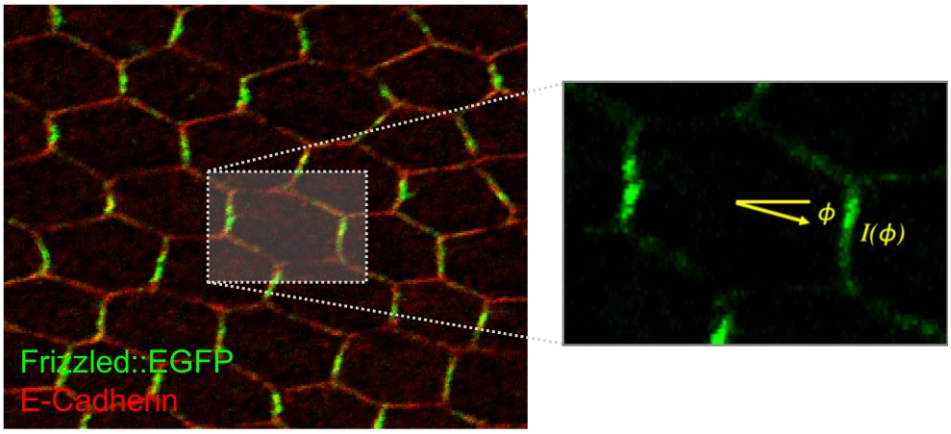

Figure 2.9: Asymmetric subcellular localisation of Fz::EGFP on the cell junctions at approximately 30 hAPF

$I(\theta)$ represents the peak Fz intensity on cell boundaries at an angle θ with respect to centroid of the cell.

b) At the end of pupal wing development, actin-rich trichomes are localised on the distal cell junction where Fz is localised. The displacement of actin-rich trichomes initiation from the centroid of the cell can be quantified in terms of polarity direction. In the case of core polarity mutants, hair initiation occurs in the cell centre in a random orientation [Gubb and Garcia-Bellido, 1982; Wong and Adler, 1993].

c) The final orientation of adult wing hair is directly related to the site of hair initiation.

Since I am interested in earlier developmental stages (from 24 to 30 hAPF), the last two indicators of polarity that occur later in the development (after 32 hAPF) are not relevant in this project.

For this purpose, I have developed a new method to quantify the asymmetrical distribution of protein on cell boundaries based on Principal Component Analysis (PCA). This algorithm computes the angle that produces the largest variance of weighted intensities from the centroid of the cell, which corresponds to the first principal component axis. In terms of polarity magnitude, if the proteins are homogeneously distributed on the cell boundaries, then the polarity magnitude should be zero. However, if the proteins are asymmetrically segregated to opposite cell junctions, it will give a strong polarity magnitude readout.

In order to calculate polarity, the angle θ_i, which lies between the x-axis and the line that passes through the centroid of the cell $\bar{r}$ and the i-th point on the cell boundary, $r_i = \begin{pmatrix} x_i \\ y_i \end{pmatrix}$, can be calculated as follows (Figure 2.9):

$$\theta_i = \arg\left(r_i - \bar{r}\right). \tag{11}$$

In order to mitigate the effect of denseness of points on the calculation of covariance matrix, the weighting $d\theta_i$ is calculated based on the angle spanned by the point i:

$$w_i = d\theta_i = \frac{1}{2}\left(\theta_{i+1} - \theta_{i-1}\right). \tag{12}$$

For each point i on the cell boundary with intensity I_i, all the intensities are normalised so that it is independent of the image format (for example, 8-bit, 12-bit, 16-bit, and etc):

$$\hat{I}_i = \ln\left(k \cdot I_i\right), \tag{13}$$

where k is the normalisation factor (≈ 1000 empirically). The transformed coordinates, $(\hat{x}_i, \hat{y}_i)$, can then be determined as follow:

$$\hat{x}_i = \hat{I}_i \cos\left(\theta_i\right), \tag{14}$$

$$\hat{y}_i = \hat{I}_i \sin\left(\theta_i\right). \tag{15}$$

Next, covariance matrix, $\boldsymbol{\sigma}$, is calculated as follow:

$$w_\Sigma = \sum_{i=1}^{n} w_i, \tag{16}$$

$$\sigma_{xx} = \frac{1}{w_\Sigma} \sum_{i=1}^{n} w_i \hat{x}_i^2, \tag{17}$$

$$\sigma_{xy} = \sigma_{yx} = \frac{1}{w_\Sigma} \sum_{i=1}^{n} w_i \hat{x}_i \hat{y}_i, \tag{18}$$

$$\sigma_{yy} = \frac{1}{w_\Sigma} \sum_{i=1}^{n} w_i \hat{y}_i^2, \tag{19}$$

$$\boldsymbol{\sigma} = \begin{bmatrix} \sigma_{xx} & \sigma_{xy} \\ \sigma_{yx} & \sigma_{yy} \end{bmatrix}, \tag{20}$$

where w_Σ is the sum of all weightage and $\sigma_{\mu\nu}$ are the covariances.

Eigenvalues λ_1, λ_2 with $\lambda_1 \geq \lambda_2$ and eigenvectors v_1, v_2 of the covariance matrix $\boldsymbol{\sigma}$ are computed accordingly. Using the eigenvalues and covariances, I defined the magnitude of polarity p and the angle of polarity θ for a single cell as

$$p = \sqrt{\lambda_1} - \sqrt{\lambda_2}, \tag{21}$$

$$\theta = \frac{1}{2} \tan^{-1}\left(\frac{2\sigma_{xy}}{\sigma_{xx} - \sigma_{yy}}\right). \tag{22}$$

The angle of polarity θ is measured with respect to the PD axis, i.e., the x-axis of an image. Polarity angle measurement ranges between $-90°$ and $+90°$, with 0° oriented along the PD axis and $\pm 90°$ oriented along the AP axis.

For initial testing, I quantified planar polarity in wild-type wings expressing Fz::EGFP at 32 hAPF (Figure 2.10A). Cell boundaries are extracted and processed as described in Section 2.3. Accurate segmentation is a pre-requisite for correct

quantification of asymmetric protein localisation, as even the slightest misplaced boundaries in segmentation can result in incorrect quantification. By employing the PCA algorithm, the magnitude and angle of polarity of a single cell can be quantified (Figure 2.10B).

To provide a more intuitive visualisation of the magnitude and angle of polarity data combined from multiple wings, a heatmap is created using MATLAB. The polarity angles are divided equally into 18 bins, with each having the bin size of 10 degrees. The bin size of polarity magnitude, on the other hand, is adapted according to the data so that majority of the data will have an undistorted illustration due to the polar nature of this heatmap. The heatmap is then smoothened/interpolated for better visual appeal. In this protractor-like heatmap, polarity magnitude is the distance away from the centre of the half circle, meanwhile the polarity angle distribution spans from $-90°$ to $+90°$. The proximodistal (PD) axis of the wing corresponds to the horizontal axis of the heatmap. The percentage of cells is represented by different colours (red – high percentage of cells; blue – low percentage of cells).

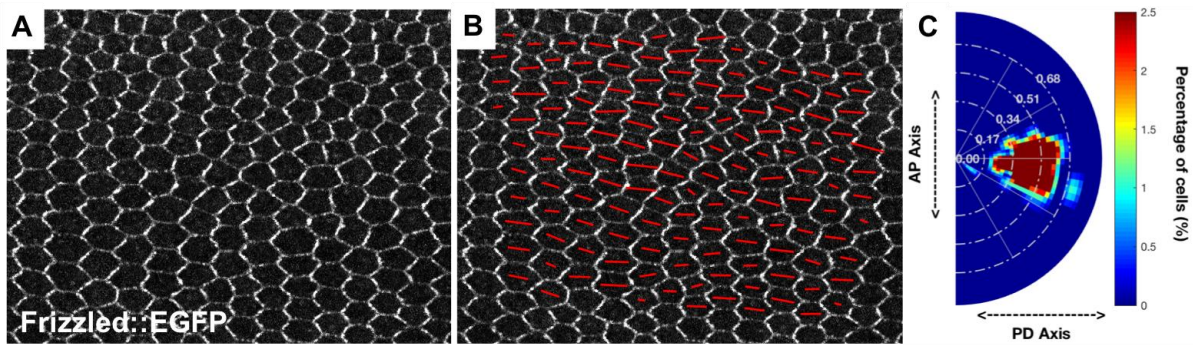

Figure 2.10: Quantification of planar polarity on *Drosophila* pupal wing

(A) Confocal image of Fz::EGFP expressing wild-type wing at 32 hAPF. The distribution of Fz complexes is asymmetric, as they tend to localise on the distal cell junctions.

(B) The same image in (A) overlaid with red bars representing the polarity for each cell. Polarity is computed using PCA method, which outputs the polarity magnitude and angle. The length of red bars is proportional to the magnitude of polarity, meanwhile the angle of red bars represents the angle of polarity for a given cell.

(C) Heatmap showing the magnitude and orientation of Fz::EGFP polarity at 32 hAPF.

2.6.2 Quantification of planar polarity: Cellular and tissue scales

Polarity measurement contains both magnitude and angle readout, which is very similar to a typical two-dimensional vector. It is important to note that polarity angle has a two-fold rotational symmetry. Therefore, the conversion of polarity from polar form (magnitude and angle) to Cartesian form (x- and y-component) is slightly different than typical 2D vector conversion. Given both polarity magnitude p and polarity angle θ, polarity vector can be calculated as follows:

$$\begin{aligned}\vec{p} &= \begin{bmatrix} p_x \\ p_y \end{bmatrix} \\ &= \begin{bmatrix} p\cos(2\theta) \\ p\sin(2\theta) \end{bmatrix}. \end{aligned} \tag{23}$$

On the other hand, conversion from Cartesian to polar form to obtain polarity magnitude p and polarity angle θ is as follows:

$$\theta = \frac{1}{2}\tan^{-1}\left(\frac{p_y}{p_x}\right), \tag{24}$$

$$p = \sqrt{p_x^2 + p_y^2}. \tag{25}$$

The magnitude and angle of polarity serve as a readout for planar polarity for a single cell (Figure 2.11A). Within a group of cells, the polarity measurements can be combined in specific ways to reveal the strength of polarity as well as the polarity coordination between cells. The most direct way is to compute the average of polarity magnitude without taking its polarity angle into consideration, which is termed as the “direct” average polarity magnitude measure. It can be simply computed with the following equation:

$$p_{\text{average}} = \frac{1}{n}\sum_{i=1}^{n} p_i, \tag{26}$$

where p_i is the polarity magnitude of i-th cell. n is the total number of cells.

On the other hand, in order to capture the coordination of planar polarity between groups of cells (also known as coarse-grain) or with its immediate neighbours, I defined a “vector” average polarity measurement. Unlike direct average polarity magnitude, the vector average polarity reflects both how well proteins are polarised and aligned within a group of cells or with its immediate neighbours. First, polarity of

individual cells is converted into their vector form $\vec{p}_i$. The vector polarity average, $\vec{p}_{\mathrm{vec}}$, is computed as follows:

$$\begin{aligned}\vec{p}_{\mathrm{vec}} &= \frac{1}{n}\sum_{i=1}^{n}\vec{p}_i \\ &= \frac{1}{n}\sum_{i=1}^{n}\begin{bmatrix} p_i\cos(2\theta_i) \\ p_i\sin(2\theta_i)\end{bmatrix},\end{aligned} \tag{27}$$

where $\vec{p}_i, p_i, \theta_i$ are the polarity vector, polarity magnitude and polarity angle of i-th cell respectively. n is the total number of cells. Therefore, vector average polarity magnitude p_{vec} and angle θ_{vec} can be explicitly written as

$$p_{\mathrm{vec}} = \sqrt{\left[\frac{1}{n}\sum_{i=1}^{n}p_i\cos(2\theta_i)\right]^2 + \left[\frac{1}{n}\sum_{i=1}^{n}p_i\sin(2\theta_i)\right]^2}, \tag{28}$$

$$\theta_{\mathrm{vec}} = \frac{1}{2}\tan^{-1}\left(\frac{\frac{1}{n}\sum_{i=1}^{n}p_i\sin(2\theta_i)}{\frac{1}{n}\sum_{i=1}^{n}p_i\cos(2\theta_i)}\right). \tag{29}$$

Notice that the computed vector average polarity magnitude p_{vec} takes the polarity angle of individual cells into consideration. Therefore, $p_{\mathrm{vec}} \leq p_{\mathrm{average}}$ for all possible cases of polarity magnitudes and angles, with equality if and only if all polarity angles are equal.

To visualise the coarse-grain polarity on the scale of groups of cells, cells are divided into equal groups in a square grid. In each group, the vector average magnitude p_{vec} and angle of polarity θ_{vec} are computed as described in Equation 28 and 29 (Figure 2.11B). On the other hand, to capture local polarity coordination of individual cells with its immediate neighbours, cell's immediate neighbours are identified and the vector average magnitude p_{vec} and angle of polarity θ_{vec} are calculated as described in Equation 28 and 29 (Figure 2.11C).

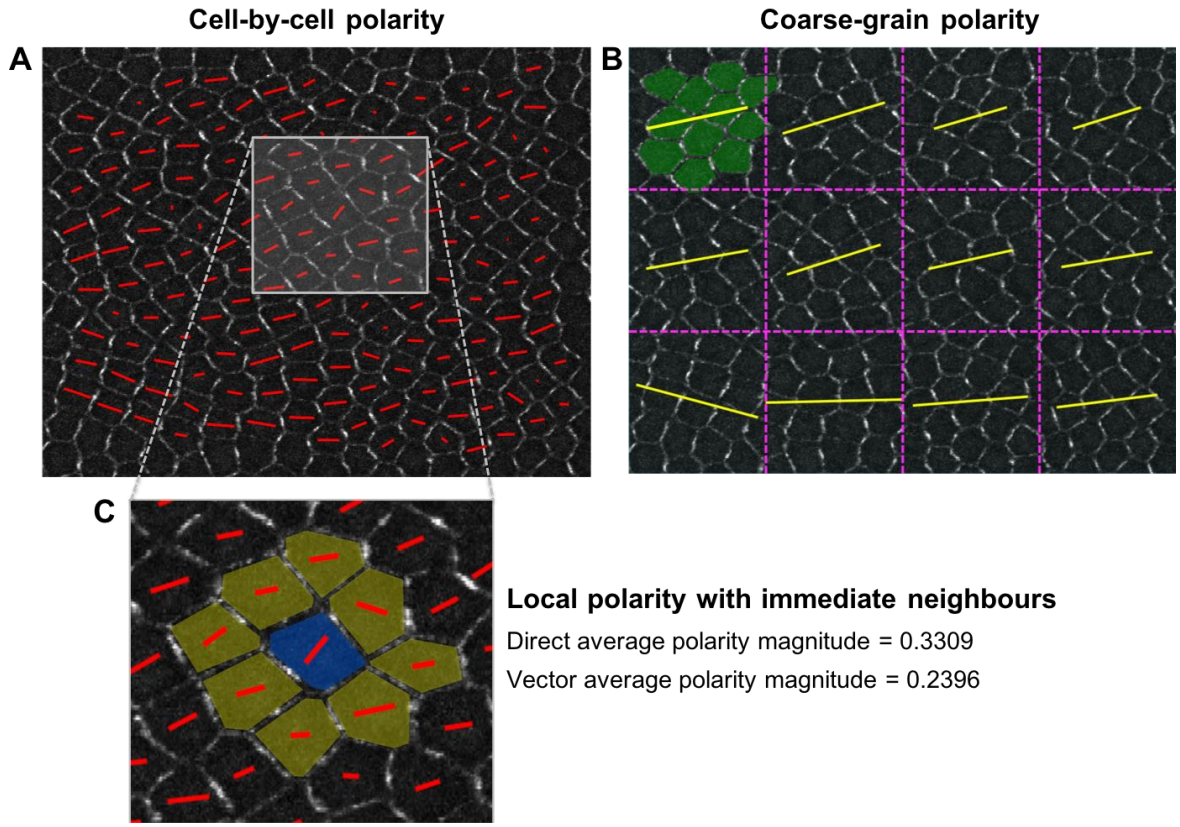

Figure 2.11: Quantification of planar polarity at cellular and tissue scales

(A) Cell-scale polarity pattern of *Drosophila* pupal wing expressing Fz::EGFP at 30 hAPF (prior to wing hair formation). The length and orientation of red bars denote the polarity magnitude and angle for a given cell respectively.

(B) Coarse-grain pattern of vector average polarity at 30 hAPF. Image is divided into group of cells with equal square grids (with dotted magenta lines) where the vector average polarity for each group of cells is computed. For each group of cells, the p_{vec} is proportional to the length of the yellow bar, while the θ_{vec} is denoted by the orientation of the yellow bar.

(C) Diagram for quantification of local polarity for blue cell with its immediate neighbours (yellow cells). Due to lack of polarity coordination with its immediate neighbouring cells, therefore p_{vec} is significantly smaller than p_{average} for the blue cell.

Additionally, I used circular statistics to quantify the degree of alignment or coordination of polarity between cells. A measure called circular variance is typically used to determine circular spread of vectorial data, which is quite similar to standard deviation. However, in order to accommodate the rotational symmetry of polarity angle, the circular angle variance $\mathrm{Var}_{\mathrm{circ}}$ for polarity angles can be computed as follows:

$$\mathrm{Var}_{\mathrm{circ}} = 1 - \sqrt{\left[\frac{1}{n}\sum_{i=1}^{n}\cos(2\theta_i)\right]^2 + \left[\frac{1}{n}\sum_{i=1}^{n}\sin(2\theta_i)\right]^2}. \quad (30)$$

where θ_i is the polarity angle of i-th cell. n is the total number of cells.

Circular angle variance ranges between 0 and 1, with 0 having complete agreement in polarity alignment, while 1 represents complete polarity misalignment. Quantification of polarity angle distribution for *Drosophila* pupal wings at two different developmental time points is as presented in Figure 2.12A-B. Earlier in development at 24 hAPF, there is a higher variation in polarity alignment between cells (with wider distribution of angles as shown in the histogram in Figure 2.12A') as compared to later in development at 32 hAPF, where polarity pattern becomes more coherent and well-aligned with each other (Figure 2.12B-B'). Therefore, this results in higher polarity angle variance at 24 hAPF as compared to 32 hAPF.

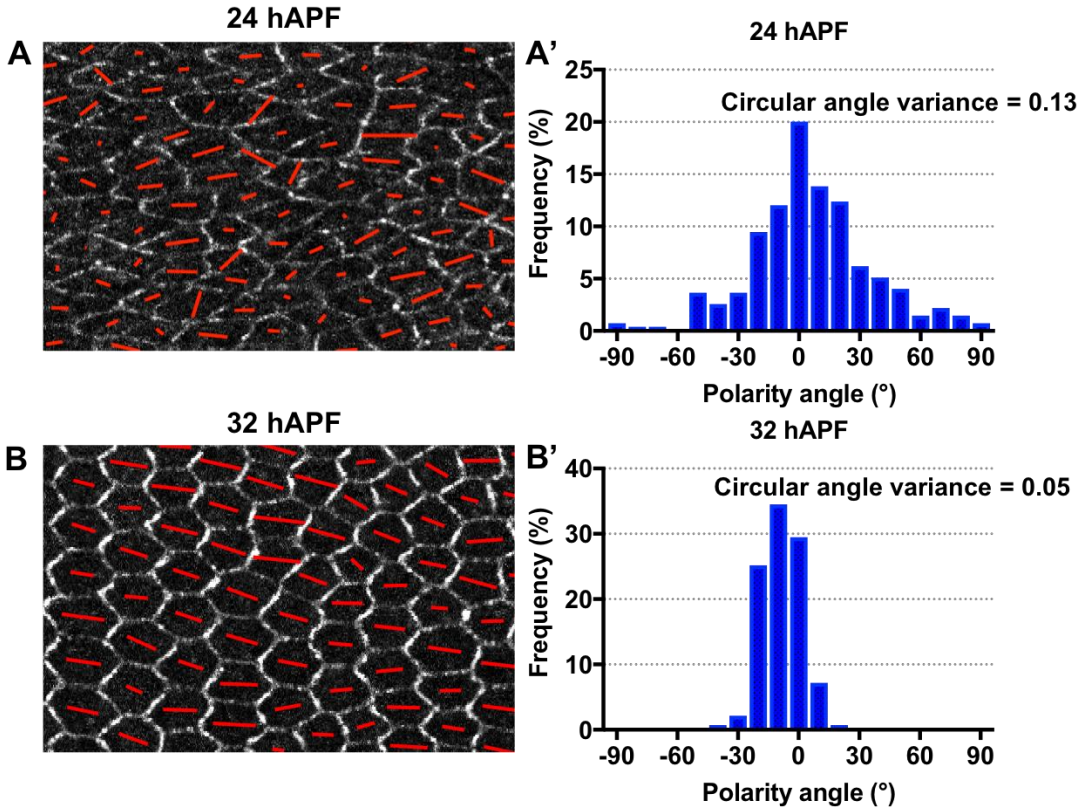

Figure 2.12: Circular angle variance captures the degree of polarity alignment between cells

(A) Cell-scale polarity pattern of wild-type wing expressing Fz::EGFP at 24 hAPF. The red

bars represent the vectorial nature of polarity pattern for a given cell.
(A') Histogram depicts a wider angular distribution at 24 hAPF with a higher circular angle variance of 0.34 (n = 3 pupal wings with 180 cells analysed).
(B) Cell-scale polarity pattern of wild-type wing expressing Fz::EGFP at 32 hAPF.
(B') Histogram shows a narrower angular distribution at 32 hAPF with a lower circular angle variance of 0.05 (n = 3 pupal wings with 200 cells analysed).
Polarity angle measurement ranges between $-90°$ and $+90°$, with $0°$ oriented along the PD axis and $\pm 90°$ oriented along the AP axis.

2.6.3 Validation of planar polarity quantification methods

Algorithm validation is an important criterion to evaluate the accuracy and robustness of different methods in quantifying planar polarity. Therefore, I validated the PCA method with two other established methods, namely the Ratio and Fourier Series method. Previously, a method for quantifying planar polarity based on the Fourier Series method has been published [Aigouy et al., 2010]. This method fits a sine wave onto the cell junction intensity profile and computes polarity magnitude based on the amplitude of the sine wave (Algorithm based on published method kindly provided by Katherine Fisher). Our group has published a method on quantifying planar polarity known as the Ratio method. This method fits a square wave onto the junctional intensity profile and computes the ratio of opposite quadrants to determine the polarity magnitude and angle [Strutt et al., 2016].

Algorithms validation on simulated cells

As previously stated, we need a measure that is insensitive to different cell shapes and sizes. Thus, to evaluate the robustness and accuracy of these methods towards varying cell geometry, I simulated cells with varying eccentricity, size, shape regularity, and amount of proteins on cell junctions. First, I tested these methods against simulated cells with varying cell area (up to four times the original area) and shape regularity (ranges from 0.5 to 0.9) as depicted in Figure 2.13A and Figure 2.14A respectively. These simulations mimic the effect of loss of Dumpy and knockdown of Rap1 in the *Drosophila* pupal wing epithelium, which results in smaller

cell size and irregular cell shape respectively [Knox and Brown, 2002; Etournay et al., 2015]. By fixing the localisation and total amount of the proteins on these simulated cell junctions, polarity magnitude computed using Fourier Series and PCA methods are least affected by variation in cell sizes and regularities as compared to the Ratio method (Figure 2.13B and Figure 2.14B). All the polarity magnitudes are normalised against its maximum magnitude to allow direct comparison between three different methods.

In terms of polarity angle measurement, both Fourier Series and PCA methods produce a consistent polarity angle readout at approximately $0°$ (along x-axis) despite varying degrees of cell size and regularity. However, polarity angle readout computed using Ratio method seems to fluctuate with $\pm 15°$ error (Figure 2.13C and Figure 2.14C). These data suggest that both Fourier Series and PCA are better suited to quantify planar polarity in cells with varying sizes and regularity.

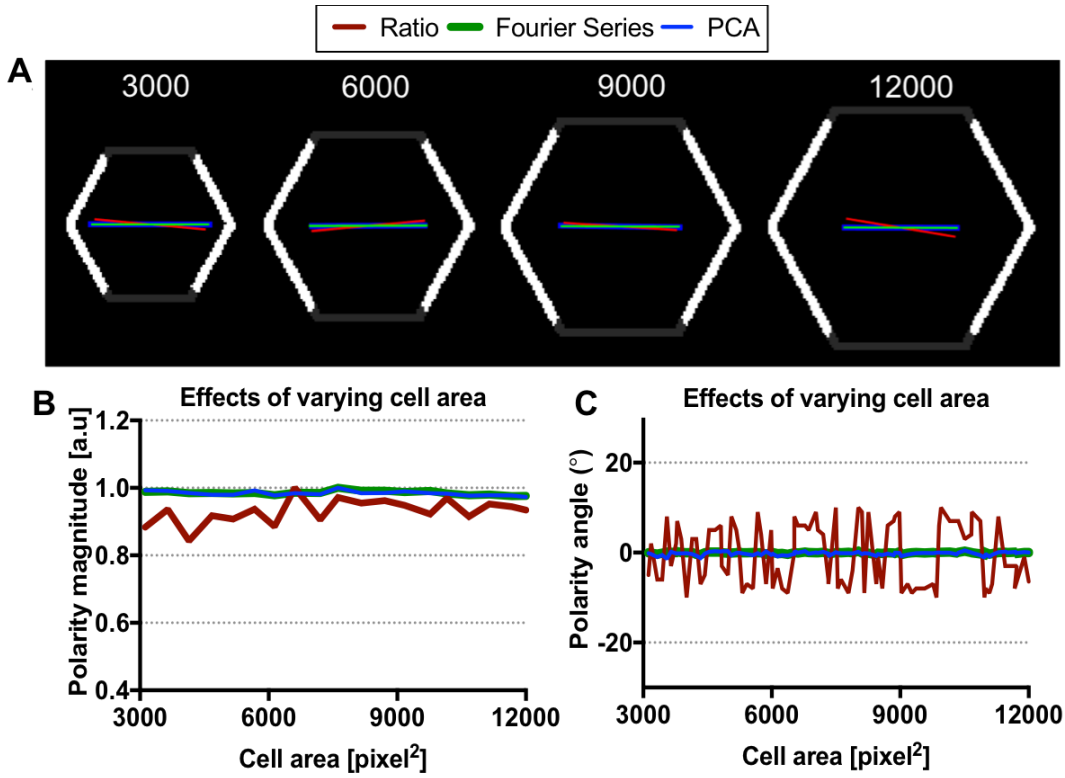

Figure 2.13: Fourier Series and PCA methods are independent of cell size

(A) Simulated cells with conserved total protein levels and distribution on cell junctions but increasing cell sizes, from 3000 pixel^2 to 12000 pixel^2 (as labelled in individual cells). The coloured bars represent the vectorial nature of polarity pattern for a given cell, which are

computed using three different methods.
(B-C) Graphs show polarity magnitudes (in arbitrary units or [a.u]) and polarity angles (in degrees) of cells with varying sizes computed using Ratio, Fourier Series and PCA methods.

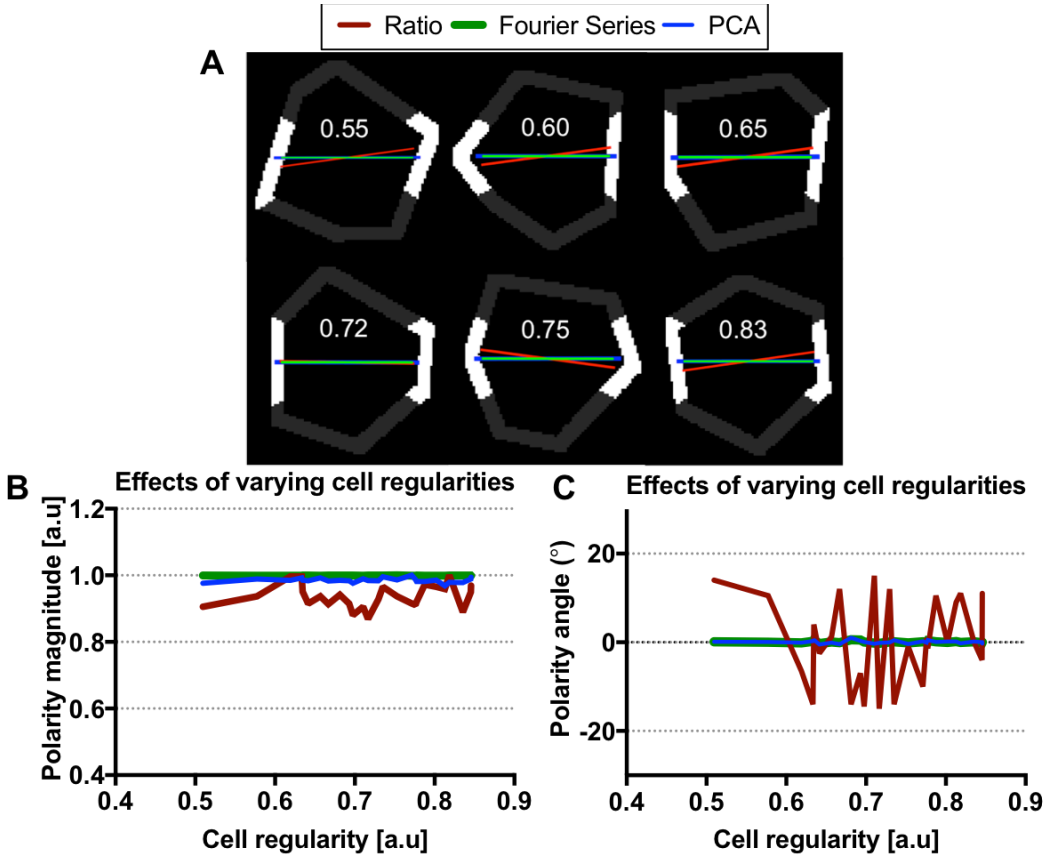

Figure 2.14: Fourier Series and PCA methods are independent of cell regularity
(A) Simulated cells with conserved total protein levels and distribution on cell junctions but increasing shape regularity, from 0.55 to 0.83. The coloured bars represent the vectorial nature of polarity pattern for a given cell, which are computed using three different methods.
(B-C) Graphs show polarity magnitudes and angles of cells with varying regularity computed using three different methods.

Apart from that, by varying cell eccentricity while fixing the localisation and total amount of the proteins on the cell junctions (Figure 2.15A), polarity magnitude computed using PCA method is proven to be independent of varying degrees of cell eccentricity (Figure 2.15B). However, polarity magnitude obtained from both Ratio and Fourier Series methods are sensitive to varying cell eccentricities (Figure 2.15B). This implies that Fourier Series method will give lower polarity magnitude for less eccentric cells and vice versa. Meanwhile, polarity magnitude computed using

Ratio method is significantly lower for cell with eccentricity below and above 0.5. In terms of polarity angle measurement, both Fourier Series and PCA methods give a constant polarity angle readout at $0°$, whereas Ratio method produces less consistent angle readout with $\pm 15°$ error for varying degrees of cell eccentricity (Figure 2.15C). This simulation result suggests that PCA method is more robust in quantifying planar polarity in cells with varying degrees of eccentricity.

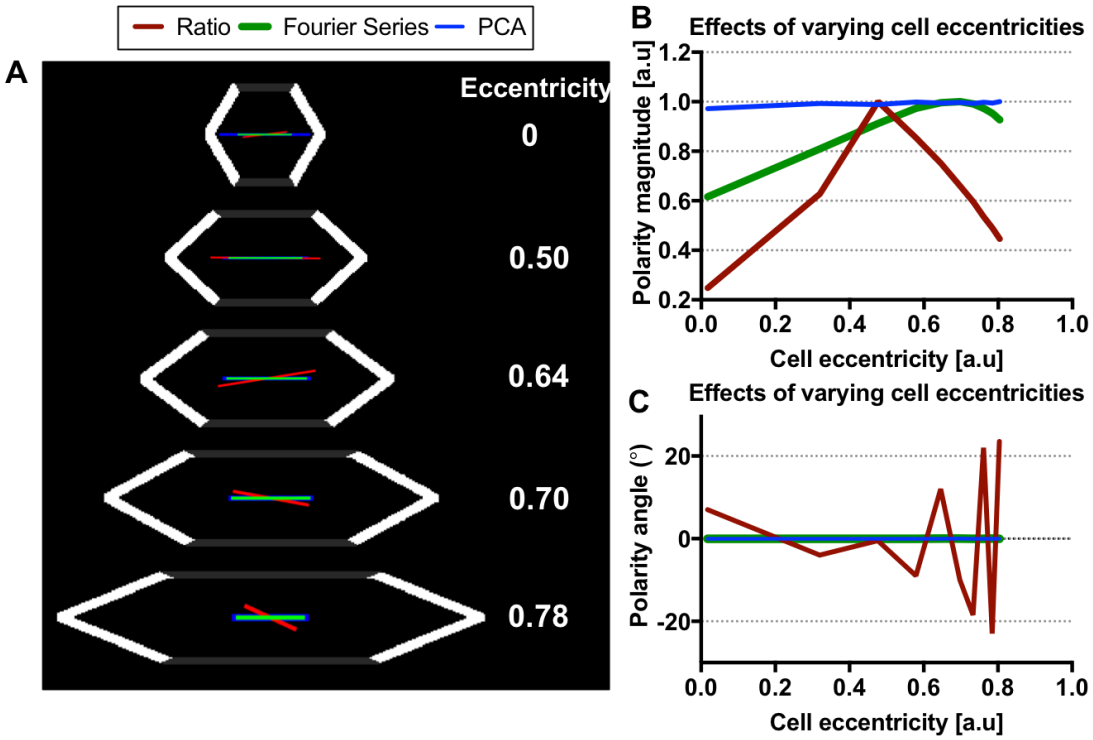

Figure 2.15: PCA method is independent of cell eccentricity

(A) Simulated cells with conserved total protein levels and distribution on cell junctions but increasing eccentricity, from 0 to 0.78 (as labelled next to the cell). The coloured bars represent the vectorial nature of polarity pattern for a given cell, which are computed using three different methods.

(B-C) Graphs show polarity magnitudes and angles of cells with varying eccentricity computed using three different methods.

Polarity magnitude signifies the strength of polarisation for a given cell. When proteins are homogenously distributed on the cell junctions, the cell is said to exhibit weak polarity with a low polarity magnitude. On the contrary, when proteins are asymmetrically distributed to the opposite cell junctions, the cell is said to be strongly polarised with a high polarity magnitude. To evaluate the ability of the algorithms to

detect the strengths of polarisation, I varied the amount of proteins on the simulated cell perimeter (the total cell perimeter is approximately 480 units) while maintaining the cell geometry (Figure 2.16B).

Experimentally, at 24 hAPF, Fz proteins are randomly distributed on the cell junctions [Classen et al., 2005]. However, by 32 hAPF, Fz becomes asymmetrically localised to the distal cell junctions, which corresponds to maximum polarity magnitude (Figure 2.16A) [Classen et al., 2005]. Due to the limited microscopy resolution, there will be proximal Fz localisation contributed by distal localisation of Fz from the proximally neighbouring cells. Therefore, I simulated hexagonal cells with 161 units of protein on each of the opposite PD cell junctions, which correspond to pupal wing cells at 32 hAPF. Ideally, one would expect that polarity magnitude increases (from cell junctions devoid of any proteins) until it reaches maximum polarity (with 161 unit of proteins equally distributed on each of the PD-junctions) before it decreases to zero (with homogeneous distribution of proteins on all the cell junctions). From simulation results, by gradually increasing the amount of proteins on both the PD-junctions, the cell becomes increasingly polarised and reaches maximum polarity when unit of proteins on each PD-junctions is approximately 120 for Ratio, 80 for Fourier Series and 140 for PCA method (Figure 2.16B-C). Polarity magnitudes then decreases steadily after reaching peak polarity as proteins become increasingly localised along AP-junctions (Figure 2.16B-C).

In terms of polarity angle, both Fourier Series and PCA methods remain constant while Ratio method is significantly affected by varying distribution of proteins on the cell junctions (Figure 2.16D). From this simulation, I found out that that there is a distinct polarity strength profile for each of the methods. Nevertheless, PCA method, which gives maximum polarity at 140 units of protein, appears to be the closest to the ideal maximum polarity at 161 units of protein on simulated cells.

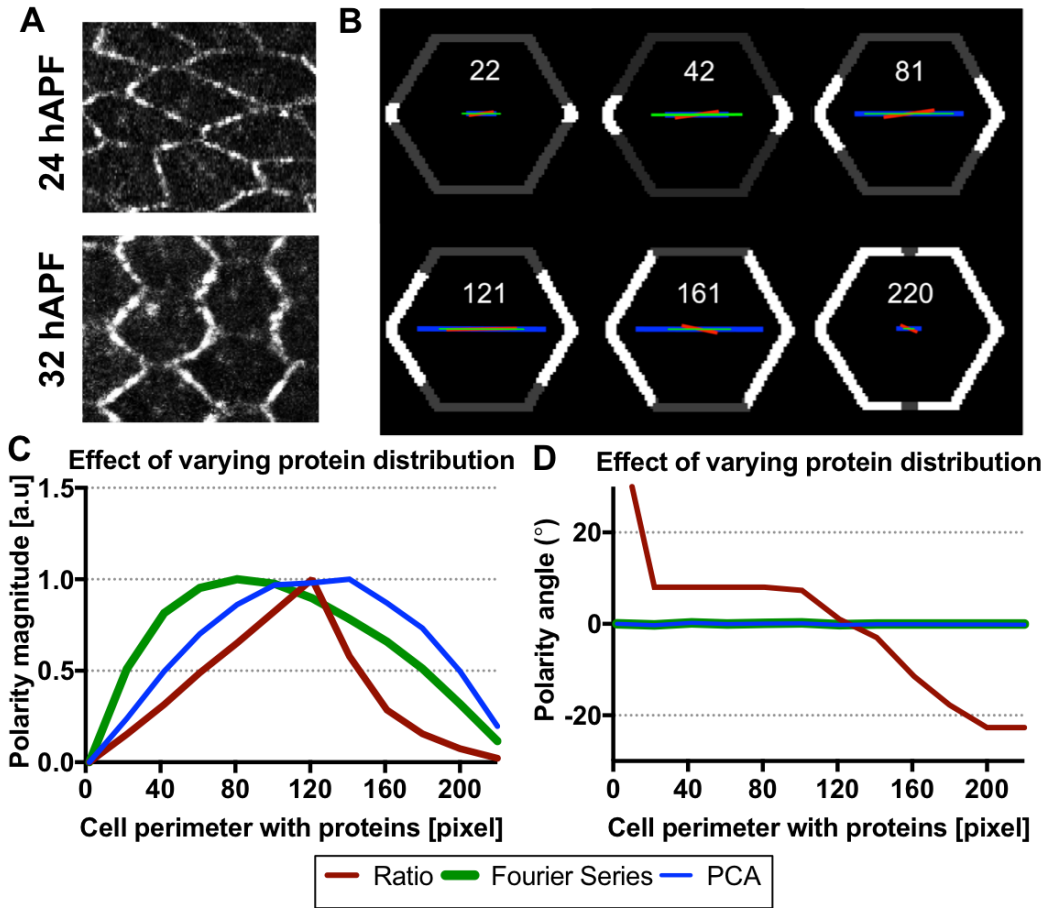

Figure 2.16: Each method has distinct polarisation strength profile based on the protein distribution on cell junctions

(A) Experimental cells of wild-type pupal wing expressing Fz::EGFP at 24 and 30 hAPF.

(B) Simulated cell with similar geometry (size, regularity and eccentricity) but varying distribution of proteins on the cell junctions. Given cell perimeter of 480 pixels in total, each side of the PD-junction containing proteins varies from 22 to 220 pixels. The coloured bars represent the vectorial nature of polarity pattern for a given cell, which are computed using three different methods.

(C-D) Graphs show polarity magnitudes and angles obtained from varying the amount of proteins on cell junctions computed using three different methods.

Furthermore, I evaluated the performance of all algorithms under simulated noisy conditions, i.e. low signal-to-noise (SNR) ratio. To this end, I artificially added Gaussian noise to the simulated cells to obtain various SNRs (Figure 2.17A). All the polarity magnitudes calculated from noise-induced images are normalised against the polarity magnitude obtained from original noise-less image. As expected, decreasing SNR resulted in less precise and consistent polarity magnitude. When

SNR goes below 10, polarity magnitudes obtained from all the methods deviate up to $\pm 10\%$ from the original noise-less condition (Figure 2.17B). Polarity angle, on the other hand, is not affected by the image noise for both Fourier Series and PCA methods but fluctuates at approximately $\pm 15°$ for Ratio method (Figure 2.17C). Overall, all the three methods perform rather robustly under noisy conditions, with $\pm 10\%$ deviation in polarity magnitude.

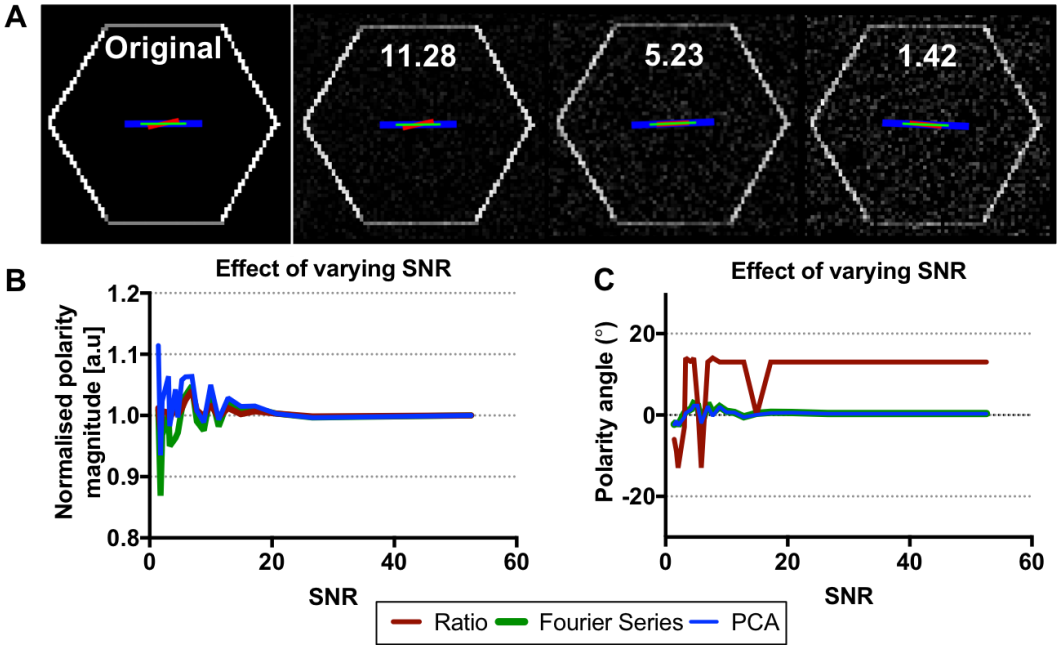

Figure 2.17: All the algorithms behave rather robustly over varying degrees of signal-to-noise ratio (SNR)

(A) Simulated cells with conserved total amount and distribution of proteins, and similar cell geometry (size, regularity and eccentricity) but varying levels of signal-to-noise ratio. The coloured bars represent the vectorial nature of polarity pattern for a given cell, which are computed using three different methods.

(B-C) Graphs show polarity magnitudes and angles obtained from images with different levels of SNR computed using three different methods.

Algorithms validation on experimental data

Having demonstrated the robustness and accuracy of the PCA method on simulated cells, I then applied it to experimental data sets such as *Drosophila* pupal wing, wing discs and embryonic epidermis, which exhibit distinct planar polarity and cell shapes.

Fz has been previously reported to become asymmetrically distributed to the distal cell junctions prior to wing hair outgrowth at 32 hAPF [Strutt, 2001]. Therefore, I quantified the asymmetrical distribution of Fz in time-lapse images of wild-type pupal wings at 24 hAPF and 30 hAPF using all the different methods. Interestingly, I found out that there is a higher correlation in polarity magnitude obtained from Ratio and Fourier Series (coefficient of determination, r^2 = 0.8854) as compared to PCA and Fourier Series (r^2 = 0.2711) at 24 hAPF, when cells are more eccentric (Figure 2.18A'). This might be due to the fact that polarity magnitudes computed from Fourier Series and Ratio methods are more sensitive to cell eccentricity, as evident from the simulation results (Figure 2.15C). Meanwhile, as cells become less eccentric/elongated and more regular by 30 hAPF, the correlation between PCA and Fourier Series increases significantly (r^2 = 0.2711 and 0.5715 at 24 and 30 hAPF) (Figure 2.18A' and 2.18B'). Qualitatively, in terms of polarity angle, both PCA and Ratio methods seem to agree well with Fourier Series at 24 hAPF and 30 hAPF respectively (Figure 2.18A'' and 2.18B'').

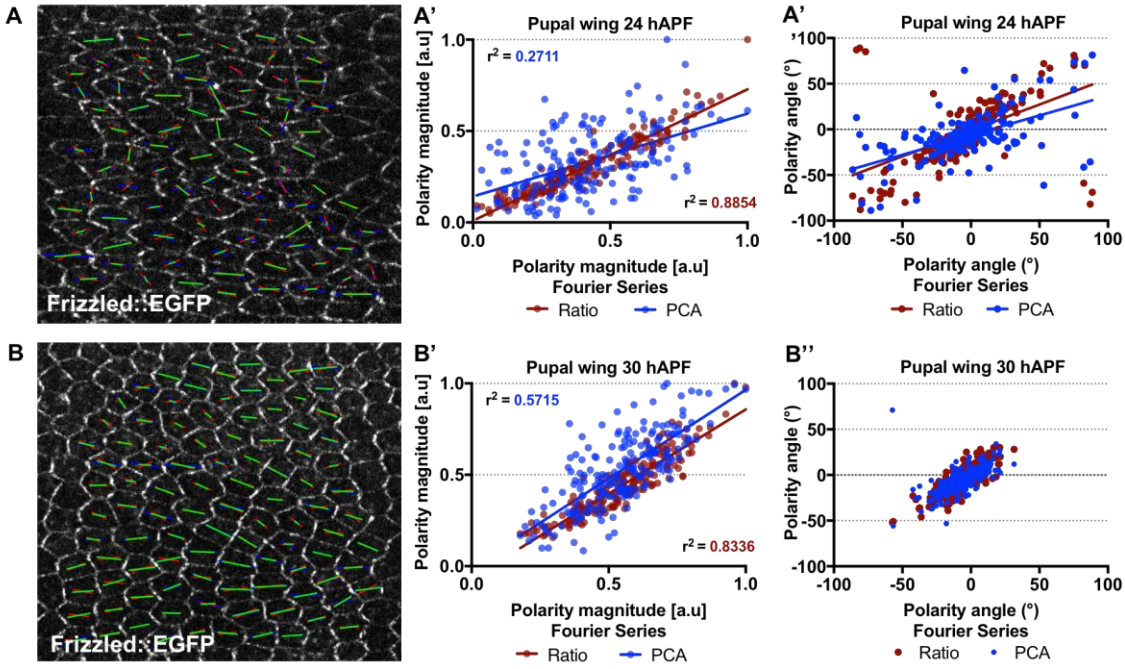

Figure 2.18: Validation of planar polarity algorithms on *Drosophila* pupal wing at different developmental time points

(A-B) Quantified cell-scale polarity pattern of wild-type wings expressing Fz::EGFP at (A) 24 hAPF and (B) 30 hAPF. The red, green and blue bars represent the vectorial nature of polarity pattern for a given cell obtained from Ratio, Fourier Series and PCA method respectively.

(A'-B') Plot of polarity magnitudes at (A') 24 hAPF and (B') 30 hAPF obtained from Ratio (red dots) and PCA (blue dots) versus Fourier Series with best fit lines shown as red and blue lines respectively. Coefficients of determination r^2 are computed accordingly.

(A''-B'') Plot of polarity angles at (A'') 24 hAPF and (B'') 30 hAPF obtained from Ratio (red dots) and PCA (blue dots) versus Fourier Series. (n = 3 pupal wings with 200 cells analysed).

All polarity magnitudes (a.u) are normalised against its maximum. All polarity angles (in degree) range between $-90°$ to $+90°$, with $0°$ corresponds to the x-axis of the image.

Another pathway that regulates planar polarity is the Fat-Dachsous system, which has been demonstrated to display subcellular asymmetries in the wing discs [Brittle et al., 2012]. Thus, I analysed the asymmetrical localisation of Dachsous in third-instar larval wing discs images (Figure 2.19A). From the wing discs results, both PCA and Fourier Series methods seem to correlate better in terms of polarity magnitude (Coefficients of determination, r^2 = 0.4415) and angle as compared to the Ratio and Fourier Series methods (r^2 = 0.0179 for polarity magnitude) (Figure 2.19A'-

A''). This might suggest that the Ratio method is not sufficiently robust to quantify cells with weak cellular asymmetry. Ratio method fits a square wave with period of π to the intensity signal around the cell periphery. However, when polarity is weak (with presence of small punctate on the cell junctions), the peak-to-peak variability becomes significant and hence, a perfectly periodic square wave might not be sufficient to describe the signal. Thus, PCA and Fourier Series methods would be a better choice for quantifying weakly polarised cells.

E-Cadherin, on the other hand, has been demonstrated to exhibit asymmetric distribution around the cell periphery, which plays an important role in regulating cell intercalation within the epidermis of *Drosophila* embryos [Bulgakova et al., 2013]. Therefore, I quantified E-Cadherin::GFP asymmetry in images of lateral epidermal cells in *Drosophila* embryos at stage 15, where the embryonic epidermal cells exhibit an elongated rectangular shape (Figure 2.19B). Based on published results from [Bulgakova et al., 2013], E-Cadherin proteins are asymmetrically localised to the shorter cell boundaries (dorsal-ventral), therefore it should exhibit approximately $\pm 90°$ angle of polarisation (along the y-axis in the image). Notably, polarity angles of embryonic epidermal cells computed using PCA method are well-aligned along $\pm 90°$ (with a circular angle variance of 0.04), in agreement with the published result from [Bulgakova et al., 2013]. On the contrary, the polarity angles obtained from both Fourier Series and Ratio methods are more dispersed from $-90°$ to $+90°$ (with circular angle variances of 0.52 and 0.50 respectively), which disagree with the results from [Bulgakova et al., 2013] (Figure 2.19B''). This demonstrates that the accuracy of both Fourier Series and Ratio methods in detecting polarity angle will be affected by elongated cells.

These two methods, however, strongly correlate with each other in terms of polarity magnitude (r^2 = 0.8443), while PCA method shows poor correlation with Fourier Series method (r^2 = 0.2712) (Figure 2.19B'). Despite of this, it is important to note that both polarity magnitude and angle are highly interdependent quantities. In the sense that an inaccurate quantification of polarity angle will lead to an incorrect measure of polarity magnitude. Hence, despite the strong correlation between Fourier Series and Ratio method, this does not necessarily imply that both results

are correct due to its inaccuracy in polarity angle detection. Besides that, simulation results on elongated cells showed that polarity magnitudes obtained from both Fourier Series and Ratio methods are susceptible to elongated cells. Therefore, PCA method would be better suited for analysing elongated cells.

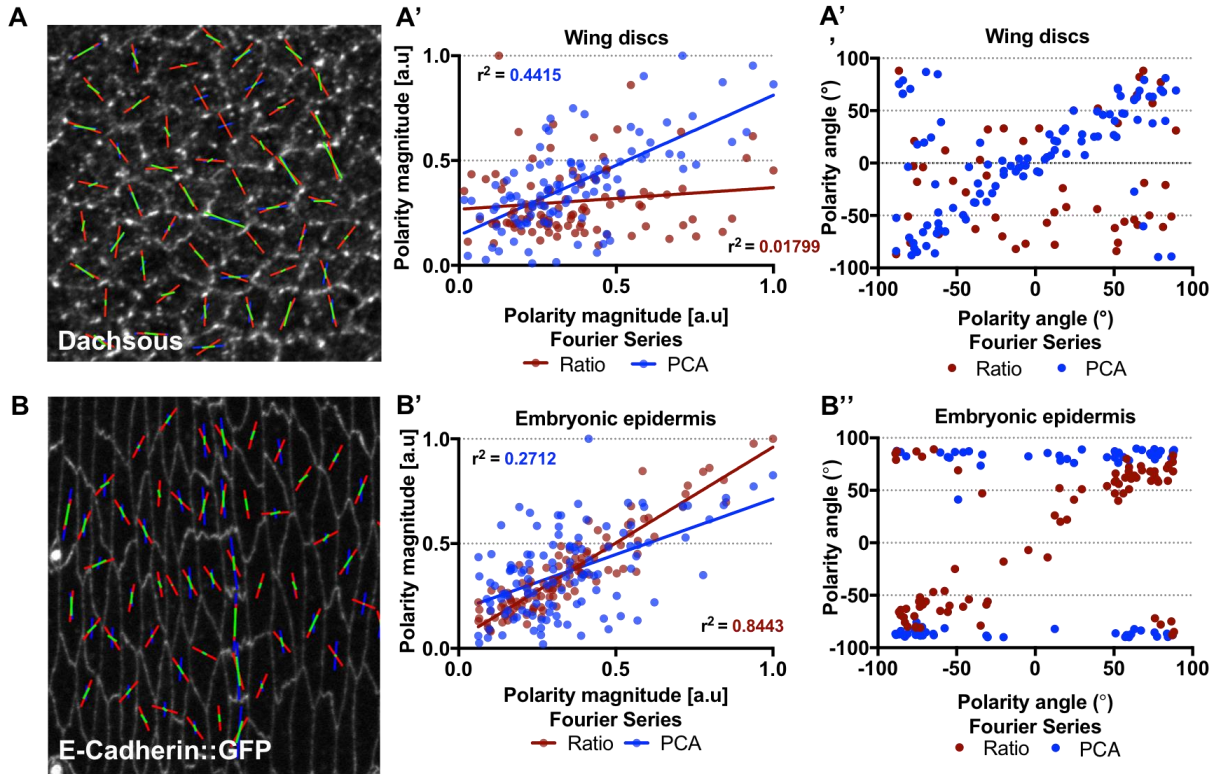

Figure 2.19: Validation of planar polarity algorithms on *Drosophila* wing discs and epidermal embryonic cells

(A) Quantified cell-scale polarity pattern of wing discs stained for Dachsous at third-instar larva. The red, green and blue bars represent the vectorial nature of polarity pattern for a given cell obtained from Ratio, Fourier Series and PCA method respectively.

(A') Plot of polarity magnitudes and angles of wing discs obtained from Ratio (red dots) and PCA (blue dots) versus Fourier Series with best fit lines shown as red and blue lines respectively. Coefficients of determination r^2 are computed accordingly.

(A'') Plot of polarity angles of wing discs obtained from Ratio (red dots) and PCA (blue dots) versus Fourier Series (n = 3 wing discs with 120 cells analysed).

(B) Quantified cell-scale polarity pattern of E-Cadherin::GFP expressing epidermal embryonic cells at stage 15. Dorsal is to the left of the image.

(B') Plot of polarity magnitudes and angles of embryonic epidermal obtained from Ratio (red dots) and PCA (blue dots) versus Fourier Series with best fit lines shown as red and blue lines.

(B'') Plot of polarity angles of embryonic epidermal cells obtained from Ratio (red dots) and PCA (blue dots) versus Fourier Series ($n = 3$ embryos with 120 cells analysed).
All polarity magnitudes (a.u) are normalised against its maximum. All polarity angles (in degree) range between $-90°$ to $+90°$, with $0°$ corresponds to the x-axis of the image. Wing discs and embryonic epidermal images were kindly provided by Katherine Fisher and Natalia Bulgakova.

2.6.4 QuantifyPolarity Graphical User Interface

The need for highly robust and accurate measurement of planar polarity on any two-dimensional epithelial tissue is essential in order to understand how tissue structure at multicellular scale is achieved through changes in polarity of individual and collective cells. Therefore, I designed and developed an easy-to-use Graphical User Interface (GUI) providing analysis tools for accurate quantification of 2D planar polarity in epithelia by incorporating all the three polarity methods - Ratio, Fourier Series and PCA (Figure 2.20). This GUI is built with MATLAB. Here, I would like to highlight several advantages of this QuantifyPolarity GUI.

First, QuantifyPolarity provides three different computational methods to quantify planar polarity. These methods are applicable to any 2D asymmetrical distribution of proteins on cell junctions, for example, asymmetrical localisation of auxin-efflux carrier PIN1 in leaf primordia, unipolarisation of Myosin II during germband extension and others [Benková et al., 2003; Tetley et al., 2016]. PCA method would be a better choice to accurately quantify planar polarity on irregular and elongated cells. Second, it is a high speed user-friendly interface, which allows users to go from segmented data to a complete quantitative analysis of planar polarity. It is capable of analysing both local and global (or coarse-grain) epithelial polarity. With automated batch processing of multiple images, users can accelerate the process of analysing polarity for single image at a time, which is often time-consuming and tedious. Third, QuantifyPolarity automatically generates and organises all the results into Microsoft Excel files for easy accessibility and further analysis. Additionally, QuantifyPolarity displays colour-coded polarity plots, allowing users to directly inspect the results of the quantification. Finally, it can operate on wide range of platforms such as Mac and Windows without requiring MATLAB software. QuantifyPolarity will be publicly available as a free software package accessible for the scientific community once published. Please refer to the Appendix section for a detailed user manual on QuantifyPolarity GUI.

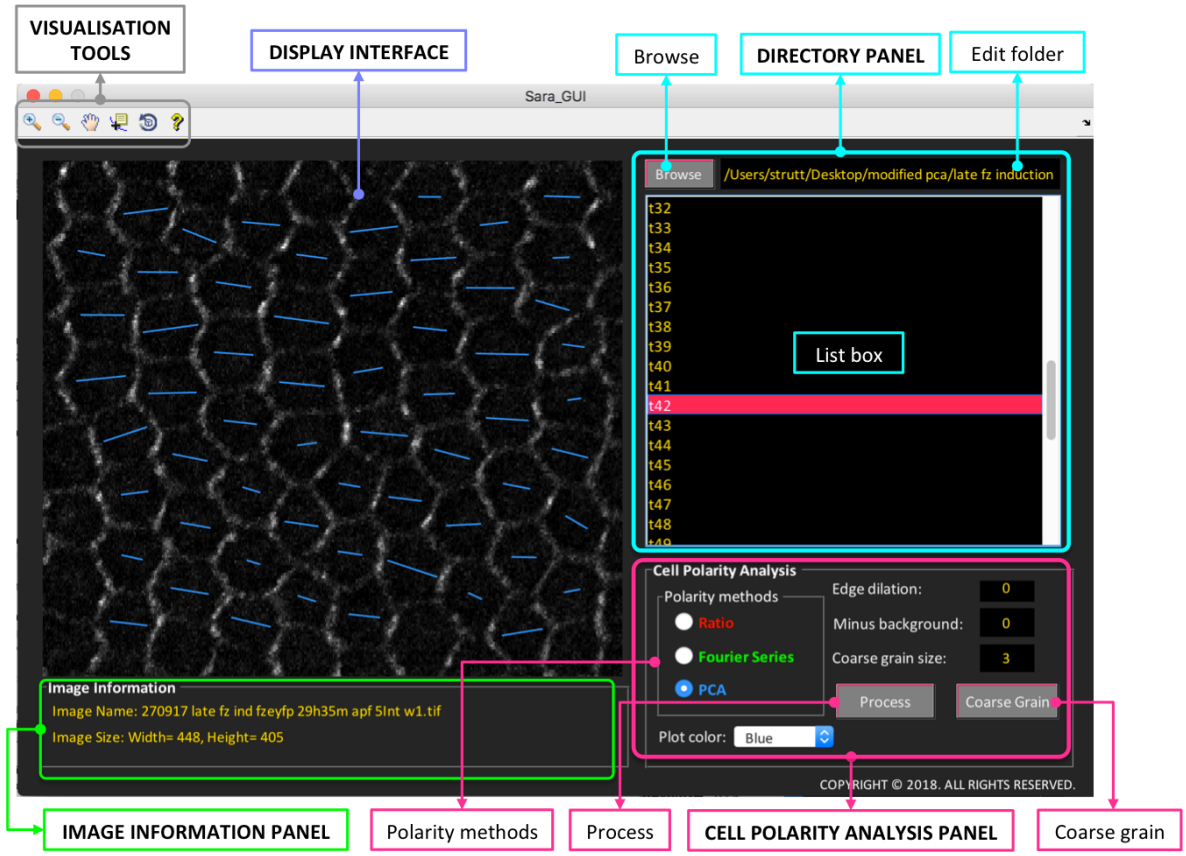

Figure 2.20: An overview of all the components available in QuantifyPolarity Graphical User Interface

2.7 Discussion

Cell shape changes throughout germband are proposed to occur in response to ventral furrow invagination, resulting in germband extension [Butler et al., 2009; Lye et al., 2015]. Similarly, during pupal wing morphogenesis, cell shape changes in pupal wing occur in response to passive mechanical forces driven by wing-hinge contraction [Etournay et al., 2015]. The relative contributions of these cell behaviour to core planar polarisation are not well understood. Therefore, in this work, I have developed several tools for the quantification of cell morphological properties such as cell shape regularity, cell eccentricity and orientation, hexagonal orientation, number of neighbours (topology) and cell apical area. These tools will enable me to dissect the individual contribution of cell shape and size on core planar polarisation pathway and vice versa during pupal wing morphogenesis.

. In a multicellular epithelial tissue, local changes in cell shape and behaviours contribute to global changes in tissue-level organisation. Since epithelial wing tissue display planar polarity within the plane of the tissue, hence it would be interesting to examine how tissue organisation at the multicellular scale might affect tissue planar polarisation and vice versa [Hale and Strutt, 2015]. Due to the lack of objective quantification method for classifying the level of epithelial tissue organisation, I have developed and validated a new quantification measure to capture the level of epithelial tissue disorganisation based on the packing density and deviation of apical area of a group of cells. Taken together the validation results on simulated Centroidal Voronoi tessellation data and actual experimental pupal wing data, this measure is indeed capable of capturing the changes in global epithelial organisation. Hence, this method will be employed for quantification of epithelial tissue organisation in pupal wings of different genotypes or conditions in the subsequent chapters.

Apart from cellular and tissue level morphological quantifications, I have developed a novel algorithm to quantify the asymmetrical distribution of protein on cell boundaries based on Principal Component Analysis (PCA). I then explored extensively the robustness of three different planar polarity quantification methods

(Fourier Series, Ratio and PCA) under various conditions, both on simulated cells and on actual experimental data. Comparing all the three methods, polarity angle obtained from Ratio method appears to be less accurate with some random fluctuations given different cell shapes, sizes as well as on simulated noise conditions. Therefore, Fourier Series and PCA methods would be a better option for quantification of polarity angle. Despite validation on experimental data for pupal wing at 24 hAPF might not be conclusive as to which method is right, however, results from other validations provide sufficient evidences that PCA is least affected by cell eccentricity. Therefore, the PCA method will be used primarily for planar polarity quantification in this thesis as experiments presented in subsequent chapters involved various extend of manipulation on cell shape.

The PCA method provides a readout for planar polarity in terms of the magnitude and angle of polarity for a single cell. The computed polarity magnitudes obtained from individual cells are combined in specific ways to reveal the strength of polarity and the polarity coordination between cells. The “Direct” average polarity magnitude, p_{average} is best suited to measure the strength of polarisation for a group of cells in general, whereas the “Vector” average polarity magnitude, p_{vec} can be used to determine the strength of polarisation and the coordination or alignment of polarity within a group of cells. There is no single right method to measure average polarity magnitude (direct or vector) as both methods serve different purposes.

Finally, I have developed a standalone and user-friendly graphical user interface, QuantifyPolarity, by incorporating three validated planar polarity methods (Fourier Series, Ratio and PCA methods). This graphical user interface enables experimentalists with no prior computational expertise to perform high-throughput polarity analysis automatically and efficiently. More importantly, QuantifyPolarity can be used to analyse any 2D asymmetrical distribution of proteins on cell boundaries, not limited to core planar polarity studies. It will be publicly available, once published, as a standalone package that allows experimentalists to perform polarity analysis.

CHAPTER 3

Quantitative analysis of core planar polarisation and cell morphology in the wild-type

3.1 Introduction

The pioneering work from [Aigouy et al., 2010] has demonstrated that during pupal wing morphogenesis, irregular and elongated cells relax to a more regular and isotropic shape with higher percentage of hexagonal cells by 32 hAPF (hour After Puparium Formation). More in-depth analysis on tissue shear due to cellular level contributions such as cell deformation, cell division and junctional rearrangement over the entire wing is well-presented in [Etournay et al., 2015]. However, there is more to discover about the evolution of tissue organisation during pupal wing morphogenesis. Moreover, these quantitation studies were primarily based on the averages of cell deformations on the tissue scale over the entire wing blade region, excluding the wing hinge region. However, due to the variation of tissue stresses in different regions of the wing as reported by [Etournay et al., 2015], I predict that cell shape and tissue organisation changes could differ across different regions of the wing. Therefore, to verify previous studies using the quantification tools that I have developed (see details in Chapter 2), I decided to quantify the temporal evolution of cell shape and tissue organisation in different regions of the wing blade, specifically the anterior and posterior regions of the wing.

Prior to emergence of polarised wing hairs, the magnitude of core planar polarisation intensifies concomitantly with relaxation of cells into a regular hexagonally packed geometry [Classen et al., 2005; Aigouy et al., 2010]. It was further reported that core planar polarity magnitude is temporally correlated to the magnitude of cell elongation during pupal wing morphogenesis [Aigouy et al., 2010]. However, as demonstrated in Chapter 2, the Fourier Series-based measure of core planar polarisation used in [Aigouy et al., 2010] is susceptible to variation of cell elongation. Therefore, there is a need to validate previous literature results using the Principal Component Analysis (PCA) method, which is insensitive to variation of cell shapes and size (see details in Section 2.6.3, Chapter 2). Furthermore, a comprehensive temporal correlation between cellular contributions such as cell regularity, size, and tissue organisation, and core planar polarisation has not been thoroughly examined.

3.2 Aims

In this chapter, I aim at performing extensive quantitative analysis on wild-type pupal wings expressing Frizzled::EGFP (Fz::EGFP) in order to confirm previous literature results with the quantification tools that I have developed. Moreover, it is essential to establish the main quantification measures for further experiments in subsequent chapters. I focus on pupal wing developmental time between 24 and 32 hAPF, when hexagonal packing predominantly occurs through cell junctional remodelling with negligible contributions from oriented cell divisions, cell apoptosis and cell flow [Aigouy et al., 2010; Etournay et al., 2015]. In Section 3.3.1 and 3.3.2, I examine the spatiotemporal evolutions of core planar polarisation, cell shape and tissue organisation at four pupal ages between 24 hAPF and 30 hAPF, at the anterior and posterior regions of wild-type pupal wing respectively. In Section 3.3.3, I compare the temporal correlation between core planar polarisation and cell packing in different regions of the wild-type wing. I wish to uncover if this temporal correlation holds true in different regions of the wing.

3.3 Results

3.3.1 The dynamic progression of core planar polarity patterns during wing morphogenesis

To investigate how core planar polarity evolves in a spatiotemporal pattern during pupal wing morphogenesis, I performed an extensive quantitative analysis of polarity establishment across different wing regions over time. I used the Principal Component Analysis (PCA) method to quantify planar polarity based on the anisotropic distribution of Fz::EGFP intensity on cell boundaries (see details in Section 2.6.1, Chapter 2). This method will give us a readout of the magnitude and angle of polarity for each cell. Here, the computed polarity magnitudes obtained from individual cells are combined in several ways to reveal the strength of polarity and the polarity coordination between cells (see details in Section 2.6.2, Chapter 2).

For coarse-grain (global) polarity quantification over the entire imaged regions (approximately more than 100 cells per region), I computed the: (1) **Direct average polarity magnitude** - by averaging over the entire region, (2) **Vector average polarity magnitude** - by vector averaging over the entire region. Apart from coarse-grain polarity, to analyse local polarity coordination with its immediate neighbouring cells, I computed the: (1) **Neighbour direct average polarity magnitude** - by averaging with its immediate neighbours, (2) **Neighbour vector average polarity magnitude** - by vector averaging with its immediate neighbours. In short, direct average polarity magnitude measures the strength of polarisation over the entire region or locally among neighbouring cells. Unlike direct average polarity magnitude, vector polarity magnitude considers not only the strength of polarisation but also the coordination of polarity between cells.

3.3.1.1 Fz::EGFP becomes increasingly polarised over time along the proximal-distal (PD) axis in the posterior of wild-type wings

I started by quantifying polarity magnitude at the posterior region of the wild-type wing from 24 to 32 hAPF. I imaged the posterior region of the wing, which lies directly below longitudinal vein 5 (Figure 3.1A and 3.1B-B'). At 24 hAPF, average polarity magnitude over the entire region is approximately 0.24 because proteins are poorly polarised. However, as Fz::EGFP becomes increasingly polarised to opposite cell junctions, the average polarity magnitude increases gradually to 0.34 by 30 hAPF (Figure 3.2B). My result is consistent with a previous study reporting that polarity magnitude increases during this developmental stage [Aigouy et al., 2010]. Thus, core planar polarisation does not develop *de novo* but rather refines or amplifies pre-existing polarity. This result is not significantly different from averaging polarity magnitude with neighbouring cells (Figure 3.2B'). On the other hand, the vector average polarity magnitude over the entire region at 24 hAPF is 0.21 and it increases to 0.31 by 30 hAPF (Figure 3.2C). Again, this result is not significantly different from vector averaging with neighbouring cells, suggesting that global and local coordination are similar (Figure 3.2C').

Vector average polarity magnitude is equivalent to direct average polarity magnitude if and only if polarity axis is perfectly aligned between neighbouring cells. Hence, the slightest deviation in polarity alignment between cells would results in lower vector average polarity magnitude as compared to direct average polarity magnitude. Evidently, for all the developmental time points, the vector average polarity magnitudes are slightly lower than the direct average polarity magnitudes.

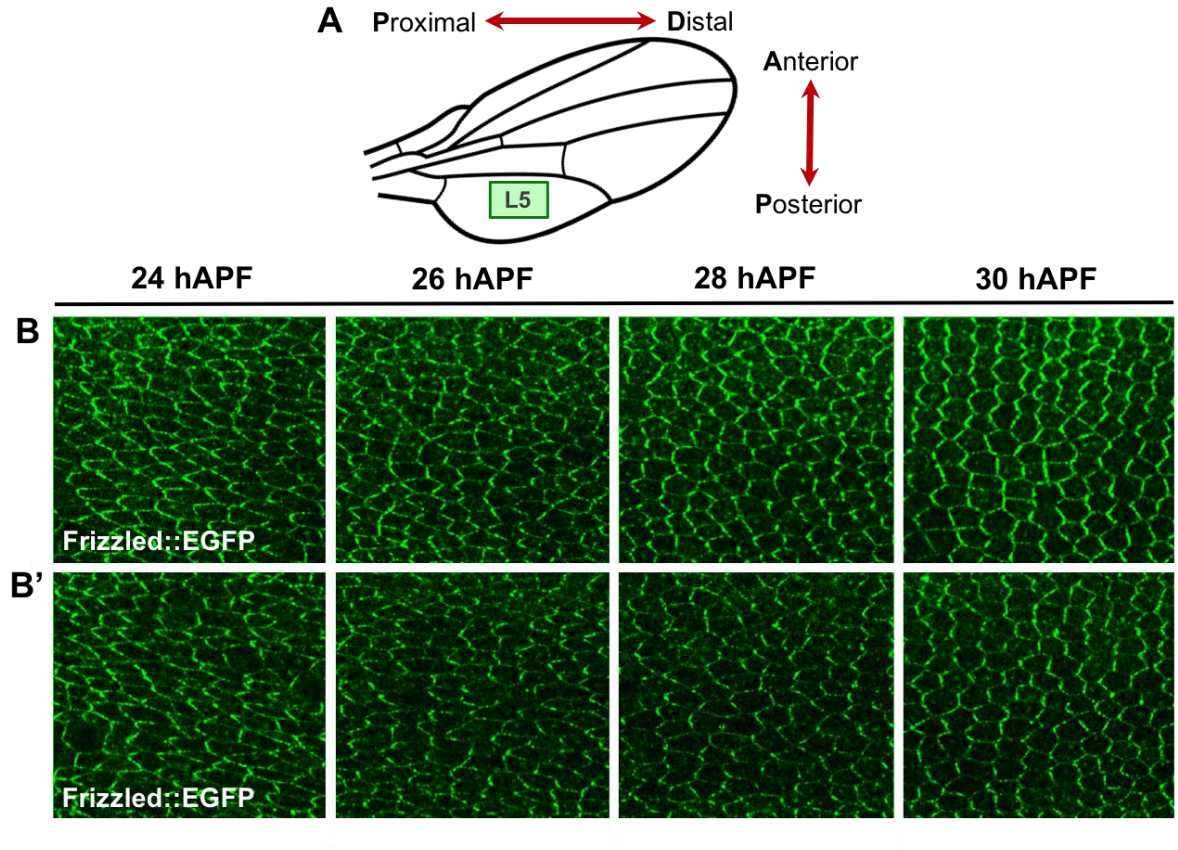

Figure 3.1: Evolution of core planar polarity in the posterior region of pupal wings

(A) Illustration of the analysed posterior region of the pupal wing blade, which lies below longitudinal vein 5. Hence, it is denoted as L5 region.

(B – B') Time-lapse confocal images of the posterior region of 2 different wild-type pupal wings expressing Fz::EGFP from 24 to 30 hAPF.

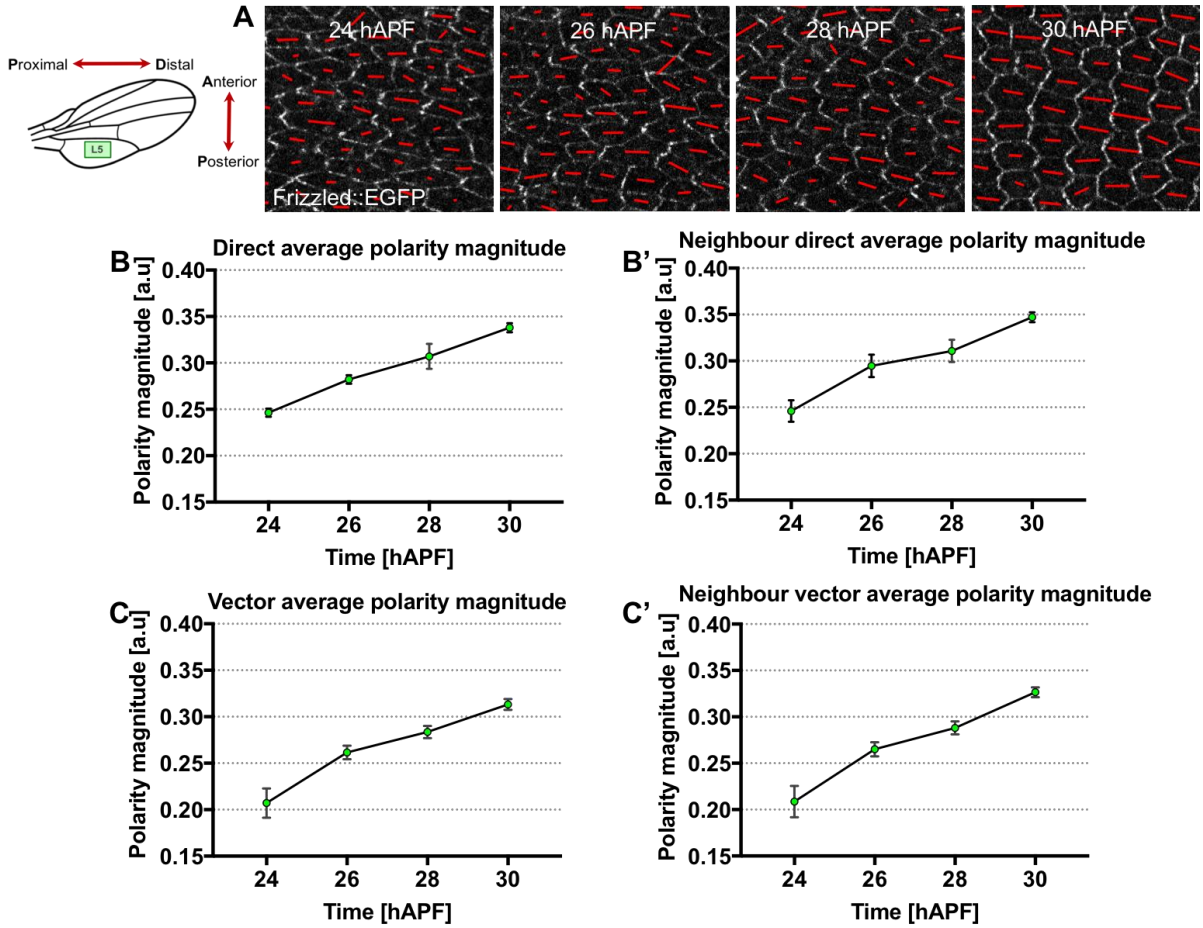

Figure 3.2: Temporal evolution of core planar polarity in the posterior region of pupal wings

(A) Time-lapse confocal images of the posterior region of a wild-type wing expressing Fz::EGFP from 24 to 30 hAPF. The length and orientation of red lines within individual cells represent the magnitude and the axis of Fz::EGFP polarity respectively.

(B – B') Direct polarity averaging of the entire region or coarse-grain (B) and with its immediate neighbouring cells (B'). Both measures increase with time.

(C – C') Vector polarity averaging of the entire region or coarse-grain (C) and with its immediate neighbouring cells (C'). Both measures increase with time.

The number of wings for each developmental time is 9. Error bar indicates mean±SEM.

To allow better visualisation of the frequency, magnitude and angle distribution of Fz::EGFP polarity patterns for a particular developmental time, I constructed a heatmap as illustrated in Figure 3.3A-A'. From the heatmap plot of polarity angle, magnitude and percentage of cells in Figure 3.3A, polarity alignment in the posterior wing at 24 hAPF varies among cells and appears to be less coordinated along the

PD axis. However, over time, polarity begins to reorient itself to align mostly along the PD axis with increasing coordination between cells by 30 hAPF (Figure 3.3A').

To determine the degree of coordination of polarity patterns over the entire region, I computed the circular angle variance, where the measure ranges from zero to one (Figure 3.3B) (zero corresponding to perfect alignment; see details in Section 2.6.2, Chapter 2). Consistently, there is a decreasing trend of polarity angle variance from 24 to 30 hAPF as the direction of polarity becomes more concentrated and aligned within a group of cells (Figure 3.3B). Once again, my result is consistent with previous study reporting that polarity increasingly aligns along PD axis during this developmental stage [Aigouy et al., 2010].

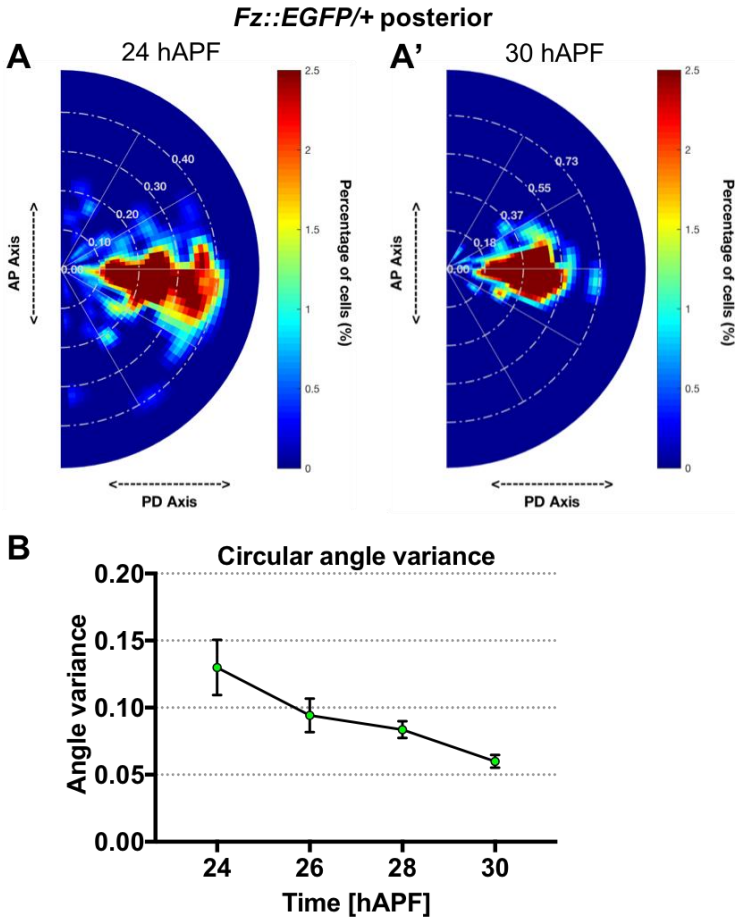

Figure 3.3: Polarity pattern coordination improves over time in the posterior wing

(A – A') Heatmaps showing the orientation and magnitude of Fz::EGFP polarity obtained from posterior wing at 24 hAPF (A) and 30 hAPF (A') respectively. In this protractor-like heatmap, the magnitude of polarity is the distance away from the centre of the half circle,

meanwhile the polarity angular distribution spans from $-90°$ to $+90°$. The percentage of cells is represented by different colours (red – high percentage of cells, blue – low percentage of cells).
(B) Quantification of polarity angle variance in the posterior region of the wing. Decreasing value for this measure expresses increasing polarity pattern coordination within a group of cells.
The number of wings for each developmental time is 9. Error bar indicates mean$\pm$SEM.

3.3.1.2 Polarity patterns of the anterior wing are similar to the posterior wing

Apart from analysing the posterior wing, I imaged the anterior region of the wing, which is located in between longitudinal vein 2 and longitudinal 3 (Figure 3.4A and 3.4B-B'). Similar to the posterior wing, average polarity magnitude over the anterior wing increases gradually from 0.27 to 0.35 between 24 to 30 hAPF (Figure 3.5B). Polarity intensifies shortly before wing hair outgrowth by 32 hAPF. The neighbour average polarity magnitudes from 24 to 30 hAPF are not significantly different from the direct average polarity magnitudes (Figure 3.5B'). On the other hand, the vector average polarity magnitude over the anterior region at 24 hAPF is 0.25 and it increases to 0.32 by 30 hAPF (Figure 3.5C). Again, this result is not significantly different from vector averaging with neighbouring cells, suggesting that global and local coordination are similar (Figure 3.5C'). Notably, different polarity magnitude measurements result in similar linearly increasing trend. Hence, I focused on the direct average polarity magnitude as the key polarity measure for all future experiments.

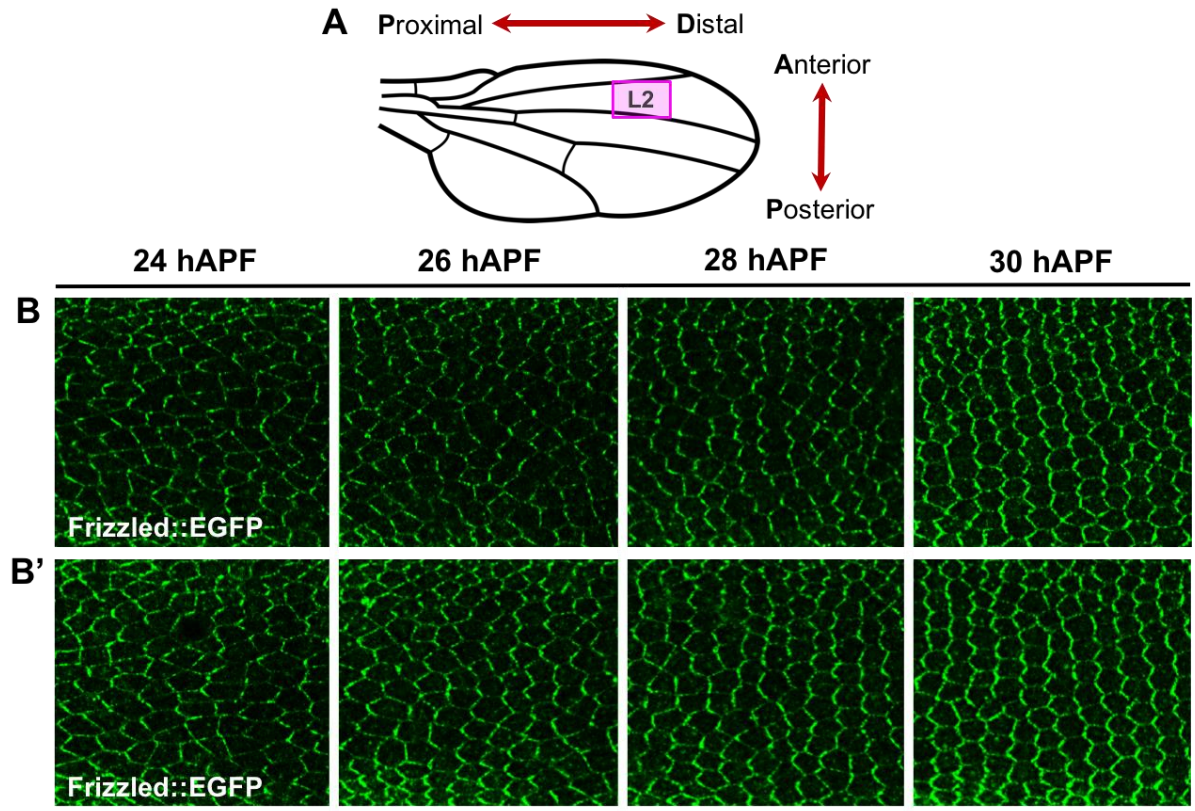

Figure 3.4: Evolution of core planar polarity in the anterior region of pupal wings

(A) Illustration of analysed anterior region of the pupal wing blade, which lies in between longitudinal vein 2 and longitudinal vein 3. Hence, it is denoted as L2 region.

(B – B') Time-lapse images of the anterior region of two different wild-type pupal wings expressing Fz::EGFP from 24 to 30 hAPF.

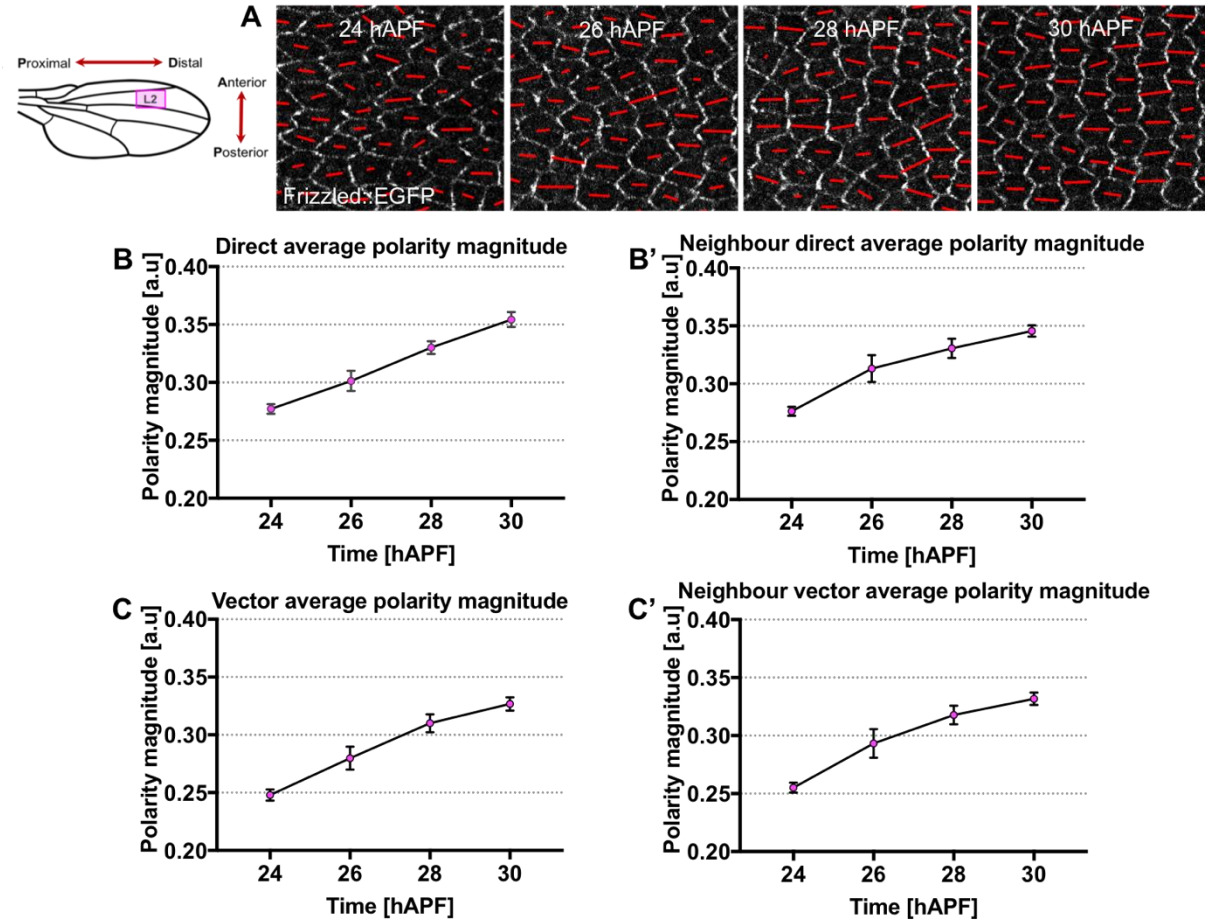

Figure 3.5: Quantification of temporal evolution of core planar polarity in the anterior region of pupal wings

(A) Time-lapse confocal images of the anterior region of a wild-type wing expressing Fz::EGFP from 24 to 30 hAPF. The length and orientation of red lines within individual cells represent the magnitude and the axis of Fz::EGFP polarity respectively.

(B – B') Coarse-grain (global) polarity quantification with direct averaging (B) and vector averaging (B') of individual cells. Both measures of Fz::EGFP polarity magnitude increase with time.

(C – C') Local polarity quantification with neighbour direct averaging (C) and neighbour vector averaging (C') with its immediate neighbours. Both measures of Fz::EGFP polarity magnitude increase with time.

The number of wings for each developmental time is 7. Error bar indicates mean±SEM.

As depicted in the heatmaps shown in Figure 3.6A and 3.6A', Fz::EGFP polarity alignment in the anterior region is less coordinated along the PD axis at 24 hAPF and becomes more concentrated along PD axis by 30 hAPF. From 24 hAPF onwards, the polarity angle variance decreases from 0.10 to 0.05 by 30 hAPF,

suggesting that the polarity alignment becomes more coordinated within the group of cells over time in the anterior region of the wing (Figure 3.6B). These results imply that the evolution of polarity patterns is similar in different regions of the wing.

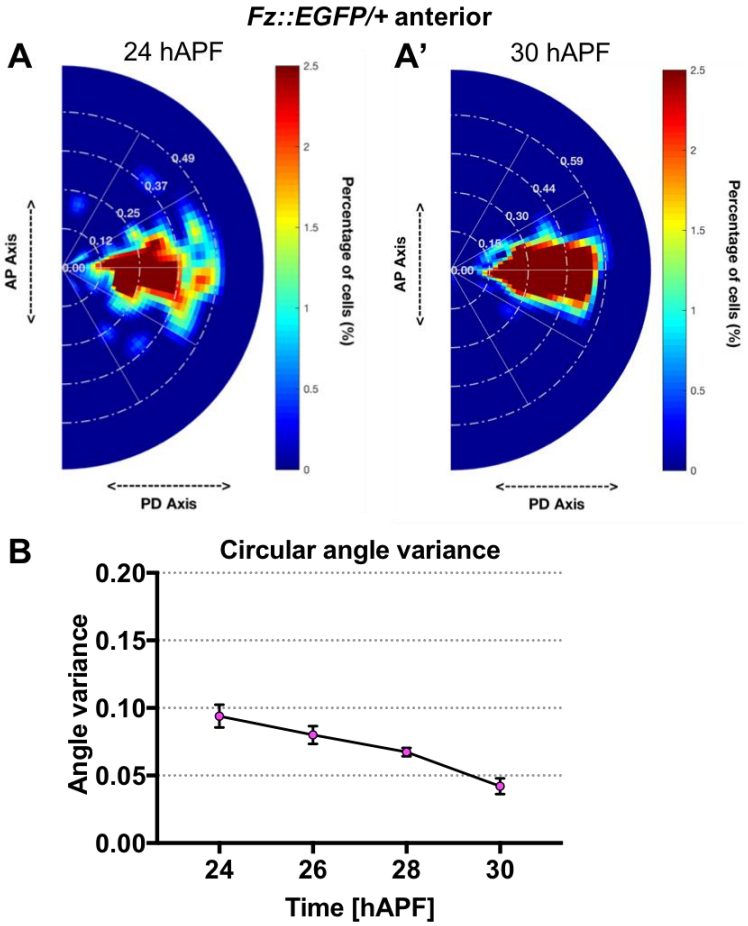

Figure 3.6: Polarity pattern coordination improves over time in the anterior wing

(A – A') Heatmaps show the orientation of Fz::EGFP polarity and its polarity magnitude obtained from anterior wing at 24 hAPF (A) and 30 hAPF (A') respectively. In this protractor-like heatmap, magnitude of polarity is the distance away from the centre of the half circle, meanwhile the polarity angular distribution span from $-90°$ to $+90°$. The percentage of cells is represented by different colours (red – high percentage of cells, blue – low percentage of cells).

(B) Quantification of polarity angle variance in the anterior region of the wing. Decreasing value for this measure expresses increasing polarity pattern coordination within a group of cells.

The number of wings for each developmental time is 7. Error bar indicates mean$\pm$SEM.

3.3.1.3 Anterior wing exhibits higher polarity magnitude as compared to posterior wing during pupal wing morphogenesis

Next, I compared the polarity magnitude and angle obtained from different regions of the wing. Due to technical limitation to distinguish proteins belonging to the cell of interest from the proteins of its neighbouring cells, it is not useful to perform cell-by-cell analysis to correlate polarity magnitude and cell morphological parameters. This is because the measure of polarity takes proteins from its neighbouring cells into account, thus it does not represent the “real” polarity for a given cell. Furthermore, planar polarity describes tissue-level organisation and coordination at cellular level, thus it is more meaningful to quantify polarisation for a group of cells.

Notably, the anterior region of the wing exhibits subtle but statistically significant higher average polarity magnitude as compared to the posterior region of the wing for all developmental time points (Figure 3.7A). Not only that, the anterior wing also exhibits lower polarity angle variance as compared to posterior wing at 24 hAPF, indicating that the polarity patterns in the anterior region of the wing are better coordinated as compared to the posterior wing (Figure 3.7B). From 26 hAPF onwards, polarity alignment gets better and it is not significantly different between both regions (Figure 3.7B). My findings reveal for the first time there is a difference in average polarity magnitude in different regions of the wing. However, it remains unknown whether there is a gradual transition in polarity magnitude along anterior-posterior axis of the wing.

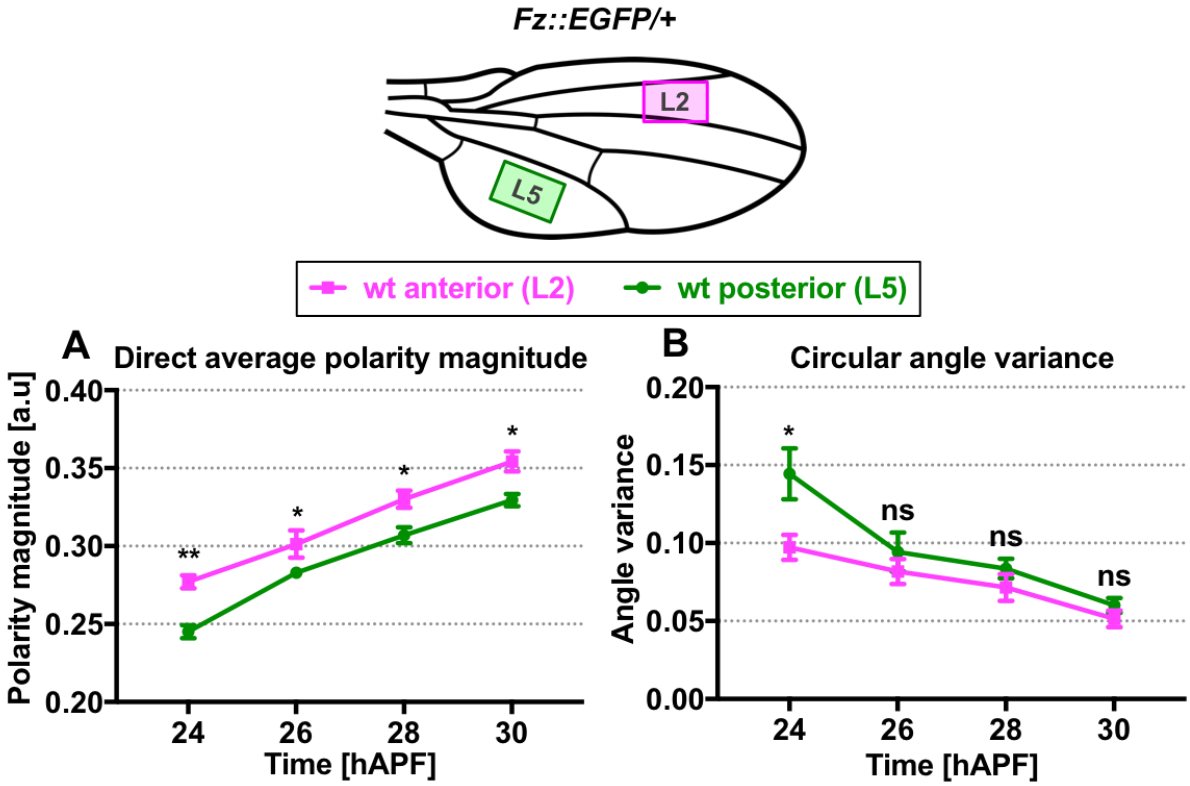

Figure 3.7: Anterior wing is better polarised as compared to posterior wing

(A) Quantified direct average polarity magnitude of anterior and posterior wing.

(B) Quantified polarity angle variance of anterior and posterior wing.

wt represents wild-type. The number of wings for each developmental stage is between 7 to 9. Error bar indicates mean±SEM. One-way ANOVA test, unpaired. Significance levels: p-value $\leq 0.005^{**}$, p-value $\leq 0.02^{*}$. ns is not significantly different.

3.3.2 The dynamic evolution of cell shapes and tissue organisation during wing morphogenesis

To examine how cell shape changes and tissue organisation evolves in a spatiotemporal pattern during pupal wing morphogenesis, I performed an in-depth analysis of cell morphological parameters and epithelial tissue organisation on different regions of Fz::EGFP-expressing wild-type pupal wings from 24 to 30 hAPF. I quantified cell morphological parameters such as cell area, eccentricity, shape regularity and number of cell sides at the cellular level (see details in Section 2.4, Chapter 2). At tissue level, I computed the level of epithelial tissue disorganisation that captures the homogeneity of cell shapes and size within a group of cells, zero being well-packed and organised with equal shapes and size of cells, while increasing values representing increasingly poor packing (see details in Section 2.5, Chapter 2).

3.3.2.1 Cell packing and tissue organisation in the posterior wing improves over time

To investigate the cellular events during pupal wing morphogenesis, I examined the posterior wing from 24 to 30 hAPF. The average apical cell area increases drastically (about 20%) between 24 to 28 hAPF before shrinking slightly (about 7%) by 30 hAPF (Figure 3.8A). As the final cell divisions and apoptosis processes are concluding by 24 hAPF, the apical area expansion might be a consequence of hinge-contraction which happens at the same time. At 24 hAPF, the posterior wing epithelium is irregularly packed with mixtures of quadrilateral (3%), pentagonal (32%), hexagonal (48%) and heptagonal (17%) cells (Figure 3.8B and 3.8B''). However, shortly before prehair emerging at approximately 32 hAPF, the posterior wing undergoes junctional rearrangement into a quasihexagonal array with approximately 70% of hexagonal cells (Figure 3.8B' and 3.8B''). Cells assemble new junctions along the PD axis, thus increasing the average number of neighbours and the percentage of hexagonal cells. Here my results are consistent with [Classen et al., 2005; Aigouy et al., 2010].

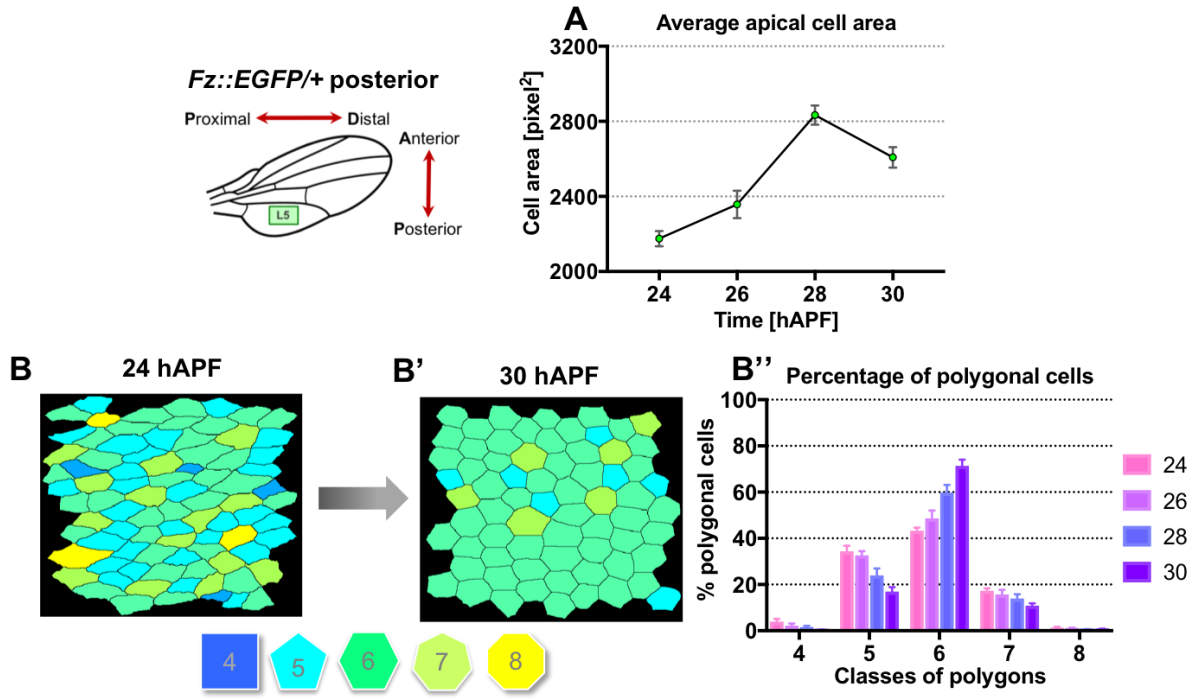

Figure 3.8: Evolution of apical cell area and polygon classes in the posterior region of pupal wing during development

(A) Quantification of average apical cell area in the posterior region of the wing.

(B – B') Processed images of the posterior wing at 24 hAPF (B) and 30 hAPF (B') respectively. Cells are colour-coded according to the number of cell sides.

(B'') Percentage of cells with four, five, six, seven and eight sides from 24 to 30 hAPF. The fraction of hexagonal cells increases from 24 to 30 hAPF.

The number of wings for each developmental stage is 9. Error bar indicates mean±SEM.

Next, I quantify cell eccentricity, shape regularity and tissue organisation during pupal wing morphogenesis. During 24 to 30 hAPF, cell shape changes from highly irregular to highly regular in geometry, resulting in an increasing fraction of regular cells over time (Figure 3.9A-B). On the other hand, cell eccentricity gradually decreases from 24 to 30 hAPF as consistent with [Aigouy et al., 2010] (Figure 3.9C). To capture global changes in the wing tissue organisation underlying cell shape changes, I analysed the epithelial organisation in the posterior region of the wing. As depicted in Figure 3.10A, at 24 hAPF, cells are inhomogeneous in terms of shapes and size, with a mixture of polygonal cells, resulting in poor packing with increased disorganisation. However, over time the tissue gradually relaxes towards better organisation, where all the cells are more homogeneous in terms of shapes and size (Figure 3.10A-B). Here, my data suggested that cell eccentricity and cell shape

regularity proceeded over the same period (from 24 to 30 hAPF), during which epithelial tissue becomes more organised and well-packed. Interestingly, from 30 hAPF to 36 hAPF, cells still undergo further relaxation towards better organisation with a slight reduction in cell eccentricity and increased shape regularity. There is a positive correlation (with coefficient of determination, r^2 = 0.9743) between cell eccentricity and tissue disorganisation from 24 to 36 hAPF (Figure 3.11A). On the contrary, cell shape regularity negatively correlates (with coefficient of determination, r^2 = 0.9599) with tissue disorganisation over this time period (Figure 3.11B). Nonetheless, these three measures are considered interchangeable for future experiments due to their strong correlations.

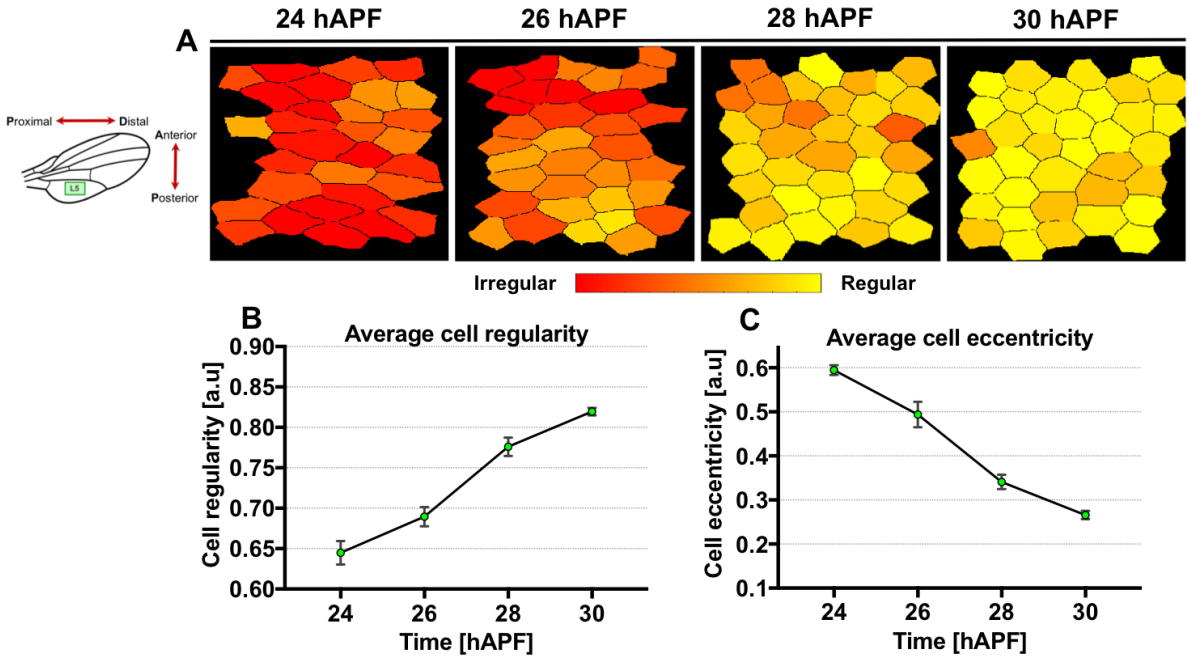

Figure 3.9: Evolution of cell eccentricity and shape regularity in the posterior region of the pupal wings during development

(A) Processed images of posterior wing from 24 to 30 hAPF. Cells are colour-coded according to the regularity of the shape, with red represent highly irregular and yellow being perfectly regular.

(B) Quantification of average cell regularity in the posterior region of the wing. On average, posterior wing cells become more regular over time.

(C) Quantification of average cell eccentricity in the posterior region of the wing. On average, posterior wing cells become less elongated over time.

The number of wings for each developmental stage is 9. Error bar indicates mean±SEM.

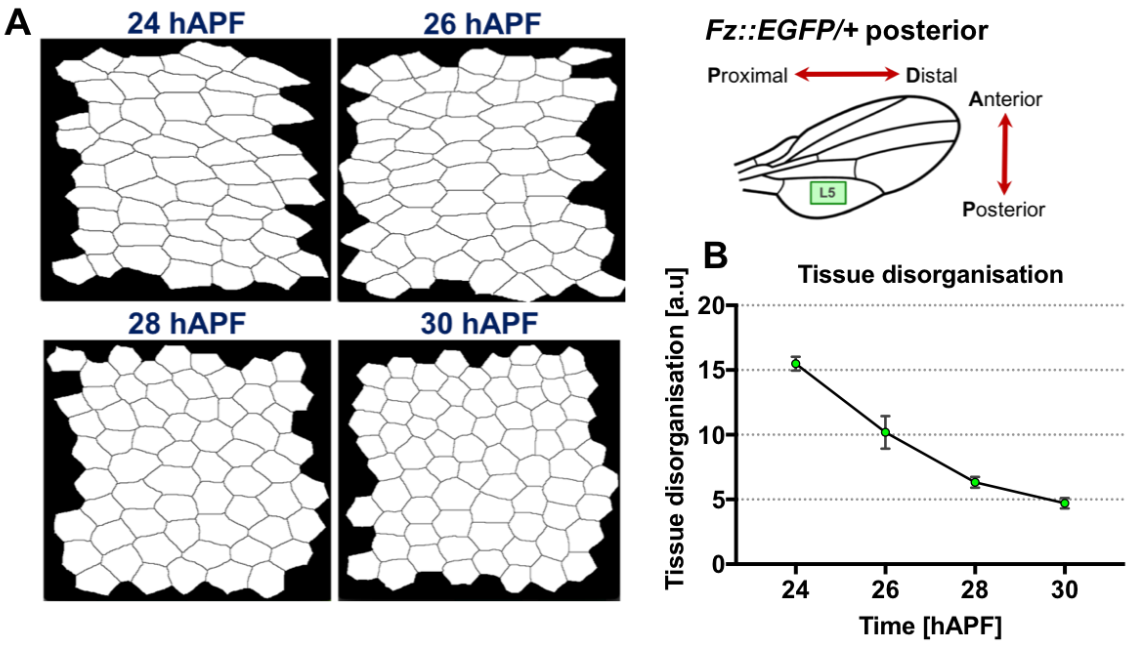

Figure 3.10: Posterior wing tissue becomes increasingly organised over time

(A) Processed time-lapse images of posterior wing from 24 to 30 hAPF.

(B) Quantification of epithelial tissue disorganisation in the posterior region of the wing. Decreasing values indicate increasing orderliness in tissue organisation. Tissue becomes increasingly organised from 24 hAPF to 30 hAPF.

The number of wings for each developmental stage is 9. Error bar indicates mean±SEM.

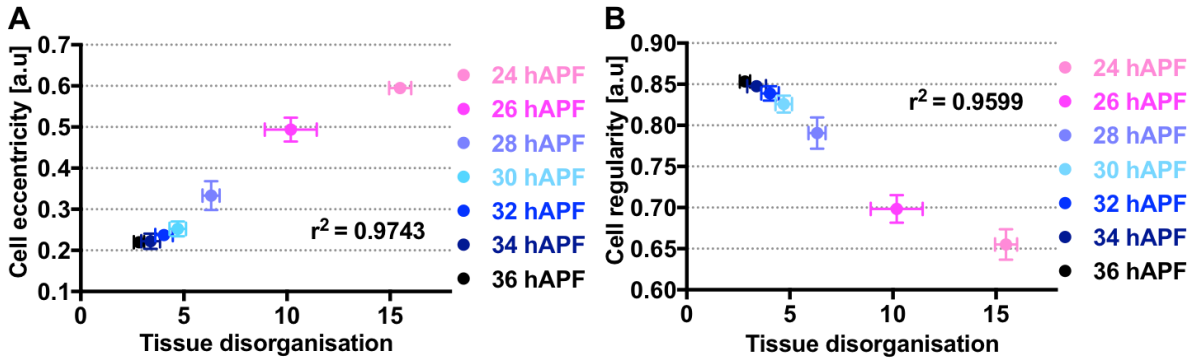

Figure 3.11: Correlation between cell eccentricity and shape regularity with tissue organisation

(A) Cell eccentricity positively correlates with tissue disorganisation from 24 to 36 hAPF.

(B) Cell shape regularity negatively correlates with tissue disorganisation from 24 to 36 hAPF.

The number of wings for each developmental time is 9. Error bar indicates mean±SEM.

3.3.2.2 Cell packing and tissue organisation in the anterior wing improves over time

Next, I examined the anterior wing between 24 to 30 hAPF. From 24 to 30 hAPF, the apical cell area increases slightly (about 6%) between 24 to 28 hAPF before decreasing by 10% at 30 hAPF (Figure 3.12A). At 24 hAPF, the wing epithelium is irregularly packed with mixtures of quadrilateral (4%), pentagonal (31%), hexagonal (48%) and heptagonal (14%) cells (Figure 3.12B''). However, by 30 hAPF, the fraction of hexagonal cells increases to approximately 74% as quadrilateral, pentagonal and heptagonal cells decrease (Figure 3.12B' and 3.12B''). Similar to the posterior wing, the anterior wing undergoes relaxation to hexagonal packing from 24 to 30 hAPF. Here, I confirmed that my results are consistent with [Classen et al., 2005; Aigouy et al., 2010].

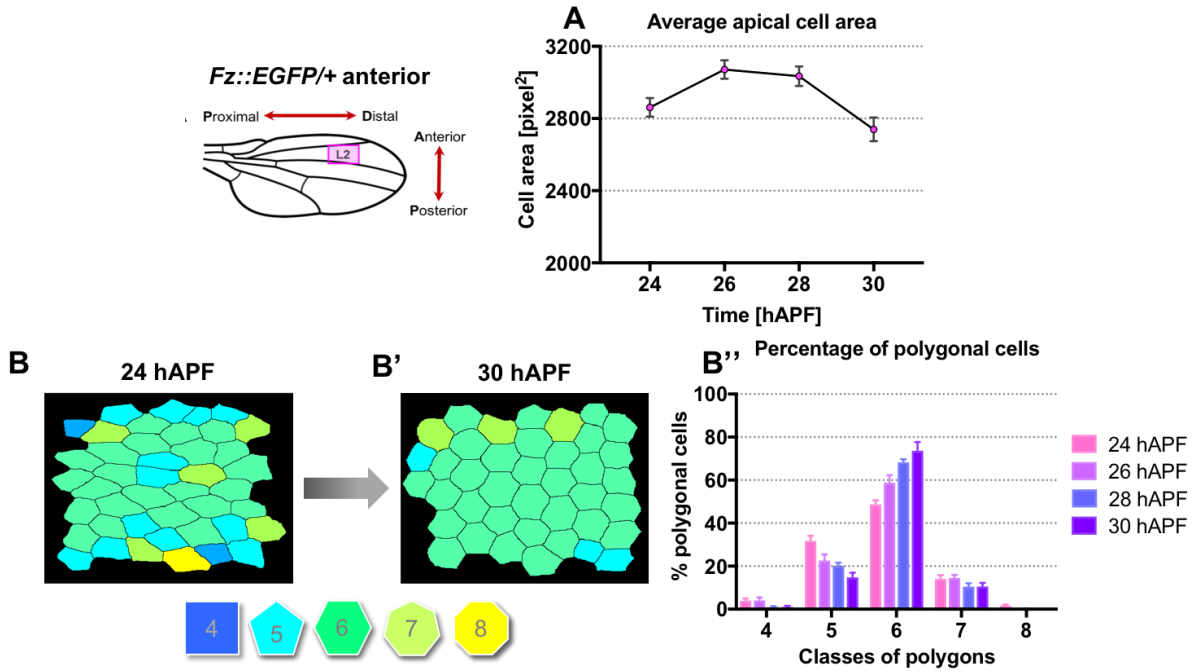

Figure 3.12: Evolution of apical cell area and polygon classes in the anterior wing during development

(A) Quantification of average apical cell area in the anterior region of the wing.

(B – B') Processed images of anterior wing at 24 hAPF (B) and 30 hAPF (B') respectively. Cells are colour-coded according to the number of cell sides.

(B'') Percentage of cells with four, five, six, seven and eight sides from 24 to 30 hAPF. The fraction of hexagonal cells increases from 24 to 30 hAPF.

The number of wings for each developmental time is 7. Error bar indicates mean±SEM.

On the other hand, regularity in cell shape increases from 24 to 30 hAPF, indicating that there is a higher fraction of regular cells by 30 hAPF (Figure 3.13A-B). A higher fraction of regular cells results in better cell packing. The average cell eccentricity within the anterior region of wild-type wings decreases linearly from 24 hAPF to 30 hAPF [Aigouy et al., 2010] (Figure 3.13C). As predicted, by quantifying epithelial tissue organisation in the anterior wing, I found that at 24 hAPF, epithelial tissue is highly disorganised and poorly packed (Figure 3.14A-B). However, tissue gradually relaxes towards better organisation from 24 hAPF onwards (Figure 3.14A-B). Overall, the temporal changes in cell eccentricity, regularity and tissue organisation in the anterior wing are similar to posterior wing.

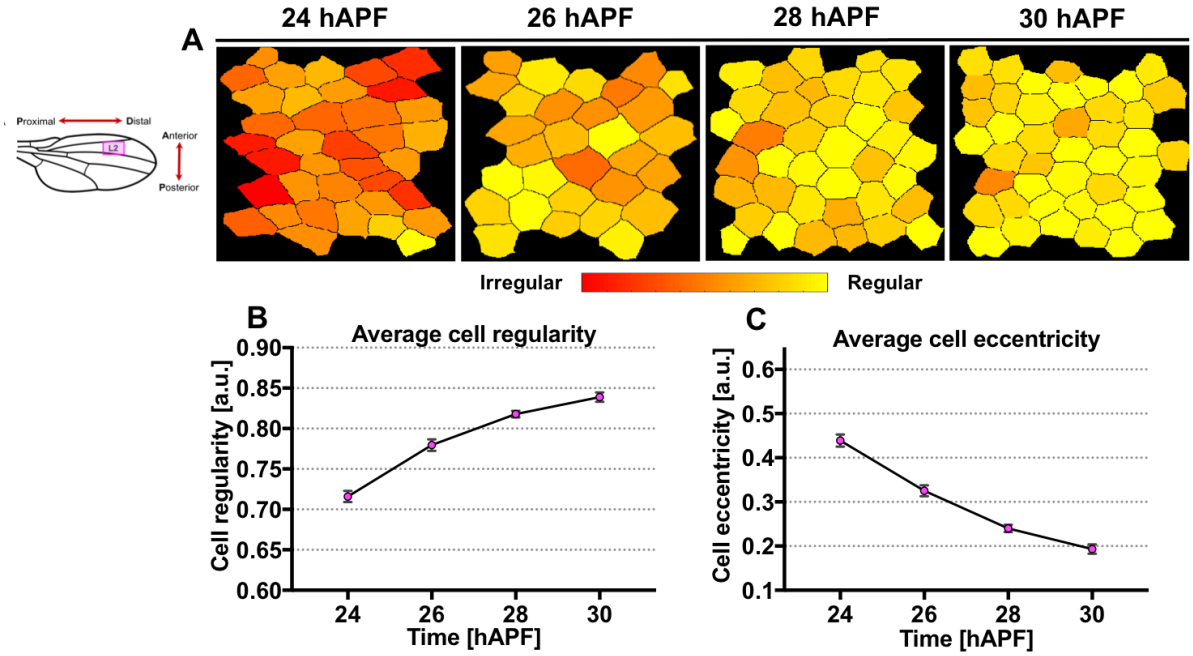

Figure 3.13: Evolution of cell eccentricity and shape regularity in the anterior wing during development

(A) Processed images of anterior wing from 24 to 30 hAPF. Cells are colour-coded according to the regularity of the shape, with red represent highly irregular and yellow being perfectly regular.

(B) Quantification of average cell regularity in the anterior region of the wing. On average, anterior wing cells become more regular over time.

(C) Quantification of average cell eccentricity in the anterior region of the wing. On average, anterior wing cells become less elongated over time.

The number of wings for each developmental time is 7. Error bar indicates mean±SEM.

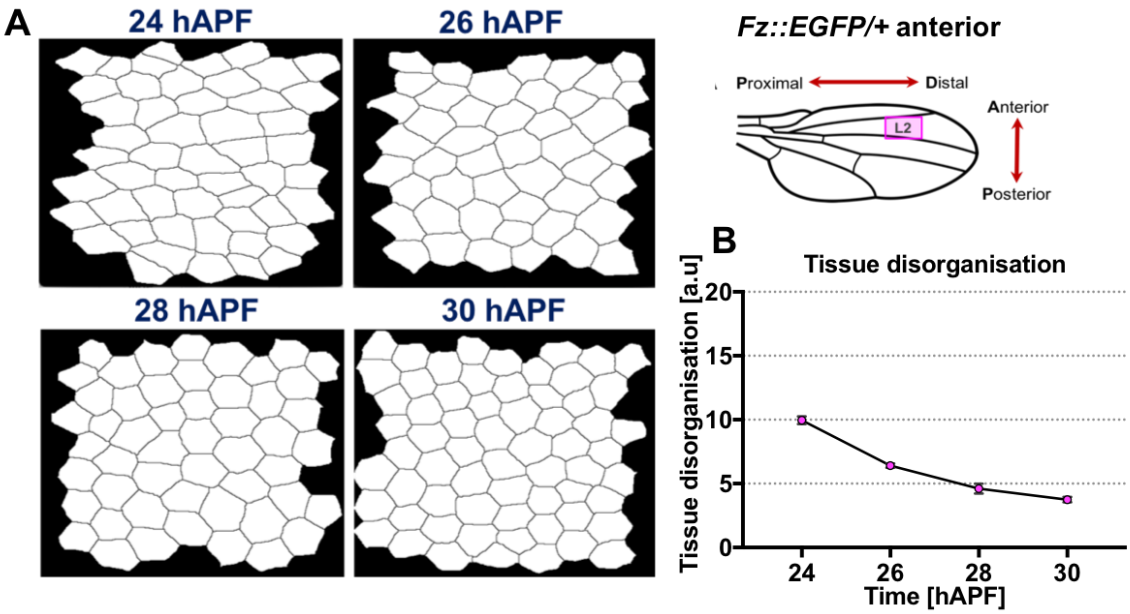

Figure 3.14: Anterior wing tissue becomes more organised over time

(A) Processed time-lapse images of anterior wing from 24 to 30 hAPF.

(B) Quantification of epithelial tissue disorganisation in the anterior region of the wing. Tissue becomes increasingly organised from 24 hAPF to 30 hAPF.

The number of wings for each developmental time is 7. Error bar indicates mean±SEM.

3.3.2.3 The epithelium in the anterior wing is better organised and well-packed as compared to the posterior wing during pupal wing morphogenesis

To investigate whether there is a morphological variation in different regions of the wing, I quantitatively compared cell shape and size variation in different regions of the wing from 24 to 30 hAPF. Quantitative comparisons of morphological variation arising at different regions of the wing at different developmental times allow us to determine when and how the variation occurs. I found significant differences in cell shapes and size earlier in development between different regions of the wing. Interestingly, as shown in Figure 3.15A, the anterior wing exhibits much larger cell size as compared to the posterior region of the wing at early phases (24 to 26 hAPF). Unlike cells in the posterior wing, cells in the anterior wing did not undergo dramatic apical area expansion. One possible explanation is the non-uniformity in stresses across the wing blade regions [Etournay et al., 2015]. Greater cell size changes from 24 to 28 hAPF in posterior wing could indicate that this region is

subjected to greater stress. As anisotropic tension gradually diminishes by 27 hAPF, cell size in both regions are not significantly different at later phase from 28 to 30 hAPF (Figure 3.15A) [Sugimura and Ishihara, 2013].

Not only that, cells in the anterior wing are less elongated as compared to the posterior wing from 24 to 28 hAPF. By 30 hAPF, cells in both regions relax to a minimum cell eccentricity (Figure 3.15B). [Etournay et al., 2015] reported that wing hinge-contraction induces anisotropic tension that elongates cells along the PD axis, leading to the peak of cell elongation at about 24 hAPF. As anisotropic tension gradually diminishes by 27 hAPF, cells eventually relax into less elongated shape by 30 hAPF. Less elongated cells in anterior wing also appear to be more regular in shape as compared to posterior wing at the same time (Figure 3.15C). Not only that, tissue organisation in anterior wing appears to be significantly better organised and well packed as compared to the posterior wing. Eventually by 30 hAPF, tissue organisation becomes not significantly different in both wing regions (Figure 3.15D). Therefore, my findings conclude that different regions of the wings exhibit different cell shapes, size and tissue organisation.

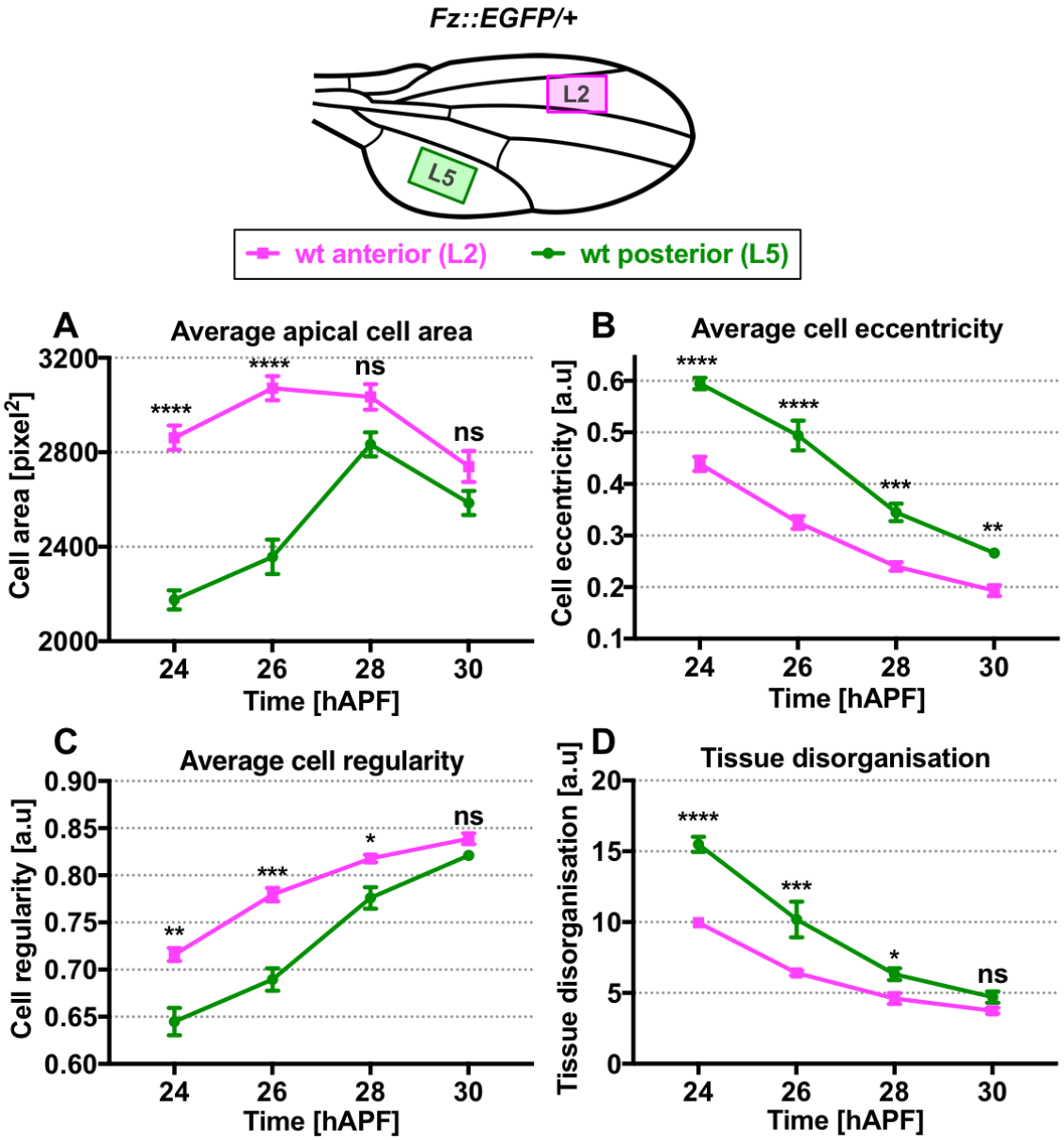

Figure 3.15: Anterior wing is better organised and well-packed as compared to posterior wing during development

(A) Quantified average apical cell area of anterior and posterior wing.

(B) Quantified average cell eccentricity of anterior and posterior wing.

(C) Quantified average cell regularity of anterior and posterior wing.

(D) Quantified epithelial tissue disorganisation of anterior and posterior wing.

wt represents wild-type. The number of wings for each developmental stage is between 7 to 9. Error bar indicates mean±SEM. One-way ANOVA test, unpaired. Significance levels: p-value $< 0.0001^{****}$, p-value $\leq 0.0002^{***}$, p-value $\leq 0.001^{**}$, p-value $\leq 0.01^{*}$. ns is not significantly different.

3.3.3 Temporal correlation between cell morphology and core planar polarisation in different regions of the pupal wing

3.3.3.1 Fz::EGFP polarity orientation correlates with the orientation of epithelial cells

To assess whether core planar polarity alignment is related to cell deformation, I plotted a circular weighted histogram to represent the distribution of the orientation of Fz::EGFP polarity and cell eccentricity in both regions of the wing. I found that polarity consistently oriented parallel to the axis of cell eccentricity for both 24 hAPF and 30 hAPF. At 24 hAPF, as cells elongate along the PD axis, the majority of the cell polarity is aligned along the PD axis of the wing epithelium (Figure 3.16A-B). As cells become less elongated but still consistently oriented along PD axis by 30 hAPF, Fz::EGFP becomes increasingly polarised and aligned parallel to the axis of cell elongation (Figure 3.16A'-B'). Therefore, these data demonstrate that there is a correlation between the Fz::EGFP polarity axis and axis of cell elongation in different regions of wild-type wings.

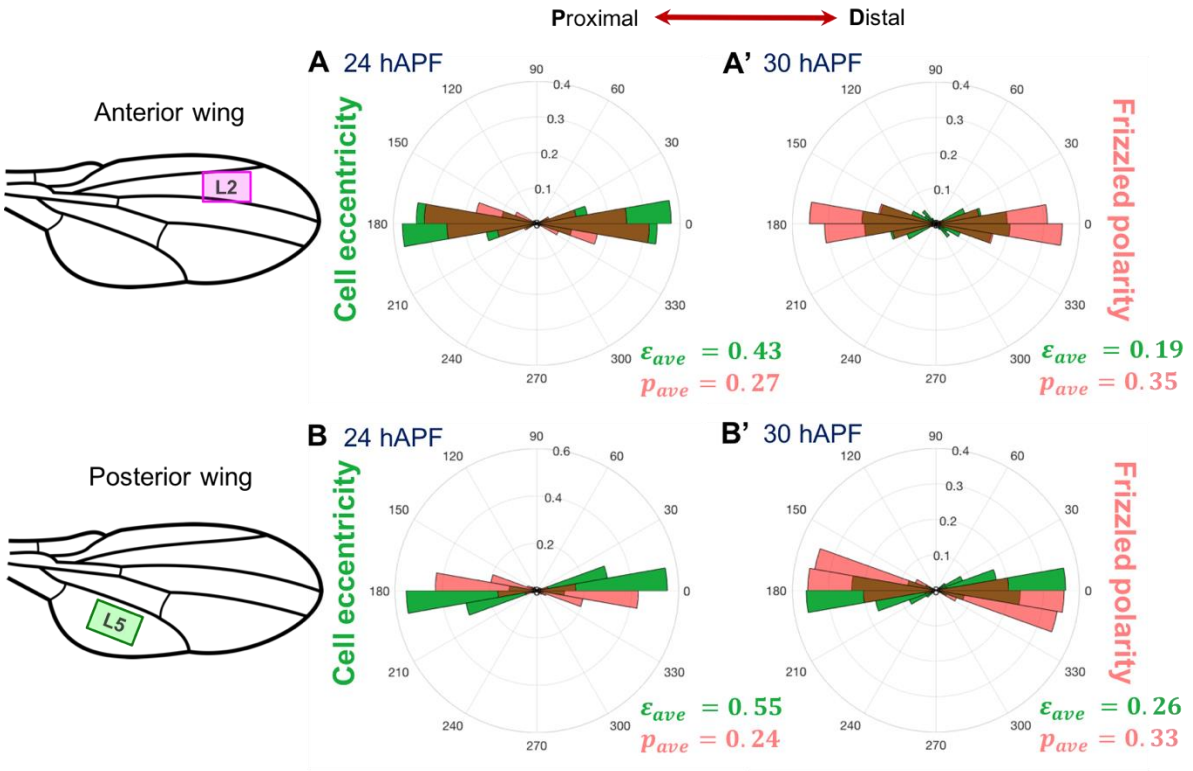

Figure 3.16: Correlation between Fz::EGFP polarity orientation and axis of cell eccentricity

(A – A') Circular weighted histogram plots display the orientation of Fz::EGFP polarity and cell eccentricity obtained from anterior wing at 24 hAPF (A) and 30 hAPF (A') respectively. (B – B') Circular weighted histogram plots display the orientation of Fz::EGFP polarity and cell eccentricity obtained from posterior wing at 24 hAPF (B) and 30 hAPF (B') respectively. ε_{ave}, the total average of averaged cell eccentricity magnitudes for all wings; p_{ave}, the total average of direct average polarity magnitudes for all wing. The number of wings for each developmental stage is between 7 to 9.

3.3.3.2 Fz::EGFP polarity magnitude correlates with cell shapes and tissue organisation in different regions of wild-type pupal wings

Next, I computed the direct average Fz::EGFP polarity magnitude and average cell eccentricity for both posterior and anterior wing. I found that average cell elongation and polarity magnitude for both regions of the wing are negatively correlated (with coefficient of determination, $r^2 = 0.9482$), in that less elongated cells exhibit higher polarity magnitude and vice versa (Figure 3.17A). On the other hand, average cell regularity and polarity magnitude are positively correlated (with coefficient of determination, $r^2 = 0.9268$), with more regular cells having higher polarity magnitude and vice versa (Figure 3.17B). In addition to that, epithelial disorganisation and polarity magnitude are negatively correlated (with coefficient of determination, $r^2 = 0.8999$), with more organised tissue having higher polarity magnitude (Figure 3.17C). I noted that the temporal progression of Fz::EGFP polarity magnitude correlates with patterned changes in cell shapes and tissue organisation over these developmental times, suggesting possible cross regulation. Interestingly, by comparing between anterior and posterior wing, I observed that the anterior wing with more regular, isotropic and organised tissue also exhibits higher polarity magnitude as compared to posterior wing for all developmental time points (Figure 3.17C).

Previous work reported that apical cell area plays a role in affecting core planar polarity system, where Fz fails to restrict prehair initiation to the distal cell junctions in substantially larger cells [Adler et al., 2000b]. Therefore, it would be interesting to find out if cell size per se can affect the ability of core proteins to polarise efficiently. Contrary to this, I found that there is a lack of correlation between apical cell area and polarity magnitude for all developmental times in wild-type pupal wings (with coefficient of determination, $r^2 = 0.2795$) (Figure 3.17D).

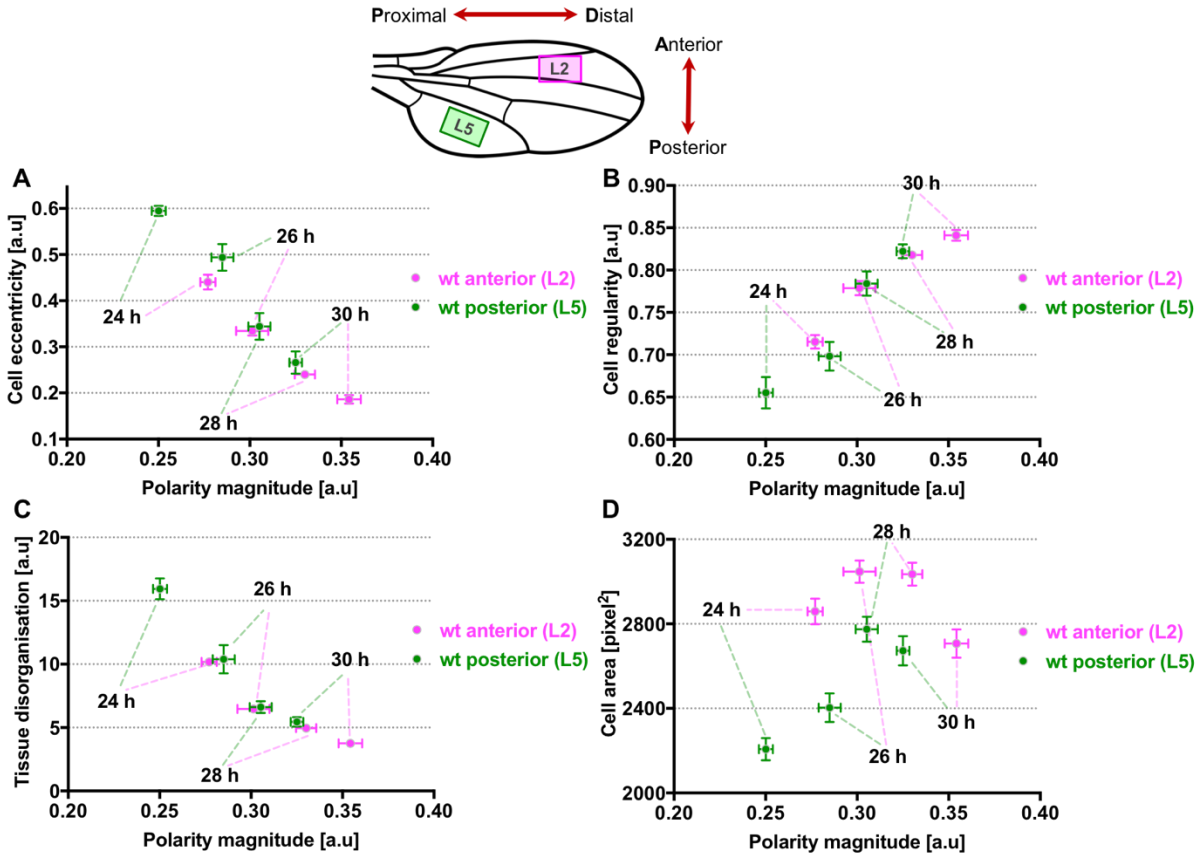

Figure 3.17: Temporal correlation between cell morphology and tissue organisation with Fz::EGFP polarity in different regions of the wing

(A) Negative correlation between average cell eccentricity and Fz::EGFP polarity magnitude.

(B) Positive correlation between average cell regularity and Fz::EGFP polarity magnitude.

(C) Negative correlation between tissue disorganisation and Fz::EGFP polarity magnitude.

(D) Lack of correlation between apical cell area and Fz::EGFP polarity magnitude.

wt represents wild-type. Each dot represents the total average of averaged values from all wings for specific developmental stage. The number of wings for each developmental stage is between 7 to 9. Error bar indicates mean±SEM.

3.4 Discussion

Previous published work has established that during the developmental period prior to emergence of polarised wing hairs, core planar proteins become increasingly polarised from initially disordered distributions. At the same time, epithelial cells relax into more isotropic shape with increasing fraction of hexagonal cells from initially elongated cells [Classen et al., 2005; Aigouy et al., 2010].

In my thesis, I first confirmed that the dynamic of PD orientation of core planar polarity system during phase II (from 24 to 30 hAPF) is consistent with [Aigouy et al., 2010]. As disorganised epithelial cells relax into a more orderly state, the core polarity protein Fz becomes increasingly polarised along the PD axis. Interestingly, the direction of Fz polarity is tightly correlated to the axis of cell elongation. Previous work showed that wing-hinge contraction leads to cell elongation along the PD axis [Aigouy et al., 2010; Etournay et al., 2015]. Interestingly, microtubules seem to preferentially align along the axis of cell elongation [Shimada et al., 2006; Harumoto et al., 2010]. They demonstrated that indeed polarised alignment of microtubules provides a directional bias for the delivery of Fz to the junctions lying orthogonal to the axis of cell elongation [Shimada et al., 2006; Harumoto et al., 2010]. In support of this, previous studies in cultured ciliated cells highlight the importance of polarised microtubules in directional biasing of core planar polarity components to the junctions lying orthogonal to the axis of cell elongation [Vladar et al., 2012; Chien et al., 2015]. On the contrary, work on murine skin reported that epidermal polarity protein polarises perpendicular to the axis of elongation despite microtubules aligned parallel to the axis of elongation [Aw et al., 2016]. Therefore, the role of microtubules in directional trafficking of core polarity proteins to opposite cell junctions remains inconclusive. This suggests that there might be alternative mechanisms of how cell shape affects the polarisation of core proteins.

In addition, my extensive quantification on cell morphological and core planar polarisation reveals differences in temporal evolution of core planar polarisation and cell morphology in different regions of the pupal wing. At approximately 24 to 28 hAPF, cell shape and tissue organisation are evidently different across the wing

blade, where cells in anterior wing appears to be more isotropic, regular and well-organised as compared to posterior wing. The question here would be: Why do cell shapes, size and tissue organisation vary in different regions of the wing blade? The variability I observed is likely to be due to differences in tissue stresses in different regions of the wing. [Etournay et al., 2015] reported that as the wing blade epithelium is under tension, there are differences in tension or stress pattern across the wing blade, where the posterior wing is subjected to higher anisotropic tension as compared to the anterior wing. Therefore, it is likely that higher anisotropic tension in the posterior wing results in more elongated and irregular cell shape, leading to increased disorganisation as compared to anterior wing.

Interestingly, my results also suggest that Fz polarity patterns in the posterior region of the wings are less coordinated as compared to the anterior wing. One plausible explanation would be that irregular epithelial packing poses a challenge for feedback propagation of polarisation signal across the epithelium. It has been proposed in [Ma et al., 2008] that irregular cell geometry causes disruption to polarity alignment. Apart from that, there is no correlation between cell apical area and polarity magnitude during 24 to 30 hAPF of pupal wing development. This is likely due to the fact that these apical cell size in wild-type wing fall within the “normal” range, thus failing to affect the core polarity system. Therefore, it would be interesting to produce substantially smaller or larger wing cells in an alternative way to test the influence of cell size on core polarisation. On the contrary, I found that there is a striking correlation between cell elongation, regularity and tissue organisation, and core planar polarity magnitude over the same developmental times in wild-type pupal wing. More importantly, these correlations still hold true in different regions of wings. Anterior wing cells that are more isotropic, regular and well-organised displayed higher Fz polarity as compared to the posterior wing cells for all developmental times.

However, correlation does not necessarily imply causation. Therefore, to demonstrate the causality effect, in subsequent chapter I will manipulate cell geometry or tissue organisation using genetic and laser ablation and quantify for planar polarisation. Addressing this question will help to understand how the planar

polarisation machinery is affected by different cell shapes, and packing or organisation, as a route to understanding molecular mechanisms of tissue planar polarisation.

CHAPTER 4

Effects of epithelial cell packing on planar polarisation

4.1 Introduction

One of the aims of this project is to understand the mechanism by which epithelial tissues develop specific packing geometries and coordinate their core planar polarity. During pupal wing morphogenesis, as the epithelial wing tissue relaxes towards a more regular packing, core polarity proteins become increasingly polarised along the proximal-distal (PD) axis. Core planar polarity proteins are junctional molecules that asymmetrically localise to the PD junctions of each cell and serve as a blueprint for distal wing hair formation.

In the previous chapter, I observed a striking temporal correlation between cell elongation, regularity and tissue organisation with core planar polarisation during pupal wing development. Interestingly, wing region that is more regular and well-organised also exhibits higher polarity magnitude and vice versa. While it is clear that correlation is not causation, these results lead to the two predictions: (1) cell shape or tissue organisation can influence core planar polarisation and/or (2) the core planar polarity pathway can promote better cell shape or tissue organisation. Alternatively, both events can be independent of each other as they just happened to occur at the same time.

Several published studies support the former prediction. Previous work showed that contraction of the wing-hinge along the PD axis results in cell elongating along the same axis [Aigouy et al., 2010; Etournay et al., 2015]. Interestingly, microtubules seem to preferentially align along the axis of cell elongation [Shimada et al., 2006; Harumoto et al., 2010; Gomez et al., 2016]. In *Drosophila*, it was demonstrated that polarised alignment of microtubules provides a directional bias for the delivery of Fz to the junctions lying orthogonal to the axis of cell elongation [Shimada et al., 2006; Harumoto et al., 2010]. This is consistent with the idea that anisotropic tension resulting from hinge-contraction guides planar polarisation reorientation across the wing epithelium [Aigouy et al., 2010]. In line with this, in ciliated epithelium of *Xenopus* larval skin, tissue strain generated by the gastrulating mesoderm results in polarised microtubules alignment along the axis of cell elongation [Chien et al., 2015]. Consistently, this results in higher fraction of stable core planar polarity

components on the junctions orthogonal to the axis of cell elongation [Chien et al., 2015]. In contrast to this, work on murine skin reported that epidermal polarity polarises perpendicular to the axis of cell elongation, despite microtubules aligning parallel to the axis of elongation [Aw et al., 2016]. Hence, it would be interesting to ask how different degree of cell elongation and orientation can affect core planar polarisation. Besides that, [Adler et al., 2000b] demonstrated that core polarity protein fails to restrict prehair initiation to the distal cell junctions in substantially larger cells. Therefore, it would be interesting to examine if cell size per se can affect the ability of core proteins to polarise efficiently. Overall, these findings motivated me to investigate the causality effect of cell shape and size on core planar polarisation machinery, in order to gain an in-depth understanding on the molecular mechanisms of tissue planar polarisation.

As epithelial cells become more regular, less eccentric and more organised over time, global polarity alignment becomes more coordinated and concentrated along the wing PD axis. The relaxation towards more regular and organised hexagonal packing is predominantly achieved via cell junctional rearrangement [Classen et al., 2005]. Indeed, pioneering work of [Aigouy et al., 2010] has suggested that cell elongation and directional cell rearrangement are plausible cues to guide global polarity alignment along PD axis in pupal wing. Noteworthy, in both *dachsous* mutants and severed wings, failure of cells to elongate along the wing PD axis and defective pattern of junctional rearrangement result in loss of global polarity coordination [Aigouy et al., 2010]. Later, [Bardet et al., 2013] demonstrated that defective cell junctional rearrangement in *pten* mutant wings results in the loss of global polarity axis coordination across the wing tissue. Here, I would like to investigate the causality effects of altered cell shape, elongation, cell rearrangement and tissue organisation on global polarity alignment across the wing tissue. Intuitively, one might predict that more regularly packed cells and organised tissue would allow better polarity propagation across tissue, thus leading to better polarity axis coordination between neighbouring cells.

In addition, it has been highlighted that loss of core polarity proteins results in hexagonal packing defects in pupal wings at 30 hAPF (hour After Puparium

Formation), suggesting that the core polarity pathway is required to promote hexagonal packing during pupal wing morphogenesis [Classen et al., 2005]. Recent work reported that knocking down expression of a key core planar polarity protein (Flamingo) did not results in hexagonal packing defects up until 27.5 hAPF [Sugimura and Ishihara, 2013]. Although, from 30 to 32 hAPF, there is a mild reduction in the fraction of hexagonal cells in *flamingo* RNAi wings as compared to wild-type wings [Sugimura and Ishihara, 2013]. Our lab further showed that core polarity protein (Frizzled) plays a role in regulating E-Cadherin endocytosis, which might mediate junctional rearrangement into hexagonal packing during pupal wing morphogenesis [Warrington et al., 2013]. Likewise, core planar polarity signalling is required to regulate cell junctional rearrangement during vertebrate gastrulation [Heisenberg et al., 2000; Wallingford et al., 2000; Jessen et al., 2002]. However, it was reported that core polarity mutant does not affect the process of cell junctional rearrangement in murine epidermal skin [Aw et al., 2016]. Hence, the role of the core planar polarity pathway in regulating cell junctional rearrangement and promoting hexagonal packing remains inconclusive.

4.2 Aims

First, I aim to demonstrate causality by showing that manipulating cell packing influences the strength of core protein polarisation in the pupal wing epithelium. In Section 4.3.1, I present several genetic manipulations and laser ablation assays to alter epithelial cell packing and quantify for planar polarisation over time. If my prediction is correct, wing cells with irregular shape and disorganised tissue would result in weaker polarity and vice versa. Addressing this question establishes the contribution of cell shape or packing to the underlying core planar polarisation mechanisms.

Second, I wish to investigate the function of the core planar polarisation pathway in regulating cell packing. In Section 4.3.2, I compare the cell shape regularity, eccentricity, number of cell sides, junctional rearrangement and epithelial organisation in wild-type and core planar polarity mutant wings. If the core planar polarity pathway is important in promoting hexagonal cell packing and cell junctional rearrangement, then I should be able to see that PD-oriented hexagonal cell packing will be impaired in the absence of core planar polarity function. Addressing these controversies allows me to establish the importance of core planar polarity pathway in regulating epithelial cell packing and tissue architecture.

Introductions to the “Effects of altered cell packing on core planar polarisation” and the “Effects of core planar polarisation on cell packing” are provided at the beginning of the relevant sections, Section 4.3.1 and 4.3.2 respectively.

4.3 Results

4.3.1 Effects of altered cell packing on core planar polarisation

A correlation between cell packing and polarity in wild-type wings does not necessarily imply a causal relationship. Hence, I wish to investigate whether altered epithelial cell packing can cause planar polarity disruption. To achieve this, I sought ways to manipulate cell shape in the *Drosophila* pupal wing genetically and optically.

First, I altered cell packing in pupal wing cells by knocking down PTEN protein (Phosphatase and tensin homolog on chromosome 10), which leads to unusual cell geometries [Ma et al., 2008; Bardet et al., 2013]. PTEN is a lipid phosphatase that dephosphorylates phosphatidylinositol(3,4,5)-triphosphate to produce PIP2. This gene was identified as a tumour suppressor that is mutated in several cancers at high frequency [Chalhoub and Baker, 2009]. [Bardet et al., 2013] showed that during junctional rearrangement, PTEN regulates Myosin II depletion on newly formed junctions necessary for their lengthening. Therefore, loss of PTEN function results in abnormal cell shape due to defective cell rearrangement (due to failure in junctional lengthening), in which cells exhibit non-hexagonal packing with a higher percentage of quadrilateral and pentagonal cells [Bardet et al., 2013]. Therefore, I wish to examine how well can cells planar polarise, given this non-hexagonal packing. In this experiment, I used the GAL4 system to drive UAS-*pten-rnai* in the posterior compartment of wings expressing Frizzled::EGFP (Fz::EGFP) and imaged from 24 to 30 hAPF (Figure 4.1A). As the control for this, I imaged the posterior region of wild-type pupal wings expressing Fz::EGFP at the same developmental times. In these experiments, junctional Fz::EGFP is used as a cell boundary segmentation marker for further image analysis.

Although there is no evidence that PTEN signalling acts directly to regulate Fz-dependent polarity pathway, I proposed an independent method to disrupt wing cell packing by knocking down Rap1, which results in heterogeneous distribution of E-Cadherin at the apicolateral cell-cell junctions. Rap1 is a small guanosine triphosphatase (GTPase) of the Ras family, which plays a crucial role in regulating

apicolateral cell-cell adhesion by maintaining evenly distributed adherens junctions around the apical circumference of each cell [Knox and Brown, 2002]. Loss of Rap1 results in aberrant cell shape as compared to wild-type cells [Knox and Brown, 2002]. I utilised the GAL4 system to drive UAS-*rap1-rnai* in the posterior compartment of wings expressing Fz::EGFP (Figure 4.3A). The posterior region of wild-type wings expressing Fz::EGFP is used as the control. Similar to the PTEN experiment, I used Fz::EGFP as a marker for cell boundary segmentation. However, cells lacking Rap1 present a challenge for image segmentation because junctional Fz::EGFP intensity is significantly lower and heterogeneously distributed in these cells. Due to this limitation, I imaged at only two developmental time points, 24 and 30 hAPF.

Studies have reported the instructive role of anisotropic mechanical tension in promoting hexagonal cell packing from 24 to 27 hAPF [Sugimura and Ishihara, 2013]. Therefore, another alternative strategy to disrupt cell packing is by withdrawing the anisotropic tension from the system. Dumpy is a large extracellular matrix protein that connects the wing to the overlying cuticle at specific locations. Removing Dumpy activity diminishes anisotropic mechanical tension in the wing [Etournay et al., 2015; Ray et al., 2015]. As the function of the Dumpy protein is well-characterised [Ray et al., 2015; Etournay et al., 2015], therefore, there are fewer concerns about unexpected cellular functions of Dumpy on the Fz-dependent polarity pathway. In this experiment, I imaged the posterior region of *dumpy*^{ov1} wings expressing Fz::EGFP, from 24 to 30 hAPF (Figure 4.5A). The posterior region of wild-type wings expressing Fz::EGFP is used as the control at the same developmental times. Likewise, junctional Fz::EGFP is used as a marker for cell boundary segmentation.

4.3.1.1 Better organised pten-rnai tissue results in stronger polarity with loss of global polarity coordination

Knocking down PTEN in the posterior compartment of the wing, I observed that, as previously published in [Ma et al., 2008; Bardet et al., 2013], *pten-rnai* tissue display strikingly unusual cobblestone and rosette packing as compared to regular

hexagonal packing, with a higher fraction of quadrilateral or square and pentagonal cells and a lower fraction of hexagonal cells (Figure 4.1B-D). Interestingly, the percentage of polygonal cells does not change dramatically over these developmental times. This could be due to the fact that loss of PTEN results in defective cell rearrangement, in which junctional lengthening and stability are perturbed [Bardet et al., 2013]. Similar to wild-type tissue, *pten-rnai* tissue undergoes relaxation into a more organised packing with higher regularity and lower eccentricity in cell shape from 24 to 30 hAPF. Despite having fewer hexagonal cells, *pten-rnai* tissue appears to be more organised and regular than that of wild-type tissue at 24 and 26 hAPF (Figure 4.1E-F). From 28 to 30 hAPF, the level of tissue organisation and cell regularity are not significantly different between *pten-rnai* and wild-type tissue despite having 25% reduction in fraction of hexagonal cells as compared to wild-type tissue (Figure 4.1E-F).

Moreover, *pten-rnai* cells appear to be less eccentric as compared wild-type cells from 24 to 28 hAPF (Figure 4.1G). This could explain why *pten-rnai* tissue is more organised as compared to wild-type at earlier time points because more regular and less elongated *pten-rnai* cells can pack more efficiently (Figure 4.1E-G). Both *pten-rnai* and wild-type cells are not significantly different in terms of apical cell area for most of the developmental times, consistent with [Bardet et al., 2013] (Figure 4.1H).

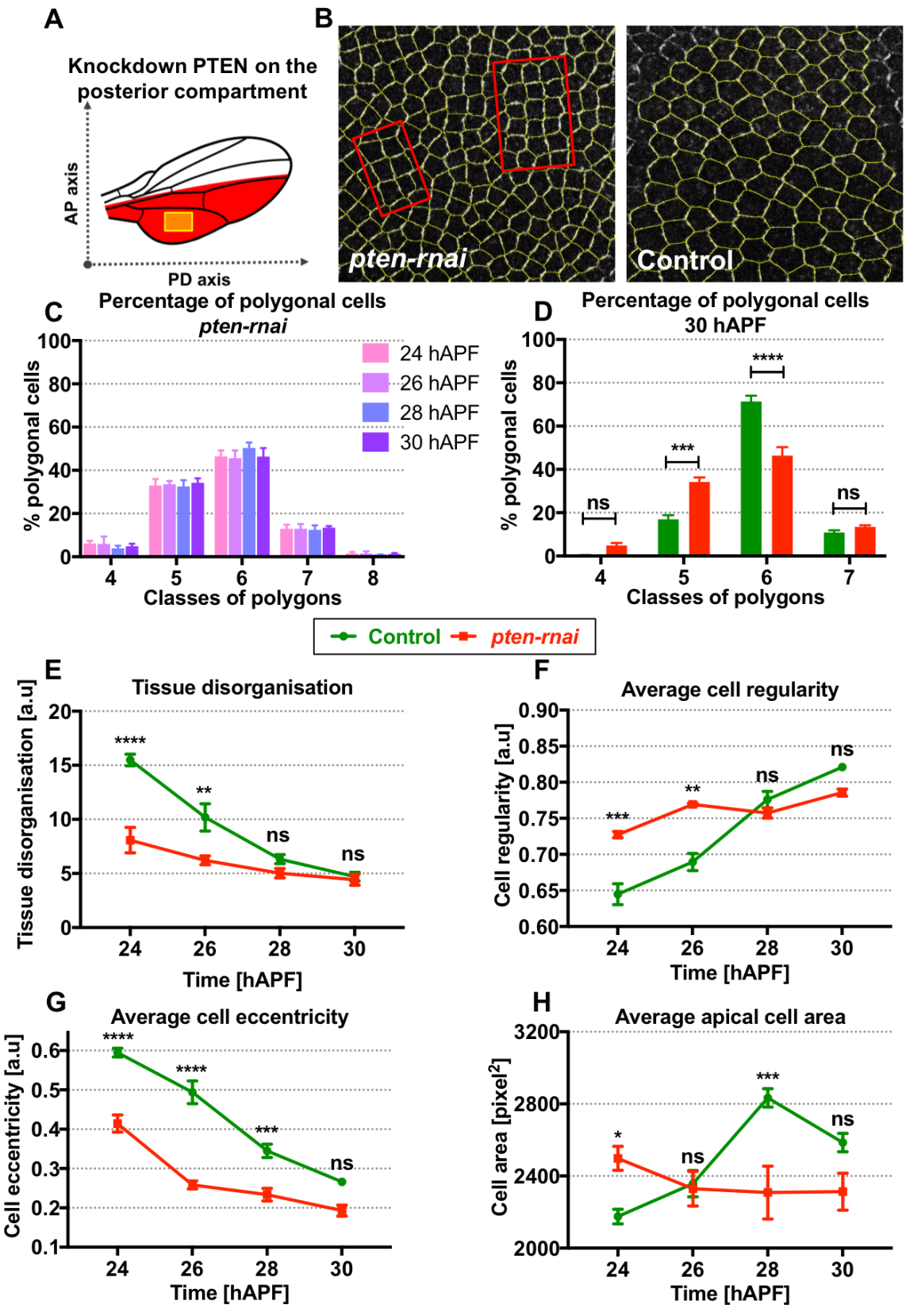
A
Knockdown PTEN on the posterior compartment
AP axis
PD axis
B
pten-rnai
Control
C
Percentage of polygonal cells
pten-rnai
24 hAPF
26 hAPF
28 hAPF
30 hAPF
% polygonal cells
Classes of polygons
D
Percentage of polygonal cells
30 hAPF
% polygonal cells
Classes of polygons
Control
pten-rnai
E
Tissue disorganisation
Tissue disorganisation [a.u]
Time [hAPF]
F
Average cell regularity
Cell regularity [a.u]
Time [hAPF]
G
Average cell eccentricity
Cell eccentricity [a.u]
Time [hAPF]
H
Average apical cell area
Cell area [pixel²]
Time [hAPF]

Figure 4.1: Knockdown of PTEN leads to distinct cobblestone pattern of cell packing

(A) *pten-rnai* expressed in the posterior compartment (marked in red) of the pupal wing using the *engrailed-GAL4* driver. Temperature raised to 25°C throughout development to activate GAL4/UAS expression.
(B) Confocal images of *pten-rnai* (Left) and wild-type control (Right) of the same region of wings expressing Fz::EGFP at 30 hAPF. Cell boundaries are depicted by yellow lines. *pten-rnai* cells display cobblestone pattern of cell packing (red frames).
(C) The percentage of *pten-rnai* cells with four, five, six, seven and eight sides from 24 to 30 hAPF. The percentage of polygonal cells does not change over the developmental times.
(D) Quantified percentage of hexagonal cells of *pten-rnai* and wild-type control wings at 30 hAPF.
(E) Quantified epithelial tissue organisation of *pten-rnai* and wild-type control wings.
(F) Quantified average cell regularity of *pten-rnai* and wild-type control wings.
(G) Quantified average cell eccentricity of *pten-rnai* and wild-type control wings.
(H) Quantified average apical cell area of *pten-rnai* and wild-type control wings.
The number of wings for each developmental stage is 6 to 9. Error bar indicates mean±SEM. One-way ANOVA test, unpaired. Significance levels: p-value $\leq 0.0001^{****}$, p-value $\leq 0.0002^{***}$, p-value $\leq 0.001^{**}$, p-value $\leq 0.01^{*}$. ns is not significantly different.

To examine whether polarity alignment correlates with the axis of cell elongation along the wing PD axis, I plotted Fz::EGFP polarity axis against *pten-rnai* cell orientation. I found that Fz::EGFP polarity axis is consistently oriented parallel to the axis of cell eccentricity from 24 to 28 hAPF of pupal wing morphogenesis (Figure 4.2A'-A''). However, by 30 hAPF, as cells relax into a more isotropic shape with varying orientation, Fz::EGFP polarity axis is no longer oriented parallel to the axis of cell elongation (Figure 4.2A'). Therefore, these data demonstrate that there is a correlation between the orientation of epithelial cells and Fz::EGFP polarity axis in *pten-rnai* wings at early but not later developmental times.

As *pten-rnai* tissue appears to be more organised and well-packed than wild-type tissue from 24-26 hAPF, I then asked would more organised *pten-rnai* tissue leads to higher average polarity magnitude, following the correlation discovered in Chapter 3.

Therefore, I compared Fz::EGFP polarity magnitude in both *pten-rnai* and control wings using “direct” average polarity magnitude measure, which quantifies the asymmetrical distribution of Fz::EGFP for each cell and averages it over the entire region (see details in Chapter 2). Previously, [Bardet et al., 2013] reported that strength of polarisation is not significantly different between *pten* and wild-type wings at 30 hAPF. However, it was not known whether strength of polarisation in *pten-rnai* tissue differs from wild-type tissue earlier in pupal development. Interestingly, more organised *pten-rnai* tissue results in significantly higher polarity magnitude as compared to wild-type tissue from 24 to 28 hAPF (Figure 4.2D). As wild-type tissue achieves a comparable organisation with *pten-rnai* tissue by 30 hAPF, average polarity magnitude is not significantly different between them, in agreement with published results (Figure 4.2B) [Bardet et al., 2013]. Despite having higher polarity magnitude, *pten-rnai* cells display higher polarity angle variance than wild-type cells, suggesting poor global polarity coordination in *pten-rnai* tissue (Figure 4.2C). This result is consistent with previous studies reported that *pten* wings exhibit loss of global polarity coordination in pupal wing [Bardet et al., 2013].

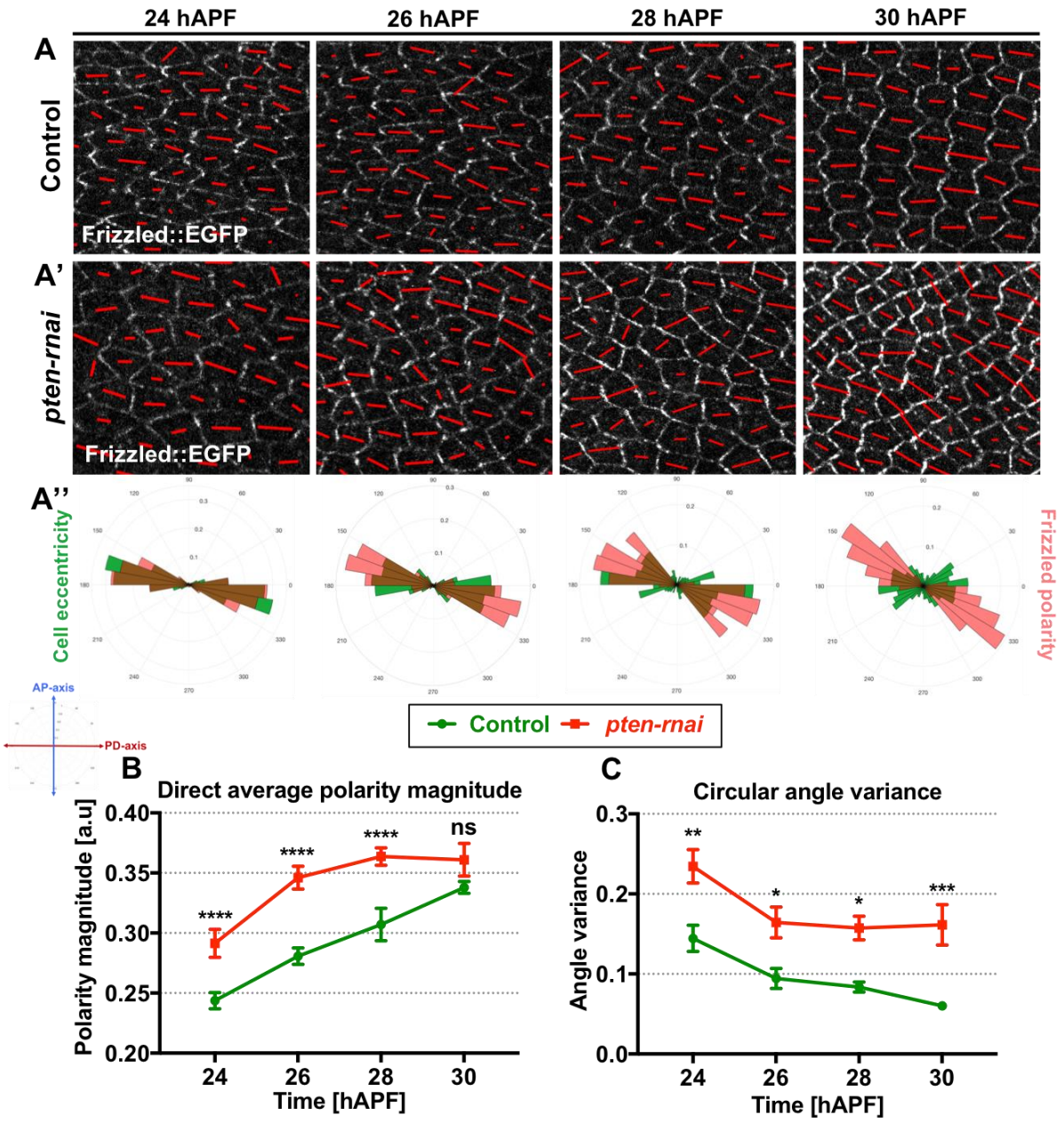

Figure 4.2: Knockdown of PTEN results in more organised tissue with higher polarity magnitude and poorer polarity coordination than control wild-type

(A) Time-lapse confocal images of a wild-type control wing expressing Fz::EGFP from 24 to 30 hAPF. The length and orientation of red lines within individual cells represent the magnitude and the axis of Fz::EGFP polarity respectively.

(A') Time-lapse confocal images of a *pten-rnai* wing expressing Fz::EGFP from 24 to 30 hAPF.

(A'') Circular weighted histogram plots display the orientation of Fz::EGFP polarity and cell eccentricity obtained from *pten-rnai* wings from 24 to 30 hAPF. AP axis correspond to y-axis while PD axis correspond to x-axis of the histogram plots.

(B) Quantified direct average polarity magnitude of *pten-rnai* and wild-type control wings.

(C) Quantified polarity angle variance of *pten-rnai* and wild-type control wings.
The number of wings for each developmental stage is 6 to 9. Error bar indicates mean±SEM. One-way ANOVA test, unpaired. Significance levels: p-value $\leq 0.0001^{****}$, p-value $\leq 0.0002^{***}$, p-value $\leq 0.001^{**}$, p-value $\leq 0.01^{*}$. ns is not significantly different.

4.3.1.2 Poorly organised rap1-rnai tissue results in weaker polarity with loss of global polarity coordination

By knocking down Rap1 in the posterior compartment of the wing, I observed that, as previously reported in [Knox and Brown, 2002], *rap1-rnai* cells display abnormal shapes with approximately 30% of pentagonal cells and 40% of hexagonal cells from 24 to 30 hAPF (Figure 4.3B-C). At 30 hAPF, there is a 35% reduction in the fraction of hexagonal cells in *rap1-rnai* tissue as compared to wild-type tissue, implying that relaxation of *rap1-rnai* tissue into regular hexagonal packing is severely impaired prior to wing hair formation (Figure 4.3D). At 24 hAPF, *rap1-rnai* and wild-type tissue exhibit similar level of tissue organisation and cell shape regularity (Figure 4.3E-F). However, by 30 hAPF, *rap1-rnai* tissue appears to be highly disorganised as compared to wild-type tissue, likely due to more elongated and irregular cells, reduced fraction of hexagonal cells and reduced uniformity in apical cell area in *rap1-rnai* tissue (Figure 4.3D-H). Interestingly, the percentage of polygonal cells, tissue organisation, eccentricity, regularity and apical area of *rap1-rnai* cells do not change significantly over the same time course (Figure 4.3E-G).

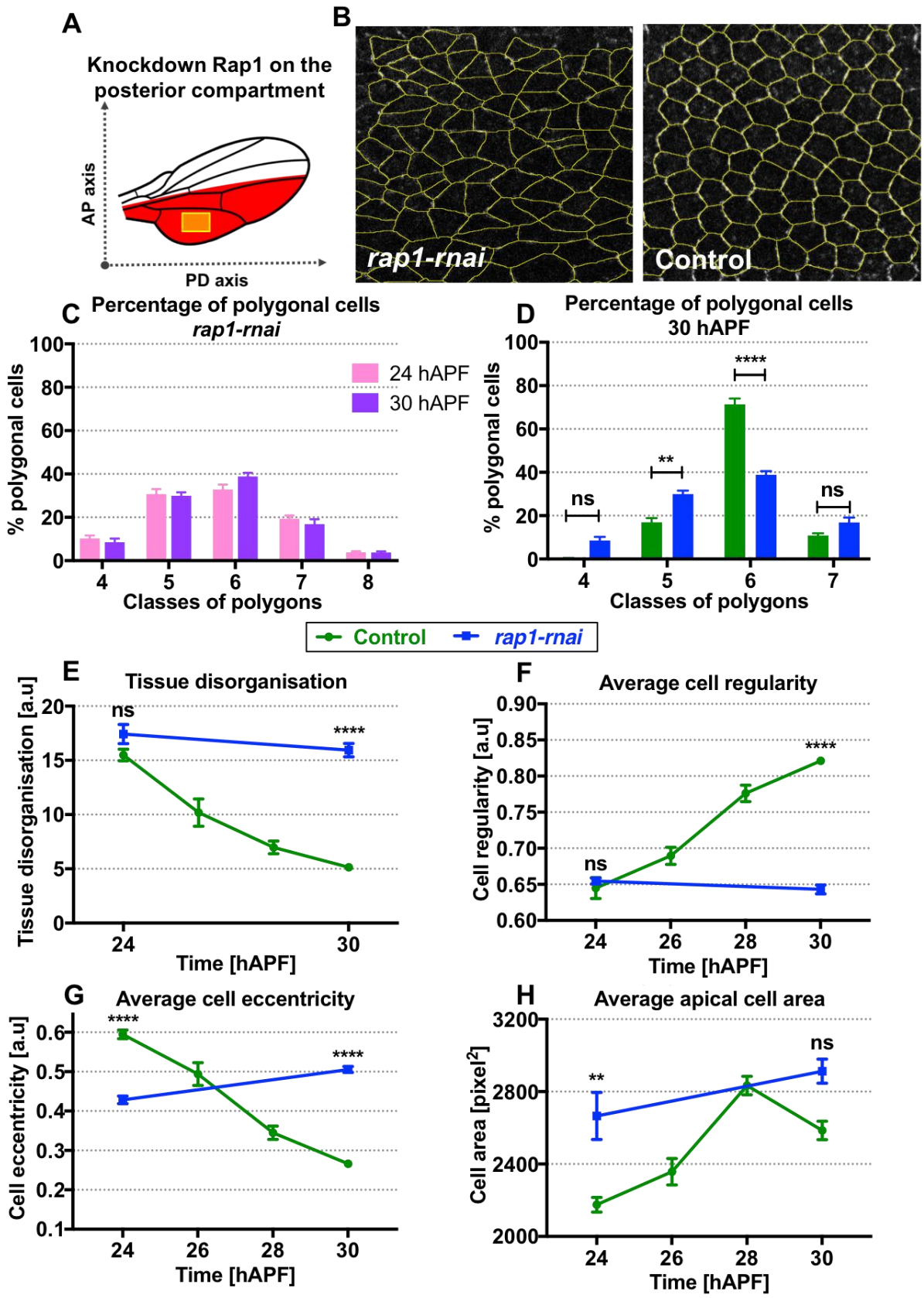

Figure 4.3: Knockdown of Rap1 GTPase leads to aberrant and irregular cell shapes

(A) *rap1-rnai* was expressed in the posterior compartment of the pupal wing (marked in red) using the *engrailed-GAL4* driver.
(B) Confocal images of *rap1-rnai* (Left) and wild-type control (Right) of the same region of wings expressing Fz::EGFP at 30 hAPF. Cell boundaries are depicted by yellow lines.
(C) The percentage of *rap1-rnai* cells with four, five, six, seven and eight sides for 24 and 30 hAPF.
(D) Quantified percentage of hexagonal cells of *rap1-rnai* and wild-type control wings at 30 hAPF.
(E) Quantified epithelial tissue organisation of *rap1-rnai* and wild-type control wings.
(F) Quantified average cell regularity of *rap1-rnai* and wild-type control wings.
(G) Quantified average cell eccentricity of *rap1-rnai* and wild-type control wings.
(H) Quantified average apical cell area of *rap1-rnai* and wild-type control wings.
The number of wings for each developmental stage is 7 to 9. Error bar indicates mean±SEM. One-way ANOVA test, unpaired. Significance levels: p-value $\leq 0.0001^{****}$, p-value $\leq 0.001^{**}$. ns is not significantly different.

To examine whether polarity alignment correlates with the axis of cell elongation, I plotted Fz::EGFP polarity axis against cell orientation obtained from *rap1-rnai* wings for both 24 and 30 hAPF. At 24 and 30 hAPF, the polarity axis is not aligned with the axis of cell elongation in *rap1-rnai* wings (Figure 4.4A'-A''). Therefore, these data demonstrate that there is no correlation between orientation of epithelial cells and Fz::EGFP polarity axis in *rap1-rnai* wings at both 24 and 30 hAPF.

To investigate the effect of epithelial organisation on core protein polarity, I then compared the strength of Fz::EGFP polarisation in both *rap1-rnai* and control wings. At 24 hAPF, polarity magnitude is not significantly different between *rap1-rnai* and wild-type cells. However, at 30 hAPF, less organised *rap1-rnai* cells exhibit, on average, significantly lower polarity magnitude than wild-type cells ($p_{average}$ for *rap1-rnai* and wild-type are 0.25 and 0.34 respectively) (Figure 4.4B). At 24 and 30 hAPF, *rap1-rnai* cells display higher polarity angle variance as compared to wild-type cells, indicating lack of global polarity coordination in *rap1-rnai* tissue (Figure 4.4C).

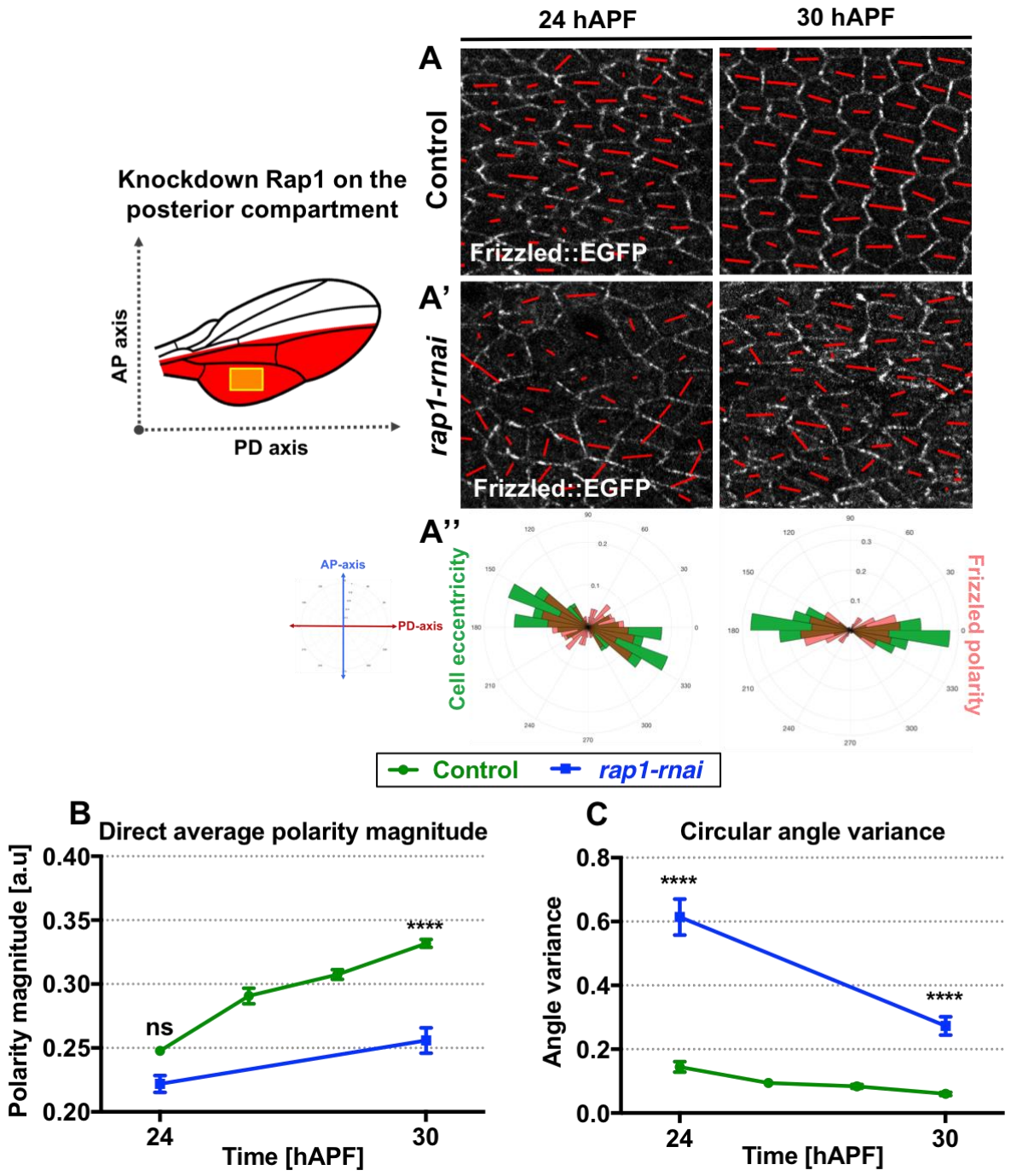

Figure 4.4: Knockdown of Rap1 GTPase results in less organised tissue with lower polarity magnitude and poorer polarity coordination than control wild-type

(A) Confocal images from a control wild-type wing expressing Fz::EGFP at 24 and 30 hAPF. The length and orientation of red lines within individual cells represent the magnitude and the axis of Fz::EGFP polarity respectively.

(A') Confocal images from a *rap1-rnai* wing expressing Fz::EGFP at 24 and 30 hAPF.

(A'') Circular weighted histogram plots display the orientation of Fz::EGFP polarity and cell eccentricity obtained from *rap1-rnai* wings at 24 and 30 hAPF.

(B) Quantified direct average polarity magnitude of *rap1-rnai* and wild-type control wings.
(C) Quantified polarity angle variance of *rap1-rnai* and wild-type control wings.
The number of wings for each developmental stage is 7 to 9. Error bar indicates mean±SEM. One-way ANOVA test, unpaired. Significance levels: p-value ≤ 0.0001^{****}. ns is not significantly different.

4.3.1.3 Better organised dumpy^{ov1} mutant tissue results in stronger polarity

Next, I examined the dynamic of cell packing and core planar polarisation in *dumpy^{ov1}* mutant wings (Figure 4.5A-B). From 24 to 30 hAPF, there is an increasing fraction of hexagonal cells in *dumpy^{ov1}* mutant wings from 45% to 70% (Figure 4.5B-C). Moreover, the distribution of polygonal cells at 30 hAPF are similar between both *dumpy^{ov1}* mutant and wild-type wings (Figure 4.5D). At 24 hAPF, *dumpy^{ov1}* mutant tissues appear to be more organised as compared to wild-type tissues (Figure 4.5E). However, from 26 to 30 hAPF, *dumpy^{ov1}* mutant wings are not significantly different from wild-type in terms of tissue organisation (Figure 4.5E).

Over the same time course, *dumpy^{ov1}* mutant cells become increasingly more regular and less eccentric (Figure 4.5F-G). In contrast to wild-type cells, *dumpy^{ov1}* mutant cells appear to be more regular and less eccentric at 24 hAPF (Figure 4.5F-G). However, from 26 to 30 hAPF, cell shape regularity and eccentricity of *dumpy^{ov1}* mutant are similar to wild-type cells (Figure 4.5F-G). Although the apical area of *dumpy^{ov1}* mutant cells is not significantly different from wild-type cells at early stages, however *dumpy^{ov1}* mutant cells are significantly smaller as compared to wild-type cells at late pupal stages (Figure 4.5H). This is consistent with published results which reported that removing Dumpy results in a shorter wing blade and reduced cell area due to a lack of wing margin connection that counteracts wing-hinge contraction [Etournay et al., 2015; Ray et al., 2015]. This assay enables us to investigate the effect of cell size reduction on core protein polarisation.

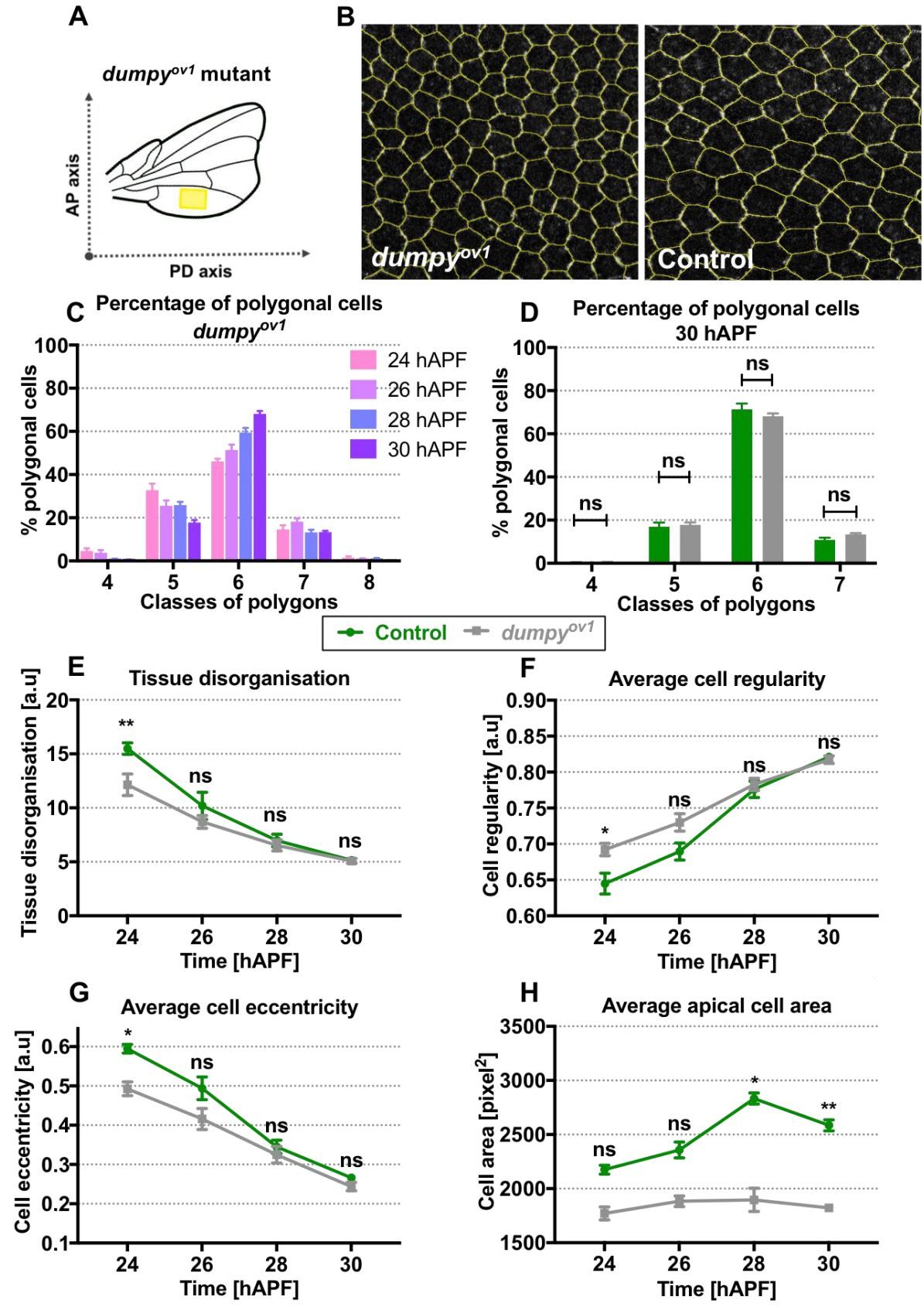

Figure 4.5: Mutation of Dumpy results in more regular and isotropic cell shapes at 24 hAPF

(A) Illustration of the analysed posterior region of *dumpy*^{ov1} mutant wings.
(B) Confocal images of *dumpy*^{ov1} (Left) and wild-type control (Right) of the same region of wings expressing Fz::EGFP at 30 hAPF. Cell boundaries are depicted by yellow lines
(C) The percentage of *dumpy*^{ov1} cells with four, five, six, seven and eight sides from 24 to 30 hAPF. The percentage of hexagonal cells improves over the developmental stages.
(D) Quantified percentage of hexagonal cells of *dumpy*^{ov1} and wild-type control wings at 30 hAPF.
(E) Quantified epithelial tissue organisation of *dumpy*^{ov1} and wild-type control wings.
(F) Quantified average cell regularity of *dumpy*^{ov1} and wild-type control wings.
(G) Quantified average cell eccentricity of *dumpy*^{ov1} and wild-type control wings.
(H) Quantified average apical cell area of *dumpy*^{ov1} and wild-type control wings.
The number of wings for each developmental stage is 9 to 10 wings. Error bar indicates mean$\pm$SEM. One-way ANOVA test, unpaired. Significance levels: p-value $\leq 0.001^{**}$, p-value $\leq 0.03^{*}$. ns is not significantly different.

To examine whether Fz::EGFP polarity alignment correlates with the axis of cell elongation, I plotted Fz::EGFP polarity against *dumpy*^{ov1} mutant cell orientation from 24 to 30 hAPF (Figure 4.6A''). I found that *dumpy*^{ov1} mutant cells align their polarity axis parallel to the axis of cell elongation over the developmental times from 24 to 30 hAPF, suggesting there is a correlation between epithelial cell orientation and Fz::EGFP polarity axis in *dumpy*^{ov1} mutant wings.

To investigate the effect of epithelial organisation on core planar polarity, I then compared the strength of Fz::EGFP polarisation in both *dumpy*^{ov1} and control wings (Figure 4.6A-A'). Fascinatingly, more organised *dumpy*^{ov1} mutant tissue exhibits higher polarity magnitude than wild-type wings at 24 hAPF (Figure 4.6B). However, average polarity magnitude is not significantly different between *dumpy*^{ov1} mutant and wild-type wings at later stages, despite *dumpy*^{ov1} cells being significantly smaller than wild-type at these stages (Figure 4.5H and 4.6B). These data suggest that cell size per se does not affect core protein polarisation. Besides that, polarity angle variance is not significantly different between *dumpy*^{ov1} mutant and wild-type cells, suggesting that global polarity coordination is not perturbed in *dumpy*^{ov1} mutant wings (Figure 4.6C).

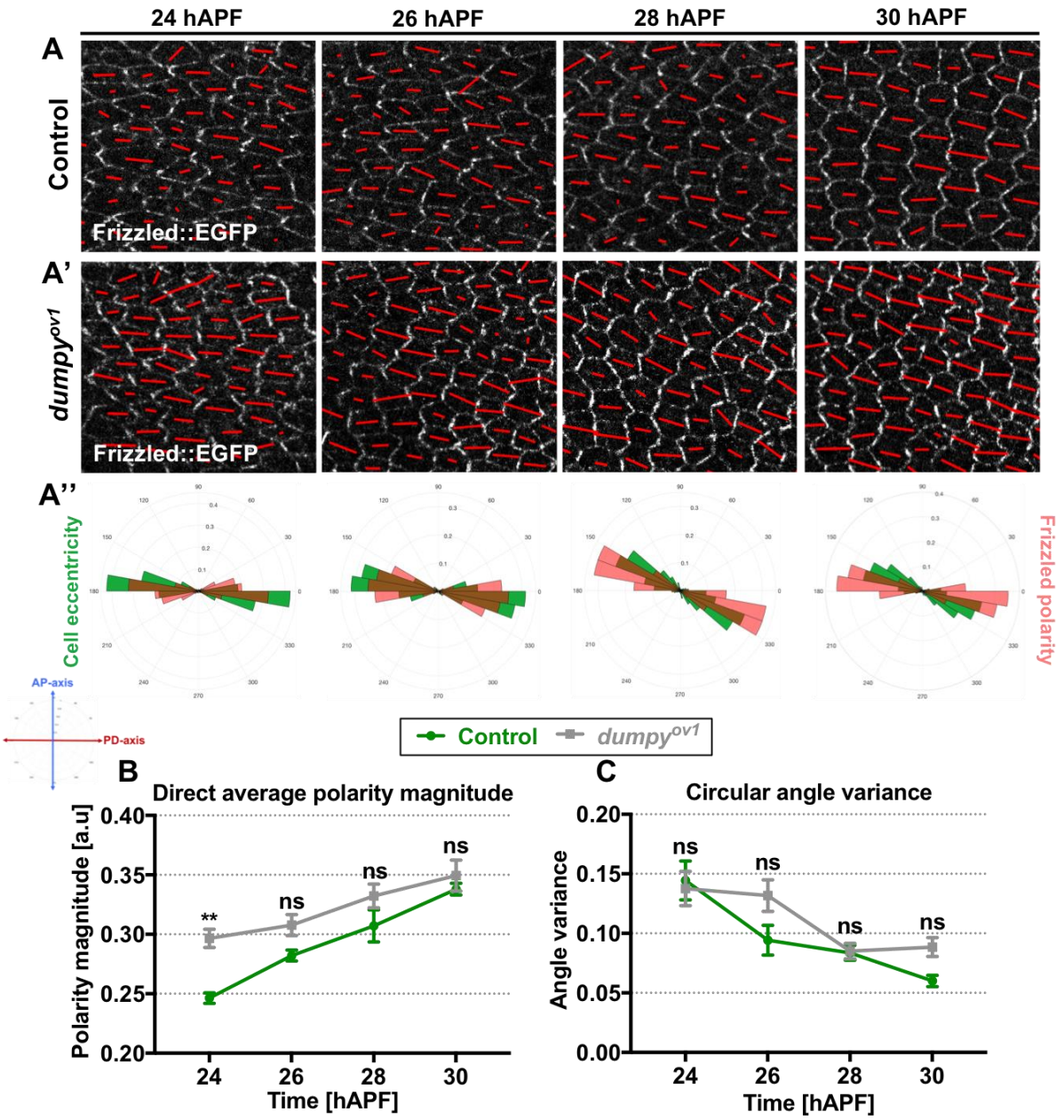

Figure 4.6: Loss of Dumpy results in more organised tissue with higher polarity magnitude than control wild-type

(A) Time-lapse confocal images from a control wild-type wing expressing Fz::EGFP from 24 to 30 hAPF. The length and orientation of red lines within individual cells represent the magnitude and the axis of Fz::EGFP polarity respectively.

(A') Time-lapse confocal images from *dumpy*^{ov1} wing expressing Fz::EGFP from 24 to 30 hAPF.

(A'') Circular weighted histogram plots display the orientation of Fz::EGFP polarity and cell eccentricity obtained from *dumpy*^{ov1} wings from 24 to 30 hAPF.

(B) Quantified direct average polarity magnitude of *dumpy*^{ov1} and wild-type control wings.

(C) Quantified polarity angle variance of *dumpy*^{ov1} and wild-type control wings.

The number of wings for each developmental stage is 9 to 10. Error bar indicates mean±SEM. One-way ANOVA test, unpaired. Significance levels: p-value $\leq 0.005^{**}$. ns is not significantly different.

As of now, I have demonstrated three different genetic manipulations on cell packing *in vivo*, which result in distinct cell shapes and tissue organisation as compared to control wild-type wings (Figure 4.7A). To examine how different cell shapes and tissue organisation correlate with the strength of core protein polarisation, I plotted average Fz::EGFP polarity magnitude against epithelial tissue organisation, cell eccentricity and regularity from 24 to 30 hAPF for all the genotypes. Interestingly, I noted that the temporal progression of Fz::EGFP polarity magnitude correlates with changes in cell shapes and tissue organisation over these developmental times irrespective of genetic manipulations. I found that epithelial tissue disorganisation and polarity magnitude are negatively correlated (with coefficient of determination, r^2 = 0.8885), in that more organised tissue exhibits higher polarity magnitude and vice versa (Figure 4.7B). Additionally, cell eccentricity and polarity magnitude are negatively correlated (with coefficient of determination, r^2 = 0.7679), with less elongated cells having higher polarity magnitude and vice versa (Figure 4.7C). On the other hand, cell shape regularity and polarity magnitude are positively correlated (with coefficient of determination, r^2 = 0.7156), in that more regular cells having higher polarity magnitude and vice versa (Figure 4.7D). Hence, these findings suggest that indeed there is a striking correlation between cell elongation, regularity and tissue organisation, and core planar polarisation, independent of different genetic perturbations on cell packing during 24 to 30 hAPF of pupal wing development.

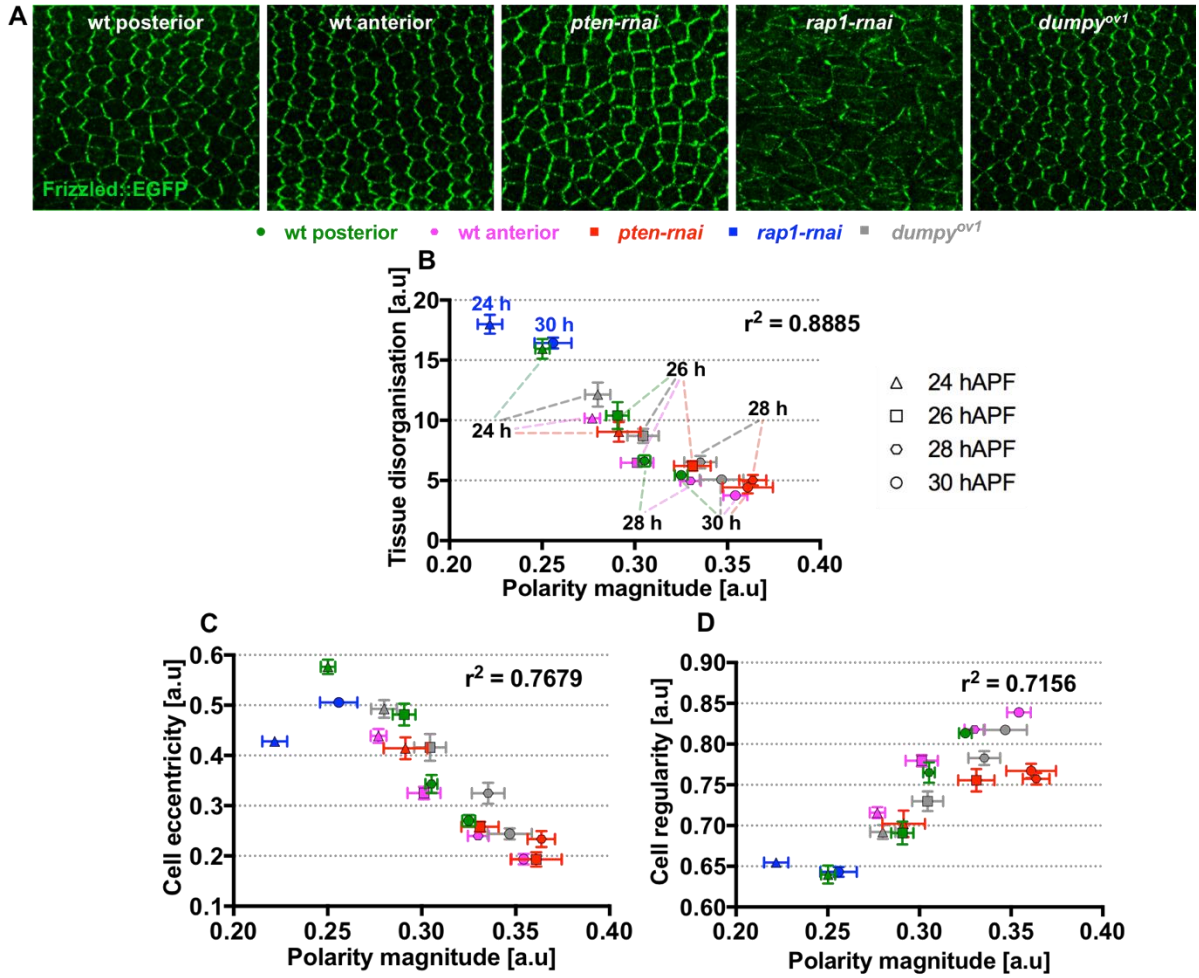

Figure 4.7: Altered epithelial organisation and cell shapes influence the ability of core proteins to polarise

(A) Confocal images of posterior and anterior wild-type control, *pten-rnai, rap1-rnai* and *dumpy*^{ov1} mutant tissues at 30 hAPF.

(B) Correlation between epithelial tissue disorganisation and Fz::EGFP polarity magnitude for all genotypes (in different colours) and developmental time points (in different shapes).

(C) Correlation between average cell eccentricity and Fz::EGFP polarity magnitude.

(D) Correlation between average cell regularity and Fz::EGFP polarity magnitude.

wt represents wild-type. The number of wings for each developmental stage is 6 to 10 wings. Error bar indicates mean±SEM.

4.3.1.4 Acute perturbation on cell shapes and epithelial organisation leads to weaker polarity and poorer global polarity coordination

Up to this point, I have presented various genetic manipulations on cell packing to assay for the changes in core protein polarisation. In these experiments, it revealed the net long-term effect of altered cell packing on core protein polarisation. However, there is insufficient temporal knowledge on how core planar polarisation changes in response to acute perturbation of cell packing. Therefore, I utilised ultraviolet (UV) laser to acutely alter wing epithelial cell packing and quantify for changes in core protein polarisation over time. Focusing on the posterior region of the wild-type wing expressing Fz::EGFP, I used two laser-ablation approaches to perturb cell packing: (1) Circular ablation and (2) Parallel vertical lines ablation.

First, I performed a circular ablation from the apical surface to basement membrane of an epithelium at 24 hAPF as depicted in Figure 4.8A. The internal control for this experiment is in the same wing region, with a distance of approximately 10 cells away from ablated region (Figure 4.8A). Upon wounding by irradiation with a UV laser, the ablated circular ring on the wing epithelium undergoes a gradual wound healing process. Approximately five to six hours post ablation, the wound is completely sealed up from ventral to dorsal (Figure 4.8B). Since there is no cell proliferation to replace the removed cells, the non-ablated surrounding cells are stretched anisotropically due to ectopic tension driven by wound constriction. Thus, this leads to poor packing or organisation of cells within the ablated region at 3- and 5-hour post ablation as compared to the control tissue (Figure 4.8B-C). Fascinatingly, less organised cells within the ablated region also exhibit lower polarity magnitude as compared to the control at 3- and 5-hour post ablation (Figure 4.8D). Not only that, there is a significantly higher polarity angle variance in the ablated region as compared to control at 3- and 5-hour post ablation, indicating weak global polarity alignment between cells (Figure 4.8E)

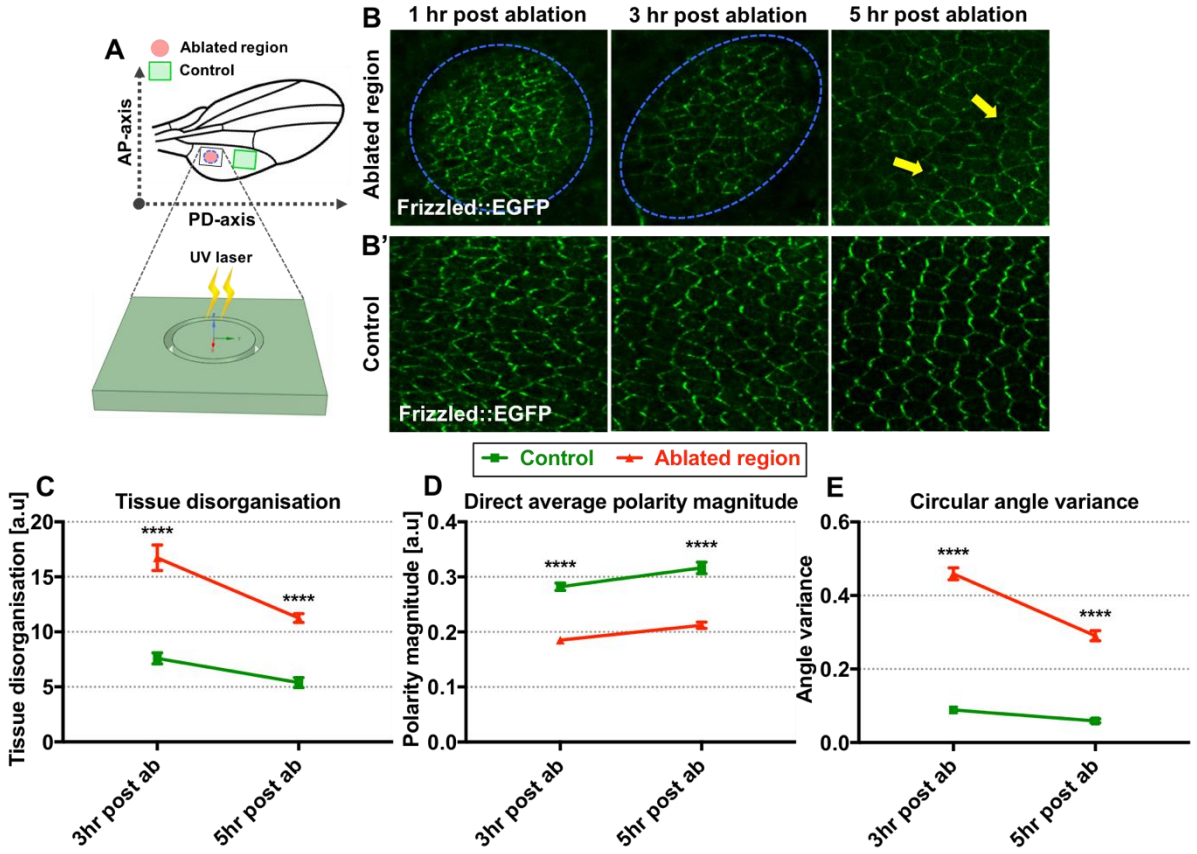

Figure 4.8: Poorly organised ablated region results in lower polarity magnitude and poorer polarity coordination than control region

(A) Diagram of pupal wing expressing Fz::EGFP showing sites of circular laser ablation cuts (represented by blue dotted line). Schematic diagram illustrating UV laser ablating along apical-basal axis in a circular manner. Cells within the ablated region are known as “Ablated region” (marked by a red circle). The control for this experiment is the cells further away from the ablated region (represented by a green box).

(B) Individual time frames of ablated region from 1- to 5-hour post ablation. The wounds are depicted by blue dotted line circles.

(B’) Individual time frames of control non-ablated region from 1- to 5-hour post ablation.

(C) Quantified epithelial tissue organisation of ablated and control regions.

(D) Quantified direct average polarity magnitude of ablated and control regions.

(E) Quantified polarity angle variance of ablated and control regions.

The number of wings for each developmental stage is 5 to 9. Error bar indicates mean±SEM. One-way ANOVA test, unpaired. Significance levels: p-value $\leq 0.0001^{****}$.

Apart from altering cell packing with circular ablation, I designed an alternative method to alter cell packing with two parallel vertical lines ablation from the apical surface to basement membrane of an epithelium at 24 hAPF, followed by live imaging at 3- and 5-hour post laser ablation (Figure 4.9A-B and Figure 4.10A). The control for this experiment is non-ablated wild-type pupal wing expressing Fz::EGFP of the same region (Figure 4.10A'). Interestingly, cells within the ablated regions appear to be significantly more elongated and irregular as compared to control of non-ablated cells at approximately 3-hour post ablation (Figure 4.9C-D). Consistent to circular ablation assay, ectopic tension generated by wound constriction results in aberrant cell shape within the ablated region. However, cell eccentricity and regularity in ablated wings are not significantly different from the control wings as the wounds are almost healed by 5-hour post ablation (Figure 4.9C-D). With this assay, I predicted that ectopic tension generated by wound closure is sufficient to alter cell shape within the ablated region.

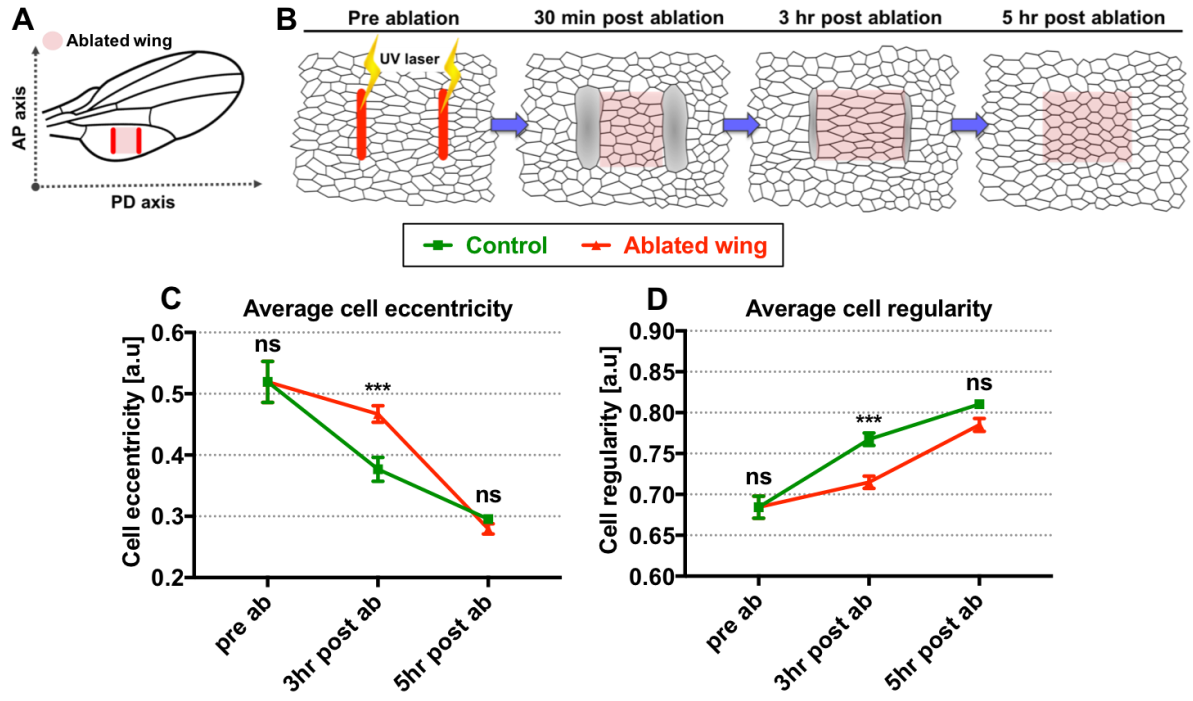

Figure 4.9: Ectopic tensions during wound closure alter cell shapes

(A) Diagram of wild-type pupal wing expressing Fz::EGFP showing sites of vertical laser ablation cuts (represented by red lines). The control for this experiment is non-ablated wild-type pupal wing expressing Fz::EGFP of the same region.

(B) Cartoons depicting two parallel vertical lines laser ablation on wing epithelium from pre-

ablation to 5-hour post ablation.
(C) Quantified average cell eccentricity of ablated and control non-ablated wings.
(D) Quantified average cell regularity of ablated and control non-ablated wings.
The number of wings for each developmental stage is 5 to 9. Error bar indicates mean±SEM. One-way ANOVA test, unpaired. p-value $\leq 0.0004^{***}$, ns is not significantly different.

Moreover, at 3-hour post ablation, ablated wings appear to be less organised as compared to control non-ablated wings (Figure 4.10B). Interestingly, less organised tissue within the ablated wings exhibits lower polarity magnitude as compared to the control at 3-hour post ablation (Figure 4.10B-C). As the wounds are almost healed by 5-hour post ablation, there is no longer any significant difference in tissue organisation between ablated and control wings (Figure 4.10B). However, average polarity magnitude of ablated wings is slightly lower than the control wings at 5-hour post ablation (Figure 4.10C). Moreover, there is higher polarity angle variance in the ablated wings as compared to the control wings at both 3- and 5-hour post ablation, indicating poor global polarity alignment between cells (Figure 4.10D). Interestingly, by 5-hour post ablation, polarity in the ablated wings fails to realign along PD axis, despite having similar tissue organisation to the control wings (Figure 4.10B and Figure 4.10D). Previous studies showed that PD-oriented stresses due to wing-hinge contraction play a role in reorienting polarity angle along the wing PD axis [Aigouy et al., 2010]. However, in the ablated wings, it is possible that the ectopic tensions generated during wound constriction could also influence the cell polarity axis. Taken together with the results from circular laser ablation experiment, these experiments proved that altering cell packing acutely can hamper the strength and alignment of core planar polarity.

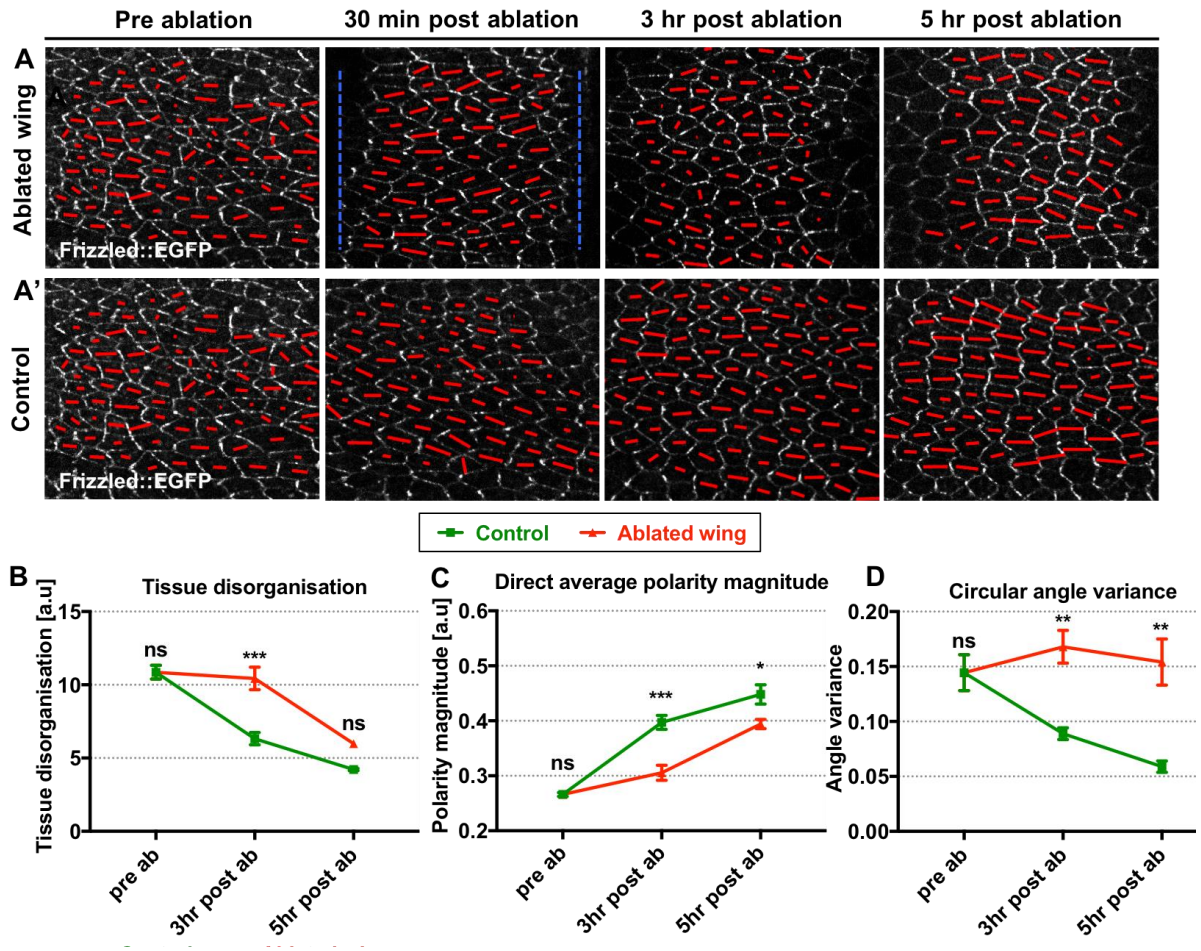

Figure 4.10: Poorly organised ablated wings results in weaker polarity magnitude and loss of global polarity coordination as compared to control wings

(A) Individual time frames of ablated wings from pre-ablation to 5-hour post ablation. The wounds are depicted by blue lines.

(A') Individual time frames of control non-ablated wings from pre-ablation to 5-hour post ablation.

(B) Quantified level of tissue disorganisation of ablated and control non-ablated wings.

(C) Quantified direct average polarity magnitude of ablated and control non-ablated wings.

(D) Quantified polarity angle variance of ablated and control non-ablated wings.

The number of wings for each developmental stage is 5 to 9. Error bar indicates mean±SEM. One-way ANOVA test, unpaired. Significance levels: p-value $\leq 0.0002^{***}$, p-value $\leq 0.001^{**}$, p-value $\leq 0.01^{*}$. ns is not significantly different.

4.3.1.5 Global polarity alignment correlates with PD-oriented cell junctional rearrangement and is independent of epithelial tissue organisaton and cell regularity and elongation

To examine the effects of altered cell shape, cell elongation and tissue organisation on global core polarity alignment across the wing epithelium, I used Fz::EGFP polarity angle variance to capture the degree of alignment or coordination of polarity angle within a wing region. Polarity angle variance ranges between 0 and 1, with 0 having complete agreement in polarity alignment, while 1 represents complete polarity misalignment (see details in Chapter 2). I then plotted Fz::EGFP polarity angle variance against epithelial organisation, cell eccentricity and regularity for all the genotypes previously examined for their effects on polarity magnitude at different developmental time points (24 to 30 hAPF). Interestingly, I found that cell eccentricity and cell regularity are weakly correlated with polarity angle variance (with coefficient of determination, r^2 = 0.1301 and 0.257 respectively) for all wild-type control, genetically manipulated and laser ablated wings (Figure 4.11A-B). On the other hand, epithelial tissue organisation and global polarity alignment are moderately correlated (with r^2 = 0.5047) (Figure 4.11C). Therefore, my data shows that there is a lack of correlation between cell elongation, regularity and tissue organisation, and global core planar polarisation alignment during 24 to 30 hAPF of pupal wing development.

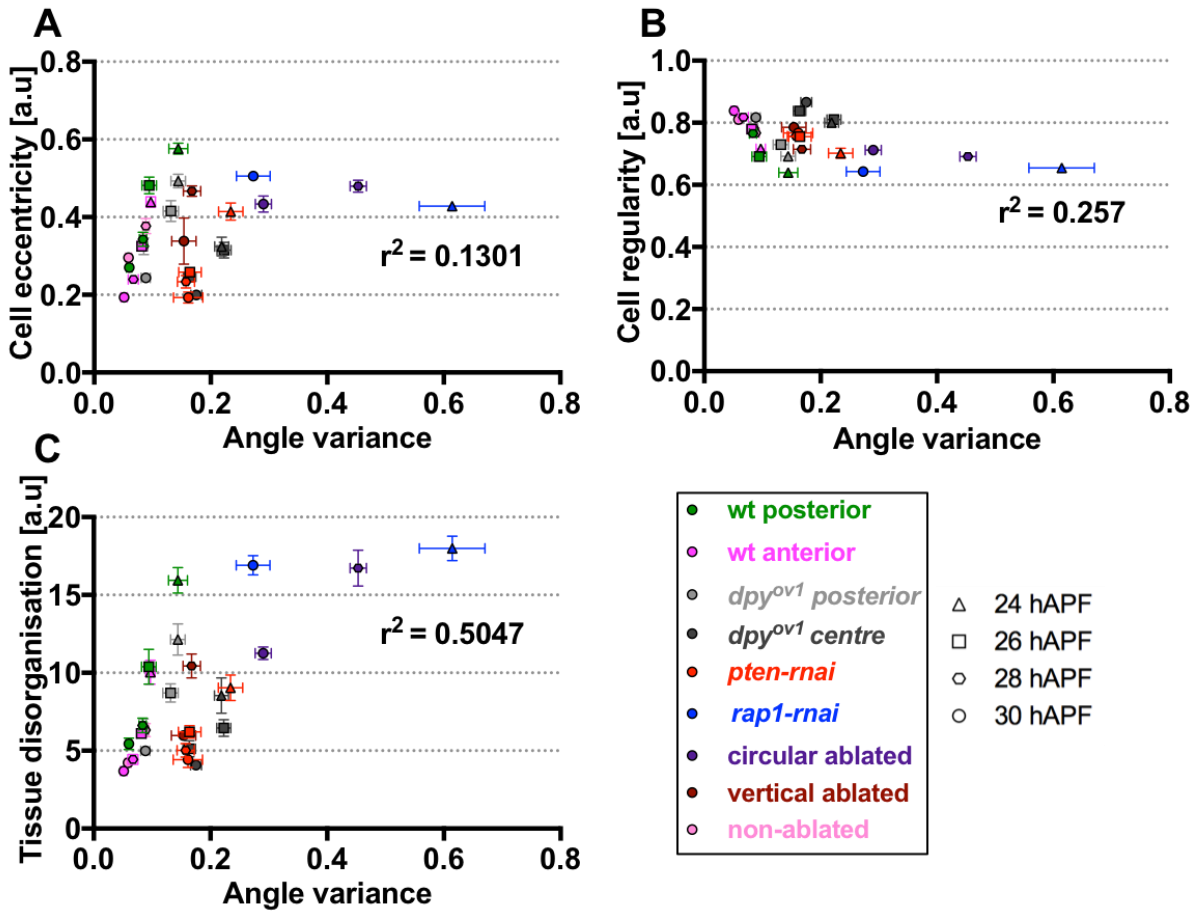

Figure 4.11: Altered cell eccentricity, regularity and epithelial tissue organisation do not affect global polarity alignment

(A) Correlation between average cell eccentricity and Fz::EGFP polarity angle variance for all genotypes (in different colours) and developmental time points (in different shapes).

(B) Correlation between average cell regularity and Fz::EGFP polarity angle variance.

(C) Correlation between epithelial tissue disorganisation and Fz::EGFP polarity angle variance.

wt represents wild-type. The number of wings for each developmental time point is 5 to 10 wings. Error bar indicates mean±SEM.

In response to tissue stretching along PD axis during Phase II, directional cell junctional rearrangement is driven by the shrinkage of AP-oriented cell junctions and expansion of new PD-oriented cell junctions [Aigouy et al., 2010; Etournay et al., 2015]. This process results in an increasing fraction of PD-oriented hexagonal cells [Sugimura and Ishihara, 2013]. Hence, the final hexagonal cell orientation can be used as a readout of PD-oriented cell junctional rearrangement. First, I quantified hexagonal cell orientation to capture the alignment of hexagonal cells in wild-type

wings from 24 to 30 hAPF (Figure 4.12A). Hexagon orientation value ranges between -1 and 1, 1 when all hexagonal cells are oriented along the PD axis and -1 when all hexagonal cells are oriented along the AP axis (see details in Chapter 2). By quantifying hexagonal cell orientation in the posterior region of wild-type wings expressing Fz::EGFP, I observed that the orientation of hexagonal cells increasingly shifted along the PD axis from 24 to 30 hAPF (Figure 4.12B). Remarkably, there is a striking temporal correlation between hexagonal cell orientation and Fz::EGFP polarity angle variance in different regions of wild-type wings from 24 to 30 hAPF, in that global polarity alignment improves as hexagonal cells become more PD-oriented (with coefficient of determination, $r^2 = 0.7865$) (Figure 4.12C).

How does directional junctional rearrangement relate to global polarity axis coordination? From the analysis of time-lapse images of wild-type wings, I observed that, new cell junctions consistently form along the PD-axis, as AP-oriented cell junctions shrink during PD-oriented junctional rearrangement (Figure 4.12D-E). These newly formed PD-junctions are devoid of core polarity proteins (Figure 4.12D). As core polarity proteins are retained on existing cell junctions and slow to accumulate on new junctions, this then biases polarity axis parallel to the newly formed junctions (Figure 4.12D), as previously shown in [Aigouy et al., 2010]. This observation has also been reported in the studies on murine epidermal skin [Aw et al., 2016]. However, it is important to note that newly formed cell junctions happen to align parallel to the axis of cell elongation in *Drosophila* pupal wing cells, resulting in polarity axis aligning parallel to the axis of cell elongation [Aigouy et al., 2010]. In contrast to that, in murine epidermal skin, formation of new cell junctions is perpendicular to the axis of cell elongation, which then biases polarity axis perpendicular to the axis of cell elongation [Aw et al., 2016]. Thus, this suggests that global polarity alignment is not directly influenced by the axis of cell elongation but rather it is linked to directional cell junctional rearrangement.

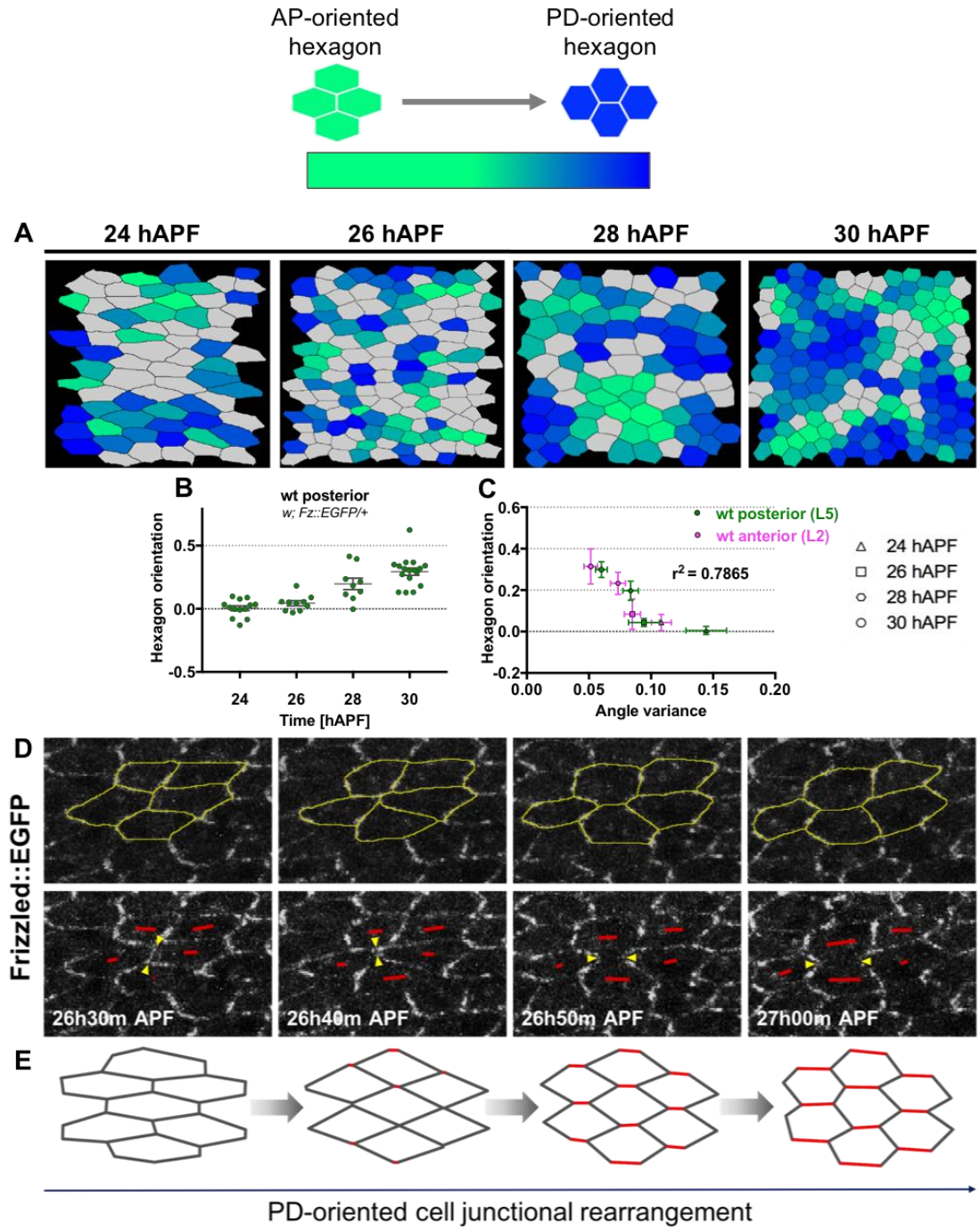

Figure 4.12: PD-oriented cell junctional rearrangement increases the fraction of PD-oriented hexagonal cells in wild-type wings

(A) Processed images of a Fz::EYFP-expressing wild-type wing from 24 to 30 hAPF. Hexagonal cells are colour-coded according to their orientation. PD- and AP-oriented hexagonal cells are represented in blue and green respectively. Grey cells represent non-hexagonal cells.

(B) Quantified average hexagonal cell orientation in the posterior region of the wild-type wings from 24 to 30 hAPF. The value approaches 1 when hexagonal cells orient along the

PD axis and -1 when hexagonal cells orient along the AP axis.
(C) Correlation between average hexagonal cell orientation and Fz::EGFP polarity angle variance in different regions of wild-type wings from 24 to 30 hAPF (represented by different shapes).
wt represents wild-type. The number of wings for each developmental time point is 7 to 17 wings. Error bar indicates mean±SEM.
(D) First row: Processed time-lapse images of a group of cells in the posterior wing tracked between 26:30 hAPF and 27 hAPF. Cell boundaries are depicted by yellow lines.
Second row: As new PD-junctions expand and are devoid of Fz::EGFP, polarity becomes more visible. Arrowhead indicates cell junctions that shrink and expand. Magnitude and axis of Fz::EGFP polarity are represented by the length and orientation of red lines respectively.
(E) Cartoon depicts how PD-oriented cell junctional rearrangement could guide polarity axis alignment. Newly formed PD-oriented cell junctions are coloured in red.

Interestingly, I found that genotypes that result in different epithelial cell shapes and tissue organisation, also result in a distinct final hexagonal orientation at 30 hAPF (Figure 4.13A-A'). In particular, hexagonal cells consistently align towards the tissue stretch axis in both anterior and posterior regions of wild-type wings, whereas hexagonal cells appear to be misoriented in *pten-rnai* and *rap1-rnai* wings (Figure 4.13A''). This implies that pattern of cell junctional rearrangement is perturbed in both *pten-rnai* and *rap1-rnai* wings. Notably, both *pten-rnai* and *rap1-rnai* wings exhibit loss of ordered global polarity alignment across the wing tissue as compared to wild-type wings. While it has not been shown before that loss of Rap1 results in defective cell junctional rearrangement, [Bardet et al., 2013] reported that *pten* mutant tissue indeed exhibits defective junctional rearrangement. Nonetheless, the mechanism underlying the role of Rap1 GTPase-dependent E-Cadherin distribution on the adherens junctions in regulating directional cell junctional rearrangement is an interesting avenue to explore in the future.

Previous studies have established that PD-oriented cell junctional rearrangement in the pupal wing is governed by PD-oriented anisotropic stresses from wing-hinge contraction and Dachsous, as both laser-ablated wings and *dachsous* mutants result in perturbed cell junctional rearrangement [Aigouy et al., 2010; Sugimura and Ishihara, 2013; Etournay et al., 2015]. Moreover, [Etournay et al., 2015] reported that

mutation of Dumpy causes the orientation of cell junctional rearrangements fail to align as effectively along PD-axis as in the wild-type wings. In support of this, I found that different regions of *dumpy*^{ov1} mutant wings exhibit different hexagonal cell orientation, in which the posterior and central (in between longitudinal vein 3 and vein 4) wing regions exhibit PD-oriented and misoriented hexagonal cells respectively (Figure 4.13A-A''). Since PD-oriented anisotropic stresses are significantly reduced in the central region as compared to the posterior region of *dumpy*^{ov1} mutant wings [Etournay et al., 2015], this could explain why cell junctional rearrangement is significantly perturbed in the central region but remains PD-oriented in the posterior region of *dumpy*^{ov1} mutant wings. I found that global polarity coordination is not affected in the posterior region of *dumpy*^{ov1} mutant wings (Figure 4.6C). However, global polarity alignment is loss in the central region of the *dumpy*^{ov1} wings (Figure 4.13C), suggesting that polarity alignment is affected by changes in cell junctional rearrangement.

Additionally, I asked how cell junctional rearrangement is perturbed in wings that had been subjected to laser ablation. At 5-hour post ablation, hexagonal cells fail to orient with the PD axis for both circularly and vertically ablated wing regions as compared to non-ablated control wings, suggesting that ablated wings exhibit defective junctional rearrangement (Figure 4.13B-B'). One possible explanation for this is that ectopic tension due to wound closure causes misoriented cell junctional rearrangement. Consequently, in both ablated wings, global polarity axis is not as well coordinated as non-ablated wings by 5-hour post ablation (Figure 4.8E and 4.10E).

To investigate the causality effects of cell junctional rearrangement on global polarity axis alignment in the pupal wing, I plotted Fz::EGFP polarity angle variance against hexagonal cell orientation for all the genotypes at 30 hAPF (and 5-hour post ablation for ablated and non-ablated wings) (Figure 4.13C). Interestingly, I found that hexagonal cell orientation is negatively correlated with Fz::EGFP polarity angle variance irrespective of the genotypes (with coefficient of determination, $r^2 = 0.8427$), in that regions of the wing with more PD-oriented hexagonal cells exhibit lower polarity angle variance while in regions of the wing containing more misoriented

hexagonal cells exhibit higher polarity angle variance (Figure 4.13C). This suggests that PD-oriented cell junctional rearrangement is essential to establish PD-oriented global polarity alignment. Overall, my findings provided evidence that global polarity alignment is a direct consequence of cell junctional rearrangement and is independent of cell elongation, regularity and epithelial tissue organisation.

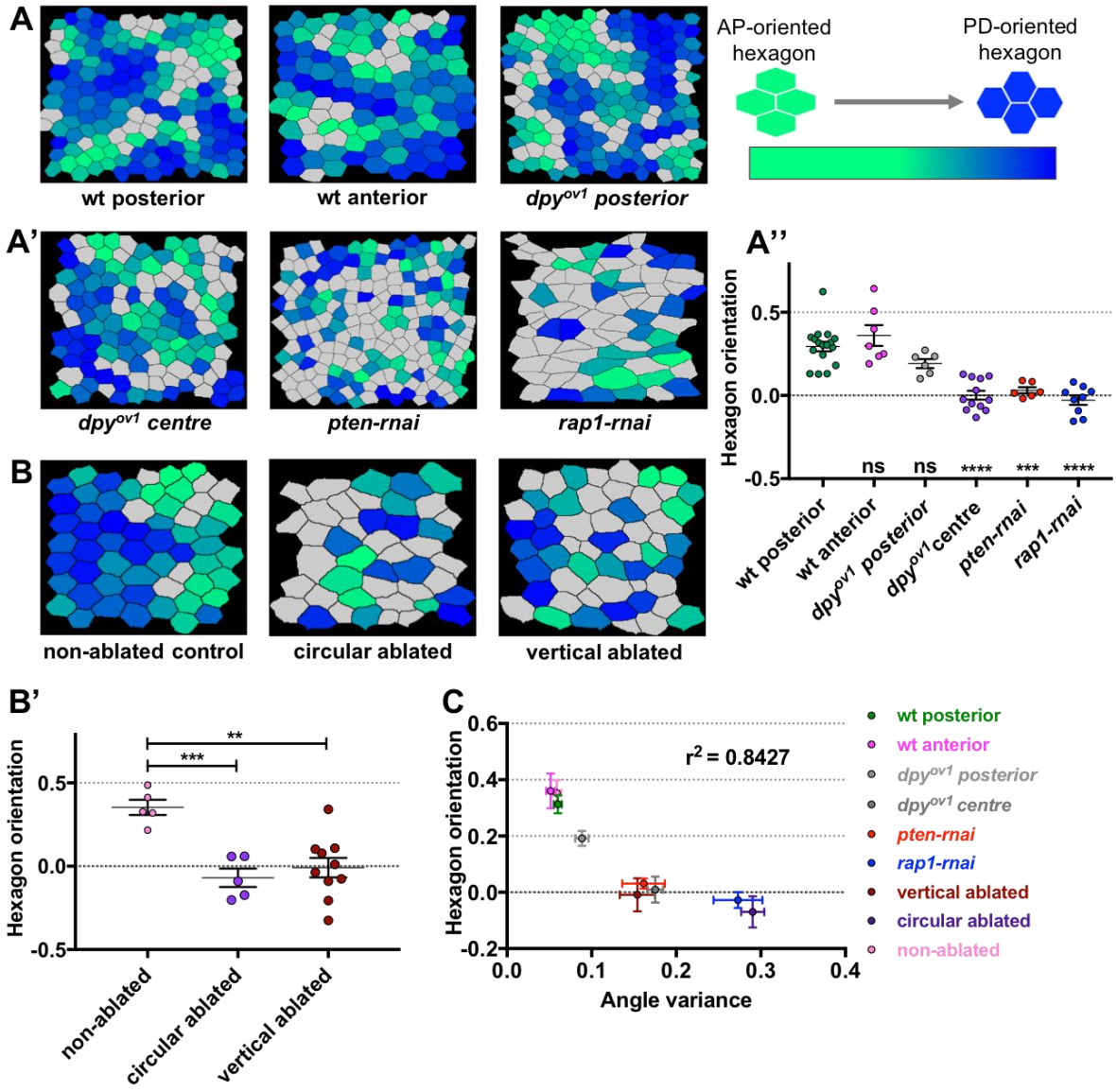

Figure 4.13: Altered cell junctional rearrangement can influence the alignment of polarity axis in the wing

(A – A') Processed images of wild-type and different genetically manipulated wings at 30 hAPF. Hexagonal cells are colour-coded according to their orientation. PD- and AP-oriented hexagonal cells are represented in blue and green respectively. Grey cells represent non-hexagonal cells.

(A'') Quantified average hexagonal cell orientation in wild-type and different genetically

manipulated wings at 30 hAPF. The value approaches 1 when hexagonal cells orient along the PD axis and -1 when hexagonal cells orient along the AP axis.
wt represents wild-type. The number of wings for each genotype is 6 to 17 wings.
(B) Processed images of non-ablated, circularly and vertically ablated wings at 5-hour post ablation.
(B') Quantified average hexagonal cell orientation in non-ablated, circularly and vertically ablated wings at 5-hour post ablation. The number of wings for each condition is 5 to 10 wings.
(C) Correlation between average hexagonal cell orientation and Fz::EGFP polarity angle variance for all genotypes (in different colours) at 30 hAPF.
The number of wings for each genotype is 5 to 17 wings. All error bars indicate mean±SEM.

4.3.2 Effects of core planar polarisation on cell packing

In the previous section, I showed that different cell packing can affect core planar polarisation. Therefore, the hypothesis that both events are independent of each other is not supported. Due to the precise temporal correlation between cell packing and core planar polarisation, there is a possibility that the core planar polarity pathway is involved in regulating cell packing as reported by [Classen et al., 2005]. To test the hypothesis that interfering with core planar polarity pathway could cause defective packing geometry, I examined the differences in cell shape, tissue organisation, cell junctional rearrangement and hexagonal packing between core planar polarity mutant and wild-type wings.

4.3.2.1 Frizzled is not required to promote hexagonal packing and better tissue organisation in Drosophila pupal wing

As hexagonal cell packing is predominantly achieved via cell junctional rearrangement [Classen et al., 2005], it is relevant to study the effect of core planar polarity pathway on cell packing from 26 to 32 hAPF, with negligible contributions from other morphogenetic events such as cell division, apoptosis, and so on. I imaged the posterior region of fz^{P21} mutant pupal wings expressing PH::mCherry to visualise cell outlines from 26 to 32 hAPF (Figure 4.11A'). fz^{P21} is a null mutation that

produces no detectable protein [Jones et al., 1996]. As a control for this, I imaged wild-type wings expressing PH::mCherry in the same region over these developmental times (Figure 4.11A).

First, I examined the cell shape regularity and percentage of hexagonal cells in pupal wings of *fz*^{P21} mutant and wild-type background. In *fz*^{P21} mutant wings, cell shape becomes increasingly regular with increasing fraction of hexagonal cells from 26 to 32 hAPF (Figure 4.11B-C). Interestingly, it appears that cell shape regularity and percentage of hexagonal cells in *fz*^{P21} mutant cells are not significantly different from those of wild-type cells from 26 to 32 hAPF (Figure 4.11B-C). These results demonstrate that Fz is not required to promote regular hexagonal packing.

To further investigate whether Fz affects other cell morphological parameters, I quantified cell eccentricity and epithelial tissue organisation of *fz*^{P21} mutant and wild-type wings. Similar to wild-type wings, *fz*^{P21} mutant cells become less elongated and more organised with increased homogeneity in cell shape and size by 32 hAPF (Figure 4.11D-E). Interestingly, I found that there are no significant differences in cell eccentricity and tissue organisation between *fz*^{P21} mutant and wild-type wings (Figure 4.11D-E). Loss of Fz therefore does not seem to affect the relaxation of cells into a more organised packing.

To test whether core planar polarity activity is involved in regulating cell junctional rearrangement due to its potential role in regulating E-Cadherin endocytosis [Warrington et al., 2017], I quantified hexagonal cell orientation in *fz*^{P21} mutant and wild-type wings. PD-oriented hexagonal cells increase from 26 to 32 hAPF in both wild-type and *fz*^{P21} mutant wings (Figure 4.11F). However, I found no significant difference in hexagonal cell orientation between *fz*^{P21} mutant and wild-type wings, suggesting that Fz is not involved in regulating cell junctional rearrangement during pupal wing morphogenesis (Figure 4.11F).

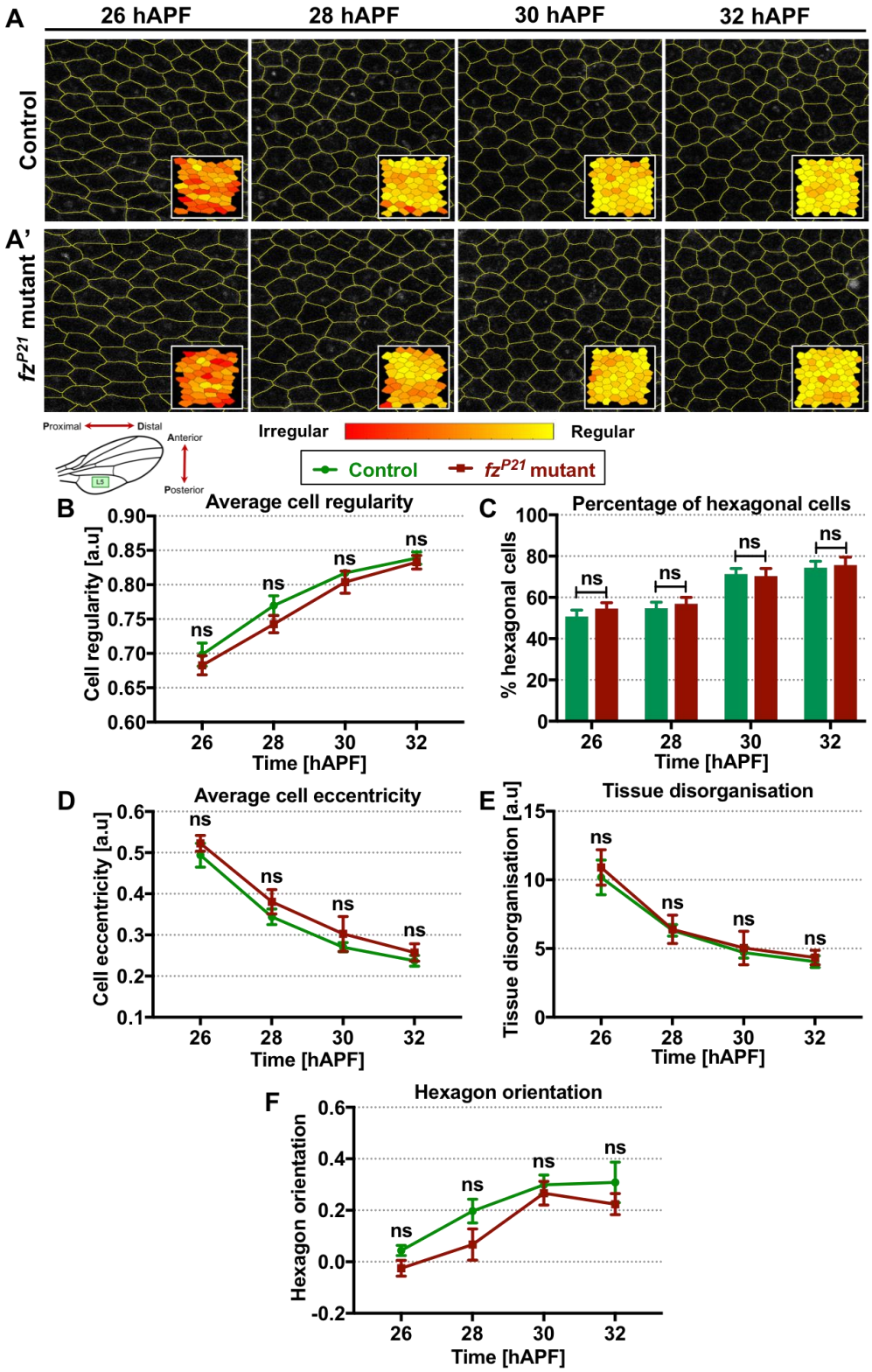

Figure 4.14: Fz is not required to achieve hexagonal packing and better tissue organisation

(A) Time-lapse confocal images from a control wing expressing PH::mCherry from 26 to 32 hAPF. Cell boundaries are depicted by yellow lines. Inset: Images are colour-coded according to the regularity of the shape, with highly irregular cells in red colour and perfectly

regular cells in yellow colour.

(A') Time-lapse confocal images from a *fz*^{P21} mutant wing expressing PH::mCherry from 26 to 32 hAPF.

(B) Quantified average cell regularity of *fz*^{P21} mutant and control wings from 26 to 32 hAPF.

(C) Quantified percentage of hexagonal cells of *fz*^{P21} mutant and control wings.

(D) Quantified average cell eccentricity of *fz*^{P21} mutant and control wings.

(E) Quantified average cell regularity of *fz*^{P21} mutant and control wings.

(F) Quantified average hexagonal cell orientation of *fz*^{P21} mutant and control wings.

The number of wings for each developmental stage is 5 to 9. Error bar indicates mean±SEM. One-way ANOVA test, unpaired. Significance levels: ns is not significantly different.

4.4 Discussion

During pupal wing morphogenesis from 24 to 30 hAPF, core proteins become increasingly polarised as cells become more hexagonally packed. Indeed, as presented in Chapter 3, there is a precise temporal correlation between cell elongation, regularity and tissue organisation with core planar polarisation in wild-type wings. Notably, these correlations remain valid in different regions of the wing, where more regular and organised tissues exhibit better polarity and vice versa. To investigate the causality effects of cell shape and packing on the ability of cell to polarise, I performed various genetic manipulations to alter cell packing and quantified for core planar polarisation.

Changes in cell shape can be attributed to active shape changes due to local intrinsic forces and passive shape changes due to extrinsic forces that act globally [Blanchard and Adams, 2011]. Local intrinsic forces play a crucial role in regulating oriented cell division and directed cell junctional rearrangement [Baena-Lopez et al., 2005; Mao et al., 2011]. PTEN and Rap1 regulate the apical distribution of actomyosin network and E-Cadherin respectively [Knox and Brown, 2002; Bardet et al., 2013]. Hence, knocking down PTEN results in organised cobblestone packing rather than characteristic honeycomb-like hexagonal packing, while loss of Rap1 results in highly disorganised tissue with reduced homogeneity in cell shapes and size. This suggests that cell shape changes could arise from intrinsic forces. Global extrinsic forces, on the other hand, drive passive cell shape changes, orientation of cell division and cell rearrangement [Aigouy et al., 2010; Behrndt et al., 2012; Campinho et al., 2013]. Mutation of Dumpy reduces anisotropic mechanical stresses in the wing, resulting in significantly smaller apical area of wing cells [Etournay et al., 2015; Ray et al., 2015]. By severing pupal wing, ectopic tensions generated by wound constriction act as ectopic global forces to influence cell shape changes. This implies that cell shape changes could also be passively influenced by global forces. However, it is worth emphasising that both local and global forces exert feedback on each other [Sugimura and Ishihara, 2013]. Ultimately, changes in cell shape at cellular-level would affect the organisation of cells at tissue-level. Collectively, these

phenotypes allow us to explore whether altered cell shapes, size and tissue organisation might affect core planar polarisation.

My results showed that more regular and isotropic cells are better polarised than irregular and elongated cells. I found that *pten-rnai* and *dumpy*^{ov1} mutant cells, which appear to be more regular, isotropic and organised than wild-type cells at early pupal wing developmental times, result in higher polarity magnitude. On the other hand, *rap1-rnai* cells, which are irregular, elongated and disorganised as compared to wild-type cells at 30 hAPF, are weakly polarised. There is a striking correlation between cell regularity, elongation and tissue organisation with polarity magnitude, independent of different genetic manipulations on cell packing. On the other hand, *dumpy*^{ov1} mutant cells with reduced apical area appear to polarise similarly to wild-type cells at 30 hAPF, suggesting that reducing cell size does not affect core protein polarisation. However, one could still argue that PTEN, Rap1 and Dumpy signalling might directly influence the core planar polarity pathway, which is not known at present.

As I could not rule out that any of these genes act directly on core planar polarity pathway, in order to obtain higher degree of confidence in the results, I carried out an alternative experiment to alter cell packing *in vivo* using laser ablation. This method also allows me to acutely disrupt cell packing and quantify the changes in core planar polarity over time. Here I demonstrated two laser-ablation approaches: circular and vertical ablation. Both methods of ablating wings lead to more disorganised tissue as compared to the control of non-ablated wings. Evidently, irregular and disorganised ablated tissue results in weaker polarity as compared to non-ablated controls, which is consistent with the results from genetically-altered cell packing.

Based on the results outlined above, I demonstrated that different cell shapes and tissue organisation can influence cell's ability to planar polarise efficiently. Thus, cell shapes and tissue organisation impact core planar polarisation. However, in these experiments, Fz protein has been expressed since embryonic stages and Fz has been increasingly polarised since 18 hAPF onwards [Aigouy et al., 2010]. Thus, what

I am quantifying is the remodelling of pre-existing polarity rather than the establishment of polarity induced *de novo* in response to different cell packing. It would be interesting to ask a different question: How do different cell shapes and tissue organisation affect the ability of core proteins to polarise *de novo*? In the next chapter, I will investigate the ability of core protein to polarise *de novo* given different cell geometries and tissue organisation.

How does core planar polarity axis relate to the axis of cell elongation? It has been speculated that cell elongation is involved in establishing PD-oriented polarity through polarised microtubules alignment along the long axis of the pupal wing cells [Aigouy et al., 2010]. Indeed, I demonstrated that in wild-type wings, cells align their polarity axis parallel to the axis of cell elongation in response to tissue stress anisotropy, in agreement with [Aigouy et al., 2010]. This correlation remains valid for most of the cases in different genetic manipulations on cell packing. However, there are two exceptions that results in uncoupling of this correlation. First, there is a poor correlation between polarity alignment and the axis of *pten-rnai* cell elongation at late pupal stages. Second, polarity axis in *rap1-rnai* cells does not consistently align with the axis of cell elongation. In fact, previous studies in murine epidermal skin reported that cell polarity consistently aligns perpendicular to the axis of cell elongation [Aw et al., 2016]. Hence, the loss of strict coupling between polarity alignment and axis of cell elongation suggests that polarity alignment is not simply a consequence of axis of cell elongation.

In Chapter 3, I showed that as wild-type wing tissue becomes more organised, less elongated and regularly packed, polarity alignment becomes increasingly coordinated between cells in the wing (with gradually decreasing polarity angle variance over time, Figure 3.7). Conversely, I questioned if irregular and elongated packing or disorganised tissues would result in poorer polarity alignment between cells. To investigate the causality effects of epithelial tissue organisation, cell elongation and cell regularity on global polarity alignment across the wing tissue, I used polarity angle variance to capture the degree of alignment of wing polarity for all genotypes with altered cell shapes and tissue organisation. It seems that indeed disorganised tissue, irregular and elongated cell shape in both *rap1-rnai* and ablated

wings lead to poor global polarity alignment across the wing tissue. However, I found that this coupling is lost in some of the genotypes. For example, central region of *dumpy*^{ov1} mutant wings with comparable cell regularity and tissue organisation as wild-type wings exhibit a loss of ordered global polarity alignment. Similarly, more regular and organised *pten-rnai* cells also exhibit weak global polarity coordination across the wing tissue, consistent with results from [Bardet et al., 2013]. Furthermore, global polarity alignment fails to recover in vertically-ablated wings despite having similar tissue organisation with the control wings by 5-hour post ablation. In support of this, I showed that global polarity alignment is poorly correlated with cell elongation, regularity and tissue organisation for all the genotypes, suggesting that global polarity alignment is not a direct consequence of cell elongation, regularity and epithelial tissue organisation.

How does directional junctional rearrangement relate to global polarity axis alignment? I observed that in wild-type wings, the orientation of cell junctional rearrangement is biased along the wing PD axis; results in the formation of new cell junctions parallel to the PD axis (PD-junctions), which are devoid of core proteins. Due to retention of core proteins on existing AP-junctions, this biases polarity parallel to the newly formed PD-junctions, in agreement with [Aigouy et al., 2010]. During phase II (from 24 to 32 hAPF), I observed that PD-oriented cell junctional rearrangement increases the fraction of PD-oriented hexagonal cells in wild-type tissue, consistent with [Sugimura and Ishihara, 2013]. In fact, as wild-type wing cells relax into more PD-oriented hexagonal packing, global polarity axis becomes more coordinated along the PD axis of the wing tissue. The precise temporal correlation of these events implies cross regulation.

To investigate the role of cell junctional rearrangement in coordinating global polarity alignment along the wing PD axis, I examined global polarity alignment in wings with altered cell junctional rearrangement using various genetic methods and laser ablation assays. Evidently, there is a striking temporal correlation between cell junctional rearrangement and global polarity alignment for all genotypes at 30 hAPF. I found that *pten-rnai* and *rap1-rnai* wings which present with defective junctional rearrangement exhibit weaker global polarity coordination. Moreover, this correlation

holds true in different regions of *dumpy*^{ov1} mutant wings, in which the posterior region with PD-oriented junctional rearrangement results in ordered global polarity coordination, whereas the central region with misoriented junctional rearrangement results in poor polarity coordination. Furthermore, in laser ablated wings where pattern of cell junctional rearrangements is perturbed also exhibit poor global polarity alignment. One possible reason could be that ectopic tension coming from wound constriction results in misoriented cell junctional rearrangement, thus biasing polarity in different orientation. Overall, my findings suggest that global polarity alignment is a direct consequence of cell junctional rearrangement.

Lastly, I showed that loss of Fz does not affect the shape regularity and percentage of hexagonal cells from 26 to 32 hAPF. I further showed that it does not affect cell eccentricity and tissue organisation in the pupal wing over the same time course. My data is not consistent with previous work that has reported the role of core planar polarity proteins such as Fz in promoting hexagonal packing, which is mediated by Rab11 and exocyst-dependent processes [Classen et al., 2005]. Although, it is important to note that *fz*^{P21} mutant wings results in the mildest but statistically significant defect in hexagonal packing as compared to other core planar polarity mutants such as in *pk* mutant wings [Classen et al., 2005]. One plausible explanation for such a discrepancy could be attributed to the differences in techniques used for imaging of *Drosophila* pupal wings. Previous work was based on fixing and mounting of pupal wings, while my work is based on *in vivo* live imaging of pupal wings. My work also highlights that loss of Fz does not affect oriented cell junctional rearrangement in pupal wing from 26 to 32 hAPF. In support of this, recently published work in mouse also showed that core planar polarity is not required to govern oriented cell junctional rearrangement [Aw et al., 2016]. Previous studies reported that orientation of cell junctional rearrangement during pupal development is regulated by several processes such as anisotropic tension generated from wing-hinge contraction, Dachsous and actomyosin network [Aigouy et al., 2010; Sugimura and Ishihara, 2013; Bardet et al., 2013]. Therefore, it is more likely that Fz is not required to regulate cell junctional rearrangement and promote hexagonal packing and tissue organisation during pupal wing morphogenesis. It would be interesting to further examine the effects of loss of other core polarity proteins (such Flamingo or

Strabismus) on cell shape, percentage of hexagonal cells, tissue organisation and cell junctional rearrangement.

CHAPTER 5

De novo establishment of core planar polarity protein asymmetry

5.1 Introduction

In Chapter 4, in effort to dissect the effects of cell shape and tissue organisation on core planar polarisation, I performed several genetic manipulations and laser ablation assays to alter epithelial cell packing and quantify for changes in core planar polarisation over time. I found that more regular cell shape and organised tissue results in stronger polarised tissue and vice versa. More importantly, in these experiments, Frizzled (Fz) has been expressed since embryonic stages and has been increasingly polarised since 18 hAPF (hour After Puparium Formation) onwards [Aigouy et al., 2010]. It was reported that core planar polarity complexes are being constantly remodelled as cell junction rearranged, whereby newly formed cell junctions derived from cell division or junctional rearrangement are slow to accumulate core complexes, while persistent cell junctions tend to retain core complexes [Aigouy et al., 2010; Aw et al., 2016]. Hence, these experiments actually revealed the effect of altered cell packing on the remodelling of pre-existing polarity as opposed to the ability of cells to establish polarity induced *de novo*.

Previous studies from our lab reported that core polarity complexes increase in stability over time after Dsh or Stbm induction in *dsh* or *stbm* mutant background, which implies that the longer the protein is expressed, the more stable it becomes over time [Warrington et al., 2017]. This is because over time core polarity proteins cluster themselves into stable and sorted intercellular complexes via feedback interactions that exhibit higher resistance against endocytosis [Strutt and Strutt, 2008; Strutt et al., 2011; Cho et al., 2015]. This leads to a prediction that it is easier to redistribute less stable proteins *de novo* during junctional rearrangement as opposed remodelling highly stable pre-existing complexes. On this basis, I speculated that cell packing might affect pre-existing complexes and complexes induced *de novo* differently. I therefore asked a different question: How does altered cell packing affect the ability of core proteins to polarise *de novo*? Furthermore, since most computational models on planar polarisation are built upon establishment of polarity *de novo*, therefore there is an urgent need to tackle this question experimentally in order to validate these theoretical models [Amonlirdviman et al., 2005; Le Garrec et al., 2006; Ma et al., 2008; Abley et al., 2013]. Addressing this

question will shed some light on the effect of cell packing on the *de novo* emergence of polarity.

It has been reported that Fz function as early as 6 hAPF is sufficient to establish global wing polarity coordination in the proximal-distal (PD) direction of the wing, while delayed Fz activity results in a swirling wing hair phenotype, in line with the idea that Fz is involved in long-range propagation of polarity throughout the wing tissue [Strutt and Strutt, 2002]. However, due to the lack of quantitative tools, experimental analysis on the effects of temporal Fz expression on core planar polarisation and cell packing during *Drosophila* pupal wing morphogenesis has not been studied in detail. The new quantitative tools that I have developed will enable me to characterise the *de novo* emergence of polarity by turning on Fz expression in a *fz* mutant background at different developmental stages [Strutt and Strutt, 2002].

5.2 Aims

The first aim of this chapter is to characterise the effect of temporal induction of core pathway activity on polarity, protein stability and cell packing during pupal wing morphogenesis. In Section 5.3.1, I use the FLP/FRT system in combination with heat shock activation to temporally activate or induce Fz::EYFP expression in a fz^{P21} mutant background [Strutt, 2001]. I perform Fz::EYFP induction at two different time points: early (2 hAPF) and late (22 hAPF) stages of pupal wing development. I then quantify changes in polarisation and cell packing over time. In an effort to understand the underlying polarisation mechanisms of both pre-existing complexes and *de novo* emergence of proteins, I further characterise the effects of temporal Fz expression on Fz stability using a tandem fluorescence timer.

Data from Chapter 4 revealed that different cell packing can affect the ability of pre-existing complexes to repolarise efficiently, in which irregular cell shapes and disorganised tissue results in weaker polarity and vice versa. Nonetheless, there are no acute studies to reveal when the defect occurs, which might help to understand why it occurs. Therefore, I wish to investigate whether manipulating cell packing can potentially influence the establishment of polarity induced *de novo*. In Section 5.3.2, I induce polarity *de novo* at 22 hAPF of pupal developmental time and quantify changes in polarisation in response to different cell packing. I first quantify polarity *de novo* on regions of the wing blade with different cell packing. Apart from that, I use laser ablation assay to acutely alter epithelial cell packing and quantify changes in polarity induced *de novo* over time.

5.3 Results

5.3.1 Timing of action of the core planar polarity pathway on the regulation of core protein polarisation and stability, and cell packing

Over 17 years ago, our lab characterised two temporal distinguishable activities of Fz in the pupal wing [Strutt and Strutt, 2002]. They reported that an early function of Fz is required to completely rescue a *fz* mutant phenotype and to achieve global wing polarity coordination, while expressing Fz late results in loss of global wing polarity coordination by monitoring the global wing trichome coordination in the adult wings [Strutt and Strutt, 2002; Strutt and Strutt, 2007]. However, not much is known about the timing of action of Fz function particularly on: (1) the strength of Fz polarisation and (2) cell packing in the pupal wing over time, which could now be detected using the quantitative tools that I have developed (see details in Chapter 2).

To induce Fz expression at different pupal developmental stages, I used the FLP/FRT system in combination with heat shock activation of gene activity. A heatshock *(hs)-FLP* transgene will allow heat-induced (2 hours at 37˚C) excision of a region flanked by compatible FRT sites as described in [Strutt, 2001] (Figure 5.1A). I used a line that upon heat shock results in activation of the *Actin5C* promoter to drive Fz::EYFP expression (*Act>STOP>fz::EYFP*) in a fz^{P21} mutant background [Strutt, 2001]. Previous work from our lab confirmed that late activation of Fz (12 hAPF onwards) results in progressively weaker global polarity coordination in the wing, suggesting that Fz is required earlier in development to achieve global polarity coordination along PD axis of the wing [Strutt and Strutt, 2007]. As an initial testing of the genetic tools, I activated Fz::EYFP expression at 24 hAPF with 2 hours of heat shock at 37˚C and then performed hourly interval time-lapse imaging from 26 hAPF to 30 hAPF to capture the changes in core planar protein polarisation over time. As shown in Figure 5.1B, upon heat shock at 24 hAPF, Fz::EYFP began to accumulate at the cell boundaries after 3 hours post induction and gradually polarised from there onwards. Although, on average, polarity magnitude increases from 26 to 30 hAPF,

however, activation of Fz::EYFP by 24 hAPF results in a swirling global polarity phenotype (Figure 5.1B). This is consistent with [Strutt and Strutt, 2007].

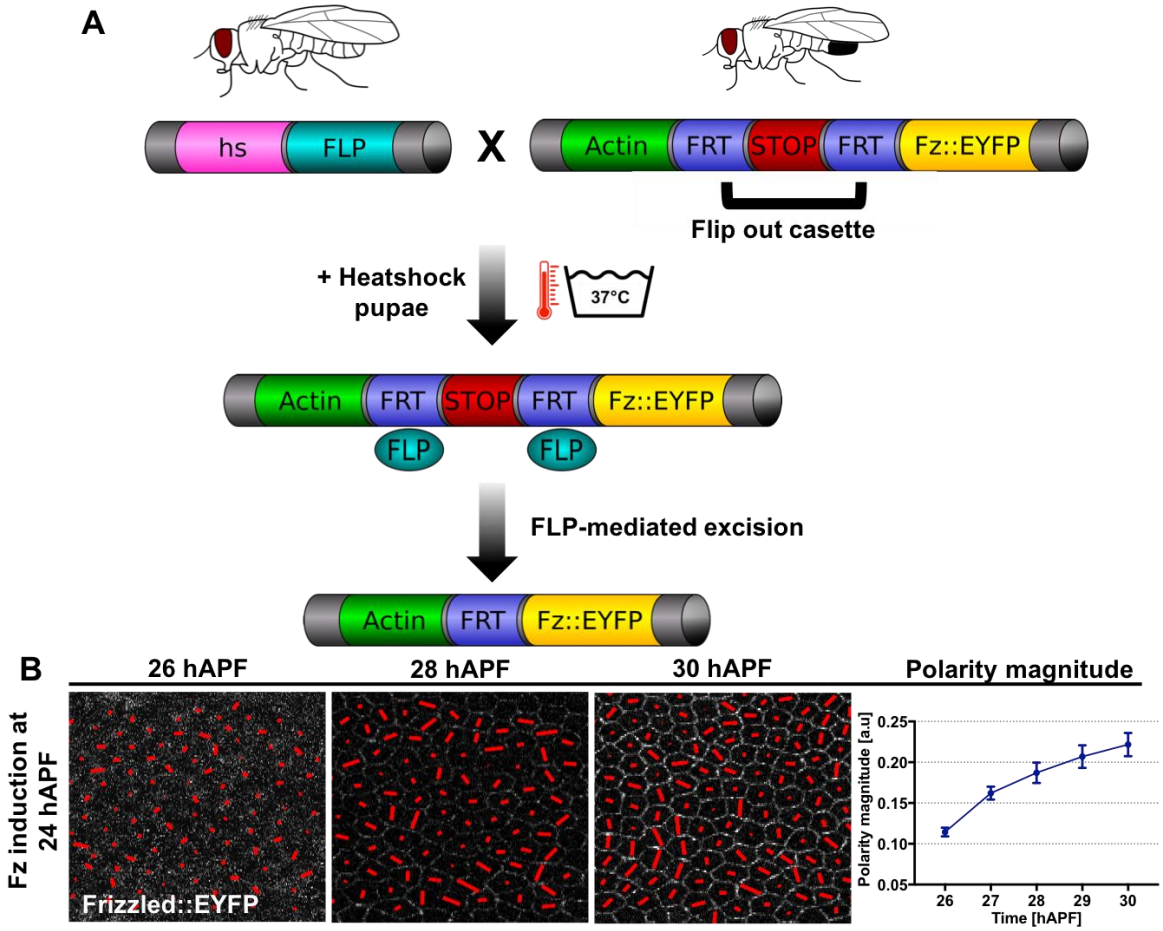

Figure 5.1: An assay to temporally activate or induce Fz::EYFP expression in *fz^{P21}* mutant wing

(A) A genetic scheme showing induction of Fz::EYFP expression.

(B) Time-lapse confocal images of pupal wing after induction of Fz::EYFP expression at 24 hAPF. The length and orientation of red lines within individual cells represent the magnitude and the axis of Fz::EGFP polarity respectively. Graph showing quantified polarity magnitude from 26 to 30 hAPF after Fz::EYFP induction at 24 hAPF.

The number of wings for each developmental stage is 6. Error bar indicates mean±SEM.

5.3.1.1 Early induction of Fz::EYFP gives normal polarity but late induction of Fz::EYFP results in a swirling polarity phenotype

I then performed an early Fz::EYFP induction at 2 hAPF (denoted as **"pre-existing"** as equivalent to having pre-existing Fz::EYFP polarity from 18 hAPF onwards) (Figure 5.2A). Indeed, early Fz::EYFP induction produces strong asymmetric polarity complexes and rescues global polarity alignment along PD-axis of the wing by 32 hAPF, in agreement with published results [Strutt and Strutt, 2002] (Figure 5.2A'-A''). Previous work reported that the appearance of asymmetric protein localisation is significantly reduced in 24 hAPF Fz::EYFP-induced wings [Strutt and Strutt, 2002]. Therefore, I performed Fz::EYFP activation at 22 hAPF (denoted as **"*de novo*"**), where asymmetric protein complexes can still form (Figure 5.2B-B'). Similar to the activation of Fz::EYFP at 24 hAPF, activation of Fz::EYFP at 22 hAPF also results in loss of global polarity alignment along PD axis by 32 hAPF (Figure 5.2B'').

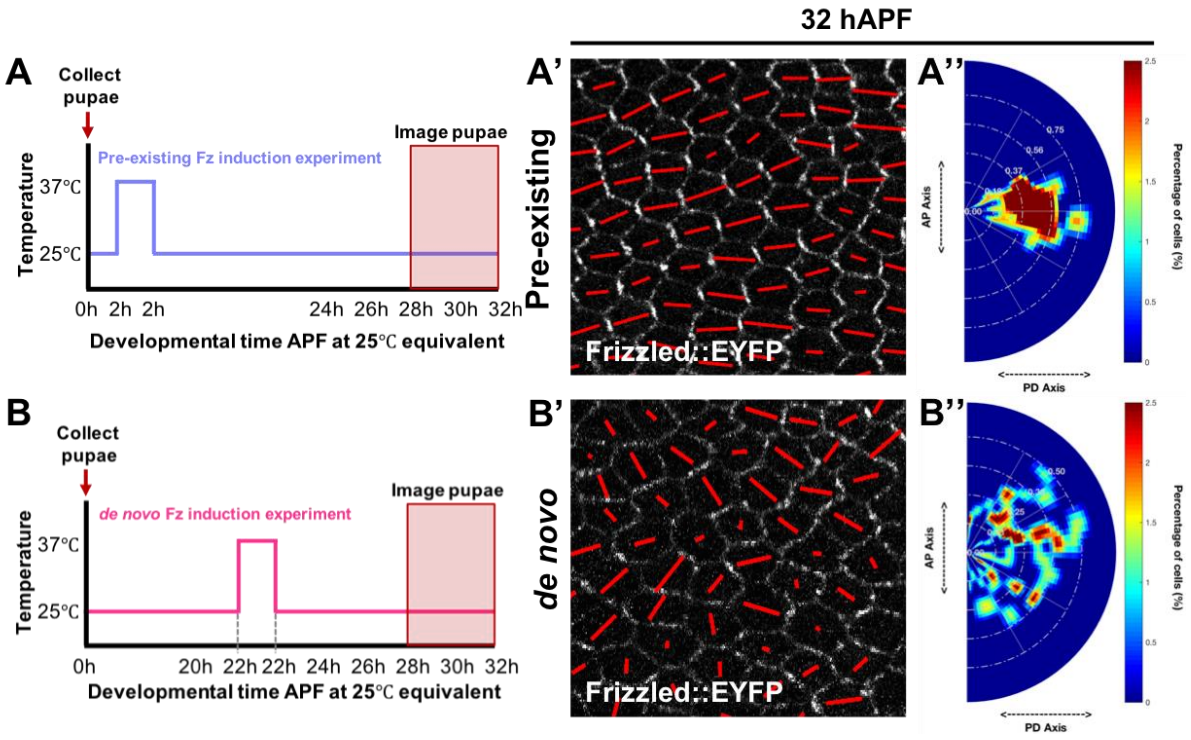

Figure 5.2: Early induction of Fz::EYFP expression rescues global polarity phenotype while late induction of Fz::EYFP results in a swirling polarity phenotype

(A) Experimental timeline for early (pre-existing) Fz::EYFP induction experiment. Heat shock at 38°C is applied at 2 hAPF to induce Fz::EYFP expression. Note that pupal developmental stops for the period of heat shock at 38°C [Warrington et al., 2017]. Pupae were raised at 25°C for all developmental stages.

(A') Confocal image of a 32 hAPF *fz*^{P21} mutant wing, rescued with induction of Fz::EYFP expression at 2 hAPF. The length and orientation of red lines within individual cells represent the magnitude and the axis of Fz::EGFP polarity respectively.
(A'') Heatmap showing the angle and magnitude of Fz::EYFP polarity of early induced wing at 32 hAPF. In this protractor-like heatmap, magnitude of polarity is the distance away from the centre of the half circle, meanwhile the polarity angular distribution spans from $-90°$ to $+90°$. The percentage of cells is represented by different colours (red – high percentage of cells, blue – low percentage of cells).
(B) Experimental timeline for late (*de novo*) Fz::EYFP induction experiment. Heat shock at 38°C is applied at 22 hAPF to induce Fz::EYFP expression.
(B') Confocal image of a 32 hAPF *fz*^{P21} mutant wing, rescued with induction of Fz::EYFP expression at 22 hAPF.
(B'') Heatmap showing the angle and magnitude of Fz::EYFP polarity of late induced wing at 32 hAPF.
Timeline adapted from [Warrington et al., 2017]. The number of wings for each genotype is 4.

5.3.1.2 Temporal induction of Fz::EYFP expression reveals that maximum achievable polarity is independent of tissue organisation but is dependent on the timing of Fz::EYFP activity

How does temporal Fz induction affect Fz polarisation and stability over time? To unravel the temporal changes in core planar polarisation in early and late induction experiments, I quantified polarity magnitude in both pre-existing and *de novo* experiments from 28 to 32 hAPF for consistency (Figure 5.3A-B and 5.3A'-B'). To assess whether induced-Fz::EYFP polarity alignment is related to cell deformation, I plotted Fz::EYFP polarity angle against cell orientation. I found that in early induction (pre-existing) experiments, Fz::EYFP polarity angle is consistently oriented parallel to the axis of cell eccentricity from 28 to 32 hAPF of pupal wing morphogenesis (Figure 5.3A''). However, in late induction (*de novo*) experiments, despite cells being consistently oriented along PD axis, the angle of Fz::EYFP polarity is more dispersed in a swirling polarity phenotype (Figure 5.3B'').

To assess the respective timing of the action of the core planar polarity pathway on the regulation of cell geometry, I quantified cell shape and epithelial tissue organisation in both early induction (pre-existing) and late induction (*de novo*) wings. My results showed that both pre-existing and *de novo* tissues exhibit similar level of tissue organisation from 28 to 32 hAPF (Figure 5.3C). Moreover, there are no significant differences in cell eccentricity and regularity between pre-existing and *de novo* cells over the same developmental time course (Figure 5.3D-E). However, later induction of Fz activity results in a subtle but statistically significant defect in hexagonal cell orientation as compared to early Fz induction, implying that cell junctional rearrangement is perturbed in late Fz induction wings (Figure 5.3F).

In these experiments, I performed two measures of core planar polarisation: (1) “direct” average polarity magnitude measure which indicates the strength of polarisation of a group of cells and (2) polarity angle variance measure which captures the degree of coordination/alignment of polarity angle within a group of cells. Interestingly, the average polarity magnitude in *de novo* wings are significantly lower than pre-existing wings over the same developmental times, despite having similar cell shape and tissue organisation (Figure 5.3C and 5.3G). As Fz::EYFP began to accumulate at the cell boundaries after 3 hours post induction and gradually polarised from there onwards, polarity *de novo* fails to reach maximum achievable polarity by 32 hAPF ($p_{average}$ for pre-existing and *de novo* tissues are 0.41 and 0.24 respectively) (Figure 5.3G). Consequently, delayed activation of Fz::EYFP at 22 hAPF results in higher polarity angle variance as compared to early activation of Fz::EYFP, suggesting poor global wing polarity coordination in *de novo* tissue (Figure 5.3H). This also confirms that Fz::EYFP is required much earlier in pupal development to achieve global polarity coordination along the wing PD axis.

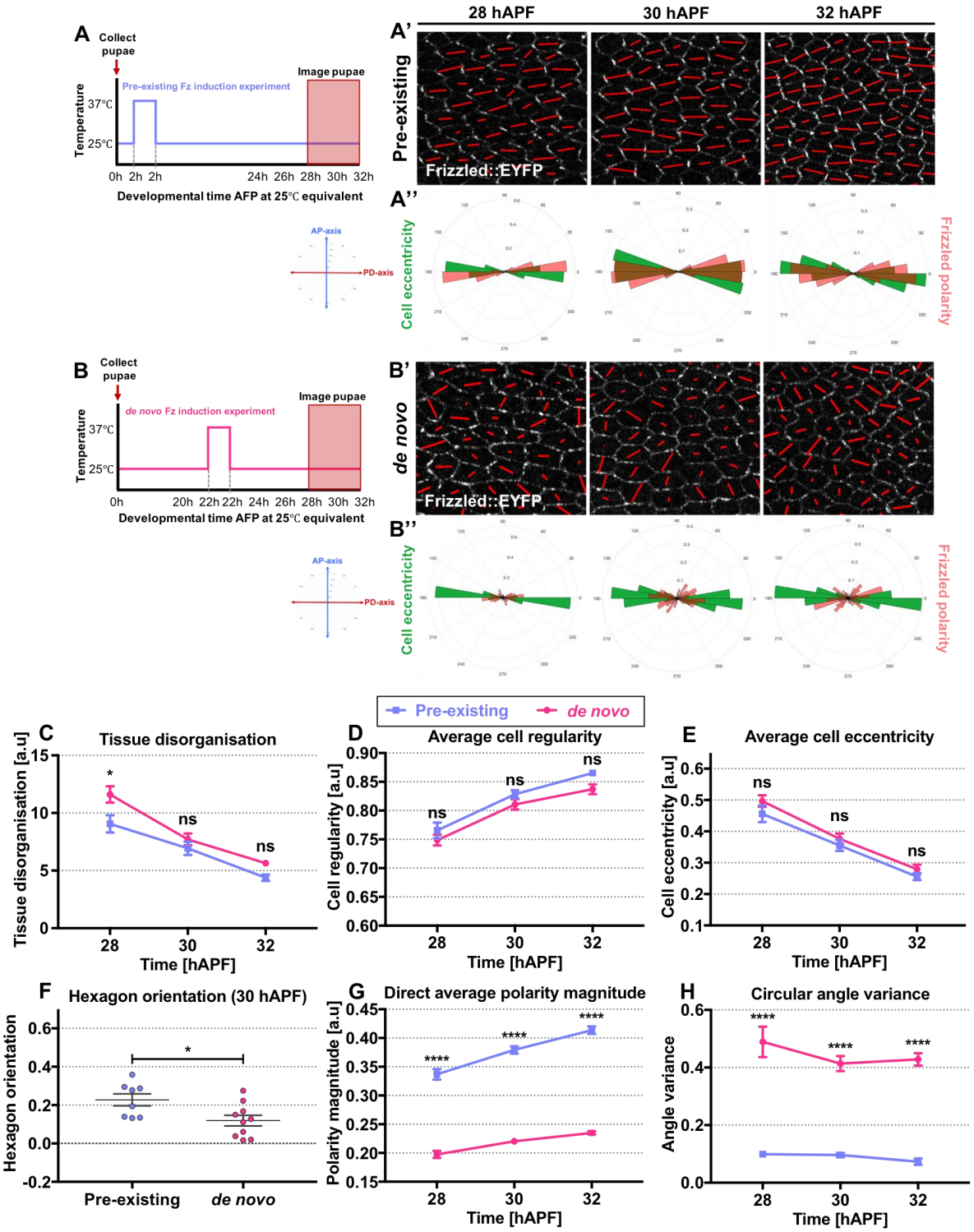

Figure 5.3: Induction of Fz::EYFP activity at different developmental times results in distinct core planar polarisation but similar cell shape and tissue organisation

(A) Experimental timeline for pre-existing Fz::EYFP induction experiment.

(A') Time-lapse confocal images of a pre-existing Fz::EYFP-induced wings from 28 to 32 hAPF. The length and orientation of red lines within individual cells represent the magnitude and the axis of Fz::EGFP polarity respectively.

(A'') Circular weighted histogram plots display the orientation of pre-existing Fz::EYFP polarity and cell eccentricity obtained from 28 to 32 hAPF.
(B) Experimental timeline for *de novo* Fz::EYFP induction experiment.
(B') Time-lapse confocal images of a *de novo* Fz::EYFP-induced wing from 28 to 32 hAPF.
(B'') Circular weighted histogram plots display the orientation of *de novo* Fz::EYFP polarity and cell eccentricity obtained from 28 to 32 hAPF.
(C) Quantified level of tissue disorganisation of pre-existing and *de novo* wings.
(D) Quantified average cell regularity of pre-existing and *de novo* wings.
(E) Quantified average cell eccentricity of pre-existing and *de novo* wings.
(F) Quantified average hexagonal cell orientation of pre-existing and *de novo* wings at 30 hAPF.
(G) Quantified direct average polarity magnitude of pre-existing and *de novo* wings.
(H) Quantified polarity angle variance of pre-existing and *de novo* wings.
All pre-existing and *de novo* Fz::EYFP-induced wings are fz^{P21} mutant rescued with induction of Fz::EYFP expression at 2 and 22 hAPF respectively.
The number of wings for each developmental stage is 7 to 10. Error bar indicates mean±SEM. One-way ANOVA test, unpaired. Significance levels: p-value ≤ 0.0001****, p-value ≤ 0.03*. ns is not significantly different.

5.3.1.3 Fz::EYFP exhibits lower stability in de novo complexes than in pre-existing complexes

I then investigated how Fz stability changes over time, after early and late induction of Fz expression. Here I used tandem fluorescence timer (tFT) as a proxy for protein stability.

A tFT is comprised of two spectrally separable fluorescent proteins that undergo fluorophore maturation with different kinetics, namely the fast-maturing fluorescent protein and the slow-maturing fluorescent protein. In this experiment, I used a fast-maturing sfGFP and a slow-maturing mKate fluorescent proteins with different maturation times [Shcherbo et al., 2009; Khmelinskii et al., 2012]. A pool of Fz fused to mKate-sfGFP (*fz::sfGFP-mKate*) will become green-fluorescent within minutes after synthesis and gradually attain red-fluorescent representing proteins that lasted for over 20 minutes after synthesis (Figure 5.4A). The ratio of mKate (red) to sfGFP

(green) fluorescence intensities from a single time-point fluorescence imaging snapshot provides a readout of protein stability [Khmelinskii et al., 2012; Barry et al., 2015]. A high readout of mKate/sfGFP intensity ratio indicates increased in the relative amount of stable protein, while changes in sfGFP intensity indicate changes in net protein production.

To assess the differences in Fz stability between early and late induction of Fz expression, I induced *fz::sfGFP-mKate* expression using hs-FLP/FRT system at two different times during pupal development (at 2 hAPF and 22 hAPF). Pupae were heat shocked for 2 hours at 37°C to excise the *FRT-STOP-FRT* cassette. *fz::sfGFP-mKate* was expressed in a fz^{P21} mutant background after excision of the *FRT-STOP-FRT* cassette from *Act>STOP>fz::sfGFP-mKate.*

I first induced *fz::sfGFP-mKate* expression earlier in development (at 2 hAPF, hence, denoted as pre-existing polarity), followed by 2-hour interval time-lapse imaging from 28 to 34 hAPF (Figure 5.4B-B'). For every developmental time point, I imaged both the sfGFP (green) and mKate (red) fluorescence channels for fluorescence intensity measurement. In pre-existing experiments, normalised sfGFP intensities increase from 28 to 34 hAPF, indicating higher protein production as compared to protein degradation over time (positive net production) (Figure 5.4D). Similarly, normalised mKate intensities increase slightly over time, implying an increased in the amount of longer-living or stable proteins over time (Figure 5.4D).

Next, I induced *fz::sfGFP-mKate* expression later in development (at 22 hAPF, hence, denoted as *de novo* polarity), followed by 2-hour interval time-lapse imaging from 28 to 34 hAPF (Figure 5.4C-C'). Similarly, in *de novo* experiments, both normalised sfGFP and mKate intensities increase from 28 to 34 hAPF (Figure 5.4E).

To determine the relative amount of stable protein within the total protein population for a given developmental time point, I computed the ratio of mKate to sfGFP intensities [Khmelinskii et al., 2012]. Surprisingly, in both pre-existing and *de novo* experiments, the ratio of mKate to sfGFP intensity decreases over time, suggesting that relative amount of stable to total proteins decreases with time (Figure 5.4D and

5.4F). On the contrary, our lab previously showed that the relative stable amount of endogenous Fz::EGFP expression increases over time in wild-type wings using Fluorescence Recovery After Photobleaching (FRAP) assay [Warrington et al., 2017].

Hence, I speculated that my results could be attributed to the following caveats. After the activation of the *Act-fz::sfGFP-mKate,* it takes time for protein production/degradation to achieve a steady state, and before this happens, there will be a preponderance of sfGFP that it is being produced faster than it is being degraded. Consistently, my results indicate that steady state sfGFP fluorescence levels cannot be achieved within these time window (over 26 hours of protein expression) (Figure 5.4D-E). Hence, in order to be able to compare fluorescence timer ratio over time, it is necessary to determine if sfGFP fluorescence intensities reach a steady state after longer hour of induction, otherwise it would give higher levels of faster maturing protein independently of the fluorescence timer function which assumes steady state protein levels. On the other hand, assuming that *Actin5C* transcription level has reached a steady state, however, degradation rate is still lower than production rate, hence sfGFP intensities wouldn't reach a constant level. It is important to examine if *Actin5C* transcription level reaches a steady state during these developmental time points. With the given caveats, it is therefore not useful to compare fluorescence timer ratio of mKate to sfGFP over time.

The rates of *Actin5C* transcript production/degradation and protein production/degradation for *fz::sfGFP-mKate* may vary at different developmental times due to changing cellular physiology. *Actin5C* promoter, for instance, might change the expression levels at different points during pupal life and the degradation machinery may change its rate of activity. However, these should be identical for any age-matched samples. Therefore, I compared the fluorescence timer ratio of mKate to sfGFP values for matching developmental age samples from pre-existing and *de novo* experiments. I found out that there is a significant reduction in the relative amount of stable proteins in *de novo* as compared to pre-existing experiments for all developmental time points (Figure 5.4F). This is consistent with the fact that *de novo* polarity magnitude is lower than pre-existing polarity (Figure 5.3F). This could be due

to the fact that there is insufficient time for *de novo* emergence of proteins to form stable core polarity complexes within 6 hours post Fz induction. In parallel with previous work reported that the amount of stable Fz protein is significantly higher in early Dsh induction in *dsh* mutant background as compared to late induction [Warrington et al., 2017]. This implies that indeed the longer the protein is expressed the more stable and polarise it becomes over time [Warrington et al., 2017].

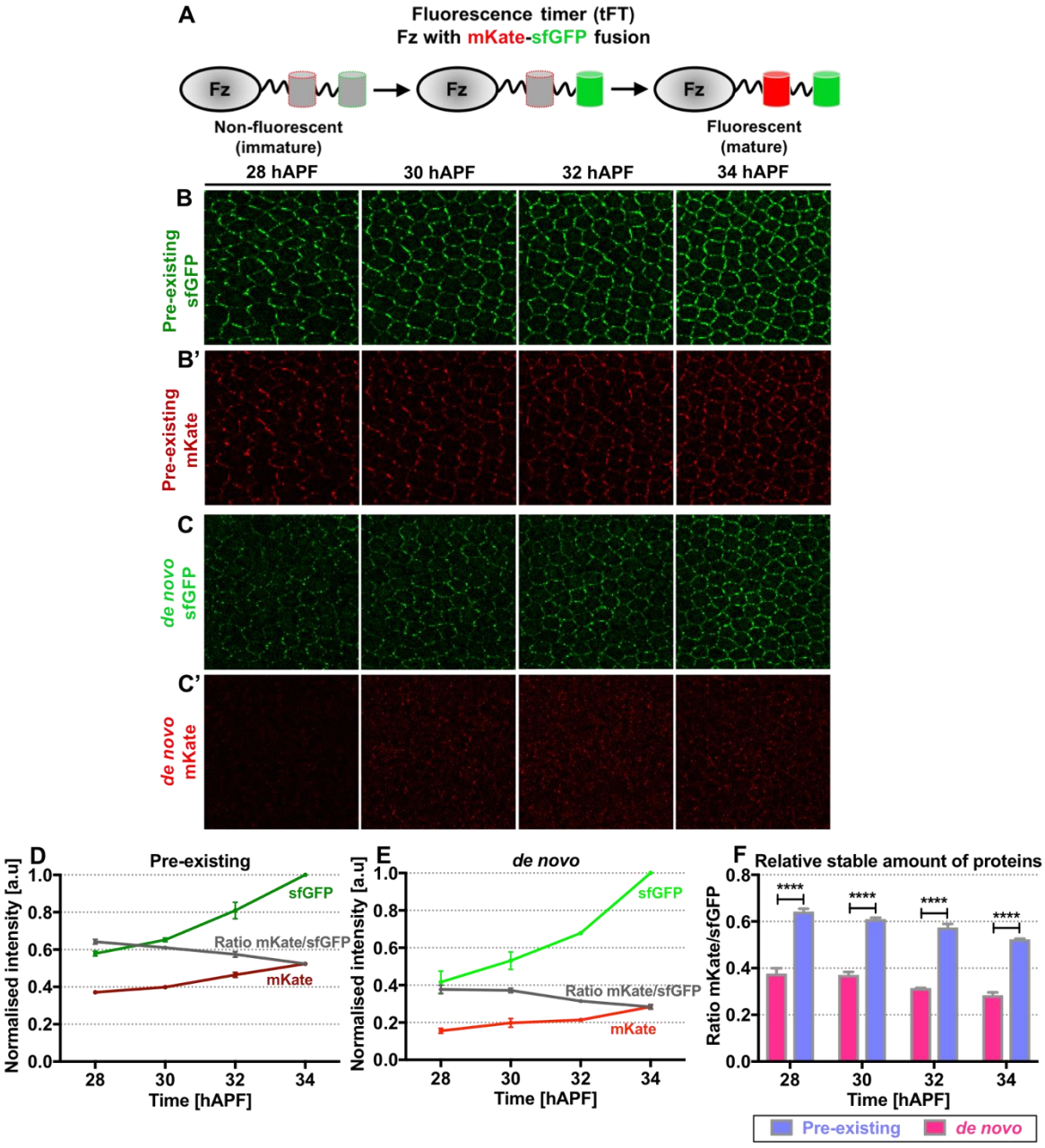

Figure 5.4: Pre-existing complexes exhibit higher relative amount of stable proteins as compared to *de novo* complexes

(A) Cartoon illustrating the behaviour of tandem fluorescence timer fused to Fz.
(B – B') Time-lapse confocal images of pre-existing Fz wings in sfGFP (B) and mKate (B') channels from 28 to 34 hAPF.
(C-C') Time-lapse confocal images of *de novo* Fz-induced wings in sfGFP (C) and mKate (C') channels from 28 to 34 hAPF.
(D) Graph showing pre-existing Fz fluorescence intensity curves of sfGFP and mKate over time. Ratios of pre-existing mKate/sfGFP fluorescence intensity are computed over time. Fluorescence intensities are normalised to the brightness of sfGFP at 34 hAPF.
(E) Graph displaying *de novo* Fz fluorescence intensity curves of sfGFP and mKate over time. Ratios of *de novo* mKate/sfGFP fluorescence intensity are computed accordingly.
(F) Comparison between ratios of mKate/sfGFP in pre-existing and *de novo* Fz from 28 to 34 hAPF.
All pre-existing and *de novo* Fz-induced wings are fz^{P21} mutant rescued with induction of Fz-mKate-sfGFP expression at 2 and 22 hAPF respectively.
The number of wings for each developmental stage is 4. Error bar indicates mean$\pm$SEM. One-way ANOVA test, unpaired. Significance levels: p-value ≤ 0.0001 ****. ns is not significantly different.

5.3.2 Effects of cell packing on the establishment of polarity induced *de novo*

5.3.2.1 Different cell packing in different regions of the wing does not affect de novo polarity

To investigate the effect of cell packing on polarity induced *de novo*, I quantified polarity establishment in different regions of the wing blade at 28 and 30 hAPF accordingly (Figure 5.5A'-B'). This is because I previously found that the anterior region of the wing is more organised and well-packed as compared to the posterior region of the wing blade (see details in Chapter 3) (Figure 5.5A-B). I activated Fz::EYFP expression in fz^{P21} mutant wing at 22 hAPF with the administration of heat shock and then performed imaging at 28 hAPF and 30 hAPF. Consistently, the anterior wings is more regular and less eccentric as compared to the posterior region of wing (Figure 5.5C-D). Moreover, the tissue appears to be more organised in the anterior region of the wing than the posterior (Figure 5.5E). Remarkably, polarity magnitude is similar in different regions of Fz::EYFP-induced wings despite variability in tissue organisation and cell shapes (Figure 5.5C-F). This suggests that while different cell packing affects pre-existing polarity, it does not affect polarity that is induced *de novo*.

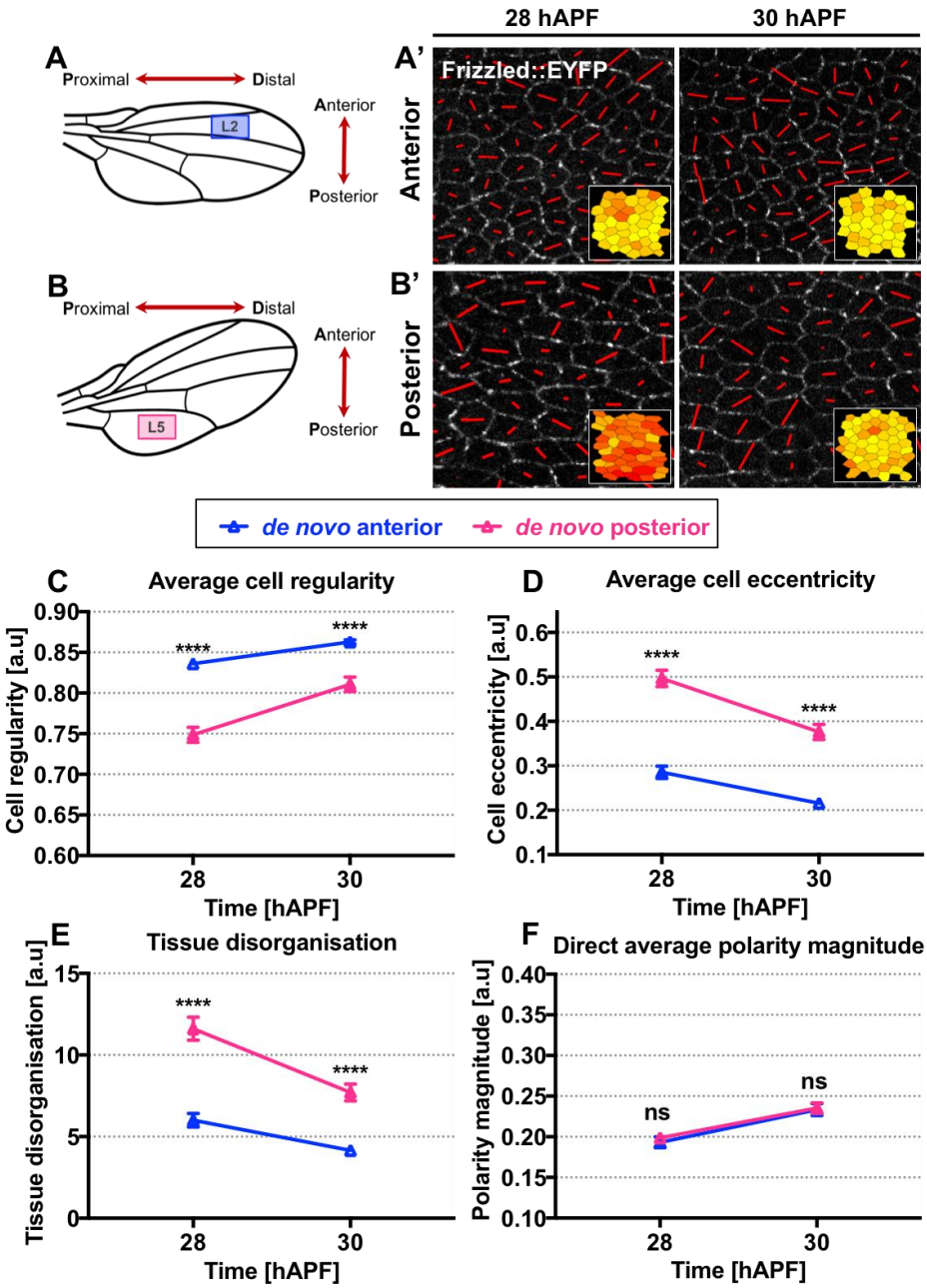

Figure 5.5: Establishment of polarity induced *de novo* is independent of cell shape and tissue organisation

(A) Diagram illustrating the anterior region of pupal wing blade, that lies in between longitudinal vein 2 and longitudinal vein 3, denoted as L2 region.

(A') Confocal images of the anterior region of *de novo* Fz::EYFP-induced wing at 28 and 30 hAPF. The length and orientation of red lines within individual cells represent the magnitude and the axis of Fz::EGFP polarity respectively. Inset image is quantified cell shape regularity of the same wing.

(B) Diagram illustrating the posterior region of pupal wing blade, that lies below longitudinal vein 5, denoted as L5 region.

(B') Confocal images of the posterior region of *de novo* Fz::EYFP-induced wing at 28 and 30 hAPF. Inset image is quantified cell shape regularity of the same wing.

(C) Quantified average cell regularity of *de novo* Fz::EYFP-induced anterior and posterior wings.

(D) Quantified average cell eccentricity of *de novo* Fz::EYFP-induced anterior and posterior wings.

(E) Quantified level of tissue disorganisation of *de novo* Fz::EYFP-induced anterior and posterior wings.

(F) Quantified direct average polarity magnitude of *de novo* Fz::EYFP-induced anterior and posterior wings.

All *de novo* Fz::EYFP-induced wings are fz^{P21} mutant rescued with induction of Fz::EYFP expression at 22 hAPF.

The number of wings for each developmental stage is 8 to 10. Error bar indicates mean$\pm$SEM. One-way ANOVA test, unpaired. Significance levels: p-value ≤ 0.0001****. ns is not significantly different.

5.3.2.2 Acute perturbation on cell packing does not affect de novo polarity

Apart from analysing different regions of the wing, I wished to provide additional evidence that cell packing does not affect polarity induced *de novo*. I carried out parallel vertical lines laser ablation assay to acutely ablate and alter wing epithelial cell packing, shortly after the induction of Fz::EYFP expression in fz^{P21} mutant background at 22 hAPF (Figure 5.6A-A'). I then quantified the changes in establishment of polarity *de novo* at 3- and 5-hour post ablation (Figure 5.6A'). As a control for this, I treated the same genotype to a heat shock but without UV laser ablation and quantified for changes in polarity *de novo* over the same period (Figure 5.6B'). This will not alter cell packing *in vivo* and should further reveal any effects due to heat shock alone.

From the analysis of cell morphology, I found that cells in the ablated wings are less regular and more elongated as compared to the control of non-ablated wings at 3-hour post ablation (Figure 5.6C-D). Not only that, ablated tissue appears to be less organised as compared to the control at 3-hour post ablation, consistent with acute laser ablation results presented in Chapter 4 (Figure 5.6E). As wound heals by 5-hour post ablation, cell shapes and tissue organisation are not significantly different between the ablated and control wings (Figure 5.6C-E). Notably, acutely altering cell packing does not lead to consistent changes in polarity magnitude, as polarity magnitude is similar between the ablated and control wings (Figure 5.6F). Taken together with the results from analysing different regions of the wing (Section 5.3.2.1), it seems that altered cell packing does not affect polarity establishment *de novo*.

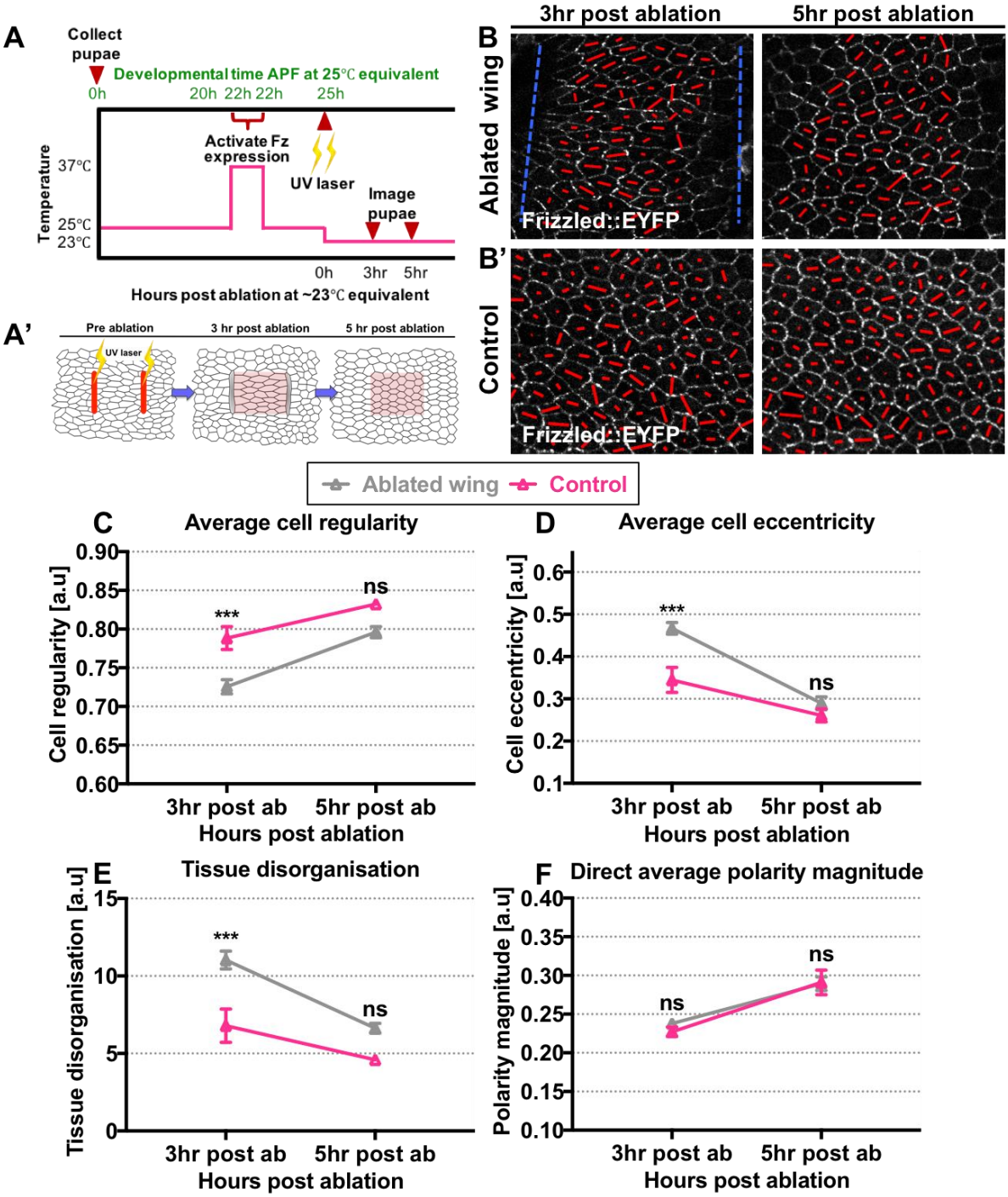

Figure 5.6: Acute perturbation on cell packing does not affect polarity *de novo*

(A) Experimental timeline for laser ablation shortly after *de novo* Fz::EYFP induction. Heat shock at 38°C is applied at 22 hAPF to induce Fz::EYFP expression. Pupae were raised at approximately 23°C post ablation.

(A') Illustration of *Drosophila* pupal wings depicting two vertical lines laser ablation from pre-ablation to 5-hour post ablation.

(B) Individual time frames of an ablated wing expressing Fz::EYFP for 3- and 5-hour post ablations. The wounds are depicted by blue lines.
(B') Individual time frames of a control non-ablated wing expressing Fz::EYFP for 3- and 5-hour post ablations.
(C) Quantified average cell regularity of ablated and control non-ablated wings.
(D) Quantified average cell eccentricity of ablated and control non-ablated wings.
(E) Quantified level of tissue disorganisation of ablated and control non-ablated wings.
(F) Quantified direct average polarity magnitude of ablated and control non-ablated wings.
The number of wings for each developmental stage is 3. Error bar indicates mean$\pm$SEM. One-way ANOVA test, unpaired. Significance levels: p-value ≤ 0.0006 ***. ns is not significantly different.

5.4 Discussion

On the tissue level, my results agree with [Strutt and Strutt, 2002] that Fz activity is required as early as 2 hAPF to completely rescues *fz* mutant phenotype and to achieve PD-oriented polarity across the wing tissue. Notably, experimental analysis on the temporal requirement of core proteins for tissue patterning revealed that transmembrane core proteins such as Fz and Strabismus (Stbm) are required from 6 hAPF onwards to achieve global polarity coordination along the wing PD axis, prior to wing hair formation [Strutt and Strutt, 2002; Strutt and Strutt, 2007]. On the cellular level, my results demonstrated that temporal activation of Fz at different developmental times results in different strength (magnitude) of polarisation. Early Fz activity results in significantly higher average magnitude of polarity as compared to late Fz activity. This suggests that a period of 6 hours post Fz induction is insufficient for core protein to reach its maximum achievable polarisation in the developing pupal wing.

In Chapter 4, I demonstrated that directional cell junctional rearrangement is involved in establishing ordered global polarity alignment along the wing PD axis. Interestingly, activating Fz activity shortly before phase II results in a severe loss of global polarity coordination (swirling phenotype), despite having a subtle defect in cell junctional rearrangement as compared to early Fz induction. This implies that directional cell junctional rearrangement alone, which occurs in phase II (24 to 32 hAPF), may not be adequate to orient polarity induced *de novo* along the wing PD axis. Indeed, [Aigouy et al., 2010] reported that oriented cell division, which occurs in phase I (15 to 24 hAPF), produces tissue shear to reorient polarity towards the wing PD axis.

One of my main goals is to understand the mechanisms by which cell shape and tissue organisation regulate core planar polarisation. In Chapter 4, I demonstrated that there is a linear relationship between tissue organisation and magnitude of polarity, in which more organised tissue results in higher polarity magnitude and vice versa. Interestingly, temporal activation of Fz activity results in similar cell shape and tissue organisation but significantly different magnitude of Fz polarity, in which *de*

novo wings exhibit significantly lower polarity magnitude than pre-existing wings. One explanation for this is that maximum achievable polarity is independent of tissue organisation but rather it is dependent on the timing of Fz activity (in which polarity becomes increasingly stronger the longer Fz is present). Another way of interpreting these results is that strongly polarised tissue is equally as well-organised and packed as compared to weakly polarised tissue. This is consistent with the findings from Chapter 4 where cell packing and tissue organisation are similar in fz^{P21} mutant and wild-type wings. Overall, my findings from the fz^{P21} mutant and temporal activation of Fz support that Fz activity is not required to achieve regular hexagonal cell packing and organised tissue in the developing pupal wing.

On the contrary, the establishment of polarity *de novo* is similar in different regions of the wing despite variability in cell shape and tissue organisation in different regions of the wing blade. I further confirmed this observation using laser ablation assay to acutely alter cell packing upon activation of Fz in fz^{P21} mutant wings. Again, I found out that *de novo* establishment of polarity is similar between altered cell packing and non-altered cell packing. Overall, these findings established that cell packing does not affect the ability of core polarity protein to planar polarise in a *de novo* manner. It would be interesting to examine how altered cell packing and size in *pten* and $dumpy^{ov1}$ mutant tissues affect the establishment of polarity *de novo*.

Why does perturbation on cell packing significantly affects pre-existing polarity to polarise efficiently but not polarity induced *de novo*? One plausible explanation could simply be that early stages of polarisation are insensitive to irregular cell packing as polarity induced *de novo* has not reach maximum polarisation. Alternatively, as mentioned previously, core proteins are constantly being remodelled during cell junctional rearrangement before relaxing into final packing or organisation [Aigouy et al., 2010]. This could reflect a difference in the ability of the cell to redistribute “stable” pre-existing complexes, as opposed to depositing them in a planar polarised pattern *de novo* during cell junctional rearrangement. Using a tandem fluorescence timer as a proxy for protein stability, I provided evidence that pre-existing complexes contains higher relative amount of stable proteins as compared to complexes *de novo*. Hence, I speculated that remodelling of pre-existing polarity upon cell

junctional rearrangement might be obstructed as it might be slower to remodel/repolarise these stable complexes as opposed to establishing polarity complexes *de novo*.

CHAPTER 6

General Discussion

6.1 State of the art: Quantitative image analysis

The *Drosophila* pupal wing is an outstanding model organism to study changes in epithelial cell packing and core planar polarisation due to the precise temporal correlation between these two events during development. Prior to emergence of polarised wing hairs, core planar proteins become increasingly polarised from initially random distributions, as epithelial cells relax into a more isotropic shape, with an increasing fraction of hexagonal cells from initially irregular cells [this work; Classen et al., 2005; Aigouy et al., 2010]. However, the dynamical processes by which planar polarity is established and maintained, as cells change shape and rearrange within the plane of a tissue, remain elusive. More importantly, how different cell geometry or tissue organisation quantitatively accounts for the underlying mechanism of core planar polarisation is a major question in developmental biology.

Most of the *in vivo* live imaging experiments require high-throughput image analysis of cell polarity to ensure large datasets can be analysed robustly and automatically. In this work, I utilised computer algorithms to quantify polarity in an efficient, unbiased manner. Previous planar polarity quantification methods such as Fourier Series and Ratio methods [Aigouy et al., 2010; Strutt et al., 2016] can be sensitive to variations in cell shape, hence making it difficult to uncouple planar polarity from cell shape. I have therefore developed a novel method to quantify planar polarity based on principal component analysis (PCA), which is independent of cell shapes and size. To allow for automated, high-throughput polarity analysis and information storage, I have implemented a standalone and user-friendly graphical software tool called QuantifyPolarity, by incorporating three validated polarity methods. These methods can be used to quantify any two-dimensional asymmetrical distribution of proteins on cell junctions, not limited to core planar polarity studies.

Furthermore, a comprehensive quantitative analysis of epithelial morphogenesis at the cellular and tissue level is required to capture the temporal dynamics of cell shape and tissue organisation over time. Existing methods based on polygonal distribution and cell morphology are insufficient to characterise the degree of tissue

organisation [Zallen and Zallen, 2004; Classen et al., 2005; Blankenship et al., 2006; Farhadifar et al., 2007; Nagpal et al., 2008; Patel et al., 2009; Kram et al., 2010; Mao et al., 2011; Escudero et al., 2011; Gibson et al., 2011; Heller et al., 2016; Sanchez-Gutierrez et al., 2016]. Apart from developing tools for quantification of cell morphological properties, I have also developed a new quantification measure to capture the level of epithelial tissue disorganisation based on the packing density and deviation of the apical area of a group of cells. Essentially, a group of regular and isotropic cells would be able to pack into organised tissue more efficiently as compared to irregular and elongated cells. Indeed, this tissue organisation measure is positively correlated to cell regularity and negatively correlated to cell eccentricity. Additionally, along with the advancement in *in vivo* live imaging, genetics and laser ablation, I have been able to quantitatively investigate the effects of cell shape on core planar polarisation and vice versa.

6.2 Causal relation between cell shape and tissue organisation and core planar polarisation - what is the cause and the effect?

This work primarily sets out to investigate the interplay between cell shape and core planar polarisation. By employing all the quantification tools that I have developed, I first confirmed that the core polarity protein, Frizzled (Fz) becomes increasingly polarised along the proximal-distal (PD) axis of the wing as wing tissue relaxes into a more regular and organised configuration, from 24 hAPF (hour After Puparium Formation) to shortly before wing hair formation at 32 hAPF [Classen et al., 2005; Aigouy et al., 2010]. The precise temporal correlation between polarity and tissue organisation holds true in different regions of the developing pupal wing, specifically the anterior and posterior regions of the wing. Interestingly, the more regular and organised anterior region of the wing exhibits higher polarity as compared to the irregular and disorganised posterior region of the wing. Consequently, two intriguing possibilities that arise are: (1) cell shape or tissue organisation can influence core polarity pathway signalling and/or (2) the core planar polarity pathway can promote better cell shape or tissue organisation.

There are several theories to support the former possibility. Previous studies suggested that cell elongation due to mechanical strain orients the axis of core planar polarity through the polarised alignment of apical microtubules parallel to the axis of cell elongation [Shimada et al., 2006; Aigouy et al., 2010]. Indeed, previous studies in *Drosophila* and in cultured ciliated cells highlighted the importance of polarised microtubules in directional trafficking of vesicular-based core planar polarity components to the junctions lying orthogonal to the axis of cell elongation [Shimada et al., 2006; Harumoto et al., 2010; Vladar et al., 2012; Matis et al., 2014; Chien et al., 2015]. However, quite on the contrary, studies on murine skin reported that core planar proteins polarise on the junctions parallel to the axis of cell elongation, despite microtubules being aligned parallel to the axis of elongation [Aw et al., 2016]. Therefore, the role of microtubules in biasing transport of core polarity proteins to opposite cell junctions remains inconclusive. It would be intriguing to

investigate how cell elongation can affect core planar polarisation. Apart from that, previous work reported that cell apical area plays a role in affecting the core planar polarity system, where core polarity protein fails to restrict prehair initiation to the distal cell junctions in substantially larger cells [Adler et al., 2000]. Therefore, it would be interesting to find out if cell size per se can affect the ability of core proteins to polarise efficiently.

Over the years, there are several controversies regarding the role of core planar polarity in promoting hexagonal cell packing. It was first reported in [Classen et al., 2005] that loss of core polarity proteins results in defective hexagonal packing. In fact, [Classen et al., 2005] demonstrated that loss of Fz results in a subtle but statistically significant defect in hexagonal packing as compared to other core planar polarity protein such as Prickle. Recent work reported that wings in which core planar polarity genes are knocked down exhibit a subtle defect in hexagonal packing late in pupal development [Sugimura and Ishihara, 2013]. Our lab further demonstrated that the core polarity system regulates the endocytosis of E-Cadherin, which might promote junctional rearrangement during pupal wing morphogenesis [Warrington et al., 2013]. One consequence of cell junctional rearrangement is an increase in the fraction of hexagonal cells in the wing epithelium [Sugimura and Ishihara, 2013]. Similarly, in vertebrates, core planar polarity signalling is required to regulate cell rearrangement during gastrulation [Heisenberg et al., 2000; Wallingford et al., 2000; Jessen et al., 2002]. Conversely, [Aw et al., 2016] reported that loss of core planar polarity does not affect the process of cell junctional rearrangement in murine epidermal skin.

Considering that there might be a feedback mechanism between core planar polarisation and cell shape, it might be difficult to solve this cause-and-effect relationship. Nonetheless, to clear up these controversies, I performed a more in-depth quantification on cell shape and tissue organisation in a core polarity mutant background using state of the art quantification tools and *in vivo* live imaging. My results showed that the loss of core polarity protein Fz does not significantly affect the tissue organisation, cell shape and percentage of hexagonal cells from 26 to 32 hAPF of pupal developmental times. One plausible explanation for such a

discrepancy could be due to differences in the experimental methods applied. Previous work was based on dissecting, fixing and mounting of pupal wings [Classen et al., 2005], while my work is based on *in vivo* live imaging of pupal wings which minimises mechanical perturbation on the pupal wings. Additionally, I found no significant difference in hexagonal cell orientation between fz^{P21} mutant and wild-type wings, suggesting that Fz activity is not required in regulating cell junctional rearrangement during pupal wing morphogenesis, in agreement with [Aw et al., 2016].

Moreover, temporal activation of Fz at different pupal wing developmental time results in different strength of polarisation, whereby early Fz activity results in significantly stronger polarised wing tissue as compared to late Fz activity. Notably, tissue organisation, cell shape and percentage of hexagonal cells are not significantly different between strongly polarised and weakly polarised wing tissues. Overall, my data from the fz^{P21} mutant and temporal activation of Fz support the idea that Fz activity is not required to promote regular hexagonal packing and organised tissue in the developing pupal wing. In support of this, it was demonstrated that loss of core polarity function does not disrupt microtubules alignment [Shimada et al., 2006; Harumoto et al., 2010; Matis et al., 2014]. As microtubules alignment is determined by cell shape in *Drosophila* epithelial tissue [Gomez et al., 2016], hence, this indirectly suggest that loss of core planar polarity function does not affect cell shape. Further quantification of cell packing on wings mutant for other core planar polarity proteins (such as Strabismus or Flamingo) should provide a more conclusive verdict.

6.2.1 How do cell shape and tissue organisation affect core planar polarity magnitude?

Having clarified that epithelial cell packing and tissue architecture are independent from the core planar polarity system, I further demonstrated the causality effects of cell packing on core planar polarisation. I first manipulated wing epithelial packing using various genetic methods and laser ablation and then quantified for changes in core planar polarisation. Cells acquire a regular hexagonal order when there is a

uniform distribution of adhesiveness (E-Cadherin) and contractility (actomyosin) on their junctions [Farhadifar et al., 2007]. Hence, one can simply disrupt the formation of hexagonal packing by altering the adhesiveness and contractility properties of a cell. Previous studies have reported the regulation of epithelial cell junctional lengthening by PTEN [Bardet et al., 2013], cell-cell adhesion via Rap1 GTPase [Knox and Brown, 2002] and wing shape due to anisotropic mechanical tension by Dumpy [Etournay et al., 2015]. Knocking down these genes results in very a distinct cell shapes, size and tissue organisation in pupal wings as compared to a regular hexagonal packing in wild-type control wings [this work; Knox and Brown, 2002; Bardet et al., 2013; Ray et al., 2015; Etournay et al., 2015]. One caveat in these genetic manipulation experiments is that it revealed the net long-term effect of altered cell packing on core protein polarisation. There is insufficient temporal knowledge on how core planar polarisation changes in response to acute perturbation on cell packing. Therefore, I used a UV laser to acutely ablate and alter wing epithelial cell packing and quantify for changes in core planar polarity over time. These assays allow us to investigate the effects of altered cell shapes, size and tissue organisation on core planar polarity signalling pathway.

My present findings showed that there is a linear relationship between tissue organisation and magnitude of polarity, independent of different genetic manipulations on cell packing, in which more regular, isotropic shape and organised tissue results in stronger polarity magnitude and vice versa. In support of this, acute perturbation on cell packing results in irregular and disorganised tissue with lower polarity magnitude as compared to non-ablated controls. One plausible explanation is that irregular and disorganised epithelial tissue would pose as a challenge for feedback propagation of polarisation signals across the epithelium. However, since core proteins have been expressed from embryonic stages and polarised since 18 hAPF onwards, these experiments reveal the effect of altered cell packing on the remodelling of pre-existing polarity. I therefore asked a different question: How does altered cell shapes and tissue organisation affect the ability of core proteins to polarise *de novo*?

To investigate the effects of cell packing on *de novo* polarisation of core protein, I activated or induced core protein expression late in pupal development and quantified the changes in polarisation in response to different cell geometries. Interestingly, by examining the establishment of polarity induced *de novo* in different regions of the wing blade with variability in cell packing and ablated wings with disrupted cell packing, my findings showed that cell packing does not affect the ability of core proteins to planar polarise in a *de novo* manner. In addition to that, strength of polarity is dependent on the timing of the core planar polarity activity and is independent of cell shapes and tissue organisation.

I infer that this could reflect a dissimilarity in the ability of the cell to redistribute "stable" pre-existing complexes, as opposed to depositing them in a planar polarised pattern *de novo* during cell junctional rearrangement. Using a tandem fluorescence timer as a proxy for protein stability, I provided evidence that pre-existing complexes contain a higher relative amount of stable proteins as compared to complexes induced *de novo*. Despite the caveats with fluorescence timer analysis as elaborated in Chapter 5, my fluorescence timer result is consistent with previous work which reported that stability of core polarity protein (Fz) is significantly higher in early Dsh induction in *dsh* mutant background as compared to late induction [Warrington et al., 2017]. Additionally, it was demonstrated that Fz is required early in pupal development to be able to cluster and sort itself into stable complexes, which exhibit higher resistance against endocytosis [Strutt and Strutt, 2008; Strutt et al., 2011; Cho et al., 2015].

This implies that defects in core planar polarisation is not a direct consequence of irregular and disorganised cell packing itself but rather reflects the remodelling of pre-existing core polarity complexes in response to tissue deformation. Recent studies suggested that active cell junctional rearrangement in response to tissue deformation requires disassembly and reassembly of pre-existing junctional core polarity complexes [Aw et al., 2016]. Hence, I speculate that this might hinder the core planar polarisation mechanisms upon cell junctional rearrangement as it is slower to remodel these stable complexes as opposed to establishing polarity complexes induced *de novo*. This might explain why perturbation on cell packing

significantly affects the ability of pre-existing complexes to polarise efficiently but not polarity complexes induced *de novo*. Hence, I hypothesise that the rate of polarisation is slower in remodelling of pre-existing polarity as compared to establishment of polarity *de novo*.

As for future work, I will induce remodelling of pre-existing polarity using core polarity protein overexpression assays to test for this hypothesis. Previous studies have demonstrated that core polarity proteins overexpression promotes remodelling and reorientation of polarity orthogonal to the boundary of overexpression [Usui et al., 1999; Strutt et al., 2001; Tree et al., 2002]. However, there is no systematic study has been made of the dynamics of such remodelling. Hence, I will quantify the rate of change of polarity over time during remodelling and compare it to the rate of change of polarity induced *de novo*.

6.2.2 How do cell shape and tissue organisation affect core planar polarity alignment?

As suggested by [Aigouy et al., 2010], the effect of cell elongation on polarity alignment could be attributed to microtubules aligning parallel to the axis of cell elongation. Polarised microtubules have been implicated in directional trafficking of core polarity proteins to the opposite cell junctions [Shimada et al., 2006; Harumoto et al., 2010]. It was suggested that small difference in microtubules asymmetry generates an initial bias of core proteins activity across the PD cell boundary, which is subsequently amplified by a positive feedback loop [Shimada et al., 2006; Harumoto et al., 2010; Matis et al., 2014]. Indeed, I found that cells align their polarity axis parallel to the axis of cell elongation in response to tissue stress anisotropy in wild-type wings, consistent with [Aigouy et al., 2010]. This correlation is true for most of the cases under different genetic manipulations on cell packing. However, this correlation is contradicted by several cases. First, there is a poor correlation between cell polarity alignment and the axis of *pten-rnai* cell elongation at late pupal wing stages. Second, polarity axis in *rap1-rnai* cells does not consistently align with the axis of cell elongation. In fact, previous studies on murine skin reported that epidermal polarity axis aligns perpendicular to the axis of cell

elongation, despite microtubules aligning parallel to the axis of elongation [Aw et al., 2016]. Hence, this raise the possibility that there may exist stronger mechanisms that influence how cells coordinate their polarity axis. Taken together these data, this implies that polarity alignment is not simply a consequence of the axis of cell elongation.

The pioneering work of [Aigouy et al., 2010] has reported that wing-hinge contraction induces simultaneous active tissue remodelling and global core polarity coordination along the PD axis in response to anisotropic mechanical tension. This led me to question the effects of altered epithelial cell packing on global core polarity alignment across the wing tissue. I used circular angle variance to capture the degree of alignment/coordination of polarity between a group of cells. My results revealed that more organised, isotropic and regular wild-type and *dumpy*^{ov1} mutant tissues exhibit a well-coordinated global polarity alignment (lower circular angle variance), while disorganised, elongated and irregular *rap1-rnai* tissue exhibits a loss of global polarity alignment (higher circular angle variance). This, however, is contradicted by better organised, isotropic and more regular *pten-rnai* tissue, that exhibits disrupted global polarity alignment. Additionally, global polarity alignment fails to recover in ablated wings despite having a similar level of tissue organisation, cell regularity and elongation as the non-ablated control wings. I found that there is a lack of correlation between tissue organisation, cell regularity and elongation with global polarity alignment, independent of different genetic manipulations and laser ablation on cell packing. Thus, these data strongly imply that epithelial organisation and cell shape do not influence global polarity alignment, in the sense that more organised tissue with regular and isotropic cell shape do not necessarily result in strong global polarity coordination and vice versa.

It has been proposed that stretch-induced directional cell junctional rearrangement plays a role in coordinating the global polarity alignment [Aigouy et al., 2010; Aw et al., 2016]. During phase II (from 24 to 32 hAPF) of pupal wing morphogenesis, wing cells undergo directional junctional rearrangement (PD-oriented) in response to tissue stretching along the PD axis to balance out intrinsic and extrinsic forces [Aigouy et al., 2010; Sugimura and Ishihara, 2013; Etournay et al., 2015]. The

formation of new PD-oriented junctions and shrinking of AP-oriented junctions increases the fraction of PD-oriented hexagonal cells [this work; Sugimura and Ishihara, 2013]. Because core polarity proteins are persistent on old cell junctions and are slow to form/cluster on new junctions, this biases the cell polarity axis parallel to the newly formed junctions in both *Drosophila* pupal wing [this work; Aigouy et al., 2010] and murine epidermal skin [Aw et al., 2016]. I observed that, as wild-type wing cells relax into more PD-oriented hexagonal packing, polarity axis becomes more globally coordinated along PD axis of the wing tissue [this work; Sugimura and Ishihara, 2013]. In fact, cell junctional rearrangement and global polarity alignment are temporally correlated in different regions of wild-type wings from 24 to 30 hAPF. Moreover, global polarity coordination is not affected in the posterior region of *dumpy*^{ov1} mutant wings with PD-oriented cell junctional rearrangement. Conversely, as observed in wings with defective cell junctional rearrangement such as *pten-rnai*, *rap1-rnai*, central region of *dumpy*^{ov1} mutant and ablated wings, my work revealed that defective junctional rearrangement results in weaker global polarity coordination in these tissues. Notably, there is a striking correlation between cell junctional rearrangement and global polarity alignment for all genotypes at 30 hAPF. Collectively, my work highlights that global polarity alignment is a direct consequence of cell junctional rearrangement.

6.3 Final conclusions

In this thesis, I have developed and validated unique computational tools capable of harnessing the rich content of images in terms of cell morphology, epithelial tissue organisation and planar polarisation. Focusing on the key core protein Fz, the work in this thesis has provided insight into the effects of epithelial cell shapes and tissue organisation on the ability of core planar polarity proteins to polarise efficiently. I have demonstrated how different cell shape and tissue organisation can affect the ability of pre-existing core planar polarity complexes to redistribute, but do not affect the efficiency of core proteins to planar polarise in a *de novo* pattern. Moreover, my findings show that global polarity alignment is a direct consequence of cell junctional rearrangement and is independent of cell elongation, regularity and tissue organisation. On the other hand, my data support the hypothesis that regulation of

cell shapes, hexagonal packing and tissue organisation are independent of Frizzled activity during *Drosophila* pupal wing morphogenesis.

CHAPTER 7

Materials and Methods

7.1 Fly stocks and genetics

All the flies used in this study are described in Table 1 and raised at 25°C, unless otherwise stated. The *fz*^{P21} is a null mutation that produces no detectable protein [Jones et al., 1996].

Temporal expression of Fz::EYFP in the pupal wing was generated using the hs-FLP/FRT system. Fz::EYFP was expressed in a *fz*^{P21} mutant background after excision of the *FRT-STOP-FRT* cassette from *Act>STOP>fz::EYFP* using hs-FLP following 2 hours of heat shock at 37°C at the indicated times [Strutt, 2001]. Previous work from our lab confirmed that pupal development halts for the period of heat shock at 37°C based on time of trichome emergence [Warrington et al., 2017]. Fz::EYFP expression levels driven by *Actin5C* promoter fall within an acceptable physiological range for polarity gene expression as quantified in [Strutt et al., 2011]. Fz::EYFP was expressed at two different developmental time points (2 hAPF and 22 hAPF) and live imaging was carried out at the same developmental time at 28 hAPF.

For all experiments except the temporal induction experiments, white prepupae were collected, rinsed in water and aged at 25°C for 24 hours before dissection and live imaging.

7.2 Dissection and mounting of pupal wings for *in vivo* live imaging

Pupae were dissected and mounted as described in [Classen et al., 2008]. Briefly, pupae were glued in place with a piece of tape. Using a pair of fine scissor and forceps, the puparium case was carefully removed from above the developing pupae to expose the wing without injuring the pupae. The exposed pupae wing was covered in a drop of Halocarbon 700 oil and was then taped onto a 2.5 cm glass-bottomed dish (Iwaki) with the pupae wing facing the coverslip.

7.3 Live imaging of pupal wings

Live imaging was performed using an inverted Nikon A1 confocal microscope with a Nikon 60x apochromatic objective lens oil (NA = 1.4). The pinhole was set to 1.2 Airy Unit (AU). A heated stage was set to 25°C. To maintain constant power for all imaging sessions, laser power was constantly checked and calibrated before each imaging session. For imaging of green and red channels, a 488 nm laser with a 525-550 band pass filter was used to detect EGFP/EYFP/sfGFP and a 561 nm laser with a 550-595 band pass filter was used to detect PH::mCherry/mKate. Images were taken in different regions of the pupal wing with 1024 x 1024 pixels per z-slice and 0.80 nm/pixel. For each wing, 12-bit z-stacks (with ~40 slices per stack, 0.5 μm/slice) were acquired at every 1- to 2-hour interval for approximately 6 hours.

After long-term time-lapse imaging, pupae were kept and survived to at least pharate stage and >95% to eclosion stage, indicating minimal tissue damage during dissection and imaging.

7.4 Image projection and segmentation

Microscopy images were exported into .TIFF format using Nikon software (NIS-Elements AR) for further processing. These z-stack images were automatically surface extracted and projected using PreMosa as described in [Blasse et al., 2017] to obtain a 2D projected image of the apical band of monolayer epithelial tissues. In brief, this algorithm generates an initial height map which contains information of each z-slice with the brightest pixels. To quantify proteins localising on the apical band, Fz::EGFP/Fz::EYFP/Fz::sfGFP z-stack images were used to generate the height map. To yield a smooth and optimise height map, smoothing (with median filter) and artifacts correction processes were carried out [Blasse et al., 2017]. The final height map was used to project the manifold of interest onto a 2D image [Blasse et al., 2017].

In some experiments where there is only PH::mCherry (Plekstrin Homology domain) channel as the cell boundary marker, it is difficult to identify and extract the apical cell junction signals automatically using either ImageJ or PreMosa (Figure 7.1A-B). This is because the PH::mCherry signals appeared on the entire cell junctions (from apical surface to basement membrane). Hence, a manual and user-friendly 2D surface extraction graphical user interface was developed using MATLAB (MathWorks) to manually select of the apical section of each z-slice in the z-stack images (Figure 7.1C-D). A height map, which contains the apical section of each z-slice, is generated based on the selected manifold of interest. Gaussian smoothing is then applied to the height map to smooth out regions between neighbouring slices. In the last step, the final height map, which contains the selected apical coordinates information for each z-slice, is projected onto a 2D image plane. The height map generated from the PH::mCherry channel of a multi-channel input images, can be subsequently reapplied to other channel images.

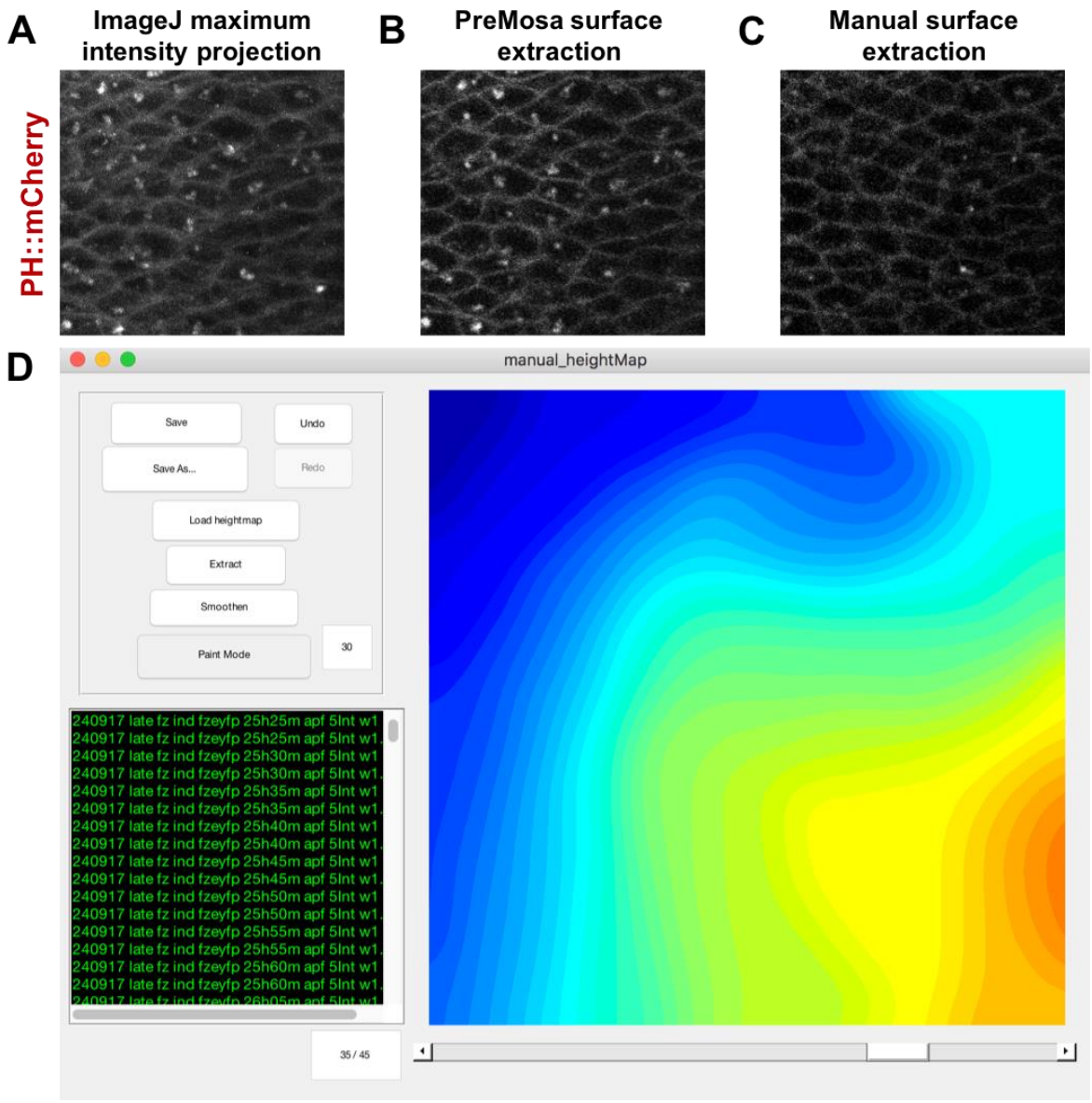

Figure 7.1: A manual surface extraction Graphical User Interface (GUI) was developed to accurately extract the apical band of epithelial cells expressing PH::mCherry

Examples of 2D projected image of epithelial cells expressing PH::mCherry using

(A) Maximum intensity projection in ImageJ.

(B) PreMosa [Blasse et al., 2017].

(C) Manual surface extraction GUI [this work].

(D) A glance of the manual surface extraction GUI layout.

To identify epithelial cell boundaries, the pre-processed image was segmented using a semi-automated cell segmentation software, Packing Analyzer [Aigouy et al., 2010] (see details in Chapter 2). This skeletonised representation of the cell boundaries was used for subsequent image analysis (see details in Chapter 2).

7.5 Laser ablation experiments

Laser ablation experiments were performed in Stephan Grill's laboratory in Technische Universität Dresden (TUD), Germany. Ablations were induced using a custom-built ultraviolet laser ablation system as described in [Grill et al., 2001]. A pulsed laser (355 nm and 1000 Hz) was used for ablation.

Circular ablation was performed with a radius of $60\ \mu m$ in the centre region below longitudinal vein 5 of the pupal wing. 25 consecutives laser pulses were focused on equally spaced points (known as a shot) on the region of interest (ROI), with a density of 2 shots/μm. Cell height (z-depth) was determined manually by tracing PH::mCherry marker from the apical surface to basement membrane of epithelial cells in the z-direction. z-slices with a z-depth of ~15 μm were ablated to achieve 3-dimensional ablation of the circular ROI. As each z-slice is 1 μm apart, this yields approximately 15 z-slices per pupa.

Two parallel vertical lines ablation was carried out in the similar region as circular ablation, with two 60 μm length of parallel lines (separated with a width of 30 μm) oriented perpendicular to the longitudinal vein 5 of the pupal wing. 25 consecutives laser pulses were delivered to the ROI, with a density of 2 shots/μm. z-depth of approximately 15 μm with 1 μm/slice (from apical surface to basement membrane of a single layer epithelium) was ablated to achieve complete ablation.

Subsequent long-term imaging of the ablated and non-ablated control wings were then carried out on an inverted Zeiss LSM 780 AxioObserver confocal microscope with a Zeiss LCI Plan-NeoFluar 63x/1.3 Imm Korr objective lens oil (NA = 1.3). The pinhole was set to 1.3 Airy Unit (AU). Laser power was fine-tuned to achieve

constant power between different imaging sessions. Imaging was carried out at room temperature, ~23°C. For imaging of the green channel, a 488 nm laser with a 490-562 band pass filter was used to detect EGFP/EYFP. Images were taken at the posterior region of the pupal wing with 512 x 512 pixels per z-slice and 1.69 nm/pixel. For each wing, 16-bit z-stacks (with ~40 slices per stack, 0.5 μm/slice) were acquired at every 2-hour interval post ablation for approximately 5 hours.

After long-term time-lapse imaging, pupae were kept and survived to at least pharate stage and >95% to eclosion stage, indicating minimal tissue damage caused by ablation and imaging.

7.6 Fluorescence timer quantification

For quantifying fluorescence intensity of epithelial cell junctions with two different fluorescence channels (sfGFP and mKate) of the same wing, z-stack images were acquired for both channels (with ± 1 slice from the top and bottom of the most in-focus z-slice, 0.5 μm/slice; pixel size of 50 nm; 512 x 512 pixels per z-slice) and z-projection using average intensity (ImageJ) was applied onto the z-stacks to obtain the final image. A cell junction mask was generated from the final image of sfGFP channel using Packing Analyzer [Aigouy et al., 2010]. The segmented mask was subsequently used to measure intensity of pixels in segmented junctions for both channels.

The mean junctional intensity for both fluorescence channels of each wing was determined using a MATLAB script. For live imaging, the measured mean junctional intensities were subtracted from laser off background. The mean junctional intensities were then corrected for distance from the coverslip as previously described in [Strutt et al., 2016]. For computing the relative amount of stable protein, the fluorescence timer ratio was determined by taking the ratio of mKate to sfGFP corrected mean junctional intensities of the given wing for each developmental time [Khmelinskii et al., 2012].

7.7 Circular weighted histogram

To investigate the correlation between cell polarity angle and axis of cell elongation, several parameters were determined on a cell-by-cell basis: (1) magnitude and angle/axis of polarity and (2) magnitude and angle/axis of cell eccentricity (see details in Chapter 2). These parameters were combined from multiple wings and then represented by a circular weighted histogram using MATLAB built-in function (*"polar histogram"*). Data was grouped into 20 bins, with each bin representing a unique polarity angle. The histogram was weighted by the average magnitude of polarity within each bin to capture both the angles and strength of polarity. The length of each bin represents the average magnitude of polarity, meanwhile the orientation of each bin represents the axis of average polarity (labelled in red). After plotting the magnitude and axis of polarity, the magnitude and axis of average cell eccentricity was computed and overlaid on top of the circular weighted histogram (labelled in green), whereby the length and orientation of each bin represents the average magnitude of cell eccentricity and the axis of cell eccentricity respectively.

7.8 Statistics

Quantification measures such as polarity magnitude, cell regularity, cell eccentricity, number of cell sides, hexagonal cell orientation and cell apical area for multiple genotypes were averaged per wing. The resulted data from multiple wings obtained from different pupae (n, number of wings) were compared using an unpaired one-way ANOVA test (GraphPad Prism). If it was statistically significant, a following post hoc test called Tukey-Kramer's multiple comparison was used to compare all genotypes of the same developmental time point within an experiment. In all graphs, error bars are shown as Standard Error of Mean (SEM), unless otherwise mentioned. In some experiments, coefficient of determination test (r^2) was computed to determine how strong the linear relationship was between two variables using GraphPad Prism.

To estimate the number of wings required per genotype for statistical significance, G*Power test (with a power of 0.80 and α of 0.05) was performed using mean polarity magnitude and standard deviation of control wings. A sample size of approximately 6 wings per genotype was determined. However, due to the constraints and complexity of some experiments (for example, in the laser ablation and fluorescence timer experiments), the ideal number of wings was not always obtained.

Table 7.1: List of key resources (experimental models, software and reagent) used

RESOURCE	SOURCE	IDENTIFIER	ASSOCIATED FIGURES
Experimental models: Organisms/Strains			
white (w^{1118})	Bloomington Drosophila Stock Center	FBgn0003996	Fig 2.1 - 2.12; Fig 2.18 - 2.20; All figures in Chapter 3; Fig 4.1 - 4.13
Fz::EGFP	David Strutt [Strutt et al., 2016]	N/A	Fig 2.1 - 2.12; Fig 2.18 - 2.20; All figures in Chapter 3; Fig 4.1 - 4.13
Engrailed-GAL4	Bloomington Drosophila Stock Center	FBal0052377	Fig 4.1 - 4.4; Fig 4.7; Fig 4.11- 4.13
y v; P{y+, v+, UAS-pten-RNAi[JF01859]}attP2	Bloomington Drosophila Stock Center	FBal0219868	Fig 4.1 - 4.2; Fig 4.7; Fig 4.11- 4.13
y v; P{y+, v+, UAS-Rap1-RNAi[HMJ21898]}attP40	Bloomington Drosophila Stock Center	FBal0300407	Fig 4.3 - 4.4; Fig 4.7; Fig 4.11- 4.13
dumpy^{ov1}	Bloomington Drosophila Stock Center	FBal0002834	Fig 4.5 - 4.7; Fig 4.11- 4.13
frizzled (fz^{P21})	Paul Adler [Jones et al., 1996]	FBal0004937	Fig 4.11; Fig 5.1 - 5.3; Fig 5.4 - 5.6
PH::mCherry	Yohanns Bellaïche [Herszterg et al., 2013]	N/A	Fig 4.11; Fig 5.1 - 5.3; Fig 5.5 - 5.6
hs-FLP	Bloomington Drosophila Stock Center	FBst0000006	Fig 5.1 - 5.3; Fig 5.4 - 5.6
Act>STOP>fz::EYFP	David Strutt [Strutt, 2001]	FBal0150490	Fig 5.1 - 5.3; Fig 5.5 - 5.6
Act>STOP>fz::sfGFP-mKate	David Strutt	N/A	Fig 5.4

Software/Graphical User Interfaces			
NIS Elements AR version 4.60	Nikon	N/A	N/A
Packing Analyzer version 8.5 Beta	Suzanne Eaton [Aigouy et al., 2010]	N/A	N/A
ImageJ version 2.0.0	https://fiji.sc	N/A	N/A
MATLAB_R2016b	MathWorks	N/A	N/A
GraphPad Prism version 7.0c	GraphPad software	N/A	N/A
G*Power version 3.1	http://www.gpower.hhu.de	N/A	N/A
QuantifyPolarity v1.0	This work	N/A	N/A
Manual surface extraction	This work	N/A	N/A
Reagent			
Halocarbon 700 oil	Halocarbon products	CAS: 9002-83-9	N/A

Bibliography

ABLEY, K., DE REUILLE, P. B., STRUTT, D., BANGHAM, A., PRUSINKIEWICZ, P., MAREE, A. F., GRIENEISEN, V. A. & COEN, E. 2013. An intracellular partitioning-based framework for tissue cell polarity in plants and animals. *Development,* 140**,** 2061-74.

ADLER, P. N. 1992. The genetic control of tissue polarity in Drosophila. *BioEssays,* 14**,** 735-741.

ADLER, P. N. 2002. Planar signaling and morphogenesis in Drosophila. *Developmental cell,* 2**,** 525-535.

ADLER, P. N. 2012. The frizzled/stan pathway and planar cell polarity in the Drosophila wing. *Current topics in developmental biology.* Elsevier.

ADLER, P. N., VINSON, C., PARK, W. J., CONOVER, S. & KLEIN, L. 1990. Molecular structure of frizzled, a Drosophila tissue polarity gene. *Genetics,* 126**,** 401-416.

ADLER, P. N., ZHU, C. & STONE, D. 2004. Inturned localizes to the proximal side of wing cells under the instruction of upstream planar polarity proteins. *Current Biology,* 14**,** 2046-2051.

ADLER, P. N., KRASNOW, R. E. & LIU, J. 1997. Tissue polarity points from cells that have higher Frizzled levels towards cells that have lower Frizzled levels. *Current Biology,* 7**,** 940-949.

ADLER, P. N., TAYLOR, J. & CHARLTON, J. 2000a. The domineering non-autonomy of frizzled and van Gogh clones in the Drosophila wing is a consequence of a disruption in local signaling. *Mechanisms of development,* 96**,** 197-207.

ADLER, P. N., LIU, J. & CHARLTON, J. 2000b. Cell size and the morphogenesis of wing hairs in Drosophila. *genesis,* 28**,** 82-91.

ADLER, P. N., VINSON, C., PARK, W. J., CONOVER, S. & KLEIN, L. 1990. Molecular structure of frizzled, a Drosophila tissue polarity gene. *Genetics,* 126**,** 401-416.

AIGOUY, B., FARHADIFAR, R., STAPLE, D. B., SAGNER, A., ROPER, J. C., JULICHER, F. & EATON, S. 2010. Cell flow reorients the axis of planar polarity in the wing epithelium of Drosophila. *Cell,* 142**,** 773-86.

AKHSHI, T. K., WERNIKE, D. & PIEKNY, A. 2014. Microtubules and actin crosstalk in cell migration and division. *Cytoskeleton,* 71**,** 1-23.

ALBERTS, B. 2010. Cell biology: the endless frontier. *Molecular biology of the cell,* 21**,** 3785-3785.

AMBERG, D. C. 1998. Three-dimensional imaging of the yeast actin cytoskeleton through the budding cell cycle. *Molecular biology of the cell,* 9**,** 3259-3262.

AMONLIRDVIMAN, K., KHARE, N. A., TREE, D. R., CHEN, W.-S., AXELROD, J. D. & TOMLIN, C. J. 2005. Mathematical modeling of planar cell polarity to understand domineering nonautonomy. *Science,* 307**,** 423-426.

AW, W. Y., HECK, B. W., JOYCE, B. & DEVENPORT, D. 2016. Transient tissue-scale deformation coordinates alignment of planar cell polarity junctions in the mammalian skin. *Current Biology,* 26**,** 2090-2100.

AW, W. Y. & DEVENPORT, D. 2017. Planar cell polarity: global inputs establishing cellular asymmetry. *Current opinion in cell biology,* 44**,** 110-116.

AXELROD, J. D. 2001. Unipolar membrane association of Dishevelled mediates Frizzled planar cell polarity signaling. *Genes & development,* 15**,** 1182-1187.

BAENA-LÓPEZ, L. A., BAONZA, A. & GARCÍA-BELLIDO, A. 2005. The orientation of cell divisions determines the shape of Drosophila organs. *Current Biology,* 15**,** 1640-1644.

BARDET, P.-L., GUIRAO, B., PAOLETTI, C., SERMAN, F., LÉOPOLD, V., BOSVELD, F., GOYA, Y., MIROUSE, V., GRANER, F. & BELLAÏCHE, Y. 2013. PTEN controls junction lengthening and stability during cell rearrangement in epithelial tissue. *Developmental cell,* 25**,** 534-546.

BARRY, J. D., DONÀ, E., GILMOUR, D. & HUBER, W. 2016. TimerQuant: a modelling approach to tandem fluorescent timer design and data interpretation for measuring protein turnover in embryos. *Development,* 143**,** 174-179.

BASTOCK, R., STRUTT, H. & STRUTT, D. 2003. Strabismus is asymmetrically localised and binds to Prickle and Dishevelled during Drosophila planar polarity patterning. *Development,* 130**,** 3007-3014.

BEHRNDT, M., SALBREUX, G., CAMPINHO, P., HAUSCHILD, R., OSWALD, F., ROENSCH, J., GRILL, S. W. & HEISENBERG, C.-P. 2012. Forces driving epithelial spreading in zebrafish gastrulation. *Science,* 338**,** 257-260.

BENKOVÁ, E., MICHNIEWICZ, M., SAUER, M., TEICHMANN, T., SEIFERTOVÁ, D., JÜRGENS, G. & FRIML, J. 2003. Local, efflux-dependent auxin gradients as a common module for plant organ formation. *Cell,* 115**,** 591-602.

BLAIR, S. S. 2007. Wing vein patterning in Drosophila and the analysis of intercellular signaling. *Annu. Rev. Cell Dev. Biol.,* 23**,** 293-319.

BLANCHARD, G. B. & ADAMS, R. J. 2011. Measuring the multi-scale integration of mechanical forces during morphogenesis. *Current opinion in genetics & development,* 21**,** 653-663.

BLANKENSHIP, J. T., BACKOVIC, S. T., SANNY, J. S., WEITZ, O. & ZALLEN, J. A. 2006. Multicellular rosette formation links planar cell polarity to tissue morphogenesis. *Developmental cell,* 11**,** 459-470.

BLASSE, C., SAALFELD, S., ETOURNAY, R., SAGNER, A., EATON, S. & MYERS, E. W. 2017. PreMosa: extracting 2D surfaces from 3D microscopy mosaics. *Bioinformatics,* 33**,** 2563-2569.

BRITTLE, A., THOMAS, C. & STRUTT, D. 2012. Planar polarity specification through asymmetric subcellular localization of Fat and Dachsous. *Current biology,* 22**,** 907-914.

BRITTLE, A. L., REPISO, A., CASAL, J., LAWRENCE, P. A. & STRUTT, D. 2010. Four-jointed modulates growth and planar polarity by reducing the affinity of dachsous for fat. *Current Biology,* 20**,** 803-810.

BRODSKY, M. H. & STELLER, H. 1996. Positional Information along the Dorsal–Ventral Axis of theDrosophilaEye: Graded Expression of thefour-jointedGene. *Developmental biology,* 173**,** 428-446.

BRYANT, D. M. & MOSTOV, K. E. 2008. From cells to organs: building polarized tissue. *Nature reviews Molecular cell biology,* 9**,** 887.

BULGAKOVA, N. A., GRIGORIEV, I., AKHMANOVA, A. & BROWN, N. H. 2013. Dynamic microtubules produce an asymmetric E-cadherin–Bazooka complex to maintain segment boundaries. *J Cell Biol,* 201**,** 887-901.

BURAK, Y. & SHRAIMAN, B. I. 2009. Order and stochastic dynamics in Drosophila planar cell polarity. *PLoS computational biology,* 5**,** e1000628.

BUTLER, L. C., BLANCHARD, G. B., KABLA, A. J., LAWRENCE, N. J., WELCHMAN, D. P., MAHADEVAN, L., ADAMS, R. J. & SANSON, B. 2009. Cell shape changes indicate a role for extrinsic tensile forces in Drosophila germ-band extension. *Nature cell biology,* 11**,** 859.

CAMPANALE, J. P., SUN, T. Y. & MONTELL, D. J. 2017. Development and dynamics of cell polarity at a glance. *J Cell Sci,* 130**,** 1201-1207.

CAMPINHO, P., BEHRNDT, M., RANFT, J., RISLER, T., MINC, N. & HEISENBERG, C.-P. 2013. Tension-oriented cell divisions limit anisotropic tissue tension in epithelial spreading during zebrafish epiboly. *Nature cell biology,* 15**,** 1405.

CASAL, J., STRUHL, G. & LAWRENCE, P. A. 2002. Developmental compartments and planar polarity in Drosophila. *Current Biology,* 12**,** 1189-1198.

CASAL, J., LAWRENCE, P. A. & STRUHL, G. 2006. Two separate molecular systems, Dachsous/Fat and Starry night/Frizzled, act independently to confer planar cell polarity. *Development,* 133**,** 4561-4572.

CHAE, J., KIM, M.-J., GOO, J. H., COLLIER, S., GUBB, D., CHARLTON, J., ADLER, P. N. & PARK, W. J. 1999. The Drosophila tissue polarity gene starry night encodes a member of the protocadherin family. *Development,* 126**,** 5421-5429.

CHALHOUB, N. & BAKER, S. J. 2009. PTEN and the PI3-kinase pathway in cancer. *Annual Review of Pathological Mechanical Disease,* 4**,** 127-150.

CHALMETA, R., HURTADO, F., SACRISTÁN, V. & SAUMELL, M. 2013. Measuring regularity of convex polygons. *Computer-Aided Design,* 45**,** 93-104.

CHEN, W.-S., ANTIC, D., MATIS, M., LOGAN, C. Y., POVELONES, M., ANDERSON, G. A., NUSSE, R. & AXELROD, J. D. 2008. Asymmetric homotypic interactions of the atypical cadherin flamingo mediate intercellular polarity signaling. *Cell,* 133**,** 1093-1105.

CHIEN, Y.-H., KELLER, R., KINTNER, C. & SHOOK, D. R. 2015. Mechanical strain determines the axis of planar polarity in ciliated epithelia. *Current Biology,* 25**,** 2774-2784.

CHO, E. & IRVINE, K. D. 2004. Action of fat, four-jointed, dachsous and dachs in distal-to-proximal wing signaling. *Development,* 131**,** 4489-4500.

CHO, E., FENG, Y., RAUSKOLB, C., MAITRA, S., FEHON, R. & IRVINE, K. D. 2006. Delineation of a Fat tumor suppressor pathway. *Nature genetics,* 38**,** 1142.

CHO, B., PIERRE-LOUIS, G., SAGNER, A., EATON, S. & AXELROD, J. D. 2015. Clustering and negative feedback by endocytosis in planar cell polarity signaling is modulated by ubiquitinylation of prickle. *PLoS genetics,* 11**,** e1005259.

CHU, C.-W. & SOKOL, S. Y. 2016. Wnt proteins can direct planar cell polarity in vertebrate ectoderm. *Elife,* 5**,** e16463.

CLARK, H. F., BRENTRUP, D., SCHNEITZ, K., BIEBER, A., GOODMAN, C. & NOLL, M. 1995. Dachsous encodes a member of the cadherin superfamily that controls imaginal disc morphogenesis in Drosophila. *Genes & development,* 9**,** 1530-1542.

CLASSEN, A.-K., ANDERSON, K. I., MAROIS, E. & EATON, S. 2005. Hexagonal packing of Drosophila wing epithelial cells by the planar cell polarity pathway. *Developmental cell,* 9**,** 805-817.

CLASSEN, A.-K., AIGOUY, B., GIANGRANDE, A. & EATON, S. 2008. Imaging Drosophila pupal wing morphogenesis. *Drosophila.* Springer.

COLLIER, S. & GUBB, D. 1997. Drosophila tissue polarity requires the cell-autonomous activity of the fuzzy gene, which encodes a novel transmembrane protein. *Development,* 124**,** 4029-4037.

COLLIER, S., LEE, H., BURGESS, R. & ADLER, P. 2005. The WD40 repeat protein fritz links cytoskeletal planar polarity to frizzled subcellular localization in the Drosophila epidermis. *Genetics,* 169**,** 2035-2045.

DAHMANN, C., OATES, A. C. & BRAND, M. 2011. Boundary formation and maintenance in tissue development. *Nature Reviews Genetics,* 12**,** 43.

DAS, G., JENNY, A., KLEIN, T. J., EATON, S. & MLODZIK, M. 2004. Diego interacts with Prickle and Strabismus/Van Gogh to localize planar cell polarity complexes. *Development,* 131**,** 4467-4476.

DE LA LOZA, M. D. & THOMPSON, B. 2017. Forces shaping the Drosophila wing. *Mechanisms of development,* 144**,** 23-32.

DE MARCO, P., MERELLO, E., PIATELLI, G., CAMA, A., KIBAR, Z. & CAPRA, V. 2014. Planar cell polarity gene mutations contribute to the etiology of human neural tube defects in our population. *Birth Defects Research Part A: Clinical and Molecular Teratology,* 100**,** 633-641.

DEANS, M. R., ANTIC, D., SUYAMA, K., SCOTT, M. P., AXELROD, J. D. & GOODRICH, L. V. 2007. Asymmetric distribution of prickle-like 2 reveals an early underlying polarization of vestibular sensory epithelia in the inner ear. *Journal of Neuroscience,* 27**,** 3139-3147.

DEVENPORT, D. & FUCHS, E. 2008. Planar polarization in embryonic epidermis orchestrates global asymmetric morphogenesis of hair follicles. *Nature cell biology,* 10**,** 1257.

DRUBIN, D. G. & NELSON, W. J. 1996. Origins of cell polarity. *Cell,* 84**,** 335-344

ESCUDERO, L. M., COSTA, L. D. F., KICHEVA, A., BRISCOE, J., FREEMAN, M. & BABU, M. M. 2011. Epithelial organisation revealed by a network of cellular contacts. *Nature communications,* 2**,** 526.

GAO, B., AJIMA, R., YANG, W., LI, C., SONG, H., ANDERSON, M. J., LIU, R. R., LEWANDOSKI, M. B., YAMAGUCHI, T. P. & YANG, Y. 2018. Coordinated directional outgrowth and pattern formation by integration of Wnt5a and Fgf signaling in planar cell polarity. *Development,* 145**,** dev163824.

GIBSON, W. T., VELDHUIS, J. H., RUBINSTEIN, B., CARTWRIGHT, H. N., PERRIMON, N., BRODLAND, G. W., NAGPAL, R. & GIBSON, M. C. 2011. Control of the mitotic cleavage plane by local epithelial topology. *Cell,* 144**,** 427-438.

GOMEZ, J. M., CHUMAKOVA, L., BULGAKOVA, N. A. & BROWN, N. H. 2016. Microtubule organization is determined by the shape of epithelial cells. *Nature communications,* 7**,** 13172.

GONG, Y., MO, C. & FRASER, S. E. 2004. Planar cell polarity signalling controls cell division orientation during zebrafish gastrulation. *Nature,* 430**,** 689.

GOODRICH, L. V. & STRUTT, D. 2011. Principles of planar polarity in animal development. *Development,* 138**,** 1877-1892.

GRILL, S. W., GOÈNCZY, P., STELZER, E. H. & HYMAN, A. A. 2001. Polarity controls forces governing asymmetric spindle positioning in the Caenorhabditis elegans embryo. *Nature,* 409**,** 630.

GUBB, D. & GARCÍA-BELLIDO, A. 1982. A genetic analysis of the determination of cuticular polarity during development in Drosophila melanogaster. *Development,* 68**,** 37-57.

GUO, N., HAWKINS, C. & NATHANS, J. 2004. Frizzled6 controls hair patterning in mice. *Proceedings of the National Academy of Sciences,* 101**,** 9277-9281.

HALE, R. & STRUTT, D. 2015. Conservation of planar polarity pathway function across the animal kingdom. *Annual review of genetics,* 49**,** 529-551.

HARUMOTO, T., ITO, M., SHIMADA, Y., KOBAYASHI, T. J., UEDA, H. R., LU, B. & UEMURA, T. 2010. Atypical cadherins Dachsous and Fat control

dynamics of noncentrosomal microtubules in planar cell polarity. *Developmental cell,* 19**,** 389-401.

HAZELWOOD, L. D. & HANCOCK, J. M. 2013. Functional modelling of planar cell polarity: an approach for identifying molecular function. *BMC developmental biology,* 13**,** 20.

HEISENBERG, C.-P., TADA, M., RAUCH, G.-J., SAÚDE, L., CONCHA, M. L., GEISLER, R., STEMPLE, D. L., SMITH, J. C. & WILSON, S. W. 2000. Silberblick/Wnt11 mediates convergent extension movements during zebrafish gastrulation. *Nature,* 405**,** 76.

HELLER, D., HOPPE, A., RESTREPO, S., GATTI, L., TOURNIER, A. L., TAPON, N., BASLER, K. & MAO, Y. 2016. EpiTools: an open-source image analysis toolkit for quantifying epithelial growth dynamics. *Developmental cell,* 36**,** 103-116.

HERSZTERG, S., LEIBFRIED, A., BOSVELD, F., MARTIN, C. & BELLAICHE, Y. 2013. Interplay between the dividing cell and its neighbors regulates adherens junction formation during cytokinesis in epithelial tissue. *Developmental cell,* 24**,** 256-270.

HIROKAWA, N., OKADA, Y. & TANAKA, Y. 2009. Fluid dynamic mechanism responsible for breaking the left-right symmetry of the human body: the nodal flow. *Annual Review of Fluid Mechanics,* 41**,** 53-72.

HORVITZ, H. R. & HERSKOWITZ, I. 1992. Mechanisms of asymmetric cell division: two Bs or not two Bs, that is the question. *Cell,* 68**,** 237-255.

IZUMI, Y., HIROSE, T., TAMAI, Y., HIRAI, S.-I., NAGASHIMA, Y., FUJIMOTO, T., TABUSE, Y., KEMPHUES, K. J. & OHNO, S. 1998. An atypical PKC directly associates and colocalizes at the epithelial tight junction with ASIP, a mammalian homologue of Caenorhabditis elegans polarity protein PAR-3. *The Journal of cell biology,* 143**,** 95-106.

JESSEN, J. R., TOPCZEWSKI, J., BINGHAM, S., SEPICH, D. S., MARLOW, F., CHANDRASEKHAR, A. & SOLNICA-KREZEL, L. 2002. Zebrafish trilobite identifies new roles for Strabismus in gastrulation and neuronal movements. *Nature cell biology,* 4**,** 610.

JONES, K. H., LIU, J. & ADLER, P. 1996. Molecular analysis of EMS-induced frizzled mutations in Drosophila melanogaster. *Genetics,* 142**,** 205-215.

KANCA, O., CAUSSINUS, E., DENES, A. S., PERCIVAL-SMITH, A. & AFFOLTER, M. 2014. Raeppli: a whole-tissue labeling tool for live imaging of Drosophila development. *Development,* 141**,** 472-480.

KANG, K. H. & REICHERT, H. 2015. Control of neural stem cell self-renewal and differentiation in Drosophila. *Cell and Tissue Research,* 359**,** 33-45.

KHMELINSKII, A., KELLER, P. J., BARTOSIK, A., MEURER, M., BARRY, J. D., MARDIN, B. R., KAUFMANN, A., TRAUTMANN, S., WACHSMUTH, M. & PEREIRA, G. 2012. Tandem fluorescent protein timers for in vivo analysis of protein dynamics. *Nature biotechnology,* 30**,** 708.

KIBAR, Z., VOGAN, K. J., GROULX, N., JUSTICE, M. J., UNDERHILL, D. A. & GROS, P. 2001. Ltap, a mammalian homolog of Drosophila

Strabismus/Van Gogh, is altered in the mouse neural tube mutant Loop-tail. *Nature genetics,* 28**,** 251.

KLEIN, T. J. & MLODZIK, M. 2005. Planar cell polarization: an emerging model points in the right direction. *Annu. Rev. Cell Dev. Biol.,* 21**,** 155-176.

KNOX, A. L. & BROWN, N. H. 2002. Rap1 GTPase regulation of adherens junction positioning and cell adhesion. *Science,* 295**,** 1285-1288.

KRAM, Y. A., MANTEY, S. & CORBO, J. C. 2010. Avian cone photoreceptors tile the retina as five independent, self-organizing mosaics. *PloS one,* 5**,** e8992.

LAWRENCE, P. & SHELTON, P. 1975. The determination of polarity in the developing insect retina. *Development,* 33**,** 471-486.

LAWRENCE, P. A., CASAL, J. & STRUHL, G. 2002. Towards a model of the organisation of planar polarity and pattern in the Drosophila abdomen. *Development,* 129**,** 2749-2760.

LAWRENCE, P. A., CASAL, J. & STRUHL, G. 2004. Cell interactions and planar polarity in the abdominal epidermis of Drosophila. *Development,* 131**,** 4651-4664.

LE GARREC, J. F., LOPEZ, P. & KERSZBERG, M. 2006. Establishment and maintenance of planar epithelial cell polarity by asymmetric cadherin bridges: a computer model. *Developmental dynamics: an official publication of the American Association of Anatomists,* 235**,** 235-246.

LECUIT, T. & LE GOFF, L. 2007. Orchestrating size and shape during morphogenesis. *Nature,* 450**,** 189.

LEE, H. & ADLER, P. N. 2002. The function of the frizzled pathway in the Drosophila wing is dependent on inturned and fuzzy. *Genetics,* 160**,** 1535-1547.

LOGAN, C. Y. & NUSSE, R. 2004. The Wnt signaling pathway in development and disease. *Annu. Rev. Cell Dev. Biol.,* 20**,** 781-810.

LYE, C. M., BLANCHARD, G. B., NAYLOR, H. W., MURESAN, L., HUISKEN, J., ADAMS, R. J. & SANSON, B. 2015. Mechanical coupling between endoderm invagination and axis extension in Drosophila. *PLoS biology,* 13**,** e1002292.

MA, D., YANG, C.-H., MCNEILL, H., SIMON, M. A. & AXELROD, J. D. 2003. Fidelity in planar cell polarity signalling. *Nature,* 421**,** 543.

MA, D., AMONLIRDVIMAN, K., RAFFARD, R. L., ABATE, A., TOMLIN, C. J. & AXELROD, J. D. 2008. Cell packing influences planar cell polarity signaling. *Proceedings of the National Academy of Sciences,* 105**,** 18800-18805.

MAHONEY, P. A., WEBER, U., ONOFRECHUK, P., BIESSMANN, H., BRYANT, P. J. & GOODMAN, C. S. 1991. The fat tumor suppressor gene in Drosophila encodes a novel member of the cadherin gene superfamily. *Cell,* 67**,** 853-868.

MAO, Y., RAUSKOLB, C., CHO, E., HU, W.-L., HAYTER, H., MINIHAN, G., KATZ, F. N. & IRVINE, K. D. 2006. Dachs: an unconventional myosin

that functions downstream of Fat to regulate growth, affinity and gene expression in Drosophila. *Development,* 133**,** 2539-2551.

MAO, Y., TOURNIER, A. L., BATES, P. A., GALE, J. E., TAPON, N. & THOMPSON, B. J. 2011. Planar polarization of the atypical myosin Dachs orients cell divisions in Drosophila. *Genes & development,* 25**,** 131-136.

MATAKATSU, H. & BLAIR, S. S. 2006. Separating the adhesive and signaling functions of the Fat and Dachsous protocadherins. *Development,* 133**,** 2315-2324.

MATIS, M., RUSSLER-GERMAIN, D. A., HU, Q., TOMLIN, C. J. & AXELROD, J. D. 2014. Microtubules provide directional information for core PCP function. *Elife,* 3**,** e02893.

MERKEL, M., SAGNER, A., GRUBER, F. S., ETOURNAY, R., BLASSE, C., MYERS, E., EATON, S. & JÜLICHER, F. 2014. The balance of prickle/spiny-legs isoforms controls the amount of coupling between core and fat PCP systems. *Current Biology,* 24**,** 2111-2123.

MERTE, J., JENSEN, D., WRIGHT, K., SARSFIELD, S., WANG, Y., SCHEKMAN, R. & GINTY, D. D. 2010. Sec24b selectively sorts Vangl2 to regulate planar cell polarity during neural tube closure. *Nature cell biology,* 12**,** 41.

MONTCOUQUIOL, M., SANS, N., HUSS, D., KACH, J., DICKMAN, J. D., FORGE, A., RACHEL, R. A., COPELAND, N. G., JENKINS, N. A. & BOGANI, D. 2006. Asymmetric localization of Vangl2 and Fz3 indicate novel mechanisms for planar cell polarity in mammals. *Journal of Neuroscience,* 26**,** 5265-5275.

NAGPAL, R., PATEL, A. & GIBSON, M. C. 2008. Epithelial topology. *BioEssays,* 30**,** 260-266.

NIKOLOPOULOU, E., GALEA, G. L., ROLO, A., GREENE, N. D. & COPP, A. J. 2017. Neural tube closure: cellular, molecular and biomechanical mechanisms. *Development,* 144**,** 552-566.

PATEL, A. B., GIBSON, W. T., GIBSON, M. C. & NAGPAL, R. 2009. Modeling and inferring cleavage patterns in proliferating epithelia. *PLoS computational biology,* 5**,** e1000412.

PARK, W. J., LIU, J., SHARP, E. J. & ADLER, P. N. 1996. The Drosophila tissue polarity gene inturned acts cell autonomously and encodes a novel protein. *Development,* 122**,** 961-969.

PENG, Y. & AXELROD, J. D. 2012. Asymmetric protein localization in planar cell polarity: mechanisms, puzzles, and challenges. *Current topics in developmental biology.* Elsevier.

QIAO, X., LIU, Y., LI, P., CHEN, Z., LI, H., YANG, X., FINNELL, R. H., YANG, Z., ZHANG, T. & QIAO, B. 2016. Genetic analysis of rare coding mutations of CELSR1–3 in congenital heart and neural tube defects in Chinese people. *Clinical Science,* 130**,** 2329-2340.

RAWLS, A. S. & WOLFF, T. 2003. Strabismus requires Flamingo and Prickle function to regulate tissue polarity in the Drosophila eye. *Development,* 130**,** 1877-1887.

RAY, R. P., MATAMORO-VIDAL, A., RIBEIRO, P. S., TAPON, N., HOULE, D., SALAZAR-CIUDAD, I. & THOMPSON, B. J. 2015. Patterned anchorage to the apical extracellular matrix defines tissue shape in the developing appendages of Drosophila. *Developmental cell,* 34**,** 310-322.

SAGNER, A., MERKEL, M., AIGOUY, B., GAEBEL, J., BRANKATSCHK, M., JÜLICHER, F. & EATON, S. 2012. Establishment of global patterns of planar polarity during growth of the Drosophila wing epithelium. *Current Biology,* 22**,** 1296-1301.

SANCHEZ-GUTIERREZ, D., TOZLUOGLU, M., BARRY, J. D., PASCUAL, A., MAO, Y. & ESCUDERO, L. M. 2016. Fundamental physical cellular constraints drive self-organization of tissues. *EMBO J,* 35**,** 77-88.

SHCHERBO, D., MURPHY, C. S., ERMAKOVA, G. V., SOLOVIEVA, E. A., CHEPURNYKH, T. V., SHCHEGLOV, A. S., VERKHUSHA, V. V., PLETNEV, V. Z., HAZELWOOD, K. L. & ROCHE, P. M. 2009. Far-red fluorescent tags for protein imaging in living tissues. *Biochemical journal,* 418**,** 567-574.

SÉGALEN, M., JOHNSTON, C. A., MARTIN, C. A., DUMORTIER, J. G., PREHODA, K. E., DAVID, N. B., DOE, C. Q. & BELLAÏCHE, Y. 2010. The Fz-Dsh planar cell polarity pathway induces oriented cell division via Mud/NuMA in Drosophila and zebrafish. *Developmental cell,* 19**,** 740-752.

SHIMADA, Y., USUI, T., YANAGAWA, S.-I., TAKEICHI, M. & UEMURA, T. 2001. Asymmetric colocalization of Flamingo, a seven-pass transmembrane cadherin, and Dishevelled in planar cell polarization. *Current Biology,* 11**,** 859-863.

SHIMADA, Y., YONEMURA, S., OHKURA, H., STRUTT, D. & UEMURA, T. 2006. Polarized transport of Frizzled along the planar microtubule arrays in Drosophila wing epithelium. *Developmental cell,* 10**,** 209-222.

SIENKNECHT, U. J. 2015. Current concepts of hair cell differentiation and planar cell polarity in inner ear sensory organs. *Cell and tissue research,* 361**,** 25-32.

SIMON, M. A., XU, A., ISHIKAWA, H. O. & IRVINE, K. D. 2010. Modulation of fat: dachsous binding by the cadherin domain kinase four-jointed. *Current Biology,* 20**,** 811-817.

SONG, H., HU, J., CHEN, W., ELLIOTT, G., ANDRE, P., GAO, B. & YANG, Y. 2010. Planar cell polarity breaks bilateral symmetry by controlling ciliary positioning. *Nature,* 466**,** 378.

STRUTT, D. & STRUTT, H. 2007. Differential activities of the core planar polarity proteins during Drosophila wing patterning. *Developmental biology,* 302**,** 181-194.

STRUTT, D. I. 2001. Asymmetric localization of frizzled and the establishment of cell polarity in the Drosophila wing. *Molecular cell,* 7**,** 367-375.

STRUTT, D. I., WEBER, U. & MLODZIK, M. 1997. The role of RhoA in tissue polarity and Frizzled signalling. *Nature,* 387**,** 292.

STRUTT, H., GAMAGE, J. & STRUTT, D. 2016. Robust asymmetric localization of planar polarity proteins is associated with organization into signalosome-like domains of variable stoichiometry. *Cell reports,* 17**,** 2660-2671.

STRUTT, H. & STRUTT, D. 2002. Nonautonomous planar polarity patterning in Drosophila: dishevelled-independent functions of frizzled. *Developmental cell,* 3**,** 851-863.

STRUTT, H. & STRUTT, D. 2008. Differential stability of flamingo protein complexes underlies the establishment of planar polarity. *Current Biology,* 18**,** 1555-1564.

STRUTT, H., WARRINGTON, S. J. & STRUTT, D. 2011. Dynamics of core planar polarity protein turnover and stable assembly into discrete membrane subdomains. *Developmental cell,* 20**,** 511-525.

SUGIMURA, K. & ISHIHARA, S. 2013. The mechanical anisotropy in a tissue promotes ordering in hexagonal cell packing. *Development,* 140**,** 4091-4101.

TAYLOR, J., ABRAMOVA, N., CHARLTON, J. & ADLER, P. N. 1998. Van Gogh: a new Drosophila tissue polarity gene. *Genetics,* 150**,** 199-210.

TAYLOR, J. & ADLER, P. N. 2008. Cell rearrangement and cell division during the tissue level morphogenesis of evaginating Drosophila imaginal discs. *Developmental biology,* 313**,** 739-751.

TETLEY, R. J., BLANCHARD, G. B., FLETCHER, A. G., ADAMS, R. J. & SANSON, B. 2016. Unipolar distributions of junctional Myosin II identify cell stripe boundaries that drive cell intercalation throughout Drosophila axis extension. *Elife,* 5**,** e12094.

TISSIR, F. & GOFFINET, A. M. 2013. Shaping the nervous system: role of the core planar cell polarity genes. *Nature reviews Neuroscience,* 14**,** 525.

TISSIR, F., QU, Y., MONTCOUQUIOL, M., ZHOU, L., KOMATSU, K., SHI, D., FUJIMORI, T., LABEAU, J., TYTECA, D. & COURTOY, P. 2010. Lack of cadherins Celsr2 and Celsr3 impairs ependymal ciliogenesis, leading to fatal hydrocephalus. *Nature neuroscience,* 13**,** 700.

TREE, D. R., SHULMAN, J. M., ROUSSET, R., SCOTT, M. P., GUBB, D. & AXELROD, J. D. 2002. Prickle mediates feedback amplification to generate asymmetric planar cell polarity signaling. *Cell,* 109**,** 371-381.

USUI, T., SHIMA, Y., SHIMADA, Y., HIRANO, S., BURGESS, R. W., SCHWARZ, T. L., TAKEICHI, M. & UEMURA, T. 1999. Flamingo, a seven-pass transmembrane cadherin, regulates planar cell polarity under the control of Frizzled. *Cell,* 98**,** 585-595.

VILLANO, J. L. & KATZ, F. N. 1995. four-jointed is required for intermediate growth in the proximal-distal axis in Drosophila. *Development,* 121**,** 2767-2777

VINSON, C. R. & ADLER, P. N. 1987. Directional non-cell autonomy and the transmission of polarity information by the frizzled gene of Drosophila. *Nature,* 329**,** 549.

VLADAR, E. K., ANTIC, D. & AXELROD, J. D. 2009. Planar cell polarity signaling: the developing cell's compass. *Cold Spring Harbor perspectives in biology,* 1**,** a002964.

VLADAR, E. K., BAYLY, R. D., SANGORAM, A. M., SCOTT, M. P. & AXELROD, J. D. 2012. Microtubules enable the planar cell polarity of airway cilia. *Current Biology,* 22**,** 2203-2212.

WALLINGFORD, J. B. 2012. Planar cell polarity and the developmental control of cell behavior in vertebrate embryos. *Annual review of cell and developmental biology,* 28**,** 627-653.

WALLINGFORD, J. B., ROWNING, B. A., VOGELI, K. M., ROTHBÄCHER, U., FRASER, S. E. & HARLAND, R. M. 2000. Dishevelled controls cell polarity during Xenopus gastrulation. *Nature,* 405**,** 81.

WADDINGTON, C. H. 1939. *An introduction to modern genetics*, George Allen And Unwin Ltd Museum Street; London.

WADDINGTON, C. H. 1940. The genetic control of wing development inDrosophila. *Journal of Genetics,* 41**,** 75-113.

WARRINGTON, S. J., STRUTT, H., FISHER, K. H. & STRUTT, D. 2017. A Dual Function for Prickle in Regulating Frizzled Stability during Feedback-Dependent Amplification of Planar Polarity. *Current Biology,* 27**,** 2784-2797. e3.

WANG, L., XIAO, Y., TIAN, T., JIN, L., LEI, Y., FINNELL, R. H. & REN, A. 2018. Digenic variants of planar cell polarity genes in human neural tube defect patients. *Molecular genetics and metabolism,* 124**,** 94-100.

WEIGMANN, K., KLAPPER, R., STRASSER, T., RICKERT, C., TECHNAU, G., JÄCKLE, H., JANNING, W. & KLÄMBT, C. 2003. FlyMove–a new way to look at development of Drosophila. *Trends in Genetics,* 19**,** 310-311.

WILLIAMS, M. L. & SOLNICA-KREZEL, L. 2017. Regulation of gastrulation movements by emergent cell and tissue interactions. *Current opinion in cell biology,* 48**,** 33-39.

WINTER, C. G., WANG, B., BALLEW, A., ROYOU, A., KARESS, R., AXELROD, J. D. & LUO, L. 2001. Drosophila Rho-associated kinase (Drok) links Frizzled-mediated planar cell polarity signaling to the actin cytoskeleton. *Cell,* 105**,** 81-91.

WONG, L. L. & ADLER, P. N. 1993. Tissue polarity genes of Drosophila regulate the subcellular location for prehair initiation in pupal wing cells. *The Journal of cell biology,* 123**,** 209-221.

WOOTTON, R. J. 1992. Functional morphology of insect wings. *Annual review of entomology,* 37**,** 113-140.

WU, J. & MLODZIK, M. 2008. The frizzled extracellular domain is a ligand for Van Gogh/Stbm during nonautonomous planar cell polarity signaling. *Developmental cell,* 15**,** 462-469.

YAN, J., HUEN, D., MORELY, T., JOHNSON, G., GUBB, D., ROOTE, J. & ADLER, P. N. 2008. The multiple-wing-hairs gene encodes a novel GBD–FH3 domain-containing protein that functions both prior to and after wing hair initiation. *Genetics,* 180**,** 219-228.

YANG, C.-H., AXELROD, J. D. & SIMON, M. A. 2002. Regulation of Frizzled by fat-like cadherins during planar polarity signaling in the Drosophila compound eye. *Cell,* 108**,** 675-688.

YATES, L. L., SCHNATWINKEL, C., MURDOCH, J. N., BOGANI, D., FORMSTONE, C. J., TOWNSEND, S., GREENFIELD, A., NISWANDER, L. A. & DEAN, C. H. 2010. The PCP genes Celsr1 and Vangl2 are required for normal lung branching morphogenesis. *Human molecular genetics,* 19**,** 2251-2267.

YOUNG, C. Y. 2010. *Precalculus*, John Wiley & Sons.

ZALLEN, J. A. 2007. Planar polarity and tissue morphogenesis. *Cell,* 129**,** 1051-1063.

ZALLEN, J. A. & ZALLEN, R. 2004. Cell-pattern disordering during convergent extension in Drosophila. *Journal of Physics: Condensed Matter,* 16**,** S5073.

Appendix

9.1 QuantifyPolarity 1.0 User Manual

by Sara Tan Su Ee (saratansuee@gmail.com)

Many thanks to Professor David Strutt, Dr. Katherine Fisher and Tan Weijie for the Ratio method and Fourier Series algorithms.

This is an agreement between you, the user, and QuantifyPolarity. By downloading, installing or using this software, you are agreeing to comply to the terms and conditions of this agreement.

The following rights and restrictions apply to you under this agreement:

(a) You may not sell or transfer the software in whole or in part to a third party
(b) You may not decompile, modify or disassemble the software product
(c) This software is distributed is for free and provided to you as a free service
(d) You are solely responsible to verify that the data generated by the software is correct for your application

Please read the license of MathWorks used by QuantifyPolarity.

QuantifyPolarity will be publicly available as a free software package accessible for the scientific community once published.

9.1.1 Introduction

Welcome to the QuantifyPolarity User Manual. QuantifyPolarity, is a free software, capable of quantifying planar polarity in epithelia using comprehensive mathematical formulas. QuantifyPolarity provides image visualisation and planar polarity quantification services to students, scientists and other professional establishments around the world.

This user manual provides a thorough explanation about QuantifyPolarity from its functionalities and features to a complete step-by-step walkthrough about its use.

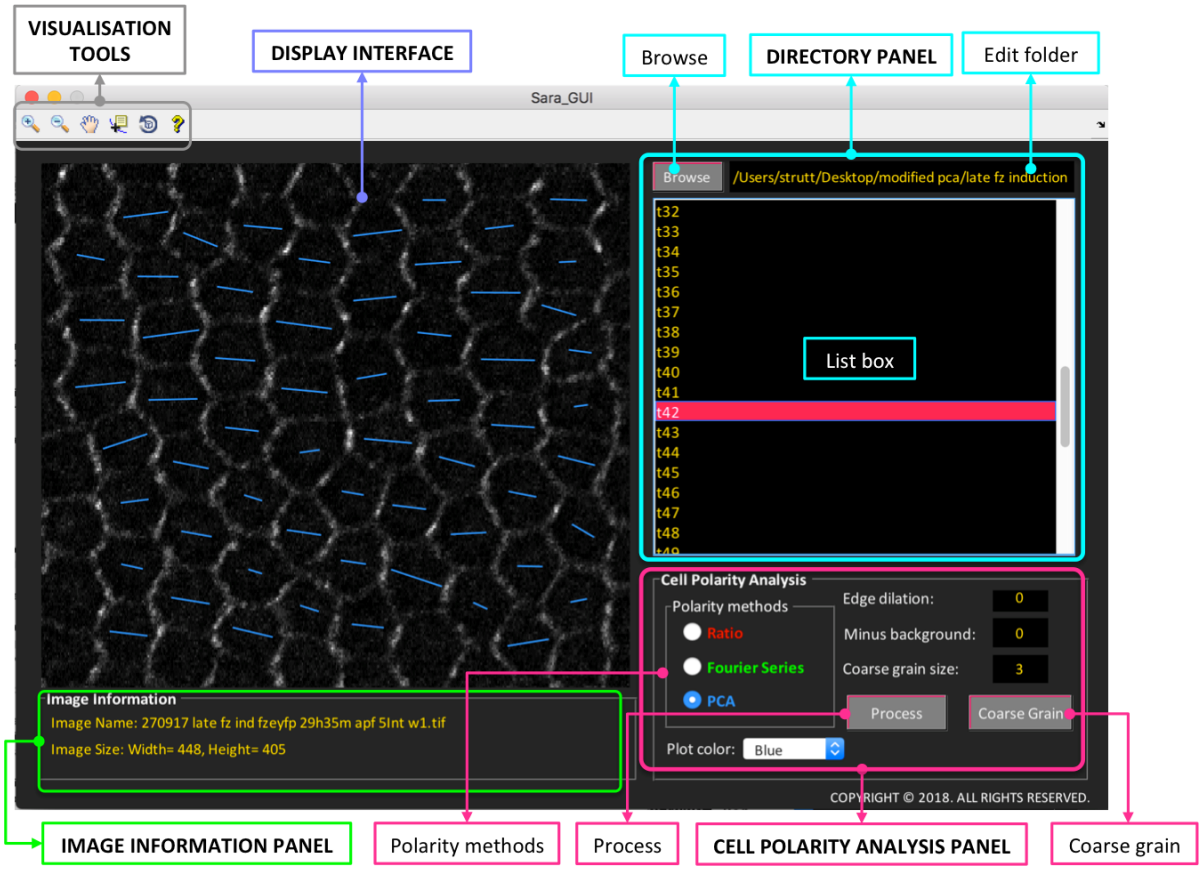

Figure 9.1: QuantifyPolarity Graphical User Interface at a Glance

Table 9.1: List of key panels with its components and functionalities

Panels	Components	Functions
Directory	Browse	Browse for folder
	Edit folder	Manually enter the folder path
	List box	• Contain list of files from current folder • Double-click: Select image *(TIF, JPG and PNG)* for display or open Microsoft Excel file *(XLSX, XLS and CSV).* • Right-click: Open the folder containing selected file
Cell Polarity Analysis	Polarity methods	Select one of the three polarity methods (Ratio, Fourier Series and Principal Component Analysis) that are suitable for your own application. Default polarity method is Fourier Series
	Plot color	To allow user to select desired colour for polarity plotting.
	Edge dilation	To dilate the segmented cell edges
	Minus background	Input image background intensity for background subtraction
	Process	To execute cell-by-cell polarity measurement on selected image/folder
	Coarse grain size	Input the size of coarse-grain analysis. For example, input of value of 3

	Coarse grain	To execute cell-by-cell polarity measurement on selected image/folder
Image Information	Image name	Display current image file name
	Image size	Display the width and height of current image
Display Interface	Plot axis	Display current selected image from "List box"
Visualisation tools	Image visualisation tools	Zoom in, Zoom out, Pan image, Data cursor and Rotate 3D

9.1.2 Getting started

Before getting started, user can perform image segmentation of fixed immunostained epithelia or image sequences of living samples expressing fluorescently tagged proteins using PackingAnalyzer, ImageJ Segmentation plugins or other image segmentation software.

Please note that it is important to ensure that the segmented mask (save as "*handCorrection.png*" or *"handCorrection.tif"*) is stored in a folder with the same name as the image as illustrated in Figure 9.2. QuantifyPolarity will only supports binary (consists of 0 and 1) segmented mask images.

Figure 9.2: Example of file arrangement for a single image and its segmentation mask

Input data:

- QuantifyPolarity supports monochrome or RGB images
- QuantifyPolarity supports images with the following file formats – *TIF, JPG,* and *PNG*
- QuantifyPolarity is capable of quantifying planar polarity of 2-dimensional images
- QuantifyPolarity does not support multiTIFF or stacked images

In general, quantification of planar polarity can be done at cellular (cell-by-cell polarity) and tissue (coarse-grain/global polarity) scales. Cell-by-cell polarity measures the strength/magnitude and angle of polarisation of individual cell (Figure 9.3A). Coarse-grain polarity, on other hand, reflects both the strength and coordination of polarity within a group of cells (Figure 9.3B). Both measures provide a readout of magnitude and angle of polarity.

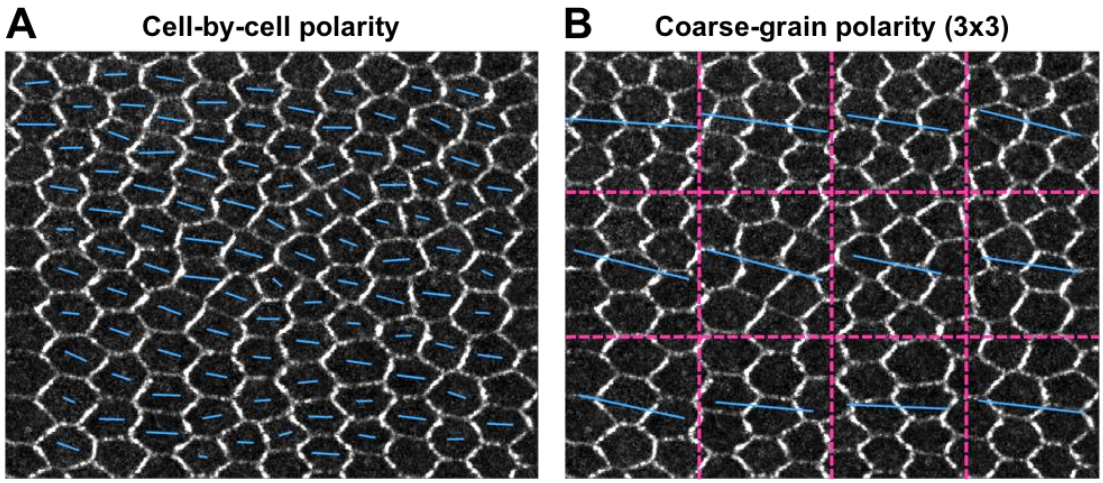

Figure 9.3: Cell-by-cell polarity vs Coarse-grain polarity quantification

(A) Cellular scale polarity pattern of *Drosophila* pupal wing expressing Fz::EGFP. The length and orientation of blue bars represent the polarity magnitude and angle for a given cell respectively.

(B) Coarse-grain polarity pattern of the same image in (A). Image is divided into 3x3 group of cells with equal square grids (represented with dotted magenta lines) where the vector average polarity for each group of cells is computed. The length and orientation of blue bars represent the polarity magnitude and angle for a given group of cells respectively.

(A) For cell-by-cell polarity quantification

i) Browse for folder of interest by clicking “Browse” button or manually entering full directory path in the “Edit folder” text box. List of current files in the selected folder will be shown in the “List box” (Figure 9.4).

ii) Double-click to select a representative image from the “List box”. If an image cannot be open/read, it will not appear in the “Display Interface”. The displayed image will be used for further planar polarity quantification.

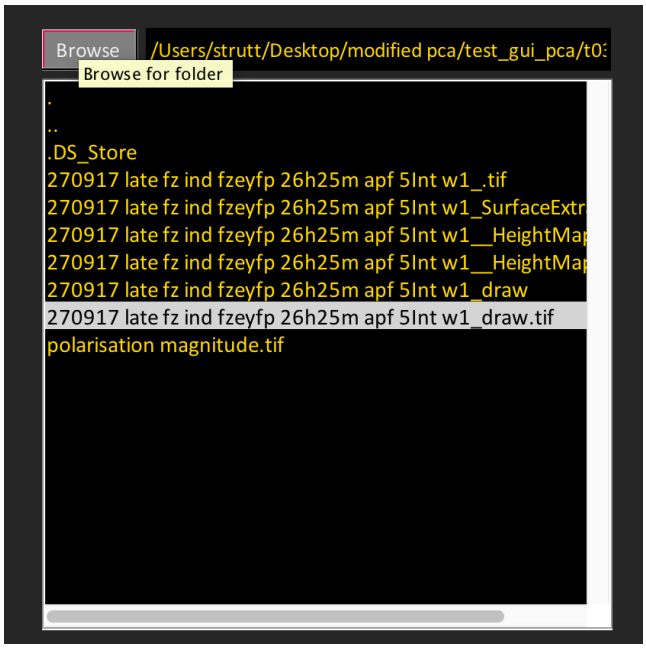

Figure 9.4: Folder and image selection

iii) Select one of the three polarity methods from “Polarity Methods” panel by ticking the button (Figure 9.5). Default polarity method is Fourier Series. User may select desired plotting colour from “Plot Color” dropdown menu. Default plotting colour is **red** for Ratio method, **green** for Fourier Series and **blue** for PCA.

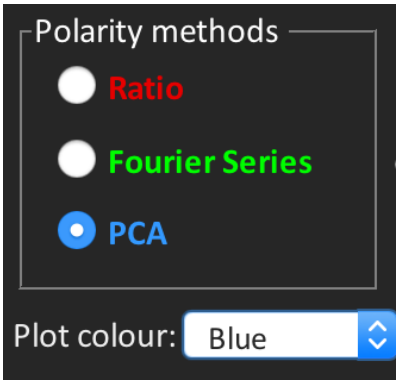

Figure 9.5: Three different polarity methods for planar polarity quantification

iv) Define the size of edge dilation and image background intensity. The input number must be a positive integer. Default values are 0.

v) Press the “Process” button for cell-by-cell polarity measurement.

vi) Option 1: To perform polarity analysis on:

   a. Single image – allow user to quantify polarity on single image
   b. Entire folder – allow user to quantify polarity on multiple images in the same folder as demonstrated in Figure 9.6

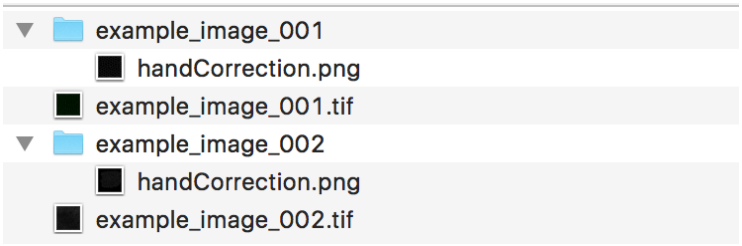

Figure 9.6: Example of files arrangement for “Entire folder” processing

vii) Option 2: To define the region of interest (ROI) for polarity analysis:

   a. Yes – allow user to manually draw a ROI on the image. Double click inside the box to confirm the selection (Figure 9.7). The ROI coordinates are automatically stored in “*crop_region.txt*”
   b. No – analyse polarity on the whole image
   c. Use existing ROI – allow user to use existing ROI coordinates

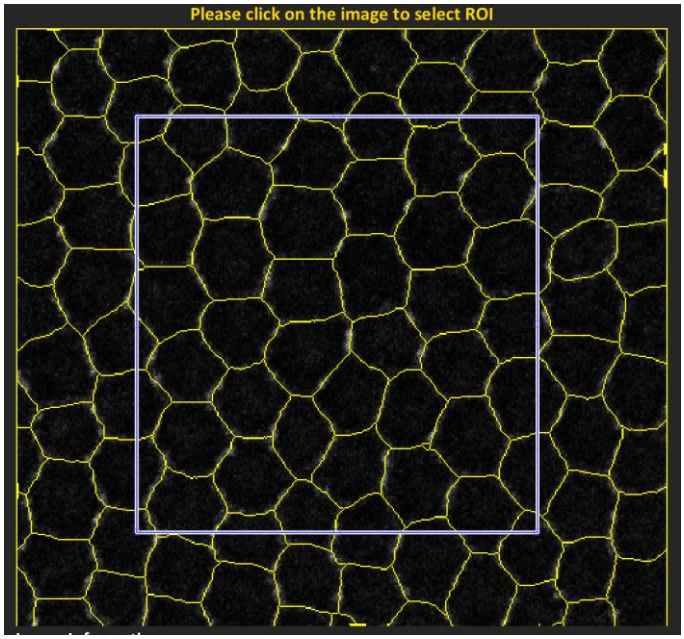

Figure 9.7: Image cropping allow user to select a ROI for polarity analysis

viii) All results are then automatically stored in the folder once processing is completed (Figure 9.8).

	A	B
1	Fourier Series magnitude	Fourier Series angle
2	0.31453	-57.695
3	0.3474	46.3223
4	0.32789	-52.9548
5	0.36455	69.7273
6	0.19094	-78.0782
7	0.68486	64.943

Figure 9.8: Example of output data stored as .CSV file

Polarity magnitude (in arbitrary unit [a.u]) and polarity angle (ranges from $-\mathbf{90}°$ to $+\mathbf{90}°$)

(B) For coarse-grain (global) polarity quantification

i) Repeat steps (i) to (iv) from (A).

ii) Next, input the size of coarse grain ranging from 1 to total number of cells. For e.g., for coarse grain size of n, it will compute a coarse polarity for a total of n x n cells. The input number must be a positive integer. Default value is 3 (Figure 9.9).

iii) Press the “Coarse Grain” button for coarse-grain polarity quantification.

iv) Repeat steps (vi) to (viii) from (A).

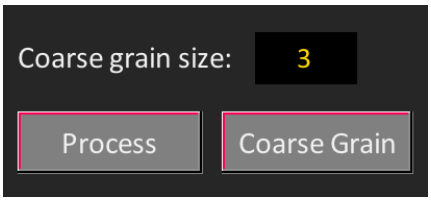

Figure 9.9: Coarse-grain polarity quantification

Input the desired coarse grain size for and click on the “Coarse Grain” button for coarse-grain polarity measurement.